Measurement of spin-dependent charged current deep inelastic scattering cross sections using the ZEUS detector at HERA

Catherine Louise Fry

Imperial College London

A thesis submitted for the degree of
Doctor of Philosophy of the University of London
and the Diploma of Imperial College

The work presented in this thesis is my own work.

Catherine Louise Fry

Abstract

Total and single-differential cross sections for $e^{\pm}p$ charged current (CC) deep inelastic scattering (DIS) at $Q^2 > 200$ GeV^2 were measured at positive and negative values of the longitudinal polarisation of the lepton beam, P_e, using data collected with the ZEUS detector at HERA. A good agreement was seen with the Standard Model (SM) prediction across the entire kinematic range of the analysis. The $e^{\pm}p$ total cross sections were fitted as a function of P_e and extrapolated to find the cross sections for a right-handed CC interaction in $e^{\pm}p$ DIS. These cross sections were consistent with the SM prediction of zero. From the extrapolated right-handed CC cross sections in $e^{\pm}p$ DIS, upper limits on the mass of a right-handed W boson were set at 170 GeV and 180 GeV, respectively, at a 95% confidence level. In addition, reduced double-differential cross sections for $e^{+}p$ and $e^{-}p$ CC DIS were extracted at $P_e = 0$ and a reasonable agreement with the SM prediction was observed.

Contents

List of Figures

List of Tables

Chapter 1

Introduction

In the search to uncover the fundamental nature of matter, the HERA accelerator in Hamburg, Germany, is at the forefront of current measurements. HERA collides electron or positron beams with proton beams at very high energies, enabling physicists to study, amongst other things, the structure of the proton. ZEUS and H1 are two general purpose detectors built around the *ep* interaction points. They measure the particles produced in the interactions and facilitate detailed studies of the Standard Model (SM) and searches for new particles.

HERA has been operating since 1992 and using the data collected, physicists have been able to construct a tremendously detailed model of the proton. The proton is made up of quarks and gluons, which are collectively referred to as partons. HERA experiments have determined the proton parton density functions (PDFs) and measured the proton structure functions with great precision across a wide kinematic range, elucidating the structure of the proton and the nature of the strong interaction.

In the years 2000 to 2002, HERA underwent an upgrade that resulted in increased luminosity and provided longitudinally polarised lepton beams to collide with the proton beams. The SM contains an electroweak interaction that is chiral; there are no right-handed weak interactions. Colliding longitudinally polarised leptons with protons is an excellent way to investigate the chiral form of the SM.

A direct test of the left-handed weak interaction is through the measurement

of charged current (CC) deep inelastic scattering (DIS) with longitudinally polarised lepton beams. CC DIS involves scattering a lepton off a proton with the exchange of a charged W boson, causing the proton to break up. In the SM there are no right-handed CC interactions or, expressed another way, no right-handed W bosons. Measuring the total cross section for CC DIS as a function of the longitudinal polarisation of the lepton beam, P_e, is an elegant test of this theory.

This thesis presents measurements of the total cross sections for e^+p and e^-p CC DIS at positive and negative values of P_e, using data collected with the ZEUS detector in the years 2004 to 2005. The measured cross sections are fitted and extrapolated to $P_e = \mp 1$, in order to extract the cross sections for right-handed CC DIS in $e^\pm p$ collisions. From the fitted cross sections for right-handed CC DIS, a lower limit is set on the mass of a right-handed W boson. In addition, single differential and reduced double differential cross sections are measured. The reduced cross sections provide new data to constrain further the proton PDFs.

The rest of this thesis is set out as follows. Chapter 2 contains an explanation of the theory describing CC DIS and presents the current status of measurements in this field. The HERA ep collider, the polarimeters and the ZEUS detector are described in Chapter 3 and in Chapter 4 the Monte Carlo simulation used in the analysis is introduced. The event reconstruction methods are presented and studied in Chapter 5. Chapter 6 provides a detailed explanation of CC event selection and background rejection. The results and detailed studies of the systematic uncertainties on the measurements are presented and discussed in Chapter 7 and the conclusions are summarised in Chapter 8.

Chapter 2

Deep inelastic scattering

This chapter provides an overview of the theory used to describe DIS and the current status of measurements in this field. First DIS at HERA [1] is introduced and the kinematic variables used to describe the DIS interaction are defined. The structure of the proton is described, firstly using the simple parton model [2] and then incorporating the theory of quantum chromodynamics (QCD) [3]. The weak interaction [3] is presented and the unpolarised and polarised forms of the cross sections for neutral and charged current DIS are given. Finally the search for right-handed charged current is introduced.

2.1 Deep inelastic scattering at HERA

DIS is the inelastic scattering of leptons off nucleons through the exchange of a γ, Z^0 or $W^{\pm}$ boson, causing the proton to break up [3]. It is a powerful tool for studying the internal structure of the nucleon and the strong and electroweak interactions. At HERA [1], electrons or positrons are scattered off protons. Experiments at other laboratories have used, for example, muons [4, 5, 6] or neutrinos [7] scattered off fixed targets of nucleons.

DIS comes in two varieties: charged current and neutral current (NC). In CC DIS a $W^{\pm}$ boson is exchanged and in NC DIS the exchanged particle is a Z^0 boson or a γ. The Feynman diagrams for these processes are given in Figure 2.1.

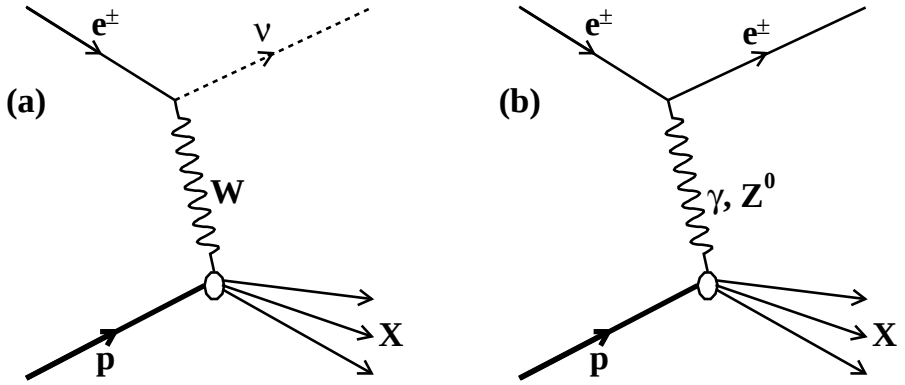

Figure 2.1: Feynman diagrams for (a) CC and (b) NC DIS of electrons or positrons scattering off protons.

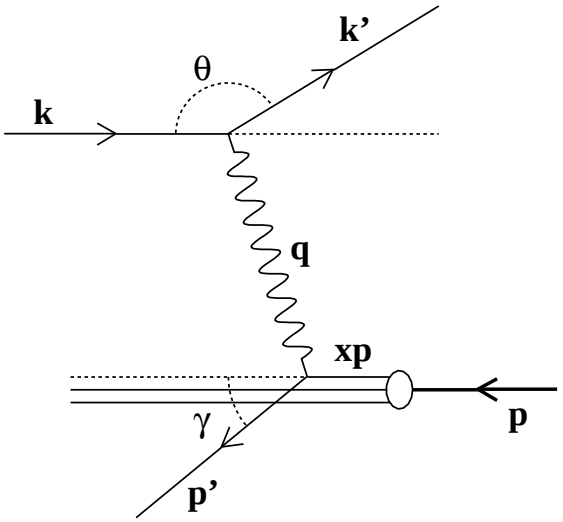

Figure 2.2: The laboratory frame definition of the angles and four-momenta of the particles involved in a DIS interaction. x is the fraction of the proton's momentum, p, carried by the struck parton.

The kinematics of DIS can be described by three Lorentz-invariant quantities: Q^2, x and y. Defining the four-momenta of the particles involved as shown in Figure 2.2, the quantities Q^2, x and y are given by the following expressions [3]:

$$Q^2 = -q^2 = -(k - k')^2, \tag{2.1}$$

$$x = \frac{Q^2}{2p \cdot q} \ , \tag{2.2}$$

$$y = \frac{p \cdot q}{p \cdot k} \ , \tag{2.3}$$

and, neglecting the masses of the incoming particles, they are constrained by:

$$Q^2 = xys, \tag{2.4}$$

where s is the ep centre-of-mass energy squared, which is given by:

$$s = (p + k)^2. \tag{2.5}$$

Q^2 can be considered as the probing power of the interaction; the larger the value of Q^2, the smaller the distance scale at which the proton's structure is probed. Treating the incoming particles as massless, the Bjorken scaling variable x is the fraction of the proton's momentum carried by the struck parton. The inelasticity of the collision is measured by y; the lower the value of y, the more inelastic the collision. The scattering angle is related to y by the following expression:

$$y = 1 - \sin^2 \frac{\theta^*}{2} \ , \tag{2.6}$$

where θ^* is the polar scattering angle in the lepton-quark centre-of-mass frame and the incoming quark is at $\theta^* = 0°$.

Using the ZEUS detector, DIS measurements are sensitive to the structure of the proton from $x \sim 10^{-6}$ to $x \sim 1$ and from $Q^2 \sim 0$ GeV^2 to $Q^2 \sim 10^5$ GeV^2. This is illustrated in Figure 2.3, where the kinematic ranges accessible to the ZEUS [8] and H1 [9] detectors are compared with those accessible to fixed-target experiments. The kinematic range of the HERA experiments reaches several orders of magnitude beyond that of the fixed target experiments, to lower x and to higher Q^2.

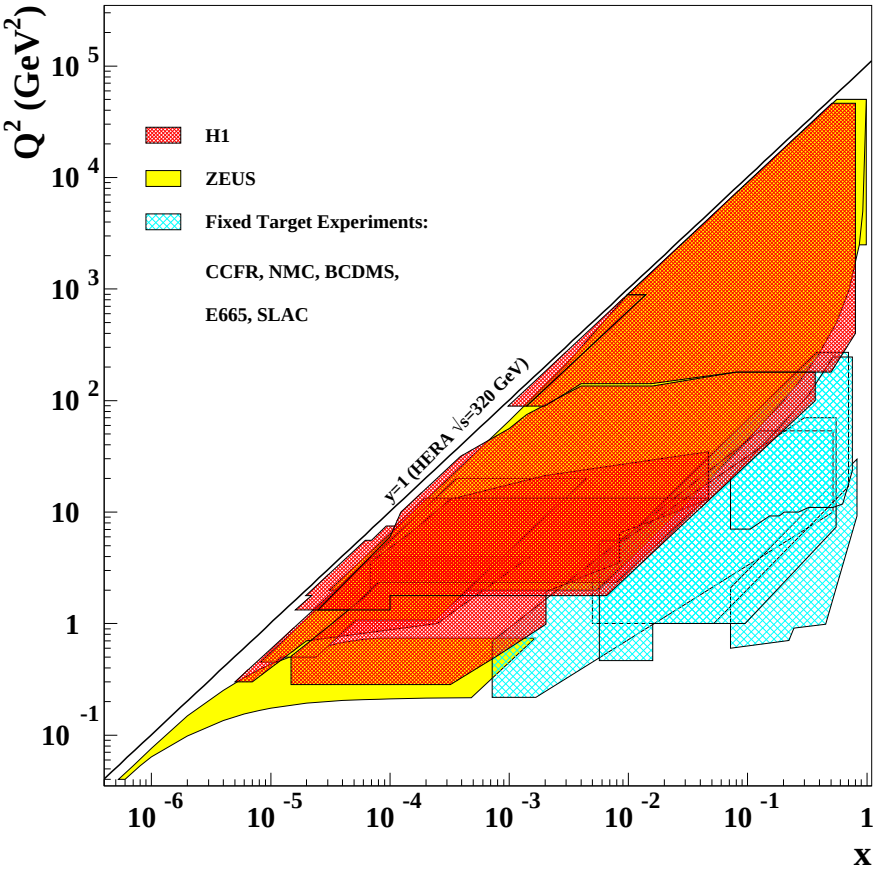

Figure 2.3: The kinematic range in x and Q^2 accessible to the ZEUS [8] and H1 [9] detectors, shown in yellow and red, respectively, compared with that accessible to the fixed target experiments, shown in turquoise. The black line indicates the kinematic limit of measurements at HERA, beyond which they are physically impossible.

2.2 The structure of the proton

In order to construct expressions for DIS cross sections, it is necessary to understand the structure of the proton and the functions used to describe it. The current description of the proton is based on the theory of QCD [3] and stems from the parton model [2], which was developed by Feynman in the 1960s.

2.2.1 The parton model

The general form of the cross section for ep DIS can be written as follows [3]:

$$d\sigma \sim L^e_{\mu\nu} W^{\mu\nu}, \tag{2.7}$$

where $L^e_{\mu\nu}$ is the leptonic tensor and $W^{\mu\nu}$ is the hadronic tensor.

Using the four momenta defined in Figure 2.2, the leptonic tensor for a purely electromagnetic exchange is given by [3] the following expression:

$$L^e_{\mu\nu} = 2\left(k'_\mu k_\nu + k'_\nu k_\mu + \frac{q^2}{2} g_{\mu\nu}\right), \tag{2.8}$$

where $g_{\mu\nu}$ is the metric tensor.

For a charge-parity conserving electromagnetic interaction, $W^{\mu\nu}$ can be expressed in terms of two independent structure functions, W_1 and W_2, and the four-momenta of the incoming proton and exchanged γ, p and q, as follows [3]:

$$W^{\mu\nu} = W_1(q^2,\nu)\left(-g^{\mu\nu} + \frac{q^\mu q^\nu}{q^2}\right) + W_2(q^2,\nu)\frac{1}{M^2}\left(p^\mu - \frac{p\cdot q}{q^2}q^\mu\right)\left(p^\nu - \frac{p\cdot q}{q^2}q^\nu\right), \tag{2.9}$$

where M is the proton mass and ν is defined as follows:

$$\nu = \frac{p\cdot q}{M}. \tag{2.10}$$

In the rest frame of the incoming proton, ν is the difference between the energies of the incoming and outgoing lepton [3].

Contracting $L^e_{\mu\nu}$ with $W^{\mu\nu}$ in the laboratory frame leads to the following cross section for electromagnetic DIS [3]:

$$\frac{d^2\sigma(ep\to eX)}{dE'd\Omega} = \frac{4\alpha^2 E'^2}{Q^4}\left(2W_1(q^2,\nu)\sin^2\frac{\theta}{2} + W_2(q^2,\nu)\cos^2\frac{\theta}{2}\right), \tag{2.11}$$

where α is the QED coupling constant and E' is the energy of the outgoing lepton.

Now consider the cross section for the scattering of the point-like spin-$\frac{1}{2}$ particles $e\mu \rightarrow e\mu$, which, in the laboratory frame, can be written as [3]:

$$\frac{d^2\sigma(e\mu \rightarrow e\mu)}{dE'd\Omega} = \frac{4\alpha^2 E'^2}{Q^4}\left(\cos^2\frac{\theta}{2} - \frac{q^2}{2m_\mu^2}\sin^2\frac{\theta}{2}\right)\delta\left(\nu + \frac{q^2}{2m_\mu}\right), \tag{2.12}$$

where m_μ is the mass of the muon and ν is still defined using equation 2.10, but with p as the four-momentum of the incoming muon and substituting m_μ for M.

If the proton is assumed to be made of non-interacting, point-like, spin-$\frac{1}{2}$ partons, then we can compare equations 2.11 and 2.12, and show that, for individual partons, i, W_1^i and W_2^i can be expressed as [3]:

$$\begin{aligned} 2W_1^i(\nu, Q^2) &= e_i^2\frac{Q^2}{2m_i^2}\delta\left(\nu - \frac{Q^2}{2m_i}\right) \text{ or} \\ 2mW_1^i(\nu, Q^2) &= e_i^2\frac{Q^2}{2m_i\nu}\delta\left(1 - \frac{Q^2}{2m_i\nu}\right), \end{aligned} \tag{2.13}$$

and

$$\begin{aligned} W_2^i(\nu, Q^2) &= e_i^2\delta\left(\nu - \frac{Q^2}{2m_i}\right) \text{ or} \\ \nu W_2^i(\nu, Q^2) &= e_i^2\delta\left(1 - \frac{Q^2}{2m_i\nu}\right), \end{aligned} \tag{2.14}$$

where the conversion $q^2 = -Q^2$ has been made and m_i and e_i are the mass and charge of parton i, respectively.

Equations 2.13 and 2.14 show that W_1^i and νW_2^i are functions only of the dimensionless variable $\frac{Q^2}{2m_i\nu}$ and not of Q^2 and ν individually. This means that for interactions with Q^2 large enough that the electron scatters off the individual point-like constituents of the proton, the following substitutions can be made [3]:

$$MW_1^i(\nu, Q^2) \rightarrow F_1^i(\omega) \text{ and} \tag{2.15}$$

$$\nu W_2^i(\nu, Q^2) \rightarrow F_2^i(\omega), \tag{2.16}$$

where ω is a dimensionless variable given by:

$$\omega = \frac{2M\nu}{Q^2}. \tag{2.17}$$

Note that the mass scale has been changed from the parton mass, m_i, to the proton mass, M.

Expressions 2.15 and 2.16 predict that if the proton is made up of point-like partons, then, at a given value of ω, the structure functions should be independent of Q^2, a behaviour called Bjorken scaling [10]. Figure 2.4 shows measurements of νW_2 at $\omega = 4$ from eN DIS experiments at the Stanford Linear Accelerator (SLAC) in the 1960s [11, 12]. In these measurements νW_2 is seen to be independent of Q^2, supporting the theory that the proton is composed of point-like partons.

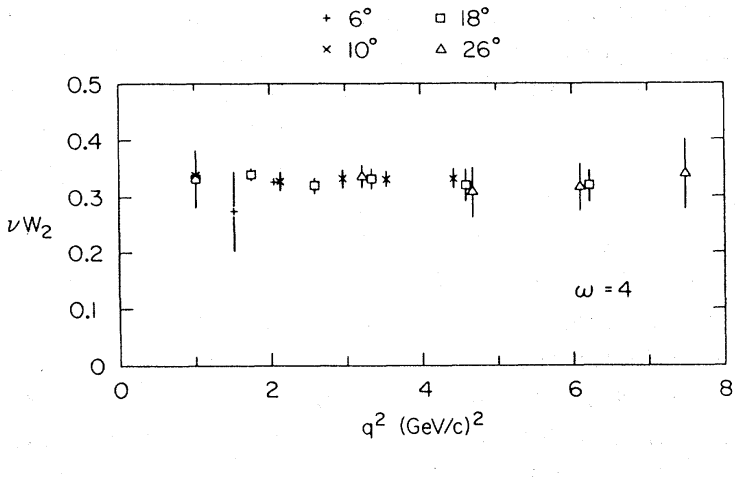

Figure 2.4: Measurements from experiments at SLAC [11, 12] demonstrating the scaling behaviour of the proton structure function νW_2 as a function of Q^2 at $\omega = 4$.

Using equations 2.13 to 2.16, for an electron scattering off a single parton, i, with charge e_i, fraction x of the proton's momentum and mass xM, F_1^i and F_2^i can be expressed as follows [3]:

$$F_1^i(\omega) = e_i^2 \frac{1}{2x^2\omega} \delta\left(1 - \frac{1}{x\omega}\right) \text{ and} \tag{2.18}$$

$$F_2^i(\omega) = e_i^2 \delta\left(1 - \frac{1}{x\omega}\right). \tag{2.19}$$

Summing these results over all the partons, i, in a proton gives [3]:

$$\begin{aligned} F_2(\omega) &= \sum_i \int dx f_i(x) e_i^2 \delta\left(1 - \frac{1}{x\omega}\right), \\ &= \sum_i \int dx f_i(x) e_i^2 x\delta\left(x - \frac{1}{\omega}\right) \text{ and} \qquad (2.20) \\ F_1(\omega) &= \frac{\omega}{2} F_2(\omega), \qquad (2.21) \end{aligned}$$

where $f_i(x)dx$ is the probability that parton i has momentum fraction $x \to x + dx$.

Then, writing equations 2.20 and 2.21 in terms of x gives [3]:

$$\begin{aligned} F_2(x) &= \sum_i e_i^2 f_i(x) x \text{ and} \qquad (2.22) \\ F_1(x) &= \frac{1}{2x} F_2(x), \qquad (2.23) \end{aligned}$$

where

$$x = \frac{1}{\omega} = \frac{Q^2}{2Mv}. \qquad (2.24)$$

Equation 2.23 is called the Callan-Gross relation [13] and it arises from the earlier assumption that partons are spin-$\frac{1}{2}$ particles[1]. Experimental evidence, presented in Figure 2.5, agrees with the Callan-Gross relation and supports the theory that partons are spin-$\frac{1}{2}$ [12].

Having established that the proton contains spin-$\frac{1}{2}$, point-like partons, physicists considered whether these partons were actually the u and d quarks that had been identified in hadron spectroscopy experiments [14]. If partons were quarks, then equation 2.22, considering only the light quarks u, d and s, could be written as [3]:

$$F_2(x) = \left(\frac{2}{3}\right)^2 x[u(x) + \bar{u}(x)] + \left(\frac{1}{3}\right)^2 x[d(x) + \bar{d}(x) + s(x) + \bar{s}(x)]. \qquad (2.25)$$

Considering the proton as containing valence quarks uud and a sea of $q\bar{q}$ pairs, with each sea quark having probability distribution $S(x)$, then, for ep DIS, equa-

[1]This assumption was made when we compared electrons scattering off partons with $e\mu$ scattering.

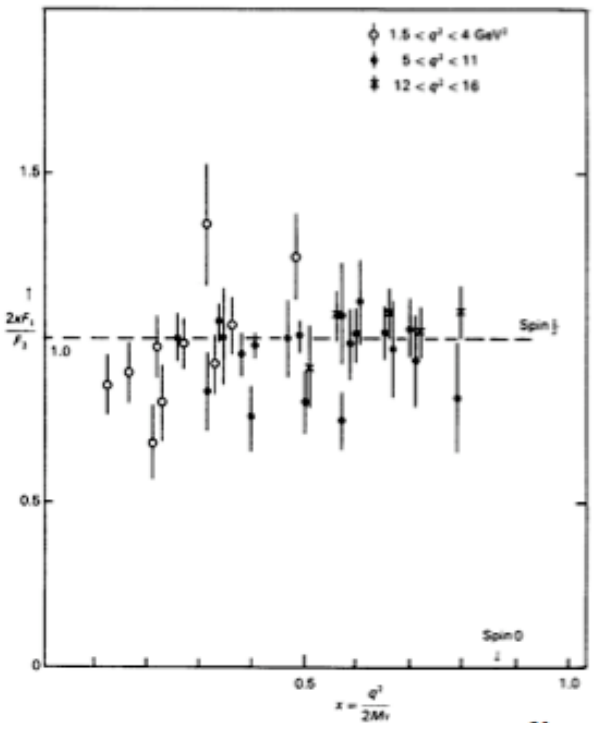

Figure 2.5: Measurements of $2xF_1/F_2$ plotted as a function of x [12]. The Callan-Gross relation is observed to hold, supporting the theory that partons are spin-$\frac{1}{2}$ particles.

tion 2.25 can be written in terms of the quark PDFs as [3]:

$$F_2^{ep}(x) = \frac{4}{9}xu_v(x) + \frac{1}{9}xd_v(x) + \frac{4}{3}xS(x), \tag{2.26}$$

where u_v and d_v are the probability distributions of the u and d valence quarks in the proton, respectively, and, using strong isospin symmetry, for en DIS equation 2.25 can be written as:

$$F_2^{en}(x) = \frac{1}{9}xu_v(x) + \frac{4}{9}xd_v(x) + \frac{4}{3}xS(x). \tag{2.27}$$

Subtracting 2.27 from 2.26 removes the sea quarks and leaves:

$$F_2^{ep} - F_2^{en} = \frac{1}{3}x(u_v(x) - d_v(x)). \tag{2.28}$$

So, if nucleons contain three bound valence quarks, measuring $F_2^{ep} - F_2^{en}$ should show a peak at $x \sim \frac{1}{3}$. This measurement was performed and the results, shown in Figure 2.6, confirm that nucleons contain three valence quarks [14].

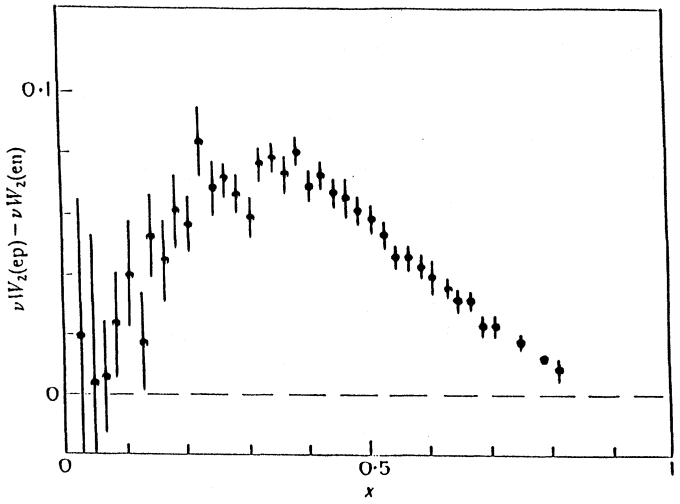

Figure 2.6: Measurement from DIS experiments at SLAC [14] of $F_2^{ep} - F_2^{en}$ as a function of x showing a peak at $x \sim \frac{1}{3}$ and supporting that model that nucleons contain three bound valence quarks.

Comparing F_2 measured from eN DIS with F_2 measured from νN DIS confirmed that the charges on the partons were the same as those attributed to the quarks: $+\frac{2}{3}$ for u-quarks and $-\frac{1}{3}$ for d-quarks [14].

After identifying partons as quarks, the final component of the parton model was the addition of gluons. If the proton is just made of quarks, then summing over the quark momenta should give the proton momentum. However, νp scattering measurements showed that the u-quarks in a proton carried 36% of its momentum and the d-quarks carried 18%, leaving 46% of the proton momentum unaccounted for [14, 15]. Physicists concluded that the rest of the proton momentum was carried by neutral particles that could not be probed by the γ. These particles were called gluons [3].

To summarise, the parton model describes the proton as being made of valence quarks (uud), sea quarks and gluons. The quarks are point-like, non-interacting, spin-$\frac{1}{2}$ particles with fractional charges, which carry around 54% of the proton's momentum. The remaining 46% of the proton's momentum is carried by the gluons.

2.2.2 Quantum chromodynamics

QCD is the theory used to describe the strong interaction, which occurs between quarks and gluons. In QCD the quarks carry colour charge, which can be red (r), green (g) or blue (b). Anti-quarks have colour charge $\bar{r}$, $\bar{g}$ or $\bar{b}$. There are eight gluons that also carry colour charge (they are bi-coloured), which means that they can self-interact unlike, for example, the photon of QED, which is electrically neutral. The coupling constant for strong interactions is α_s [3].

QCD has a significant impact on DIS measurements. In the parton model the quarks are non-interacting, meaning that they cannot emit or absorb gluons, whereas in QCD the quarks are able to emit and absorb gluons. A quark can radiate a gluon before or after it is struck by the exchanged boson, as shown in Figures 2.7 (a) and (b), and an emitted gluon can create a $q\bar{q}$ pair with which the exchanged boson could interact, as shown in Figures 2.7 (c) and (d).

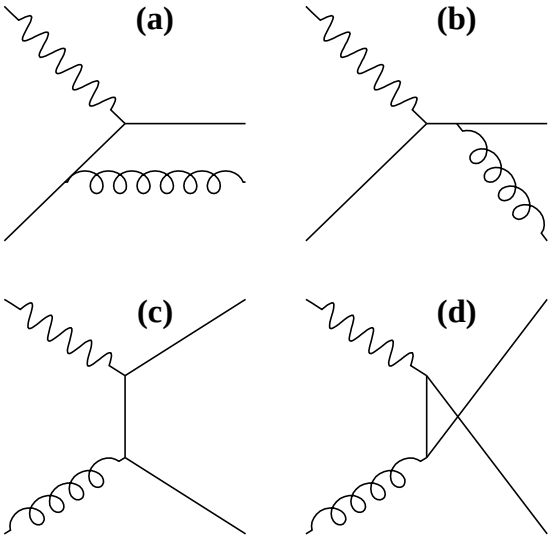

Figure 2.7: $\mathcal{O}(\alpha\alpha_s)$ QCD contributions to DIS.

At higher values of Q^2 the proton is probed at a smaller distance scale and the exchanged boson is more sensitive to the gluon radiation and $q\bar{q}$ pair production in the proton. This means that F_2 should depend on Q^2, as well as x, and the Bjorken scaling behaviour predicted by the parton model is violated.

Measurements demonstrating the scaling violation of F_2 are presented in Figure 2.8 [4, 5, 6, 16, 17]. At low values of x, F_2 increases with Q^2 and at high values of x it decreases with Q^2. This is because at high Q^2 more low-x quarks are probed.

DIS measurements can be fitted at a given Q^2 value in order to extract estimates of the proton PDFs. The PDFs are then evolved to other values of Q^2 using the DGLAP equations [19, 20, 21, 22]. Different combinations of experimental data sets can be used to constrain the PDFs. The ZEUS Collaboration performs a fit called the ZEUS-JETS fit [23], which relies entirely on ZEUS measurements of proton structure functions and jet data. Figure 2.9 shows the predictions of the ZEUS-JETS fit for the u and d valence quarks, the sea and the gluon distributions.

In Figure 2.9 the ZEUS-JETS PDFs are compared with the ZEUS-S [24], MRST [25] and CTEQ6 [26] PDFs. These fits use additional data such as: νp, μd and μp structure function measurements to constrain the sea, valence and low-x gluon distributions; di-lepton production from pN collisions to constrain the sea distribution and the ratio $\bar{d}/\bar{u}$; $W^{\pm}$ production to constrain the sea and valence distributions and the ratio d/u; and prompt photon or single jet production to constrain the high-x gluon distribution. Good agreement is seen between the predictions of all four PDFs.

Helicity conservation forbids the "head-on" scattering of a quark off a longitudinally polarised photon. However, as described earlier, the gluons in the proton can produce $q\bar{q}$ pairs with some momentum transverse to the direction of the proton momentum, which can then scatter off longitudinally polarised photons whilst conserving helicity. This contribution is included in the longitudinal structure function, which is given by F_L [3]:

$$F_L \propto \alpha_s x g(x, Q^2), \tag{2.29}$$

where $g(x, Q^2)$ is the gluon PDF.

In summary, in the QCD model of the proton, the quarks emit and absorb gluons.

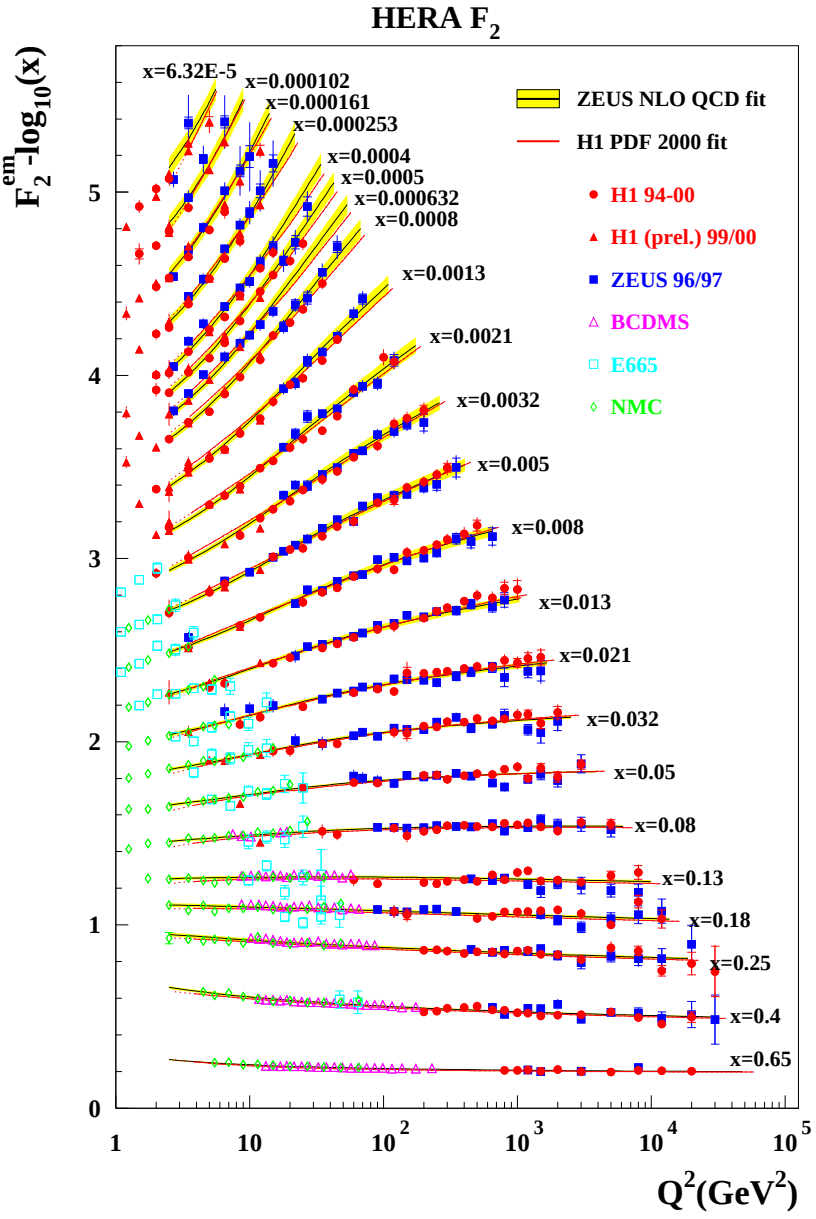

Figure 2.8: Measurements of the proton structure function F_2 as a function of Q^2 at fixed values of x from the ZEUS [16] (blue squares) and H1 [17], (red circles and triangles) experiments and three fixed target experiments [4, 5, 6] (open points). The yellow and red curves show the SM predictions evaluated using the ZEUS NLO QCD fit [18] and the H1 PDF 2000 fit [17], respectively.

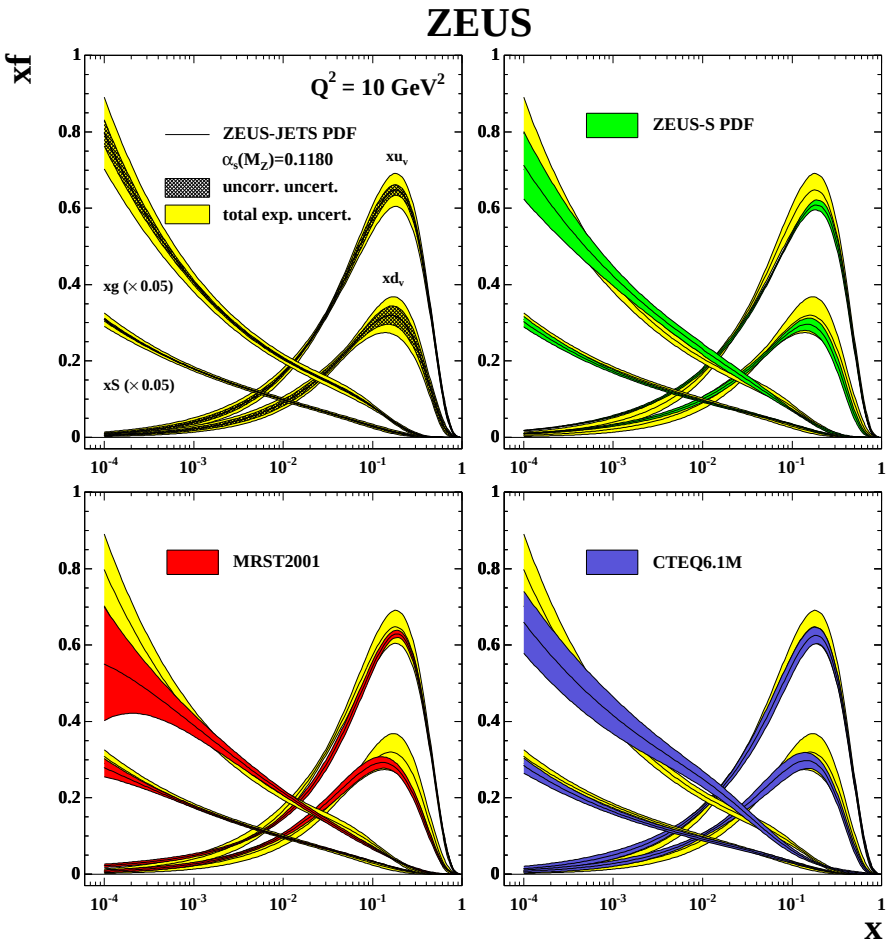

Figure 2.9: Measurements of the proton PDFs for the u and d valence quarks, the sea and the gluon. In the top left plot the yellow band shows the PDFs extracted by performing a fit purely to ZEUS data, called the ZEUS-JETS fit [23]. The other three plots compare the ZEUS-JETS PDF (yellow) with the ZEUS-S [24] (green), MRST [25] (red) and CTEQ6 [26] (purple) PDFs.

Depending on the scale at which the proton is probed, the exchanged boson is sensitive to quarks with different momentum fractions and the structure functions exhibit scaling violation. The valence, sea and gluon PDFs can be determined by fitting data, including structure function measurements. Finally, QCD introduces the structure function F_L, which is a function of the gluon PDF.

2.3 The weak interaction

The weak current can be expressed in terms of the Dirac γ-matrices as [3]:

$$\gamma^\mu \frac{1}{2}(1-\gamma^5), \tag{2.30}$$

where the γ^μ are four four-by-four matrices, which serve as coefficients of the Dirac equation, and $\gamma^5 = i\gamma^0\gamma^1\gamma^2\gamma^3$ [3]. The presence of the $1-\gamma^5$ factor gives the weak current a "vector $-$ axial-vector" form.

Under a parity transformation, vector and axial-vector currents transform as even and odd functions, respectively, which means that the "vector $-$ axial-vector" weak current violates parity conservation. The contributions from the weak interaction lead to the NC structure functions being split into two parts: a parity-conserving part, F_2, and a parity-violating part, which is described by the structure function xF_3.

xF_3 only contains contributions from Z^0 or $W^\pm$ exchange or $\gamma - Z^0$ interference. Therefore, due to the masses of the Z^0 and $W^\pm$ bosons, xF_3 is only significant at high Q^2. Figure 2.10 shows measurements of $xF_3^{\gamma Z}$ as a function of x at $Q^2 = 1500$ GeV^2 [27].

In the weak current, $\frac{1}{2}(1-\gamma^5)$ is called the projection operator, as it projects out the left-handed (right-handed) component of a fermion (anti-fermion). This means that DIS is sensitive to the helicity of the incoming lepton. At HERA the lepton beam energy is high enough that the lepton mass may be neglected and consequently the difference between handedness and helicity may also be neglected.

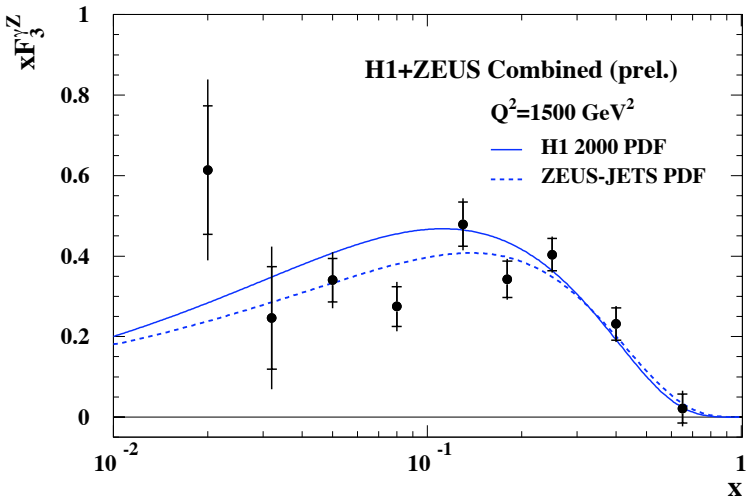

Figure 2.10: The points are measurements of the proton structure function $xF_3^{\gamma Z}$ as a function of x at $Q^2 = 1500$ GeV^2 using NC DIS data collected with the ZEUS and H1 detectors [27]. The curves show the SM prediction evaluated using the ZEUS-JETS [23] and H1 2000 PDFs [17].

It is impossible to measure the helicity of each lepton, so the quantity P_e, the longitudinal polarisation of the lepton beam, is defined as follows:

$$P_e = \frac{N_{\mathrm{R}} - N_{\mathrm{L}}}{N_{\mathrm{R}} + N_{\mathrm{L}}} \, , \tag{2.31}$$

where N_{R} and N_{L} are the numbers of right- and left-handed leptons in the beam. DIS cross-section measurements, which are performed by integrating over all ep interactions, are therefore functions of P_e.

2.4 Neutral current cross sections

The double-differential cross section for NC DIS can be expressed as [28]:

$$\frac{d^2\sigma^{\mathrm{NC}}(e^{\pm}p)}{dxdQ^2} = \frac{2\pi\alpha^2}{xQ^4}\left(Y_+F_2^{\mathrm{NC}}(x,Q^2) - y^2F_L^{\mathrm{NC}}(x,Q^2) \mp Y_-xF_3^{\mathrm{NC}}(x,Q^2)\right), \tag{2.32}$$

where α is the QED coupling constant,

$$Y_{\pm} = 1 \pm (1-y)^2, \tag{2.33}$$

and F_2^{NC}, F_L^{NC} and xF_3^{NC} are the NC proton structure functions.

$F_2^{\rm NC}$ can be written in terms of the sum of the quark and anti-quark PDFs as:

$$F_2^{\rm NC}(x,Q^2) = \sum_i A_i^{\rm L,R}(Q^2) \times \big(xq_i(x,Q^2) + x\bar{q}_i(x,Q^2)\big), \tag{2.34}$$

summing over the quark flavours, i, where the couplings A_i are given by:

$$A_i^{\rm L,R}(Q^2) = e_i^2 + 2e_ie_e(v_e \pm a_e)v_i\chi_Z + (v_e \pm a_e)^2(v_i^2 + a_i^2)\chi_Z^2. \tag{2.35}$$

Here, e_i is the fractional charge of the quark i, e_e is the lepton charge and the couplings depend on whether the leptons are L, left-handed (upper signs), or R, right-handed (lower signs).

The vector, v_f, and axial-vector, a_f, couplings of the Z^0 boson to the quarks and leptons are given by [3]:

$$v_f = T_{3f} - 2e_f \sin^2\theta_W \quad \text{and} \tag{2.36}$$

$$a_f = T_{3f}, \tag{2.37}$$

where T_{3f} is the weak isospin and θ_W is the electroweak mixing angle. T_{3f} is $+\frac{1}{2}$ for neutrinos and u-quarks and -$\frac{1}{2}$ for charged leptons and d-quarks. For anti-particles the signs are opposite.

χ_Z is the Z^0 propagator term, which is given by:

$$\chi_Z = \frac{Q^2}{Q^2 + M_Z^2}\frac{1}{\sin^2\theta_W}\ , \tag{2.38}$$

where M_Z is the mass of the Z^0 boson.

xF_3 is sensitive to the difference between the quark and anti-quark PDFs and can be written as:

$$xF_3^{\rm NC}(x,Q^2) = \sum_i B_i^{\rm L,R}(Q^2) \times \big(xq_i(x,Q^2) - x\bar{q}_i(x,Q^2)\big), \tag{2.39}$$

where the couplings B_i are given by:

$$B_i^{\rm L,R}(Q^2) = \mp 2e_ie_e(v_e \pm a_e)a_i\chi_Z \pm 2(v_e \pm a_e)^2 v_i a_i \chi_Z^2. \tag{2.40}$$

NC cross sections have been measured by the ZEUS and H1 collaborations [29, 30, 31, 32] and measurements of $d\sigma^{\rm NC}/dQ^2$ as a function of Q^2 for e^+p and e^-p collisions are presented in Figure 2.11.

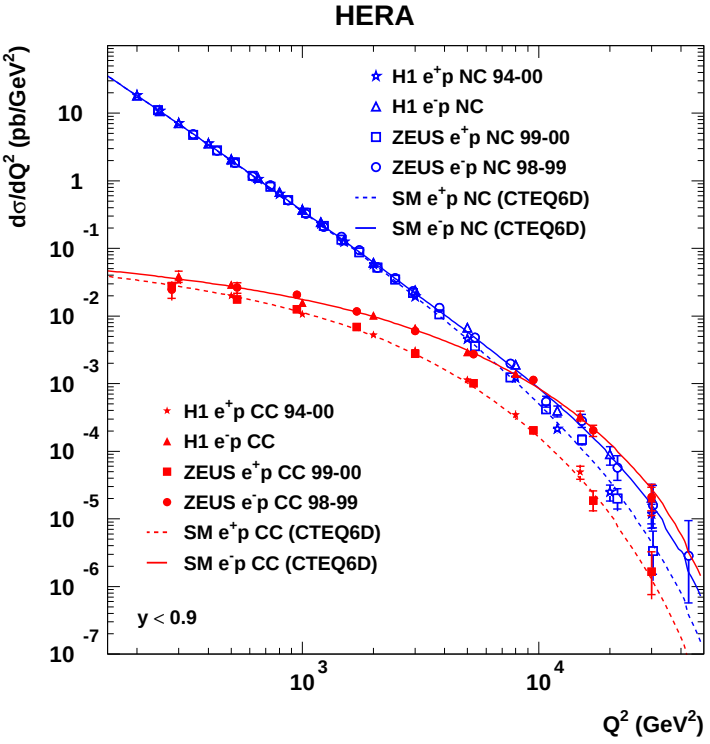

Figure 2.11: Measurements of NC (blue points) and CC (red points) cross sections $d\sigma/dQ^2$ for $y < 0.9$ as a function of Q^2 for e^+p and e^-p collisions using data collected with the ZEUS and H1 detectors [29, 30, 31, 32]. The curves show the SM predictions for these cross sections evaluated using the CTEQ6D PDFs [26].

2.4.1 Polarisation dependence

As explained in section 2.3, the weak part of the NC DIS cross section, which involves Z^0 exchange and $\gamma - Z^0$ interference, is sensitive to P_e. However, the purely electromagnetic part is not dependent on P_e. Therefore, due to the mass of the Z^0 boson, the sensitivity to P_e increases as a function of Q^2. This is illustrated in Figure 2.12 [33], which shows measurements of $d\sigma^{\mathrm{NC}}/dQ^2(e^-p)$ as a function of Q^2, at positive and negative values of P_e, and the ratio between these measurements. At low values of Q^2 the ratio is close to one, but as Q^2 increases the effect of the longitudinally polarised lepton beams causes the ratio to fall.

In order to study these cross sections in more detail, it is useful to split the NC cross section into terms depending on P_e, which involve Z^0 exchange and $\gamma - Z^0$ interference, and terms that do not depend on P_e, involving only γ exchange, as follows [34]:

$$\frac{d^2\sigma^{\mathrm{NC}}(e^{\pm}p)}{dxdQ^2} = \frac{2\pi\alpha^2}{xQ^4}[H_0^{\pm}(x,Q^2) - P_e H_{P_e}^{\pm}(x,Q^2)]. \tag{2.41}$$

The unpolarised part, $H_0^{\pm}$, is given by:

$$H_0^{\pm}(x,Q^2) = Y_+ F_2^0(x,Q^2) \mp Y_- x F_3^0(x,Q^2), \tag{2.42}$$

where

$$F_2^0(x,Q^2) = \sum_i A_i^0(Q^2) x\big(q_i(x,Q^2) + \bar{q}_i(x,Q^2)\big), \tag{2.43}$$

$$xF_3^0(x,Q^2) = \sum_i B_i^0(Q^2) x\big(q_i(x,Q^2) - \bar{q}_i(x,Q^2)\big), \tag{2.44}$$

$$A_i^0(Q^2) = e_i^2 - 2e_i v_i v_e \chi_Z + (v_i^2 + a_i^2)(v_e^2 + a_e^2)\chi_Z^2 \quad \text{and} \tag{2.45}$$

$$B_i^0(Q^2) = -2e_i a_i a_e \chi_Z + 4a_i a_e v_i v_e \chi_Z^2. \tag{2.46}$$

The polarised part, $H_{P_e}^{\pm}$, is given by:

$$H_{P_e}^{\pm}(x,Q^2) = Y_+ F_2^{P_e}(x,Q^2) \mp Y_- x F_3^{P_e}(x,Q^2), \tag{2.47}$$

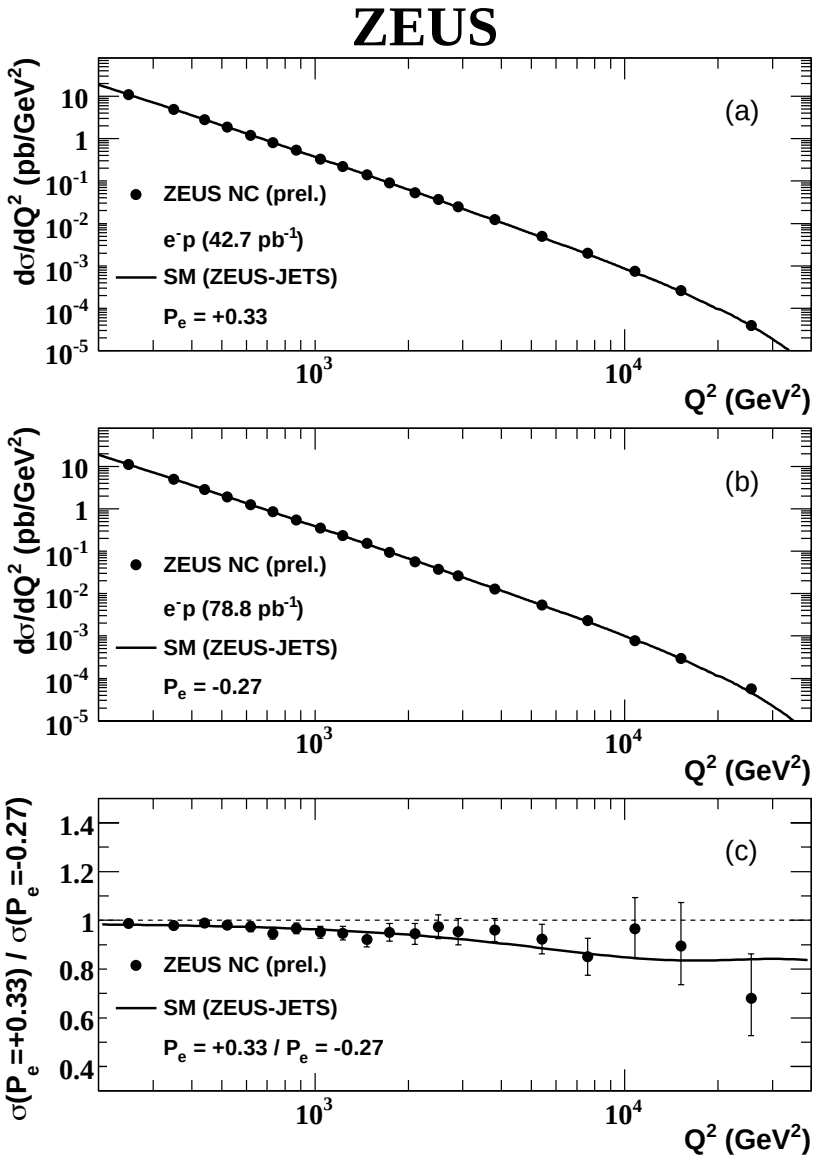

Figure 2.12: NC DIS cross sections $d\sigma/dQ^2$ as a function of Q^2 measured from e^-p collisions with (a) positive and (b) negative values of P_e [33]. The ratio between the two measurements is shown in (c) and the lines show the SM prediction evaluated using the ZEUS-JETS PDFs [23].

where

$$F_2^{P_e}(x,Q^2) = \sum_i A^{P_e}(Q^2)_i x(q_i(x,Q^2)+\bar{q}_i(x,Q^2)), \quad (2.48)$$

$$xF_3^{P_e}(x,Q^2) = \sum_i B^{P_e}(Q^2)_i x(q_i(x,Q^2)-\bar{q}_i(x,Q^2)), \quad (2.49)$$

$$A_i^{P_e}(Q^2) = 2e_i v_i a_e \chi_Z + 2(v_i^2+a_i^2)v_e a_e \chi_Z^2 \text{ and} \quad (2.50)$$

$$B_i^{P_e}(Q^2) = 2e_i a_i v_e \chi_Z - 2v_i a_i (v_e^2+a_e^2)\chi_Z^2. \quad (2.51)$$

The coupling v_e is small, so with a longitudinally unpolarised lepton beam, NC cross sections are sensitive to the axial-vector couplings a_i from xF_3^0. However, with a longitudinally polarised lepton beam, sensitivity to the vector couplings v_i is gained from $F_2^{P_e}$.

Figure 2.13 shows vector and axial-vector couplings of the Z^0 to the u and the d quarks extracted from fits to DIS measurements including data with positive and negative values of P_e [35]. Compared to measurements from experiments at other accelerators [36, 37] and measurements from the H1 experiment [38], which do not include any longitudinally polarised data, the improvement in sensitivity is clear.

2.5 Charged current cross sections

The double-differential cross section for CC DIS can be expressed as follows [28]:

$$\frac{d^2\sigma^{\mathrm{CC}}(e^{\pm}p)}{dxdQ^2} = \frac{G_F^2}{4\pi x}\frac{M_W^4}{(Q^2+M_W^2)^2}\left(Y_+F_2^{\mathrm{CC}} - y^2F_L^{\mathrm{CC}} \mp Y_-xF_3^{\mathrm{CC}}\right), \quad (2.52)$$

where G_F is the weak coupling constant, M_W is the mass of the W boson and F_2^{CC}, F_L^{CC} and xF_3^{CC} are the CC proton structure functions.

At leading order in QCD and expressing the structure functions in terms of the PDFs, the CC cross sections for $e^{\pm}p$ scattering can be written as:

$$\frac{d^2\sigma^{\mathrm{CC}}(e^{+}p)}{dxdQ^2} = \frac{G_F^2}{2\pi x}\frac{M_W^2}{(Q^2+M_W^2)^2}\left((1-y)^2\sum_{i=d,s}xq_i(x,Q^2) + \sum_{i=u,c}x\bar{q}_i(x,Q^2)\right) \quad (2.53)$$

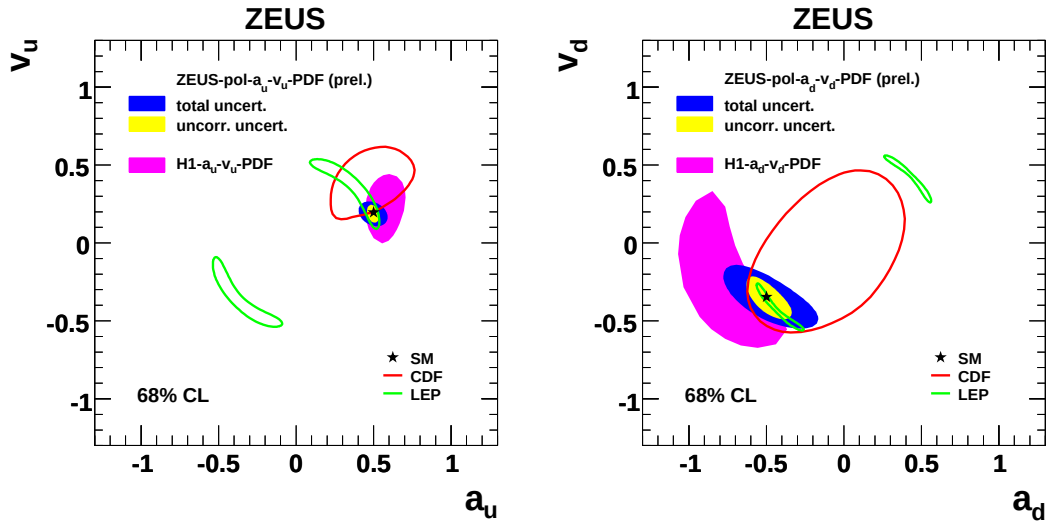

Figure 2.13: Contour plots showing 68% confidence level limits from fits to the couplings v_u and a_u (left), and v_d and a_d (right). Only the parameters on the axes were allowed to vary in each fit. The measurements are extracted from ZEUS data [35] (yellow and blue regions) which include DIS measurements with a longitudinally polarised electron beam, H1 data [38] (pink regions) without any measurements with a longitudinally polarised lepton beam, LEP data [37] (green contours) and CDF data [36] (red contours). The stars show the SM predictions.

and

$$\frac{d^2\sigma^{\mathrm{CC}}(e^-p)}{dxdQ^2} = \frac{G_F^2}{2\pi x}\frac{M_W^2}{(Q^2+M_W^2)^2}\left(\sum_{i=u,c} xq_i(x,Q^2) + (1-y)^2\sum_{i=d,s} x\bar{q}_i(x,Q^2)\right), \tag{2.54}$$

where the charge of the incoming lepton dictates which flavours of quarks and anti-quarks contribute to the cross section. e^+p and e^-p CC DIS can therefore be used to gain sensitivity to different flavour PDFs. Measurements of e^+p CC DIS are particularly important, as the d-quark PDF is currently less precisely determined than the u-quark PDF.

The double-differential cross sections can also be expressed in the form of reduced cross sections, where the coupling and propagator term is factored out to leave only the PDF sensitivity. The reduced cross sections, $\tilde{\sigma}$, are defined as follows:

$$\tilde{\sigma}(e^\pm p) = \left[\frac{G_F^2}{2\pi x}\left(\frac{M_W^4}{(Q^2+M_W^2)^2}\right)\right]^{-1}\cdot\frac{d^2\sigma^{\mathrm{CC}}(e^\pm p)}{dxdQ^2}\ . \tag{2.55}$$

Applying this definition to equations 2.53 and 2.54 gives the following reduced

cross sections at leading order in QCD:

$$\tilde{\sigma}(e^+p) = x[(\bar{u} + \bar{c}) + (1-y)^2(d+s)] \quad \text{and} \tag{2.56}$$

$$\tilde{\sigma}(e^-p) = x[(u + c) + (1-y)^2(\bar{d}+\bar{s})]. \tag{2.57}$$

Equations 2.56 and 2.57 show that for e^+p (e^-p) CC DIS the quark (anti-quark) contribution is suppressed by a factor of $(1-y)^2$. Figure 2.14 illustrates different helicity combinations of leptons scattering off quarks and indicates how, due to angular momentum conservation, the matrix element for certain combinations is suppressed by a factor of $1 - \cos\theta^*$. Recalling equation 2.6 and expressing $1-\cos\theta^*$ as $2\sin^2\frac{\theta^*}{2}$, shows that this factor is proportional to $1-y$ and therefore the cross section is suppressed by a factor of $(1-y)^2$. Since there are no right-handed neutrinos (left-handed anti-neutrinos) in the SM, for e^+p (e^-p) scattering only diagrams (b) and (d) ((a) and (c)) contribute to the CC cross section.

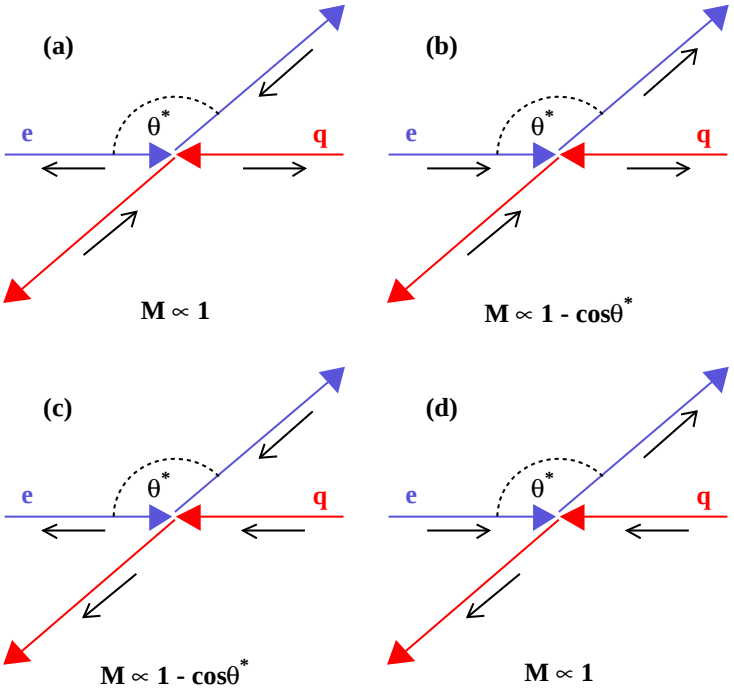

Figure 2.14: Diagrams of eq scattering in the eq centre-of-mass frame with different helicity combinations. The short black arrows indicate the direction of the fermion spin. As indicated below the diagrams, due to angular momentum conservation the matrix element, M, is suppressed by a factor of $1 - \cos\theta^*$ for certain helicity combinations.

Measurements of CC DIS can also be used to determine the electroweak parameters M_W and G_F, by performing fits to the propagator term in the cross sections.

CC DIS cross sections have been measured by the ZEUS and H1 collaborations [39, 40, 41, 31, 32] and their measurements are shown in Figure 2.11 with the NC measurements. At high Q^2, the CC and NC cross sections are comparable in size due to electroweak unification.

2.5.1 Electroweak radiative corrections

The DIS Born-level cross section must be corrected to account for various electroweak radiative processes. The lowest order ($\mathcal{O}(\alpha)$) corrections are shown in Figure 2.15 and comprise initial state radiation (ISR), final state radiation (FSR), and γ emission from the exchanged boson. The largest contribution comes from ISR from the incoming lepton.

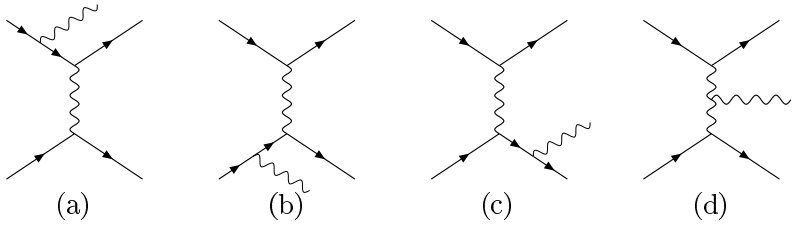

Figure 2.15: $\mathcal{O}(\alpha)$ electroweak radiative corrections to the CC cross section. (a) and (b) are ISR from the incoming quark or lepton, (c) is FSR from the outgoing quark and (d) is γ radiation from the exchanged boson.

Further corrections arise from the electroweak loops shown in Figure 2.16. The correction for the W self-energy gives the largest contribution.

2.5.2 Polarisation dependence

As explained in section 2.3, the weak interaction in DIS is sensitive to the helicity of the incoming lepton. Since CC DIS is a purely weak interaction, the cross sec-

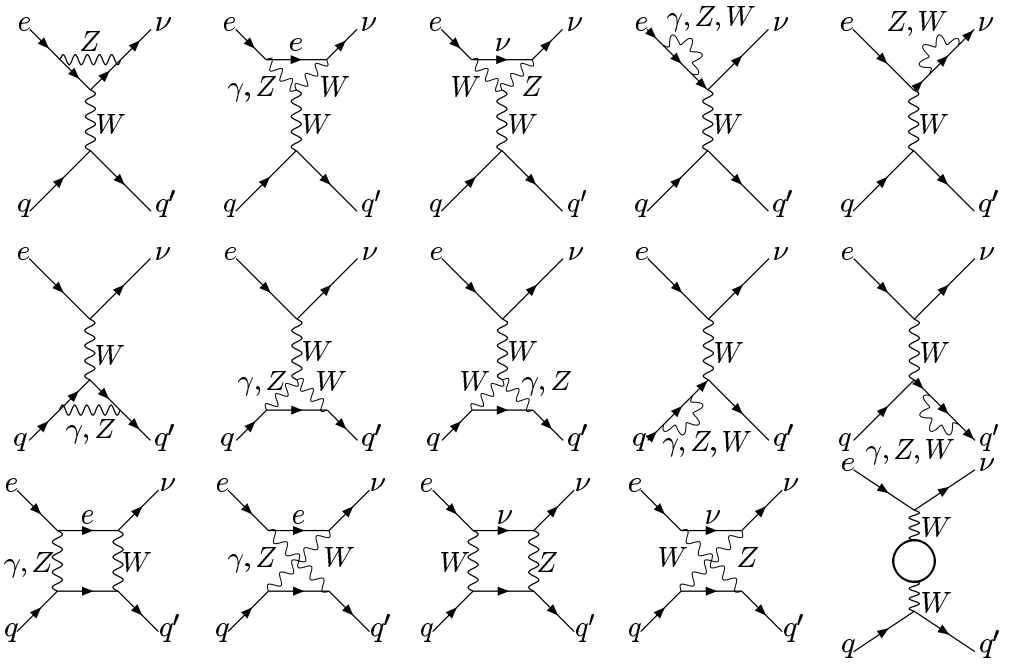

Figure 2.16: Electroweak radiative corrections to the Born-level CC cross section.

tion for CC DIS depends linearly on P_e and can be expressed as follows [34]:

$$\sigma^{\pm}_{\mathrm{CC}}(P_e) = (1 \pm P_e)\sigma_0, \tag{2.58}$$

where σ_0 is the cross section at $P_e = 0$. The SM prediction for the total CC cross section for $e^{\pm}p$ scattering as a function of P_e is shown in Figure 2.17. For $e^{\pm}p$ collisions the cross section is zero at $P_e = \mp 1$.

The ZEUS and H1 collaborations have measured the CC total cross section with longitudinally polarised positron beams [42, 43], as shown in Figure 2.18, and the dependence on P_e is clearly observed.

2.6 Right-handed charged current

In the SM there is no right-handed charged current and the electroweak interaction is represented by the group [3]:

$$SU(2)_L \times U(1), \tag{2.59}$$

where the subscript L indicates that this is a left-handed group.

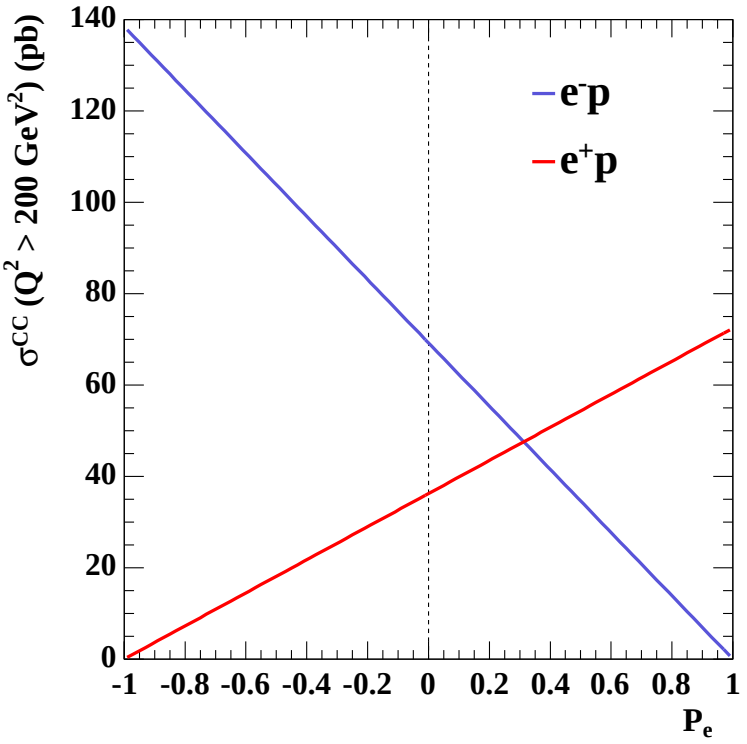

Figure 2.17: The SM prediction, evaluated with the ZEUS-JETS PDFs, for the total CC cross section for $Q^2 > 200$ GeV^2 for e^-p (blue) and e^+p (red) collisions as a function of P_e.

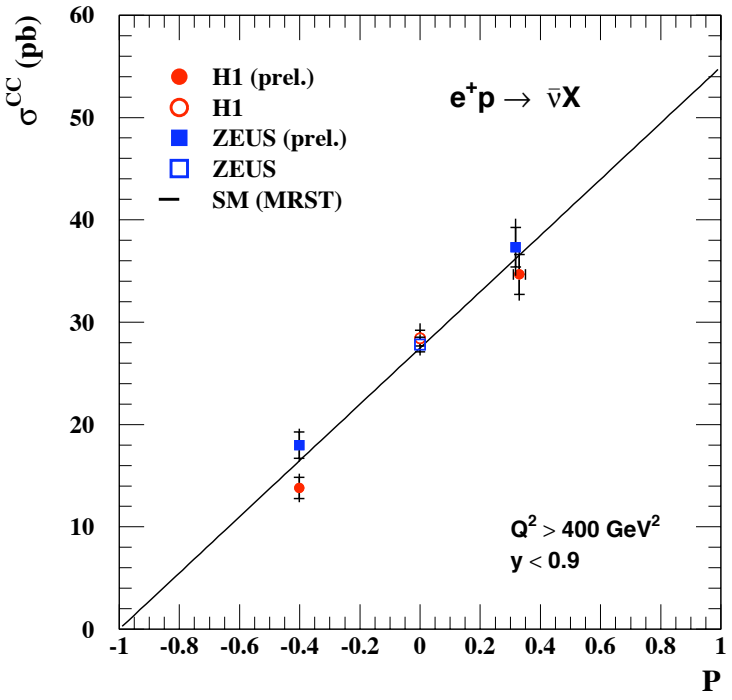

Figure 2.18: The points show measurements from the ZEUS and H1 collaborations [42, 43] of the total CC e^+p cross section for $Q^2 > 400$ GeV^2 and $y < 0.9$ with positive, negative and zero longitudinal polarisation of the positron beam. The solid line shows the SM prediction evaluated using the MRST PDFs [25].

However, extensions to the SM have been suggested and the electroweak interaction could, for example, be represented by the left-right symmetric group [44]:

$$SU(2)_L \times SU(2)_R \times U(1), \tag{2.60}$$

which would lead to the existence of right-handed $W_R^{\pm}$ bosons, a neutral Z' boson and massive right-handed neutrinos.

The UA2 experiment at CERN [45] and at the DØ and CDF experiments at the Tevatron [46, 47] have searched for the W_R boson and various limits have been placed on its mass. These limits depend on factors such as the mass of the right-handed neutrinos, the mixing matrix for right-handed quarks, the right-handed coupling constant and whether the right-handed neutrino is Dirac or Majorana.

At HERA, W_R bosons could be exchanged through the CC DIS process illustrated in Figure 2.19, which would contribute to the measured CC cross section [44].

The SM predicts that the CC cross section for $e^{\pm}p$ collisions should be zero at $P_e = \mp 1$. However, if there were right-handed CC interactions contributing to the measured cross section, then this would be non-zero.

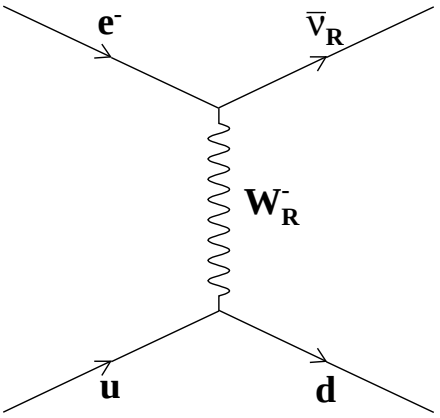

Figure 2.19: A Feynman diagram of $e^{-}p$ CC DIS exchanging a W_R boson.

One way to test for the existence of right-handed CC at HERA is to measure the $e^{\pm}p$ CC cross section as a function of P_e, extrapolate the measurements to $P_e = \mp 1$ and see if they predict a non-zero cross section. An upper limit on the cross section for right-handed CC DIS can then be transformed into a lower limit on the mass of a right-handed W boson, M_{W_R}. This limit would be based only on the assumption that the right-handed CC interaction has the same coupling constant and propagator form as the SM CC interaction.

Chapter 3

HERA and the ZEUS detector

This chapter presents the layout and operation of the HERA *ep* collider, the apparatus to provide and to measure the longitudinally polarised lepton beam and the main components of the ZEUS detector that are relevant for this analysis.

3.1 HERA

The Hadron Elektron Ring Anlage (HERA) [1] is situated at the Deutsches Elektronen-Synchrotron (DESY) laboratory in Hamburg, Germany, where electrons or positrons have been collided with protons since 1992. This time has been split into two periods: HERA-I, which ran until the year 2000, and HERA-II, which will end in 2007.

The HERA ring has a circumference of 6.3 km, around which there are currently three running experiments. The ZEUS [8] and H1 [9] experiments study the interactions caused by colliding the lepton and proton beams and the HERMES experiment [48] studies the interactions produced when the lepton beam is fired at a polarised gaseous target, in order to measure the spin structure of the nucleon. Figure 3.1 shows the location of these three experiments around the HERA ring and a fourth experiment, HERA-B [49], which is no longer in operation.

Some key parameters of the HERA-II beams are presented in Table 3.1 [50]. HERA can contain a maximum of 220 lepton and 220 proton bunches, which

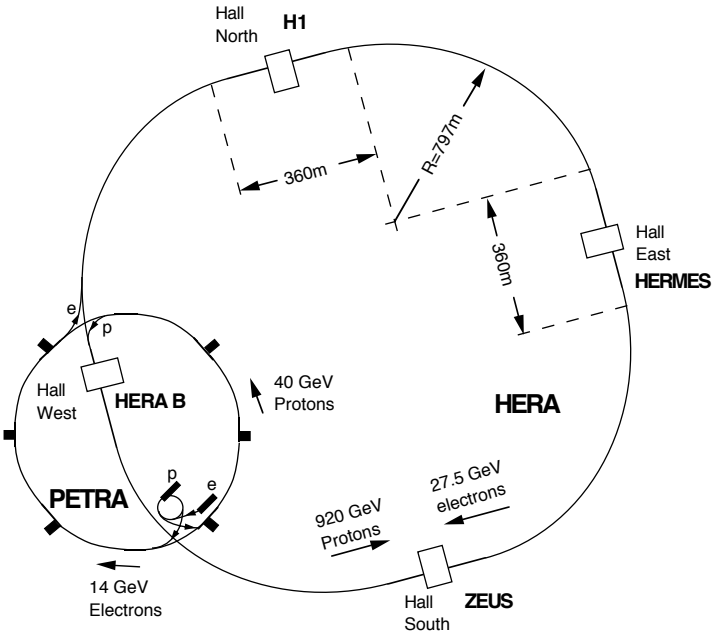

Figure 3.1: The HERA ring and pre-accelerators [1] with the four detectors H1 [9], HERMES [48], ZEUS [8] and HERA-B [49].

collide every 96 ns. However, not all bunches are filled, creating non-colliding pilot bunches that allow, for example, the study of beam-related backgrounds.

	Leptons	**Protons**
Maximum current (mA)	58	140
Maximum number of bunches	180	180
Maximum number of colliding bunches	174	
Specific luminosity (10^{30} cm^{-2} s^{-1} mA^{-2})	1.79	
Peak luminosity (10^{31} cm^{-2} s^{-1})	7.44	

Table 3.1: HERA-II design parameters [50].

Table 3.2 lists the energies and composition of the beams during different periods of operation. Between HERA-I and HERA-II the machine was upgraded [51] with the installation of new superconducting magnets to increase the luminosity and spin rotators to deliver longitudinally polarised lepton beams to the H1 and ZEUS interaction points (IPs).

HERA-I delivered an integrated luminosity of 193 pb^{-1}, a figure which has already been exceeded at HERA-II, where, from 2002 - 2005, 289 pb^{-1} was deliv-

Period	Lepton beam		Proton beam energy (GeV)	Centre of mass energy (GeV)
	Composition	Energy (GeV)		
HERA-I				
1994 - 1997	e^+	27.5	820	314
1998 - 1999	e^-	27.5	920	318
1999 - 2000	e^+	27.5	920	318
HERA-II				
2002 - 2004	e^+	27.5	920	318
2004-2005	e^-	27.5	920	318

Table 3.2: The compositions and energies of HERA's lepton and proton beams.

ered. When HERA finishes running, it is estimated that the HERA-II integrated luminosity will total around 700 pb^{-1}. The data used in this analysis were collected during the 2004 e^+p and 2004 - 2005 e^-p running periods. The luminosity delivered by HERA in the years 2002 to 2005 is shown in Figure 3.2.

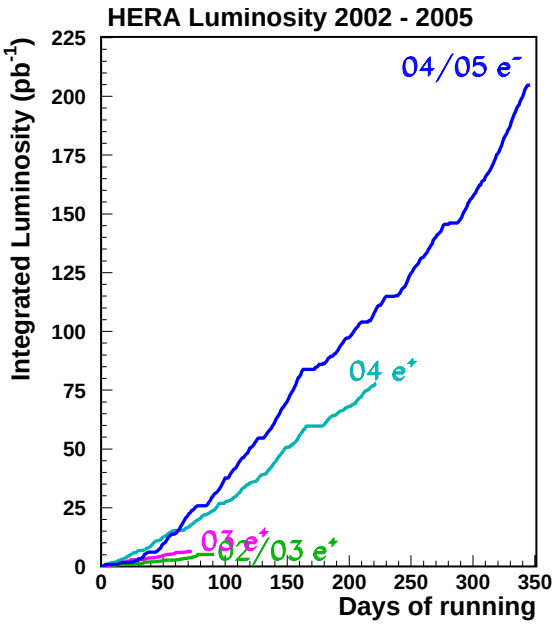

Figure 3.2: The HERA-II delivered luminosity plotted against days of running for different run periods.

3.2 Polarimetry at HERA

At HERA, many physics interactions depend on the longitudinal polarisation of the lepton beam [52, 53]. However, in a storage ring such as HERA, the lepton

beam naturally becomes transversely polarised, so the direction of the leptons' spins must be rotated in order to produce a longitudinally polarised beam. During the HERA upgrade, spin rotators were installed upstream of the H1 and ZEUS detectors, to deliver longitudinally polarised lepton beams to the experiments, and downstream, to return the polarisation direction to transverse and ensure that the polarisation is preserved around the ring. The positions of the spin rotators, the longitudinal polarimeter (LPOL) and the transverse polarimeter (TPOL) are shown in Figure 3.3.

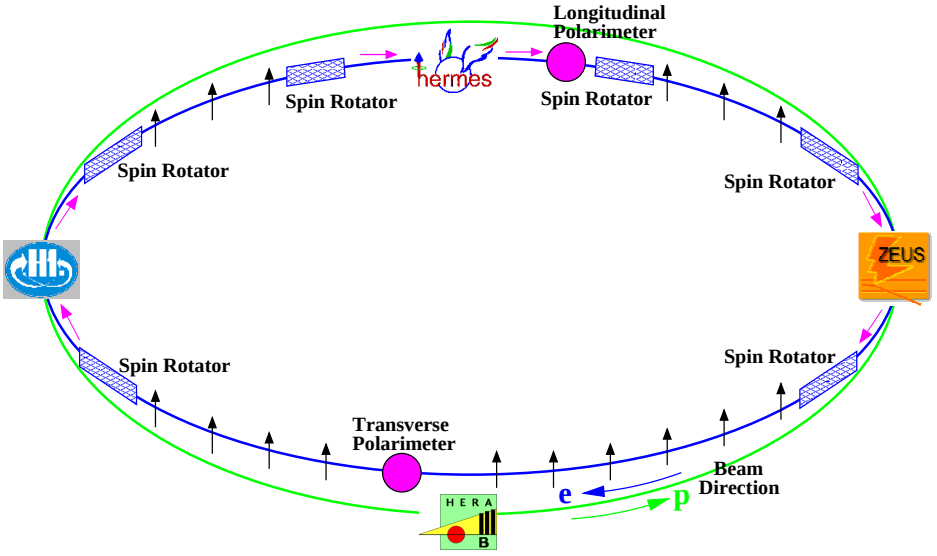

Figure 3.3: The locations of the three pairs of spin rotators, the two polarimeters and the detector experiments around the HERA ring [1]. The arrows along the lepton beam indicate the direction of the leptons' spins at different points around the ring.

3.2.1 The Sokolov-Ternov effect

The Sokolov-Ternov effect [54] is the mechanism responsible for the naturally-occuring transverse polarisation of lepton beams in storage rings. When electrons are injected into a storage ring, their spins are randomly oriented. The electrons are accelerated around the ring in the horizontal plane, perpendicular to the vertical **B**-field of the bending magnets. As the electrons are accelerated they emit photons of synchrotron radiation and this can cause the projection of an electron's spin onto the vertical axis to change direction. The probability per

unit time that an electron's spin will flip from up to down, $W_{\uparrow\downarrow}$, or from down to up, $W_{\downarrow\uparrow}$, is given by the following expression [54]:

$$W_{\downarrow\uparrow}^{\uparrow\downarrow} = \frac{5\sqrt{3}}{16}\left(1 \pm \frac{8}{5\sqrt{3}}\right)\frac{c\lambda_c r_0 \gamma^5}{\rho^3} \ , \tag{3.1}$$

where λ_c is the Compton wavelength, r_0 is the electron radius, γ is the Lorentz factor and ρ is the bending radius of the **B**-field. Since $W_{\uparrow\downarrow} > W_{\downarrow\uparrow}$, over time the lepton beam becomes transversely polarised.

The transverse polarisation of the lepton beam, P_Y, is defined as follows:

$$P_Y = \frac{N_{up} - N_{down}}{N_{up} + N_{down}} \ , \tag{3.2}$$

where N_{up} and N_{down} are the number of particles with their spins pointing upwards or downwards, respectively. The asymptotic limit of P_Y, P_{ST}, is given by:

$$P_{ST} = \frac{W_{\uparrow\downarrow} - W_{\downarrow\uparrow}}{W_{\uparrow\downarrow} + W_{\downarrow\uparrow}} = \frac{8}{5\sqrt{3}} = 0.924. \tag{3.3}$$

The lepton beam polarisation as a function of time is given as follows:

$$P_Y(t) = -P_{ST}(1 - e^{-t/\tau_{ST}}), \tag{3.4}$$

where τ_{ST} is the polarisation rise time constant and is given by:

$$\tau_{ST} = \frac{1}{W_{\uparrow\downarrow} + W_{\downarrow\uparrow}} = \frac{8\rho^3}{5\sqrt{3}c\lambda_c r_0 \gamma^5} \ . \tag{3.5}$$

At HERA τ_{ST} is 37 minutes [55].

There are a number of effects present in storage rings, which prevent the maximum polarisation, P_{ST}, being reached. For example, horizontal and longitudinal **B**-fields from misaligned magnets, the oscillation of the electrons around their central orbit path and the interactions with the proton beam, all decrease the maximum polarisation actually achieved. However, the HERA machine operators can tune the machine optics to minimise these depolarising effects [56].

3.2.2 Compton scattering

The HERA polarimeters use Compton scattering of circularly polarised laser beams off the lepton beam to measure the polarisation of the lepton beam [53]. Figure 3.4 defines the kinematics of Compton scattering in the laboratory frame.

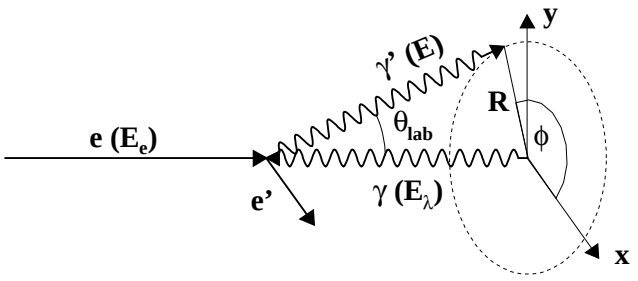

Figure 3.4: Compton scattering of a laser beam off the lepton beam in the laboratory frame.

Using E and ϕ as defined in Figure 3.4, the spin-dependent cross section for Compton scattering can be expressed as follows [57]:

$$\frac{d^2\sigma}{dEd\phi} = \Sigma_0(E) + S_1\Sigma_1(E)\cos 2\phi + S_3[P_Y\Sigma_{2Y}(E)\sin\phi + P_Z\Sigma_{2Z}(E)], \quad (3.6)$$

where S_1 and S_3 are the linear and circular components of the laser beam polarisation, respectively, P_Y and P_Z are the transverse and longitudinal components of the lepton beam polarisation, respectively, and the Σs are functions of the energy of the scattered photon.

The polarimeters determine P_Y or P_Z by measuring asymmetries between the scattered photons from circularly polarised laser beams with positive and negative helicity, as follows:

$$\frac{d^2\sigma}{dEd\phi}(S_3 > 0) - \frac{d^2\sigma}{dEd\phi}(S_3 < 0) = 2S_3[P_Y\Sigma_{2Y}(E)\sin\phi + P_Z\Sigma_{2Z}(E)], \quad (3.7)$$

which means that the asymmetries between the two laser helicity states can be measured in the photon energy, E, and its azimuthal angle, ϕ.

At the LPOL, $P_Y \sim 0$, so P_Z is determined by measuring the asymmetry in E. At the TPOL, $P_Z \sim 0$, so P_Y is determined from the asymmetry measured in both E and ϕ. It can be shown that the angle θ_{lab} depends only on the energy, E, of the backscattered photon [57] and therefore the radius, R, also depends only on E. The angle ϕ can be expressed as:

$$\phi = \sin^{-1}\left(\frac{y}{R(E)}\right), \tag{3.8}$$

meaning that the TPOL need only measure the asymmetry in E and y, rather than in E and ϕ, in order to extract P_Y.

3.2.3 The Transverse Polarimeter

Figure 3.5 shows the layout of the TPOL apparatus [58]. A 10 W continuous wave laser with a wavelength of 514 nm is circularly polarised with positive or negative helicity by a Pockels cell [59] and then guided into the tunnel by a series of mirrors and lenses. A chopper blocks the laser beam periodically in order to measure the background energy spectrum, which consists mainly of Bremsstrahlung. The Compton interaction takes place approximately 65 m upstream of the TPOL calorimeter.

The Compton photons are converted into e^+e^- pairs by one interaction length of lead, located in front of the calorimeter as shown in Figure 3.6. The calorimeter is a twelve-layer tungsten-scintillator sampling calorimeter. It is divided into two optically separate halves, up and down, each of which is read out by a separate photomultiplier tube. Between the lead converter and the calorimeter is a silicon strip detector, which can measure the vertical and horizontal positions of the e^+e^- pairs.

The online polarisation measurement

The TPOL polarisation measurement [57, 60] is performed in one minute cycles. For the first 20 seconds the chopper is closed and the Bremsstrahlung background spectrum is measured. For the remaining 40 seconds the chopper is open and the

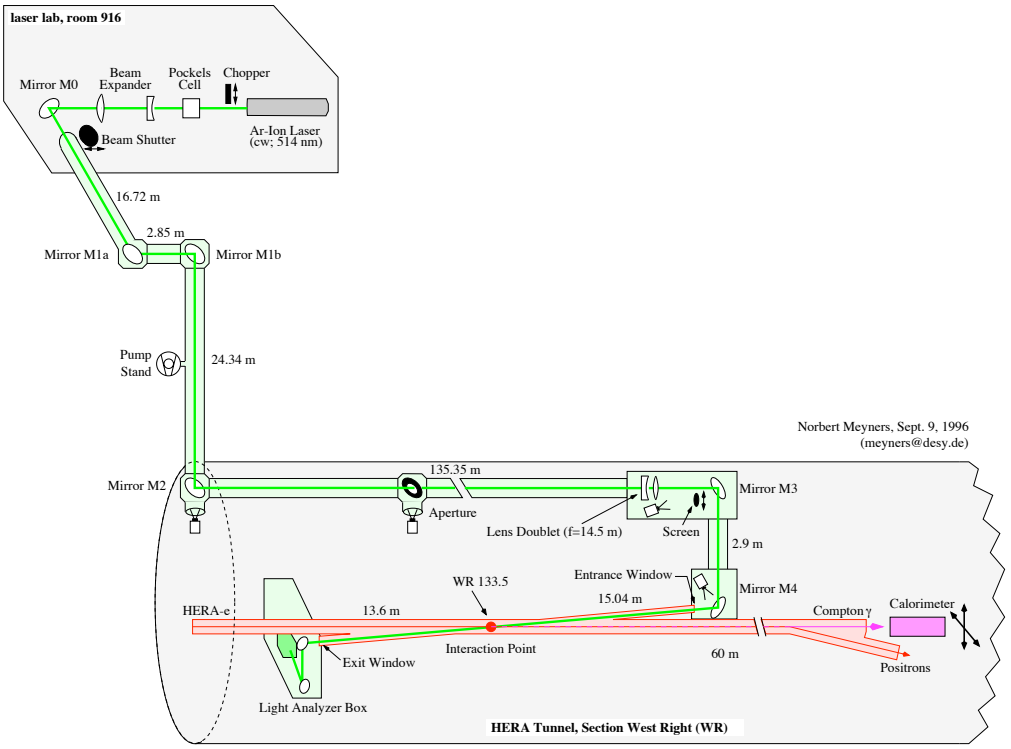

Figure 3.5: The TPOL apparatus [58], including the Ar:Ion laser, chopper, Pockels cell and calorimeter.

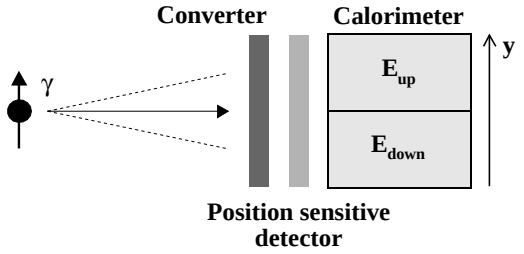

Figure 3.6: The TPOL lead converter, the position-sensitive silicon detector and the calorimeter split in two halves: up and down [58].

Pockels cell changes the laser helicity from positive to negative and back again at a frequency of 90 Hz. The energy distribution of the scattered photons is measured for each of the three states: laser off, laser on with positive helicity and laser on with negative helicity. The background energy distribution, measured with the laser off, is subtracted from the laser on energy distributions in order to remove the Bremsstrahlung.

As explained in section 3.2.2, P_Y can be determined from the asymmetries measured in the energy and vertical position of the scattered photons. However, with the calorimeter, the vertical position cannot be measured directly, so the following quantity is calculated:

$$\eta = \frac{E_{up} - E_{down}}{E_{up} + E_{down}} \ , \tag{3.9}$$

where E_{up} and E_{down} are the energies measured in the upper and lower halves of the calorimeter, respectively.

P_Y is then extracted with the following expression:

$$P_Y = |S_3| \Pi_{\mathrm{TPOL}} \frac{\bar{\eta}_+ - \bar{\eta}_-}{2} \ , \tag{3.10}$$

where $\bar{\eta}_\pm$ are the average η values in a certain energy slice for positive and negative laser helicity states, $|S_3|$ is the average magnitude of the circular polarisation of the laser and Π_{TPOL} is the analysing power of the TPOL, which is determined by Monte Carlo simulations and polarisation rise-time calibrations [58].

The TPOL measurements of the lepton beam polarisation used in this analysis were estimated to have a systematic uncertainty of 3.5 % [61] during 2004 e^+p running and 5% during 2004 to 2005 e^-p running. In the future, it is hoped that the precision of the polarisation measurement will improve to $\sim$1% [62].

One of the largest sources of systematic uncertainty on the polarisation measurement comes from the $\eta - y$ transformation [63]. This transforms the variable η, measured by the calorimeter, into a vertical position and is required for the determination of the analysing power, Π, which is then required for the determination of P_Y. The $\eta - y$ transformation used in the current measurements comes from data collected at the TPOL beam test at CERN [64]. A more accurate

$\eta - y$ transformation, determined for the actual set-up of the TPOL apparatus at HERA, would therefore help to reduce the systematic uncertainty. Such a transformation could be provided using the TPOL silicon detector.

The silicon detector

The silicon detector [64], shown in Figure 3.6, consists of 256 strips in the vertical direction and 768 strips in the horizontal direction, which measure the x and y positions of the e^+e^- pairs, respectively. The vertical strips have a pitch of 120 μm and every other strip is read out. The horizontal strips have a pitch of 80 μm and all the strips are read out. The whole silicon detector has a sensitive area of 64 $\times$ 63.6 mm^2. The detector is read out at around 100 Hz, which is significantly slower than the rate for the calorimeter. This means that a polarisation measurement made solely from the silicon detector would have considerably worse statistical precision than one using the calorimeter.

As a charged particle passes through the silicon detector, charge can be deposited in a number of strips and the signal from each strip is read out by an ADC. A clustering algorithm [64] was implemented to identify groups of strips, called clusters, representing a single charged particle passing through the detector.

In the clustering algorithm, first it is necessary to define the pulse height, S. S was calculated for each strip as follows:

$$S = RAW - PED - CM, \tag{3.11}$$

where RAW is the raw ADC count, PED is the mean pedestal value and CM is the common mode baseline shift. The noise, N, was defined as the RMS of the pulse height:

$$N = \mathrm{RMS}(S). \tag{3.12}$$

The first step in the clustering algorithm was to identify the dead strips. Strips were defined as dead if [64]:

$$N > 3.5 \text{ ADC counts} \tag{3.13}$$

and

$$S < 40 \text{ ADC counts.} \tag{3.14}$$

For the rest of the algorithm only live strips were considered.

The cluster seeds were located by searching for strips with [64]:

$$S > 15N. \tag{3.15}$$

If the distance between two cluster seeds was less than six strips, then the seeds were considered to belong to the same cluster. For analysis purposes, only events with one cluster seed were used.

If the pulse height in the strips adjacent to the cluster seed satisfied [64]:

$$S > 4N, \tag{3.16}$$

then the strips were added to the cluster. This was repeated on the next adjacent strips until no more strips could be added to the cluster.

The cluster signal was then defined simply as the sum of the pulse heights in all the cluster strips. The cluster position, P, was defined as the cluster's centre of gravity [64]:

$$P = \frac{\Sigma_i S_i p_i}{\Sigma_i S_i} \ , \tag{3.17}$$

where the sum was performed over all strips, i, in the cluster, S_i is the pulse height and p_i is the position of each strip.

As mentioned earlier, the uncertainty on the polarisation measurement could be reduced considerably with an accurate *in-situ* $\eta - y$ transformation [64], with the y position measurement taken from the silicon detector. The $\eta - y$ transformation is obtained by fitting a $y - \eta$ distribution, such as the one shown in Figure 3.7 [63], with the following function [64]:

$$y(\eta) = P_1 \log \frac{1+\eta}{1-\eta} + P_2 \left(\log \frac{1+\eta}{1-\eta} \right)^3 + P_3 \left(\log \frac{1+\eta}{1-\eta} \right)^5 + P_4 \left(\log \frac{1+\eta}{1-\eta} \right)^7 . \tag{3.18}$$

It has been shown that P_Y determination is sensitive to the size and shape of the lepton beam arriving at the TPOL. Currently, the measured polarisation is

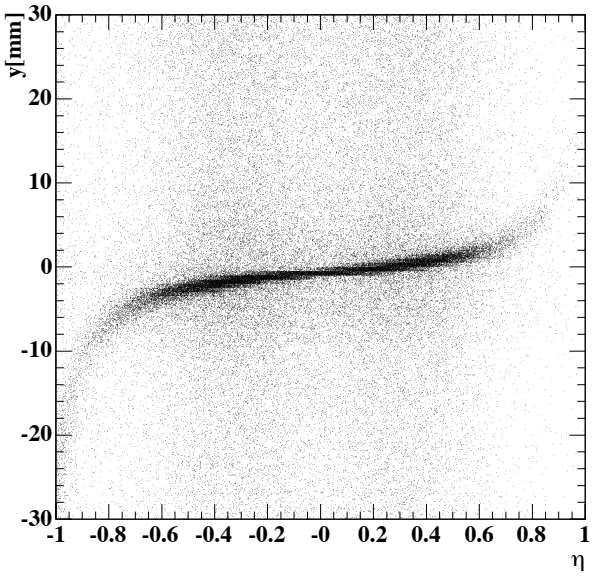

Figure 3.7: The $y - \eta$ distribution [63] measured by the TPOL silicon detector and calorimeter.

corrected based on the beam size measured in the calorimeter [61]. However, x and y position information measured with the silicon detector can be used to fit a two-dimensional distribution and extract values of the horizontal and vertical beam size as well as its tilt.

The two-dimensional distribution is given by:

$$f(x,y) = C \exp\Big(-0.5\big(v_{xx}(x-x_0)^2 + 2v_{xy}(x-x_0)(y-y_0) + v_{yy}(y-y_0)^2\big)\Big), \tag{3.19}$$

and the beam tilt, α, is calculated using the following expression:

$$\alpha = \frac{1}{2}\tan^{-1}\left(\frac{2v_{xy}}{v_{xx}-v_{yy}}\right). \tag{3.20}$$

Figure 3.8 shows an example of such a fit, which had a χ^2/degrees of freedom of 1.0 and a tilt of $3.4 \pm 0.2°$. Performing this fit at regular intervals during HERA running could provide more precise information about the size and shape of the lepton beam and improve the uncertainty on the polarisation measurement.

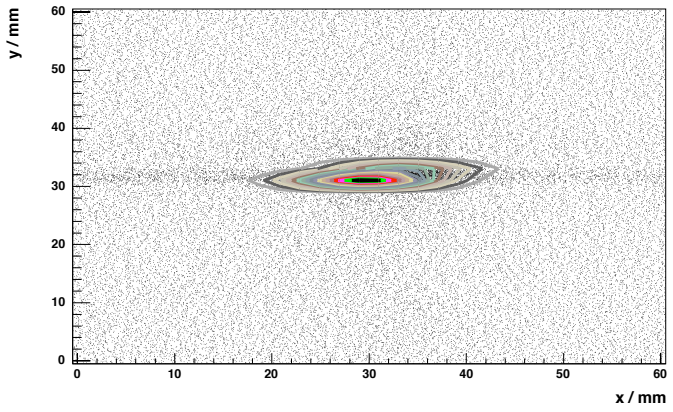

Figure 3.8: A two-dimensional ellipse fitted to data measured by the TPOL silicon detector.

3.2.4 The Longitudinal Polarimeter

The LPOL [65] measurement is similar to that of the TPOL, except that there is no asymmetry in the position of the scattered photon, so only an energy measurement is required. Figure 3.9 shows the LPOL apparatus, including a high intensity 532 nm pulsed laser, which is passed through a Pockels cell to create a circularly polarised beam. It is then directed down to the HERA tunnel, where the photons collide with the lepton beam and the average energy of the scattered photons is measured in a $NaBi(WO_4)_2$ crystal calorimeter, as shown in Figure 3.10.

The Compton photons, upon arrival at the lead plates, begin an electromagnetic shower, the charged particles of which produce Cherenkov light in the four $NaBi(WO_4)_2$ crystals that make up the calorimeter. This light is then detected by four photomultiplier tubes, one for each crystal.

The standard mode of LPOL operation is the high statistics multi-photon mode, where the energy is measured from all Compton photons produced per laser pulse. This is as opposed to the single-photon mode, which is used for studying systematic effects. The laser intensity is controlled by passing the beam through a rotatable half-wave plate and a fixed Glan-Thompson prism.

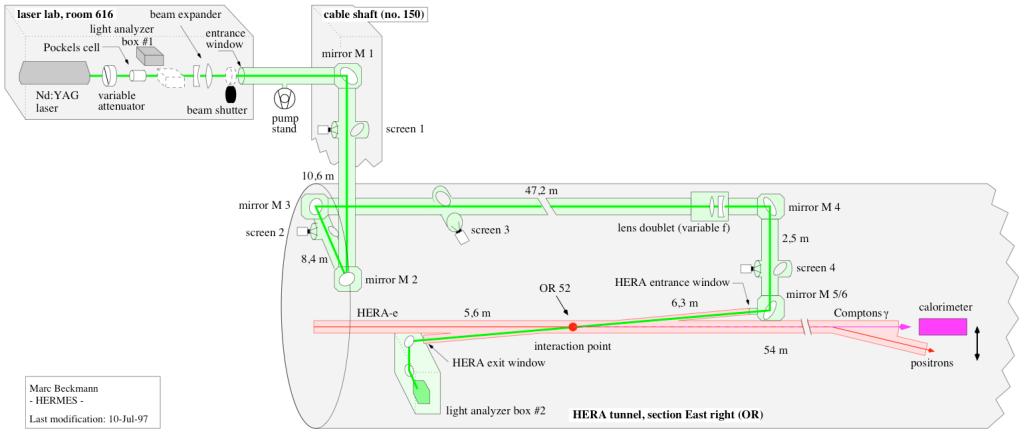

Figure 3.9: The LPOL apparatus [65] including a 3 ns × 100 mJ at 100 Hz pulsed Nd:YAG laser, a Pockels cell to provide positively and negatively circularly polarised photons and a $NaBi(WO_4)_2$ crystal calorimeter to measure the energy of the backscattered photons.

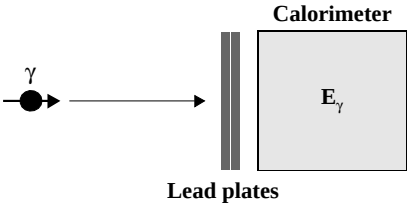

Figure 3.10: The LPOL calorimeter with two lead plates in front of it [65]. The plates provide the calorimeter with 2.2 interaction lengths of protection from synchrotron radiation.

When operating in multi-photon mode, the energy asymmetry between the two laser helicity states, A, is given by:

$$A = \frac{E_+ - E_-}{E_+ + E_-} \ , \tag{3.21}$$

where E_+ and E_- are the energies measured in the calorimeter for positive and negative laser helicity, respectively.

The longitudinal polarisation of the lepton beam, P_Z, is then extracted using the following expression [65]:

$$A = |S_3| P_Z \Pi_{\mathrm{LPOL}}, \tag{3.22}$$

where $|S_3|$ is the average magnitude of the circular polarisation of the laser, which is greater than 0.999, and Π_{LPOL} is the analysing power of the LPOL, which is determined using Monte Carlo simulation.

The LPOL measurements of the lepton beam polarisation used in this analysis were estimated to have a systematic uncertainty of 1.6 % [66] during 2004 e^+p running and 5% during 2004 to 2005 e^-p running.

3.3 The ZEUS detector

An overall view of the ZEUS detector [8] is shown in Figure 3.11. ZEUS is a general-purpose detector comprising a vast number of components, including a silicon microvertex detector, a cylindrical drift chamber, a solenoid producing a 1.43 T magnetic field, electromagnetic and hadronic calorimeters and muon chambers. The ZEUS coordinate system is right-handed, with the Z axis pointing in the direction of the proton beam and the X axis pointing towards the centre of the HERA ring.

3.3.1 The Calorimeter

The calorimeter (CAL) [67, 68, 69] is divided into three sections: the forward (FCAL), the barrel (BCAL) and the rear (RCAL) calorimeters. Together they

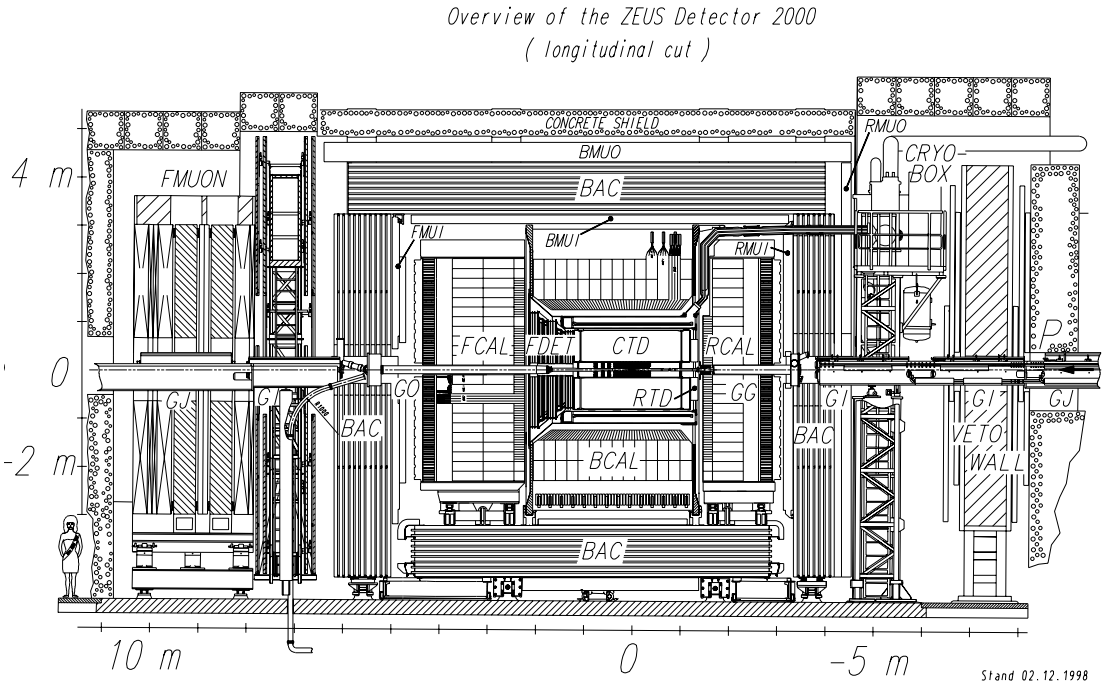

Figure 3.11: An overall view of the ZEUS detector [8].

cover 99.7 % of the solid angle around the interaction point, with holes in the FCAL and RCAL for the beam pipe.

As shown in Figure 3.12, the CAL has electromagnetic (EMC) and hadronic (HAC) cells, which measure the energy from electromagnetic and hadronic deposits. In each section there is one layer of EMC cells. In the FCAL and BCAL there are two layers of HAC cells (HAC1 and HAC2) and in the RCAL there is just one, since most of the hadronic energy is deposited in the forward direction. There are four EMC cells in front of each HAC1 cell in the FCAL and the BCAL, whereas in the RCAL there are just two EMC cells for each HAC cell.

The CAL cells are made of 3.3 mm thick layers of depleted uranium absorber, interspersed with plastic scintillator with a thickness of 2.6 mm. There are up to 185 layers in each module. This is illustrated in Figure 3.13, which shows the EMC and HAC cells in one FCAL module. Each CAL cell is connected via wavelength shifters to two photomultiplier tubes, which convert the light from the scintillators into an electrical signal. Under test beam conditions, the energy resolution of the CAL was found to be $35\%/\sqrt{E} \oplus 2\%$ for hadronic deposits and

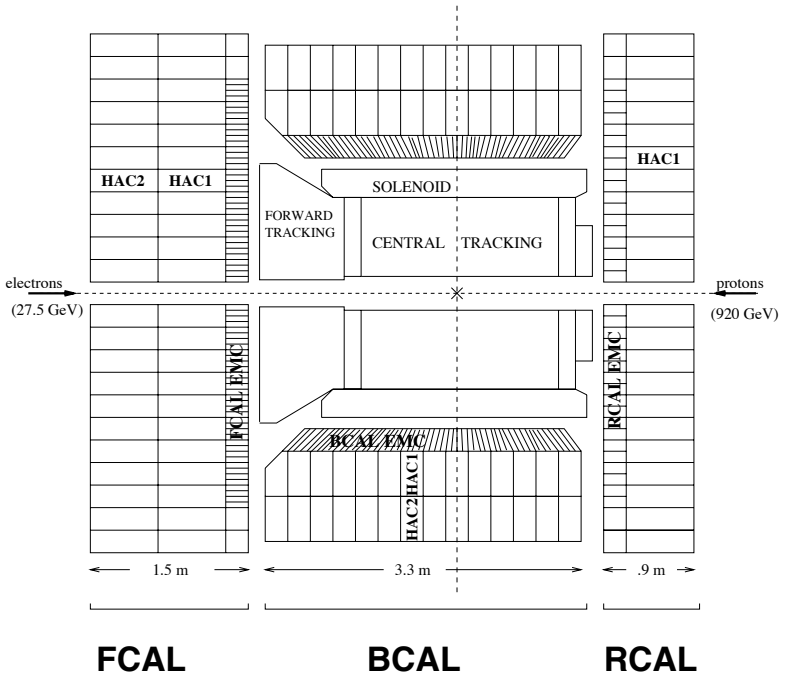

Figure 3.12: The three sections of the calorimeter with the EMC and HAC cells [67, 68].

$18\%/\sqrt{E} \oplus 1\%$ for electromagnetic deposits, with E measured in GeV [69].

When a hadron such as a $\pi^{\pm}$ showers in the CAL, it creates both electromagnetic and hadronic energy deposits. For a given $\pi^{\pm}$ showering in the CAL, the fraction of the its energy deposited in electromagnetic and hadronic energy deposits is unknown. In order to have the best possible hadronic energy resolution, it is therefore important that the CAL's response to electromagnetic and hadronic energy deposits, E and H, respectively, should be balanced. A calorimeter that has $E/H \sim 1$ is called a compensating calorimeter. In the ZEUS CAL, E and H were balanced by tuning the thicknesses of the layers of depleted uranium and plastic scilltilators [70].

The CAL also provides timing information for each energy deposit. The timing resolution is better than 1 ns for deposits with an energy greater than 4.5 GeV. The FCAL timing information can be used to reconstruct the event vertex along the Z axis [71]. For events with more than 25 GeV deposited in the FCAL, the resolution of the Z axis vertex position derived from timing information is around

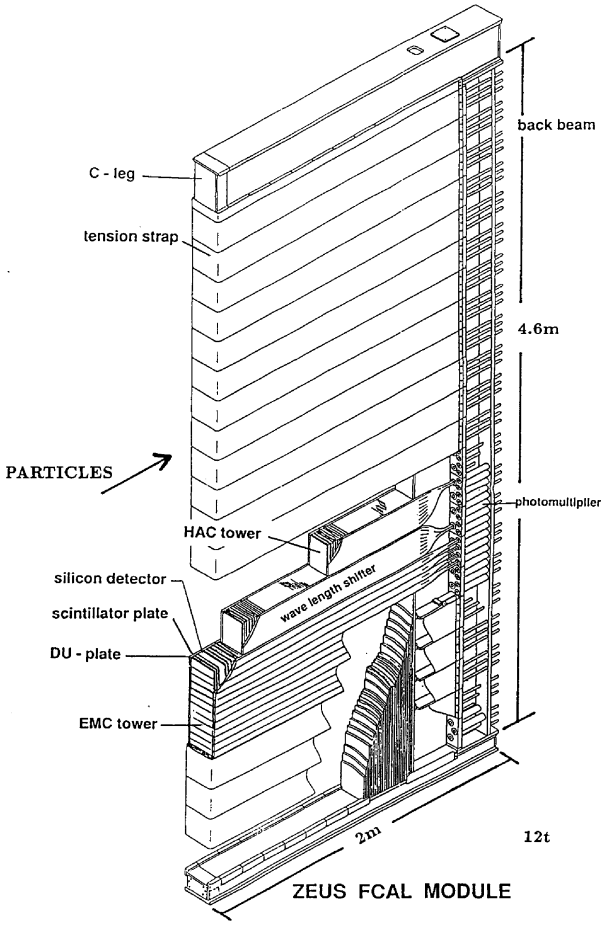

Figure 3.13: An FCAL module [68].

10 cm. This improves to about 8 cm for events with more than 100 GeV in the FCAL.

3.3.2 The Central Tracking Detector

The Central Tracking Detector (CTD) [72] is a cylindrical drift chamber that detects the tracks of charged particles with polar angles from 15° to 164°. It has an inner radius of 18.2 cm and an outer radius of 79.4 cm and operates in a solenoidal magnetic field of 1.43 T. The chamber is filled with a mixture of argon, ethane and carbon dioxide gases.

The CTD is divided into nine superlayers, each of which is divided into a further eight layers of sense wires. In total, there are 4608 sense wires. In five of the superlayers the wires are parallel to the Z axis, these are called axial superlayers, and in four of the superlayers the wires are at a small stereo angle of $\pm 5°$, these are called stereo superlayers. Figure 3.14 shows the superlayers in one octant of the CTD.

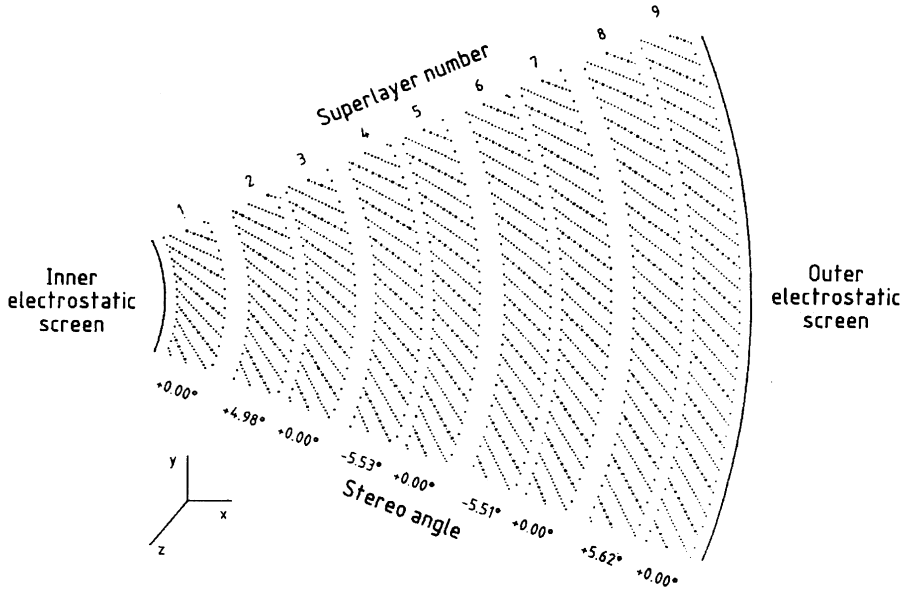

Figure 3.14: An octant of the CTD divided into nine superlayers [72]. The stereo angle in each of the superlayers is indicated.

Charged particle tracks are reconstructed from the hits in the $r - \phi$ plane using

the known positions of the wires and the drift time. The Z position is determined by combining information from the axial and stereo wires as well as the Z-by-timing system. The Z-by-timing system measures the time difference between pulses arriving at each end of the wire, to estimate the hit position along the Z axis.

The reconstructed tracks can then be used to determine the event vertex position, the particle momentum and dE/dx. The CTD provides a position resolution of 230 μm in the $r-\phi$ plane, which gives a transverse momentum resolution of $\sigma(P_T)/P_T = 0.0058P_T \oplus 0.0065 \oplus 0.0014/P_T$ (with P_T in GeV) [73].

3.3.3 The Microvertex Detector

The Microvertex Detector (MVD) [74, 75] is located inside the inner radius of the CTD and provides a precise measurement of the event vertex position and impact parameter. It has polar angle coverage from 7.6° to 160°.

The MVD is divided into two sections: the barrel section and the forward section. The barrel contains 30 ladders arranged in three layers, as shown in Figure 3.15. A ladder is made of five modules, each of which holds four silicon sensors, giving the barrel a total of 600 sensors. Each silicon sensor comprises strips of width 20 μm. However, only every sixth strip is read out, so each sensor has effectively 512 strips of width 120 μm. The forward section is made of four wheels, each of which contains two layers of 14 silicon sensors arranged perpendicularly to the Z axis. This gives a total of 112 sensors and each sensor has effectively 480 strips of width 120 μm.

Information from the CTD and MVD is combined to give a more precise measurement of the event vertex position than from the CTD or MVD alone.

3.3.4 The luminosity monitors

Two independent monitors are used to measure the luminosity at the ZEUS detector: the Photon Calorimeter (PCAL) and the Spectrometer (SPEC). Both

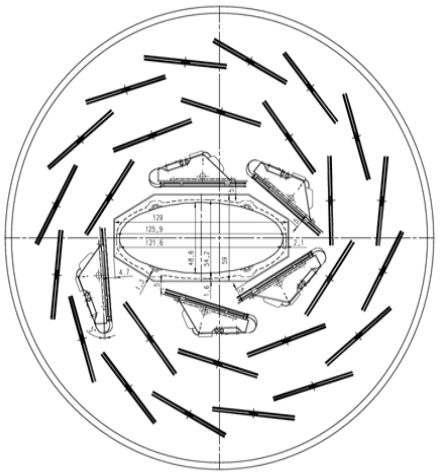

Figure 3.15: The 30 silicon ladders arranged in three layers around the elliptical beam pipe in the barrel section of the MVD [74, 75].

detectors measure the rate of photon production through the Bethe-Heitler reaction [76], $ep \rightarrow e\gamma p$. The luminosity is then determined using the following expression:

$$R = \mathcal{L}\sigma\mathcal{A}, \tag{3.23}$$

where R is the rate of events, σ is the Bethe-Heitler cross section, $\mathcal{L}$ is the luminosity and $\mathcal{A}$ is the acceptance. The Bethe-Heitler reaction is chosen because it has a large cross section that is precisely known from theory, minimising both the statistical and theoretical uncertainties on the luminosity measurement.

The Photon Calorimeter

The PCAL [77, 78] determines the luminosity by measuring the rate of Bethe-Heitler photons arriving in a lead-scintillator sampling calorimeter positioned 107 m from the IP, as shown in Figure 3.16.

A carbon filter, four radiation lengths thick, is positioned in front of the calorimeter to minimise the background from synchrotron radiation. However, the presence of the filter significantly worsens the energy resolution of the calorimeter. In order to counteract this degradation, two Cherenkov detectors measure the energy of the Bethe-Heitler photons before and after they pass through the filter.

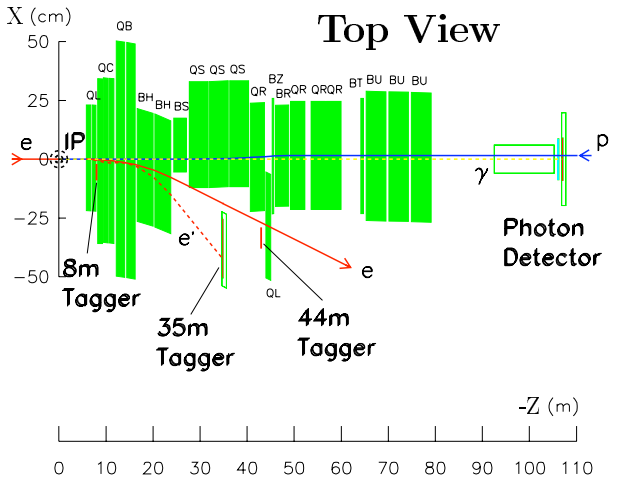

Figure 3.16: The position of the PCAL luminosity monitor [77, 78] with respect to the IP.

The radiator medium in the Cherenkov detectors is silica aerogel. Silica aerogel has a refractive index of 1.030, which means that electrons need an energy of at least 1.62 MeV to emit Cherenkov radiation in the detector. Synchrotron photons can have energies ranging up to $1-2$ MeV, so only a very small fraction of them could produce electrons, via the Compton effect, that would emit Cherenkov radiation. However, the Bethe-Heitler photons create electromagnetic showers that contain charged particles with average energies of around 20 MeV, well above the Cherenkov threshold for the detector.

The energy of the Bethe-Heitler photon, E_{BH}, is estimated by summing the energies measured in the calorimeter and the two Cherenkov detectors as follows:

$$E_{\mathrm{BH}} = aE_{\mathrm{CAL}} + bE_{\mathrm{C1}} + cE_{\mathrm{C2}}, \tag{3.24}$$

where E_{CAL}, E_{C1} and E_{C2} are the energies measured in the calorimeter and two Cherenkov detectors, respectively, and the weights, a, b and c, are determined from Monte Carlo simulation studies. E_{BH} has a resolution of $\Delta E_{\mathrm{BH}}/E_{\mathrm{BH}} = 37\%/\sqrt{E_{\mathrm{BH}}}$, with E_{BH} measured in GeV [77].

The rate at which high-energy Bethe-Heitler photons arrive is measured in a given energy range and the acceptance is estimated using Monte Carlo simulation. The luminosity is then determined using equation 3.23.

The electron (or positron) scattered in the Bethe-Heitler reaction is also detected. Since its energy is less than that of the other leptons in the beam, it is bent by a different amount by the bending magnets. The Bethe-Heitler electrons (or positrons) are detected in a second lead-scintillator calorimeter, 35 m from the IP. The measurement of these electrons (or positrons) is useful for systematic studies of the PCAL luminosity measurement. In addition, measuring an electron (or positron) without coincidence with a photon can be used to tag photoproduction events.

The systematic uncertainty on the PCAL luminosity measurement was estimated as 2.5%.

The Spectrometer

The SPEC [79, 80, 81] also measures the luminosity from the Bethe-Heitler process, but with a slightly different method. When the Bethe-Heitler photons leave the beam pipe, at about 92 m from the IP, they pass through a 3 mm thick window made of 90% copper and 10% beryllium. As the photons pass through this window, around 10% of the photons are converted into e^+e^- pairs. A dipole magnet then splits the e^+e^- pairs vertically and two tungsten-scintillator calorimeters detect them above and below the photon beam, at around 100 m from the IP. This apparatus is illustrated in Figure 3.17 [81].

The rate of coincidence in the two calorimeters is measured and from this the luminosity is determined. The main advantages of this method are that there is much less chance of confusion from event pile-up, than with the PCAL, and it is insensitive to synchrotron radiation.

The systematic uncertainty associated with the SPEC luminosity measurement was estimated to be 3.5% [80].

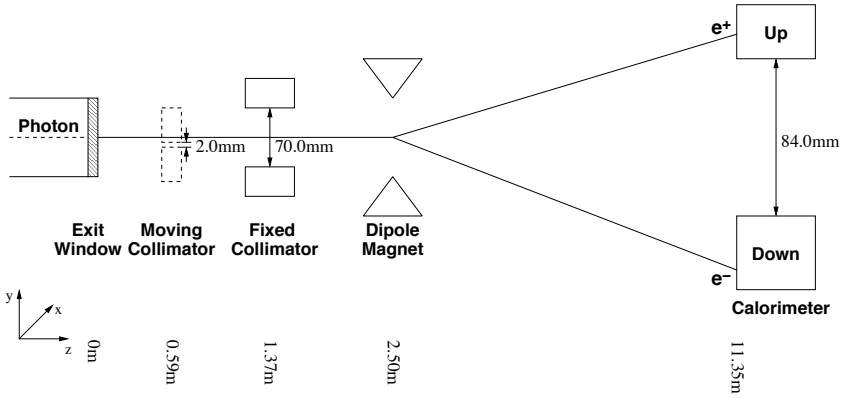

Figure 3.17: The layout of the SPEC luminosity monitor [79, 80, 81]. The exit window is 92 m from the IP. The two tungsten-scintillator calorimeters are labelled Up and Down.

3.3.5 Background vetoes

The C5 counter [8] is a scintillator located 315 cm upstream (in the RCAL direction) from the IP. It measures the timing of particles associated with the electron and proton bunches and is used in the measurement of the Z vertex position based on FCAL timing information and also in the trigger, to reject events with timing that is inconsistent with the ep bunch crossing time.

The veto wall [8] is positioned 750 cm upstream from the IP and provides another veto of non-ep events. Its main purpose is to prevent particles from the proton beam halo from entering the ZEUS detector. However, some particles are not stopped by the wall and continue into the detector. Such events can be rejected using the information recorded by the veto wall.

3.3.6 The trigger system

The ZEUS experiment operates a three-level trigger system [82] to reduce the initial event rate of around 10^7 Hz to around 5 Hz, which can be recorded. This is achieved by implementing cuts to reject background events, whilst retaining high efficiency for taking physics events and minimising dead-time. Figure 3.18 shows the complete trigger chain and the rate reduction achieved at each stage.

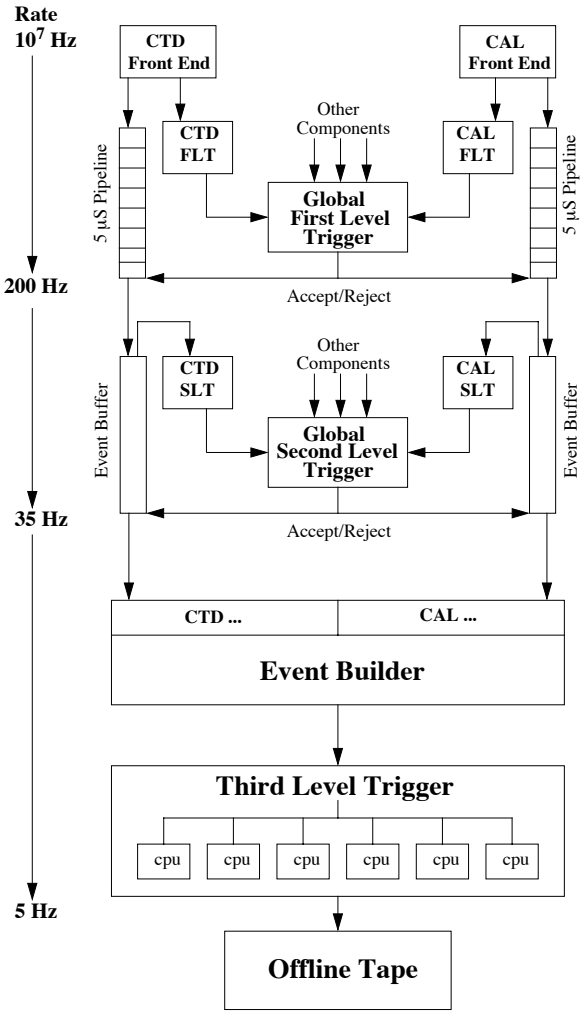

Figure 3.18: A schematic view of the ZEUS trigger system [82] and the approximate event rate into and out of each level. Only the CTD and CAL triggers are shown in detail but other components feed into the trigger system in a similar manner.

There are various sources of background, of which one of the largest is beam gas. Beam gas background is caused by leptons or protons interacting with gas particles in the beam pipe. Another source of background comes from halo muons passing through the detector. Halo muons are created when a proton interacts with part of the beam pipe close to the detector. Muons from cosmic rays can also mimic ep events if they pass through the detector, creating a further source of background.

The First Level Trigger

The main function of the First Level Trigger (FLT) is to reduce the rate by rejecting background events, in particular beam gas events. The time between bunch crossings at HERA is just 96 ns, so the FLT is hardware-based, in order to make a very fast decision on whether to keep or to reject an event. However, 96 ns is still too short a time to make a decision, so the FLT uses digital and analogue pipelines, which store the data for 5 μs until a decision has been made. Even with the pipelines, a very fast speed is still required, so the FLT only performs fairly simple operations and uses just a portion of the information available from the detector.

The detector components each have their own hardware for computing the quantities used at the FLT. The output from the component FLTs is sent via pipelines to the Global First Level Trigger (GFLT), where the decision on whether to keep or to reject the event is made. Events are passed by the GFLT through one or more of 64 slots, each of which has a specific purpose. For example, slot 60 is designed to accept charged current events, whilst minimising the background.

The calorimeter FLT (CFLT) [83] reads out the energy from each CAL tower, rather than from each cell individually, as this would be too time-consuming. In the FCAL and BCAL a tower consists of four EMC cells and the HAC cells behind them. In the RCAL a tower contains two EMC cells and the corresponding HAC cells. Towers with less than 500 MeV are considered to have zero energy and are ignored to save time. The energies read out from the individual towers

are then combined to provide global event quantities, which are digitised logarithmically. This means that a large energy range can be read out but the precision is somewhat degraded.

The global event quantities are derived from the CFLT, with the event vertex set to the nominal position of $Z = 0$ cm. Functions performed by the CFLT include the detection of isolated leptons with pattern-analysis logic and checking for missing transverse momentum, which is especially important for triggering on CC events. The CFLT also indicates possible beam gas events, which can then be rejected.

The FLT also comprises a hardware system called the Fast Clear [84]. The Fast Clear delivers a decision on whether or not an event should be aborted based on clustered CFLT information.

The CTD FLT [85] controls the rate mainly by identifying events with tracks coming from the the interaction vertex. A track originating from the vertex is a key signature of an ep interaction. At the CTDFLT, tracks are reconstructed using the position of hits in the $r - \phi$ plane, from the position of the wire that was hit, and along the Z axis, using the Z-by-timing system. The resolution in Z is better than 3 cm. In order to reduce processing time, only hits in the wires in superlayer 1 and alternate layers in superlayers 3 and 5 are read out. Pattern-recognition logic is used to determine whether a series of hits forms a track and if this track points back to the vertex or not. Event selection is based on the total number of tracks and the number of tracks originating from the event vertex.

The Second Level Trigger

The Second Level Trigger (SLT) [86] has slightly more time available than the FLT, so it is able to use the full calorimeter granularity and to perform simple tracking algorithms with momentum reconstruction. Quantities are calculated locally for each component and transferred from the components to the Global

Second Level Trigger (GSLT). At the GSLT there are around 60 slots, each with logic designed to select a certain type of physics event and reject the background to that process.

The Third Level Trigger

At the Third Level Trigger (TLT), a computer farm is used to run a slightly simpler version of the offline reconstruction software, using all the information from the detector components. Generally, the output from the SLT slots does not contain much background, so the TLT acts as a loose pre-selection for different physics processes. However, there is still some background rejection performed, particularly by the charged current slots, as the background contamination tends to be higher here due to the requirement of missing transverse momentum, which also characterises many background events.

Chapter 4

Monte Carlo simulation

In this chapter the Monte Carlo (MC) simulations that were used to create samples of charged current events and Standard Model background processes are described. First, appropriate generators are used to make samples of MC events for the various physics processes. Then the events are passed through a simulation of the ZEUS detector and trigger. Finally, the events are reconstructed using the algorithms detailed in Chapter 5.

The MC samples are weighted to the data luminosity and are used to extract the cross section measurements by determining the CC acceptance and the level of background contamination. They are also used to study the resolution and bias of the reconstructed kinematic variables.

4.1 Charged current events

CC events were generated using the DJANGOH 1.3 program [87]. DJANGOH simulates CC and NC *ep* DIS interactions using an interface between LEPTO [88], which models the leading order scattering of the lepton off the parton, and HERACLES [89], which models initial state radiation from the lepton or parton, self energy corrections and single loop weak corrections.

Two different programs were used to model the parton shower. One was ARIADNE 4.10 [90], which uses the colour dipole model (CDM). The CDM treats

the struck quark and the proton remnant as a colour dipole that radiates gluons, creating more colour dipoles, which radiate more gluons, until each dipole reaches a minimum energy. The second program used the Matrix Element Parton Shower (MEPS) model of LEPTO 6.5 [91], where the final state quarks and gluons create a shower of further quarks and gluons until they all reach some minimum energy. Both parton shower models used the Lund string model of fragmentation in JETSET 7.4 [92, 93, 94] to create the final hadronic state. The MEPS MC samples were used as a systematic check of the uncertainty associated with the choice of parton shower model.

The proton was modelled using the CTEQ5D PDFs [95]. These PDFs were determined from the following data sets: ep DIS from the H1 [96, 97] and ZEUS [98] experiments; muon scattering from the BCDMS [4], NMC [5] and E665 [6] experiments; neutrino scattering from the CCFR [7] experiment; Drell-Yan measurements (lepton pair production) from E605 [99] $p - Cu$ data and E866 [100] pp and pd data; W-lepton asymmetry from CDF [101] $p\bar{p}$ measurements; and inclusive jet data from $p\bar{p}$ collisions measured by both the DØ [102] and CDF [103] experiments.

The numbers of MEPS and ARIADNE CC events generated are listed in Tables 4.1 and 4.2, with the corresponding luminosities. Samples were generated with different minimum values of Q^2 to keep the MC statistical uncertainty insignificant across the whole kinematic range of the analysis. The events were weighted according to their true value of Q^2 and the number of events and cross section of each sample.

The CC events were simulated with zero longitudinal polarisation of the lepton beam, so the samples were weighted, according to equation 2.58, by $1 \pm P_e$ for $e^{\pm}p$ collisions, where P_e was the average polarisation of the data sample.

	Q^2 **(GeV^2)**	$\mathbf{N}_{generated}$	σ **(pb)**	$\mathcal{L}$ **(pb^{-1})**
e^+p	> 10	249,993	44.885	5,600
	> 100	241,032	39.649	6,100
	$> 5{,}000$	15,000	3.2850	4,600
	$> 10{,}000$	5,000	0.70626	7,100
	$> 20{,}000$	5,000	0.064348	78,000
e^-p	> 10	249,000	79.4136	3,100
	> 100	248,996	73.3936	3,400
	$> 5{,}000$	15,000	14.872	1,000
	$> 10{,}000$	5,000	5.5709	900
	$> 20{,}000$	5,000	1.1795	4,200

Table 4.1: CC MC samples generated using ARIADNE for e^+p and e^-p collisions with various cuts on the minimum Q^2 value of the sample.

	Q^2 **(GeV^2)**	$\mathbf{N}_{generated}$	σ **(pb)**	$\mathcal{L}$ **(pb^{-1})**
e^+p	> 10	248,000	44.879	5,500
	> 100	247,573	39.637	6,200
	$> 5{,}000$	15,000	3.2844	4,600
	$> 10{,}000$	4,995	0.70633	7,100
	$> 20{,}000$	5,000	0.064367	78,000
e^-p	> 10	250,000	79.417	3,100
	> 100	250,000	73.400	3,400
	$> 5{,}000$	15,000	14.872	1,000
	$> 10{,}000$	5,000	5.5709	900
	$> 20{,}000$	5,000	1.1795	4,200

Table 4.2: CC MC samples generated using MEPS for e^+p and e^-p collisions with various cuts on the minimum Q^2 value of the sample.

4.2 Background samples

4.2.1 Neutral current events

A NC DIS event can contribute as a background to the CC process if the final state electron is not detected and the event is incorrectly measured as having some missing transverse momentum. This can happen if the scattered electron and part or all of the jet travels through the beam pipe hole in the CAL or towards a crack between two sections of the CAL. Dead material in front of the CAL can also cause the transverse momentum to be mis-measured, as can the energy resolution of the CAL.

NC events were simulated using the same generators and PDFs as the CC samples and ARIADNE to model the parton shower. Table 4.3 lists the numbers of NC events generated for e^+p and e^-p collisions and the corresponding luminosities. As with the the CC events, the samples were generated with different minimum values of Q^2, to ensure that the statistical uncertainty was insignificant over the whole kinematic range.

	Q^2 **(GeV^2)**	$\mathbf{N}_{generated}$	σ **(pb)**	$\mathcal{L}$ **(pb^{-1})**
e^+p	> 100	938,958	8,122.0	120
	> 400	119,995	1,167.7	100
	$> 1{,}250$	49,995	197.42	250
	$> 2{,}500$	24,000	58.915	410
	$> 5{,}000$	24,000	14.844	1,600
	$> 10{,}000$	22,000	2.7936	7,900
	$> 20{,}000$	10,000	0.30999	32,000
e^-p	> 100	399,986	8,159.1	49
	> 400	492,797	1,197.0	410
	$> 1{,}250$	209,990	217.15	970
	$> 2{,}500$	104,000	71.865	1,400
	$> 5{,}000$	104,000	21.721	4,800
	$> 10{,}000$	24,000	5.3827	4,500
	$> 20{,}000$	24,000	0.85181	28,000

Table 4.3: NC MC samples generated using ARIADNE for e^+p and e^-p collisions with various cuts on the minimum Q^2 value of the sample.

4.2.2 Photoproduction

Figure 4.1 shows Feynman diagrams for direct and resolved photoproduction (PHP) events produced in *ep* collisions. In direct PHP, the photon participates in the hard scatter. In resolved PHP, the photon provides a source of partons, which then scatter off the parton. As with NC events, the mis-measurement of a jet can lead to an inflated measurement of the missing transverse momentum, causing the PHP event to contribute towards the background to the CC events.

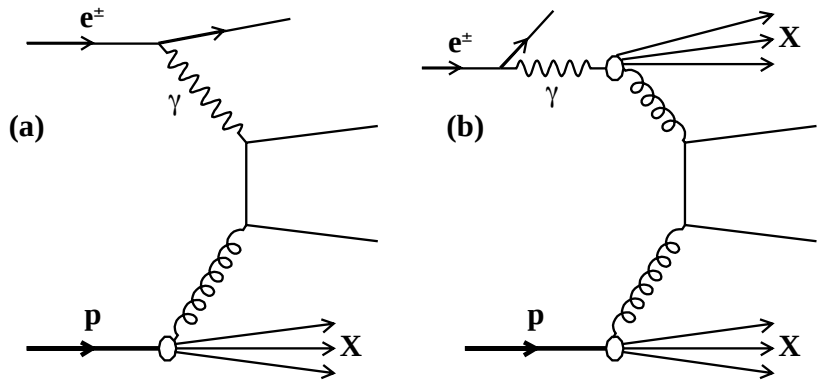

Figure 4.1: Feynman diagrams of (a) direct and (b) resolved PHP at HERA.

The HERWIG generator [104] was used to simulate samples of direct and resolved PHP events. Kinematic cuts of $E_T > 30$ GeV or $P_T > 6$ GeV were applied in order to avoid generating events in kinematic areas beyond the acceptance of this analysis and thus minimise the size of the samples. E_T, the transverse energy, and P_T, the transverse momentum, were calculated by summing over the momenta of the final state particles as follows:

$$E_T = \sum_i \sqrt{(p_X^i)^2 + (p_Y^i)^2} \text{ and} \tag{4.1}$$

$$P_T = \sqrt{\left(\sum_i p_X^i\right)^2 + \left(\sum_i p_Y^i\right)^2}, \tag{4.2}$$

where $p^i_{X,Y,Z}$ are the X, Y and Z components of the particles' momenta.

Table 4.4 lists the numbers of direct and resolved PHP events generated and the corresponding luminosities.

	Sample	$\mathbf{N}_{generated}$	σ (pb)	$\mathcal{L}$ ($\mathbf{pb}^{-1}$)
e^+p	Direct	528,985	2,830	190
	Resolved	629,825	11,900	53
e^-p	Direct	526,906	2,830	190
	Resolved	2,310,830	11,900	194

Table 4.4: Direct and resolved PHP MC events generated with $E_T > 30$ GeV or $P_T > 6$ GeV for e^+p and e^-p collisions.

4.2.3 Di-lepton production

Figure 4.2 shows a Feynman diagram for di-lepton production in an *ep* collision. At HERA, di-lepton events can be produced in elastic, quasi-elastic and DIS interactions.

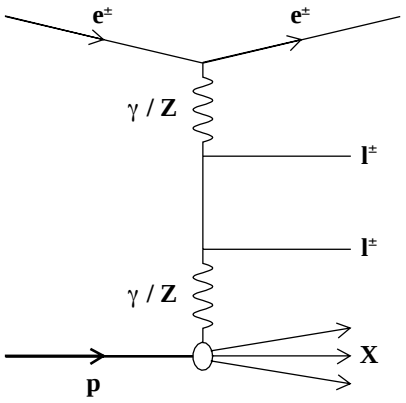

Figure 4.2: A Feynman diagram of di-lepton production in DIS at HERA.

Di-muon events may be identified as CC events, since the muons do not deposit their entire energy in the CAL and this can cause the measurement of missing transverse momentum. Di-tau events can also provide background to CC events when a tau decays to a final state involving a neutrino and missing transverse momentum is measured. The di-lepton MC samples used in this analysis were produced using the GRAPE [105] generator and are listed in Table 4.5 for each of the production channels.

	Sample	$\mathbf{N}_{generated}$	σ **(pb)**	$\mathcal{L}$ **(pb^{-1})**
e^+p	$\mu^+\mu^-$ DIS (1)	30,000	13.00195	2,300
	$\mu^+\mu^-$ DIS (2)	30,000	2.680569	11,000
	$\mu^+\mu^-$ DIS (3)	30,000	2.374704	13,000
	$\mu^+\mu^-$ DIS (4)	30,000	1.215734	25,000
	$\mu^+\mu^-$ elastic	30,000	10.20552	3,000
	$\mu^+\mu^-$ quasi-elastic (1)	30,000	4.969400	6,000
	$\mu^+\mu^-$ quasi-elastic (2)	30,000	0.1667154	180,000
	$\tau^+\tau^-$ DIS (1)	30,000	5.233473	5,700
	$\tau^+\tau^-$ DIS (2)	30,000	1.047287	29,000
	$\tau^+\tau^-$ DIS (3)	30,000	0.9540724	31,000
	$\tau^+\tau^-$ DIS (4)	30,000	0.4786053	63,000
	$\tau^+\tau^-$ elastic	30,000	6.350449	4,700
	$\tau^+\tau^-$ quasi-elastic (1)	30,000	3.562767	8,400
	$\tau^+\tau^-$ quasi-elastic (2)	30,000	0.144120	210,000
e^-p	$\mu^+\mu^-$ DIS (1)	30,000	13.05039	2,300
	$\mu^+\mu^-$ DIS (2)	30,000	2.657271	11,000
	$\mu^+\mu^-$ DIS (3)	30,000	2.368250	13,000
	$\mu^+\mu^-$ DIS (4)	30,000	1.219584	25,000
	$\mu^+\mu^-$ elastic	30,000	10.20548	2,900
	$\mu^+\mu^-$ quasi-elastic (1)	30,000	4.969400	6,000
	$\mu^+\mu^-$ quasi-elastic (2)	30,000	0.1667139	180,000
	$\tau^+\tau^-$ DIS (1)	30,000	5.248325	5,700
	$\tau^+\tau^-$ DIS (2)	30,000	1.043063	29,000
	$\tau^+\tau^-$ DIS (3)	23,796	0.9506917	25,000
	$\tau^+\tau^-$ DIS (4)	30,000	0.4798029	63,000
	$\tau^+\tau^-$ elastic	30,000	6.350560	4,700
	$\tau^+\tau^-$ quasi-elastic (1)	30,000	3.562787	8,400
	$\tau^+\tau^-$ quasi-elastic (2)	30,000	0.1044114	290,000

Table 4.5: Di-lepton production MC events produced via different physics processes for e^+p and e^-p collisions.

4.2.4 Single W production

Single W bosons can be produced at HERA through both NC interactions, as shown in Figure 4.3, and CC interactions. However, since the NC interaction can be mediated by a photon it has a cross section that is significantly greater than that of the W-mediated CC interaction. After a W boson has been produced, it can decay to a lepton and an undetected neutrino, causing the measurement of missing transverse momentum and contributing to the background to the CC events. W^+ and W^- production events were generated using the EPVEC generator [106] for both DIS and resolved processes, as listed in Table 4.6.

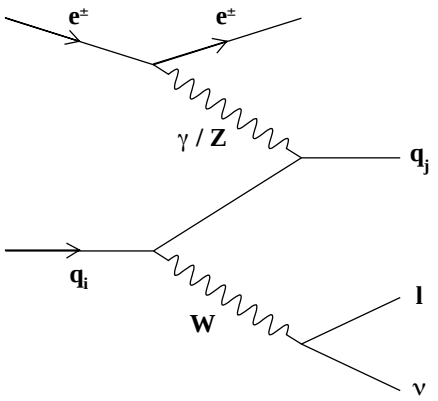

Figure 4.3: A Feynman diagram of NC W production at HERA.

	Sample	$\mathbf{N}_{generated}$	σ (pb)	$\mathcal{L}$ ($\mathbf{pb}^{-1}$)
e^+p	W^- (resolved)	10,000	0.024743	400,000
	W^- (DIS)	50,000	0.092764	540,000
	W^+ (resolved)	10,000	0.017779	560,000
	W^+ (DIS)	45,432	0.11125	410,000
e^-p	W^- (resolved)	50,000	0.024778	2,000,000
	W^- (DIS)	48,000	0.094026	510,000
	W^+ (resolved)	50,000	0.017777	2,800,000
	W^+ (DIS)	50,000	0.099255	500,00

Table 4.6: Resolved and DIS W production MC events generated for e^+p and e^-p collisions.

Chapter 5

Reconstruction of kinematic variables

The kinematic variables of each event must be accurately reconstructed from the measurements made by the ZEUS detector, in order to make accurate cross section measurements. This chapter describes the methods employed to correct for various detector effects and reconstruct the kinematic variables.

5.1 Kinematic reconstruction of DIS events

In Chapter 2 it was shown that the kinematic variables x, y and Q^2 can be expressed in terms of the four-momenta of the incoming and outgoing leptons and hadrons (see equations 2.1 to 2.3). Depending on whether there is a scattered electron or an undetected neutrino in the final state, different reconstruction methods can be employed, as described below.

5.1.1 The Jacquet-Blondel method

CC DIS events produce an undetected neutrino, so all of the information about the final state comes from the hadronic part. To reconstruct the kinematic variables for such an event, the Jacquet-Blondel method [107] is used. This method characterises the hadronic final state with the variables P_T and δ, where P_T is calculated using equation 4.2 and δ is calculated by summing over the energies

and momenta of the final state particles as follows:

$$\delta = \sum_i \left(E^i - p_Z^i\right), \tag{5.1}$$

where $p^i_{X,Y,Z}$ are the X, Y and Z components of the particle's momentum and E^i is the particle's energy.

The Jacquet-Blondel estimators of y, x and Q^2 are then given by:

$$y_{JB} = \frac{\delta}{2E_e} , \tag{5.2}$$

$$x_{JB} = \frac{P_T^2}{s y_{JB}(1 - y_{JB})} \quad \text{and} \tag{5.3}$$

$$Q^2_{JB} = s x_{JB} y_{JB}, \tag{5.4}$$

where s is the ep centre-of-mass energy squared and E_e is the energy of the incoming electron.

5.1.2 The Double Angle method

In NC DIS, there is a scattered electron in the final state, which can be well measured, and x, y and Q^2 can be reconstructed using the Double Angle method [108]. This method uses the polar angles of the scattered electron and the hadronic final state, θ and γ, respectively, where γ is calculated from P_T and δ of the hadronic final state, using the following expression:

$$\cos\gamma = \frac{P^2_{T,\text{had}} - \delta^2_{\text{had}}}{P^2_{T,\text{had}} + \delta^2_{\text{had}}} . \tag{5.5}$$

The Double Angle estimators of x, Q^2 and y are then given by:

$$x_{DA} = \frac{\sin\theta(1 - \cos\gamma)}{\sin\gamma + \sin\theta - \sin(\theta + \gamma)} , \tag{5.6}$$

$$Q^2_{DA} = 4E_e^2 x_{DA} \frac{\sin\gamma(1 + \cos\theta)}{\sin\theta(1 - \cos\gamma)} \quad \text{and} \tag{5.7}$$

$$y_{DA} = \frac{Q^2_{DA}}{s x_{DA}} . \tag{5.8}$$

5.1.3 The Electron method

A third method, the Electron method [108], uses the energy, E'_e, and polar angle of the scattered electron to reconstruct the kinematic variables as follows:

$$Q^2_e = 2E_eE'_e(1+\cos\theta), \tag{5.9}$$

$$x_e = \frac{Q^2_e}{2E_p\big(2E_e - E'_e(1-\cos\theta)\big)} \quad \text{and} \tag{5.10}$$

$$y_e = \frac{Q^2_e}{sx_e}\ , \tag{5.11}$$

where E_p is the energy of the incoming proton.

5.2 Calorimeter reconstruction

As described above, CC DIS events are reconstructed using only measurements of the hadronic final state. These measurements are made by the CAL, which means that in order to extract accurate cross section measurements, a well-understood energy measurement is essential. Noise in CAL cells, dead material in front of the CAL and backsplash from other parts of the detector can all affect the energy measured. This section describes the methods used to correct for these effects.

5.2.1 Noise suppression

Noise can arise in CAL cells due to several effects and a noise suppression routine is used to correct for each of them. One cause of noise is the radioactive decay of uranium in the CAL. This is suppressed by requiring at least 0.06 GeV measured in each EMC cell and at least 0.11 GeV in each HAC cell [109, 110, 111].

A second noise source comes from small sparks in the photomultiplier tubes (PMTs). Since each CAL cell has a pair of PMTs, such sparks can be identified by an imbalance between the energy measured in the two PMTs. Cells with less than 1 GeV and $|E_{\text{PMT 1}} - E_{\text{PMT 2}}| < 0.49E_{\text{cell}} + 0.03$ GeV are rejected [109, 110, 111].

Noise is further reduced by rejecting CAL cells with isolated energy deposits. Isolated EMC cells with more than 0.08 GeV or isolated HAC cells with more than 0.14 GeV are ignored [109, 110, 111].

Cells with consistently high energy measurements that are due, for example, to faulty PMTs or read-out electronics, are another source of noise. Such cells, termed hot cells, are identified and rejected on a run-by-run basis, by studying events selected with a random trigger from electron or proton pilot bunches.

First, the fraction of times each cell has an energy measurement above the radioactivity thresholds is calculated as follows [109, 110, 111]:

$$f_i = \frac{N_{i,\text{ above threshold}}}{N_{\text{total}}} \ , \tag{5.12}$$

where $N_{i,\text{ above threshold}}$ is the number of times cell i measured energy above the radioactivity thresholds and N_{total} is the total number of events in the sample.

Cells with $f_{\text{cell}} > f_{\text{mean}} + 5\sigma_f$ are rejected, where f_{mean} is the mean and σ_f is the width of the f distribution for all cells [109, 110, 111]. The procedure is performed twice for BCAL cells. The whole procedure is repeated again after cells with sparks have been rejected.

Next, the mean energy measured by a cell for each run is calculated as follows [109, 110, 111]:

$$E_{\text{cell}}^{\text{mean}} = \frac{\Sigma E_{\text{cell}}}{N_{\text{total}}} \ . \tag{5.13}$$

Cells with $E_{\text{cell}}^{\text{mean}} > E_{\text{mean}} + 5\sigma_E$ are rejected, where E_{mean} is the mean and σ_E is the width of the $E_{\text{cell}}^{\text{mean}}$ distribution for all cells [109, 110, 111].

Hot cell rejection is performed on all CAL cells except those in the first RCAL and FCAL inner rings around the beam pipe, so as not to reduce the effectiveness of beam gas rejection based on the energy measured in these cells.

5.2.2 Clustering

After noise suppression, CAL cells are clustered to form islands, such that, ideally, one island contains the energy deposits created from a single particle showering

in the CAL. The islands can be used to make a better estimate of the angular position of each particle arriving at the CAL.

The clustering algorithm [112] is first performed separately on each layer of each CAL section. Cells with energy measurements are merged with their highest energy neighbouring cell, which can be across the beam hole in the FCAL, to form cell islands. Cell islands in different layers and sections of the CAL are then combined, working inwards from the HAC to the EMC, to form cone islands. The logarithmic energy-weighted centre of gravity of a cone island is taken as its position.

5.2.3 Corrections applied to islands

Various processes can affect both the amount of energy measured in the CAL and the positions of the energy deposits. In addition, the resolution of the CAL can result in reconstructed values for kinematic variables that exceed the physical limit of the variable. Routines [113, 114] had been developed to account for these effects and provide improved estimates of the kinematic variables for each event.

Both the Jaquet-Blondel and Double Angle methods are sensitive to the back-splash effect, which causes energy deposits to arrive in parts of the CAL away from the true direction of the particles produced in the *ep* interaction. Back-splash can originate either from the CAL itself or from scattering or showering in the material in front of the CAL. To eliminate such deposits, any islands with less than 3 GeV of energy and a polar angle greater than γ_{max} are removed [113, 114]. γ_{max} was tuned using NC MC samples such that the largest possible number of back-splash islands and less than 1% of non-back-splash islands were removed. This produced the following definition of γ_{max} [113, 114]:

$$\gamma_{max} = \begin{cases} 0.151 + 1.372\gamma & \text{for } \gamma < 1.95 \text{ radians,} \\ 2.826 + 0.259(\gamma - 1.95) & \text{for } \gamma > 1.95 \text{ radians,} \end{cases}$$

where γ was defined by equation 5.5. After removing back-splash islands, γ is re-calculated and the procedure repeated until the change in γ is less than 1%.

The Jaquet-Blondel method is also sensitive to any mis-measurement of the amount of energy deposited in the CAL. This can be caused by inactive material, overestimating the energy of low-energy hadrons or particles passing through the cracks between the CAL sections.

Inactive material between the IP and the CAL can cause particles to lose energy before they reach the CAL. NC MC events, simulated using a map of the inactive material, were used to determine a correction factor for each island based on its energy, the fraction of its energy in the EMC and the amount of inactive material between the IP and the island [113, 114].

The energy of low-energy hadronic deposits tends to be overestimated, since at low energy there is a greater probability for the particles to deposit energy by ionisation, rather than showering, and the CAL is around 60% more sensitive to energy deposits from ionisation than it is to those from showering. The energy of very low-energy deposits can be overestimated even further due to the different values of the energy cuts used to remove the radioactive noise from the EMC and HAC sections of the CAL. Islands are corrected for both of these effects based on their energy and the fraction of their energy in the EMC [113, 114].

Particles passing through the cracks between the CAL sections can completely or partially escape detection by the CAL and their energy is mis-measured. This effect is corrected for as a function of γ [113, 114].

The final correction applied to the Jacquet-Blondel variables accounts for the fact that all measurements are dependent on the energy resolution of the CAL, which can lead to estimating unphysical values of the kinematic variables. For the true values for any event, the following must be true:

$$\delta < 2E_e \text{ and} \tag{5.14}$$

$$\frac{P_T^2}{1 - y_{JB}} < s. \tag{5.15}$$

These requirements are enforced by firstly scaling δ down to the median of a Gaussian probability distribution centred on the measured value of δ, with a width equal to the resolution of δ and defined to be zero for values of $\delta > 2E_e$.

$y_{JB} = \delta/2E_e$ is then recalculated and a similar procedure is applied to restrict $Q^2_{JB} = P^2_T/(1 - y_{JB})$ to be in the range $0 < Q^2_{JB} < s$, whilst taking into account the new resolution on y_{JB}[1] [113, 114].

5.2.4 Bias and resolution of charged current events

The correction methods described in the previous section were assessed by studying the bias and resolution of the reconstructed variables before and after correction, which were estimated by fitting a Gaussian to the following distribution:

$$\frac{X_{\text{reconstructed}} - X_{\text{true}}}{X_{\text{true}}} \, , \tag{5.16}$$

where X is the variable being studied using CC MC. The Gaussian mean and σ provide estimates of the fractional bias and resolution, respectively.

Figure 5.1 shows the fractional bias before and after correction of x_{JB}, y_{JB}, Q^2_{JB} and P_T, plotted against their true values with the error bar representing the fractional resolution. After correction, improvements in the bias are observed for all variables across the entire kinematic range. The resolution also improves, most notably at high-x. Generally, there is very little bias, the worst region being $x < 0.01$, where the bias rises to around 10%. The resolution is best at high-x and high-y, at less than 10%, and is fairly uniform across the whole Q^2 range, at around 20%.

Figure 5.2 shows the fractional bias and resolution of x_{JB} and Q^2_{JB} in bins of x and Q^2 for both e^+p and e^-p collisions. As seen already in Figure 5.1, the resolution is best at high x and is fairly uniform across the Q^2 range. There is little difference between the reconstruction of e^+p and e^-p events.

[1] This was defined to be the distance from the median value, towards the kinematic limit, covering 67% of the integrated probability between the median and the limit.

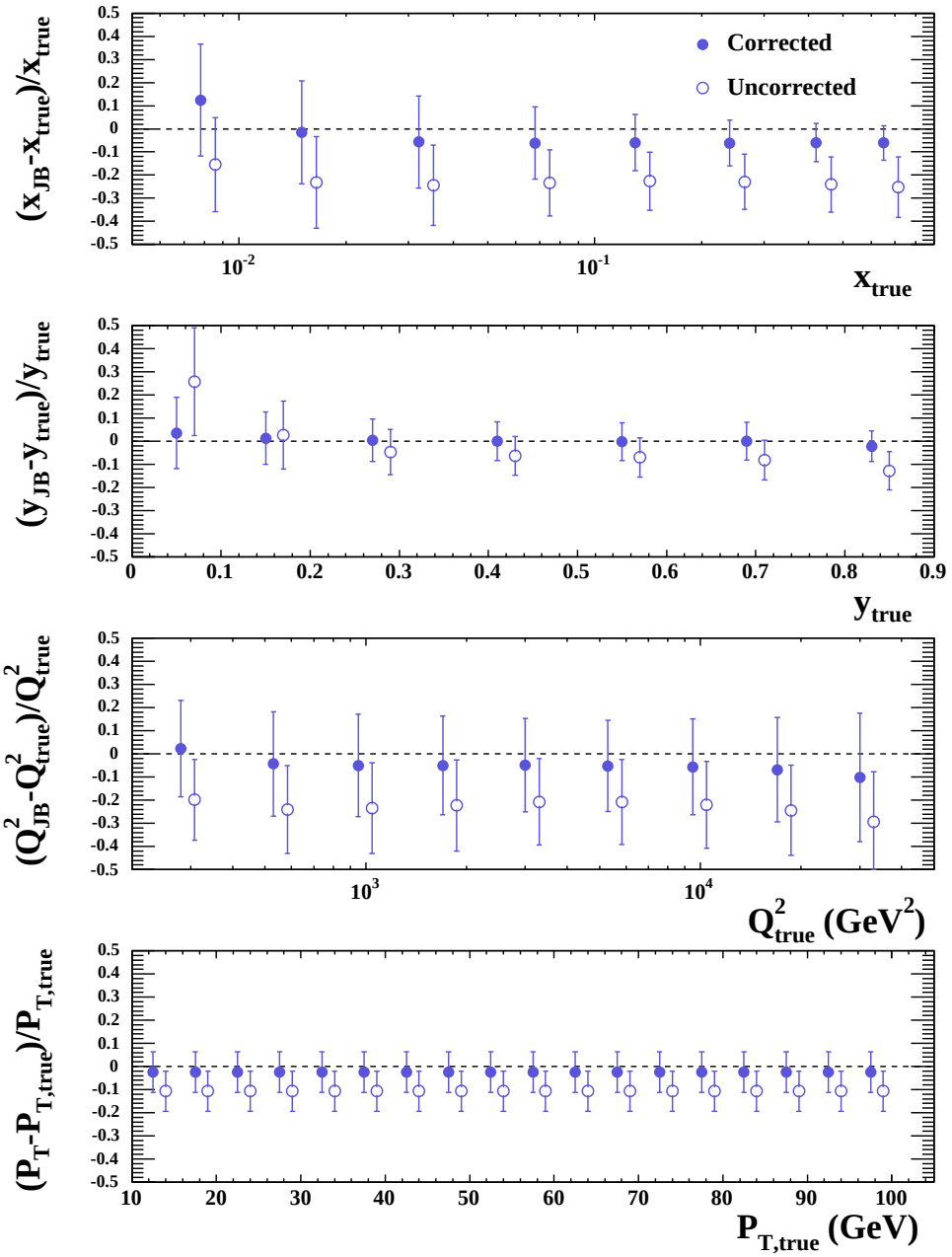

Figure 5.1: The fractional bias of the corrected (filled points) and uncorrected (open points) estimators of x_{JB}, y_{JB}, Q^2_{JB} and P_T, plotted against their true values. The error bars represent the fractional resolution at each point.

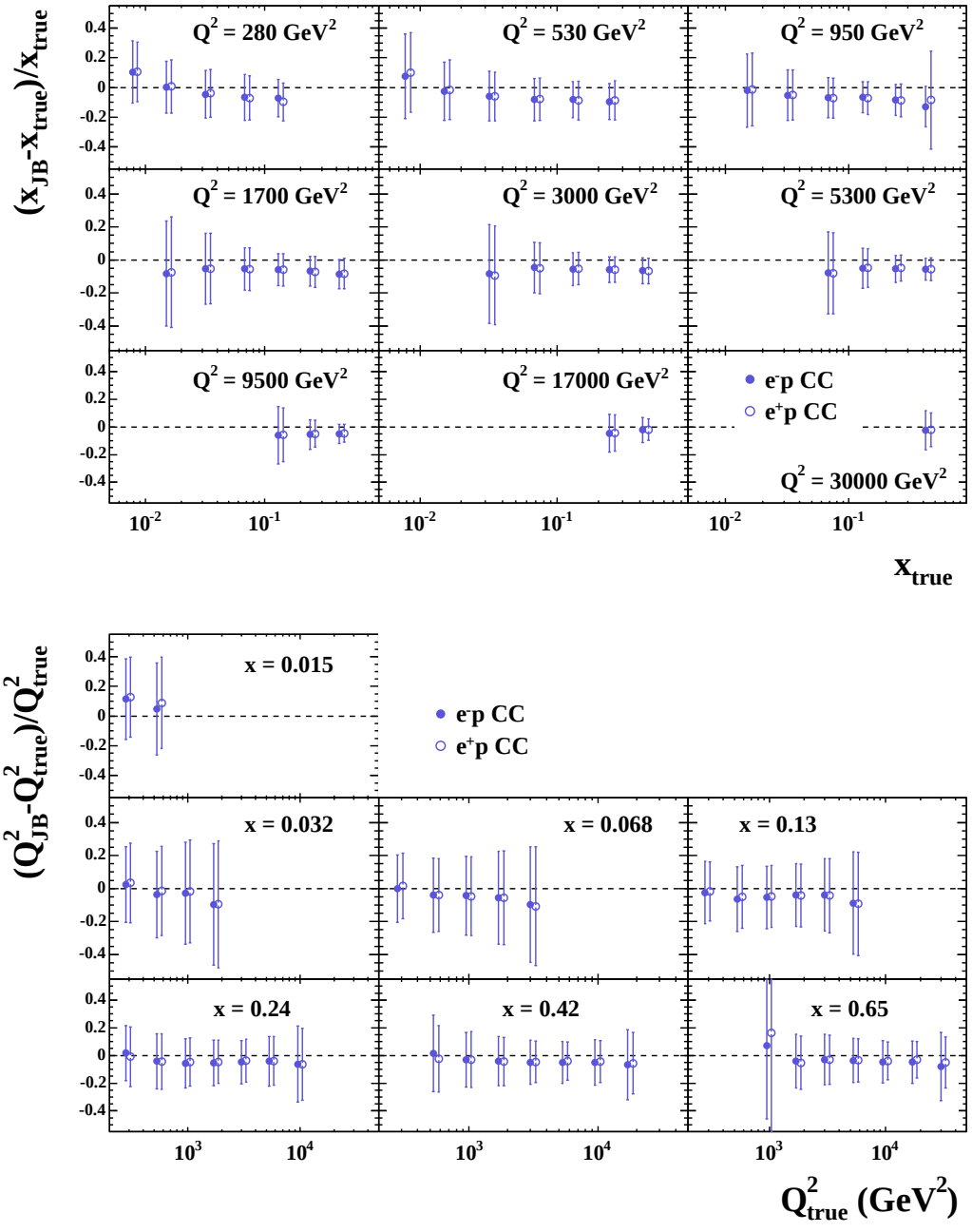

Figure 5.2: The fractional bias of the corrected x_{JB} estimator plotted against x in bins of fixed Q^2 (top) and the fractional bias of the corrected Q^2_{JB} estimator plotted against Q^2 in bins of fixed x (bottom) for e^-p (filled points) and e^+p (open points) collisions. The error bars indicate the fractional resolution at each point.

5.3 Track reconstruction

The tracks of charged particles are reconstructed from the hits measured in the CTD and MVD. Track reconstruction consists of two main steps: pattern recognition and track fitting. The reconstructed tracks are then used to determine the position of the primary and, possibly, secondary vertices of the event.

A pattern recognition algorithm [115] is run over the CTD and MVD hits, which begins by looking for seeds formed from three hits in the outermost CTD superlayer. It then proceeds inwards through the CTD and MVD, fitting hits to the track in the $X-Y$ plane and using information from the Z-by-timing system, the CTD stereo superlayers and the MVD, to fit the Z position of the track. This is repeated starting from each seeds in the outermost superlayer and then from each seed in the next inner superlayer and so on, until all seeds have been used.

A five parameter helix is fitted to the CTD hits associated with each pattern recognition track [115]. The helix is used as the input to a Kalman filter [116, 117], which works inwards adding in MVD hits and accounting for the effects of MVD material and the edge of the beam pipe on the trajectories of the charged particles[2].

5.4 Reconstruction of the interaction vertex position

Two methods are used to determine the position of the interaction vertex of an event. The tracking vertex, which is reconstructed from the hits measured in the CTD and MVD, is suitable for events with charged particles passing through the acceptance region of the CTD. However, for CC events with the hadronic final state detected in the forward region, there is little or no tracking information, so for these events the Z vertex position is reconstructed using FCAL timing information.

[2]There were no stand-alone MVD tracks in the track reconstruction used in this analysis.

5.4.1 Vertex reconstruction from tracks

The tracks described in section 5.3 are fed into a Kalman filter [118], which runs over the tracks one by one to locate the primary vertex. Tracks that are not associated with the primary vertex are used to locate eventual secondary vertices. The Z vertex position reconstructed from tracks for e^+p and e^-p CC data and MC is shown in Figure 5.3. There is reasonable agreement between the data and the MC and the effect on the extracted cross section measurements from any differences is discussed in sections 7.4.8 and 7.4.10.

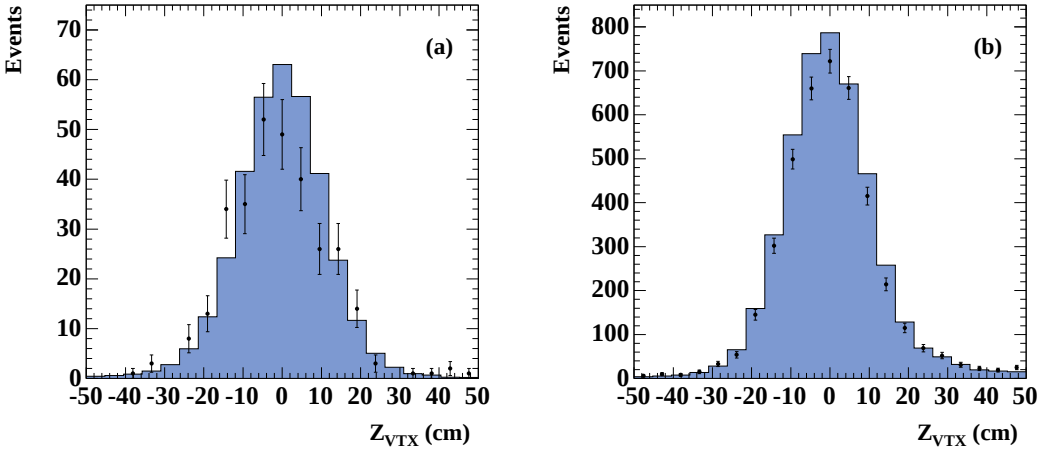

Figure 5.3: The Z vertex position reconstructed from tracks for (a) e^+p and (b) e^-p CC data (points) and MC (histograms).

5.4.2 Vertex reconstruction from FCAL timing information

For events with FCAL energy deposits, the Z vertex position can be reconstructed from FCAL timing information. First, the interaction time, t_{int}, and interaction vertex, Z_{int}, are determined from the C5 counter with the following expressions [71]:

$$t_{int} = \frac{1}{2}(t_{e,\mathrm{C5}} + t_{p,\mathrm{C5}}) - \mathrm{C5}_{t\ \mathrm{offset}} \quad \text{and} \tag{5.17}$$

$$Z_{int} = \frac{c}{2}(t_{e,\mathrm{C5}} - t_{p,\mathrm{C5}}) - \mathrm{C5}_{Z\ \mathrm{offset}}, \tag{5.18}$$

where $\mathrm{C5}_{Z\ \mathrm{offset}} = 297$ cm and $\mathrm{C5}_{t\ \mathrm{offset}} = 37.3$ ns, and $t_{e,\mathrm{C5}}$ and $t_{p,\mathrm{C5}}$ are the times at which the electron and proton are detected in the C5 counter, respectively.

The arrival times of the energy deposits in each FCAL cell, t_{cell}, are estimated from the weighted average of the time measured in the two PMTs of each cell, $t_{PMT\ 1,2}$, as follows [71]:

$$t_{cell} = \frac{\frac{1}{\sigma_1^2} t_{PMT\ 1} + \frac{1}{\sigma_2^2} t_{PMT\ 2}}{\frac{1}{\sigma_1^2} + \frac{1}{\sigma_2^2}} \ , \tag{5.19}$$

where $\sigma_{1,2}$ are the timing resolutions for the PMTs, which are estimated as a function of the energy measured in the PMT, E_i, using:

$$\sigma_i = 0.4 + \frac{1.4}{E_i} \ , \tag{5.20}$$

where E_i is in GeV.

The initial t_{cell} estimates are then corrected according to the following variables [71]:

- the ZEUS run number;
- the cell energy;
- how much energy is deposited in surrounding cells;
- the total FCAL energy;
- the fraction of energy in the EMC;
- shifts between cells in the FCAL inner ring; and
- the scale difference between the FCAL time and that expected from the tracking vertex position.

The correction factors were determined using NC DIS data with an electron track measured in the CTD [71].

The Z vertex position is then estimated for each FCAL cell as follows [71]:

$$Z_i = \frac{R_0^2 - A^2}{2(A + Z_{cell})} \ , \tag{5.21}$$

where $A = ct_{cell} - ct_{int} - Z_{int} + R_0$, $R_0^2 = X_{cell}^2 + Y_{cell}^2 + Z_{cell}^2$ and X_{cell}, Y_{cell} and Z_{cell} are the FCAL cell coordinates.

The final estimate of the Z vertex position is the average of these estimates, weighted by the timing resolution for each cell, which is given as follows [71]:

$$Z_{FCAL} = \frac{\sum_i \frac{1}{\sigma_i^2} Z_i}{\sum_i \frac{1}{\sigma_i^2}} \ , \tag{5.22}$$

where the sum is performed over all FCAL cells and the timing resolutions, σ_i, are determined by equation 5.20.

In the MC, the CAL timing is not well simulated and cannot be used to reconstruct the Z vertex position. Instead, the true Z vertex position is smeared by a Gaussian function, the parameters of which are determined from NC measurements, to estimate the reconstructed vertex position.

The Z vertex position reconstructed from the FCAL timing information for e^+p CC data and MC is shown in Figure 5.4.

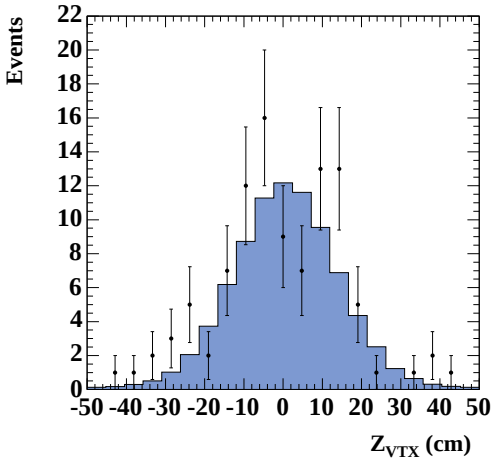

Figure 5.4: The Z vertex position reconstructed from FCAL timing information for e^+p CC data (points) and MC (histogram).

5.4.3 Vertex efficiency, bias and resolution

In order to assess the two vertex-finding methods, it is useful to plot the Z vertex-finding efficiency, bias and resolution as a function of γ_0, where γ_0 is the polar

angle of the hadronic final state with respect to the nominal Z vertex position, zero.

Vertex-finding efficiency, ϵ, is defined as follows:

$$\epsilon = \frac{\text{Number of events with a reconstructed vertex}}{\text{Number of events}}. \tag{5.23}$$

The bias and resolution of the reconstructed vertex position can be measured using MC to create histograms of $Z_{\text{reconstructed}} - Z_{\text{true}}$. The bias and resolution are estimated by taking the mean and RMS of this distribution, respectively.

The efficiency, bias and resolution of the Z vertex position for CC DIS events reconstructed from tracks and from FCAL timing information are shown in Figure 5.5, plotted as a function of γ_0. The vertex-finding efficiency is one for all values of γ_0 for the FCAL timing vertex and for $\gamma_0 > 0.4$ radians for the tracking vertex. For $\gamma_0 < 0.4$ radians, the tracking vertex-finding efficiency falls steeply and reaches zero at around 0.1 radians. At high values of γ_0, the resolution for the tracking vertex is a few mm with no bias. This worsens to a resolution of 2 to 4 cm with a bias of 1 to 2 cm for $\gamma_0 < 0.4$ radians. The FCAL timing vertex has a resolution of around 8 to 10 cm for all values of γ_0 and no bias.

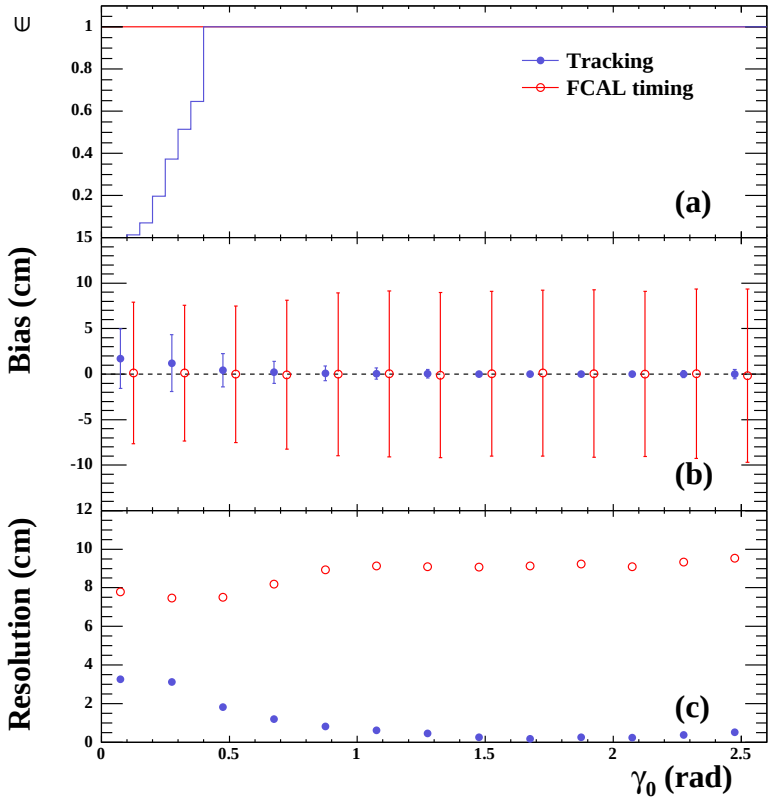

Figure 5.5: (a) Z vertex-finding efficiency, ϵ, (b) the bias of the reconstructed Z vertex position with the size of the error bar representing the resolution and (c) the resolution of the reconstructed Z vertex position, all plotted against γ_0. The blue lines and filled blue points are for the tracking vertex and the red lines and open red points are for the FCAL timing vertex.

Chapter 6

Event selection

This chapter presents an introduction to the CC selection and the types of background to be rejected. The data samples and the online and offline cuts applied to the data and MC, to select CC events and to reject background, are then described. After all selection cuts have been applied, the number of data and MC events are given and various data and MC distributions are compared.

6.1 Introduction

CC events have an undetected neutrino in the final state, which causes an imbalance in the measured P_T. Requiring events to exceed a minimum value of $P_{T,miss}$ is therefore an effective way of selecting CC events. However, many sources of background can also cause the measurement of significant $P_{T,miss}$, so additional selection criteria must be imposed to remove these backgrounds.

Background to CC events can be split into two categories: SM background and non-*ep* background. The contribution to the final sample from SM background, for example NC or PHP events, can be estimated using MC simulation and taken into account when extracting the cross sections. However, non-*ep* background, which means that the event measured in the detector was not initiated by an *ep* collision, is much harder to simulate accurately and rates can fluctuate during data-taking, making it extremely hard to estimate the amount of non-*ep* background present in the final data sample. Tight cuts had to be applied, in order to

ensure the complete removal of non-*ep* background from the final sample.

There were various types of non-*ep* background to be removed, including:

- **Beamgas events** - initiated by electrons or protons from the beams interacting with gas particles in the beampipe;
- **Halo muons** - created when protons from the edges of the proton bunches interact with the wall of the beam pipe or upstream accelerator components, such as a bending magnet, and then pass through the detector, parallel to the Z axis but generally not through the centre;
- **Cosmic muons** - created from cosmic rays and usually travelling downwards through the detector and not through the centre;
- **Off-beam protons** - protons that have drifted horizontally out of the main proton bunches are sometimes detected passing through the detector, parallel to the Z axis but not through the centre.

Particles from non-*ep* background interactions were detected either alone or, as was often the case with halo and cosmic muons, as overlay events, when an *ep* collision occurred but a particle or particles from a background interaction were also measured in the detector. In both instances, the background energy deposits tended to lie mostly in one half of the CAL and caused the measurement of significant $P_{T,miss}$.

6.2 The data samples

Data samples collected with the ZEUS detector in the years 2004 and 2005 were used. Data quality cuts ensured that the necessary detector components were functioning properly and that at least one polarimeter could provide a measurement of P_e.

The e^+p luminosity measurement was taken from the Spectrometer and for the e^-p measurement, the Photon Calorimeter was used. Difficulties with the Pho-

ton Calorimeter measurement during e^+p running meant that the Spectrometer measurement had to be used, despite the slightly greater uncertainty on this measurement.

For a given ZEUS run, the polarisation measurement was taken from the polarimeter with a measurement for the greatest amount of ZEUS gated luminosity. When the ZEUS luminosities for the two polarimeters were equal, the LPOL measurement was used. The luminosity and polarisation measurements were synchronised using the time measured by the HERA clock.

After the data quality cuts, this provided the integrated luminosities, $\mathcal{L}$, and luminosity-weighted average longitudinal lepton beam polarisations, P_e, listed in Table 6.1.

Beams	$\mathcal{L}$ (pb^{-1})	P_e
e^+p	11.5 ± 0.4	-0.41 ± 0.01
	12.3 ± 0.4	+0.32 ± 0.01
e^-p	86.4 ± 2.2	-0.27 ± 0.01
	44.1 ± 1.1	+0.33 ± 0.02

Table 6.1: The integrated luminosities and luminosity-weighted average longitudinal lepton beam polarisations of the data samples.

The absolute value of P_e is plotted as a function of ZEUS run number in Figures 6.1 (a) and (b), and the integrated luminosity collected in bins of P_e is presented in Figure 6.2.

6.3 Online selection

The online CC selection was similar to the offline selection, except that the cuts were generally slightly looser to account for the worse resolution. CC events were selected by requiring some $P_{T,miss}$ and further cuts rejected background and ensured that the trigger rate remained manageable.

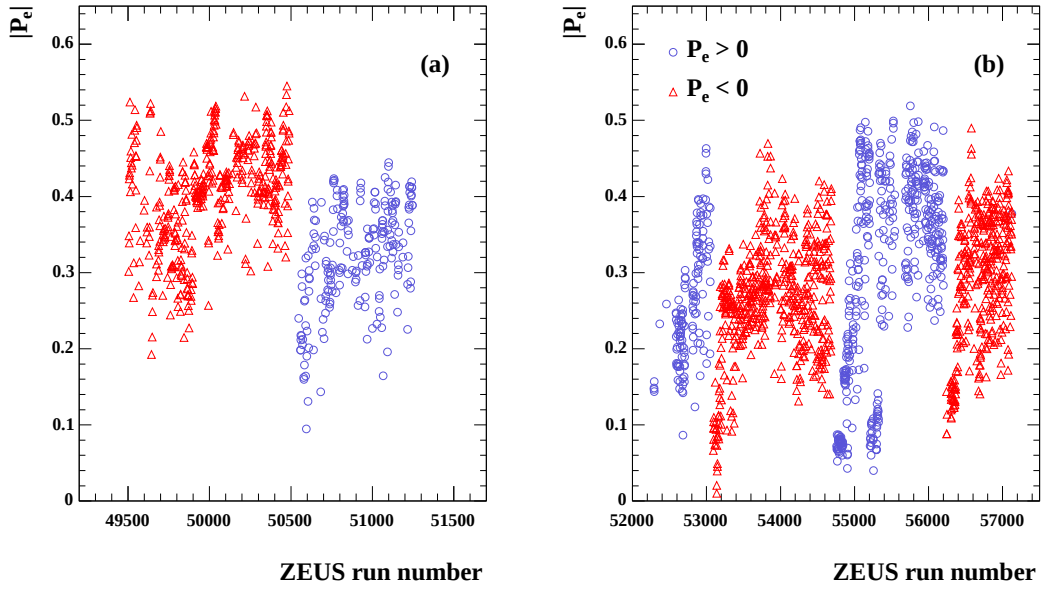

Figure 6.1: The absolute longitudinal lepton beam polarisation plotted against ZEUS run number, for the (a) 2004 e^+p and (b) 2004 - 2005 e^-p running periods. Blue circles and red triangles represent runs with positive and negative values of P_e, respectively.

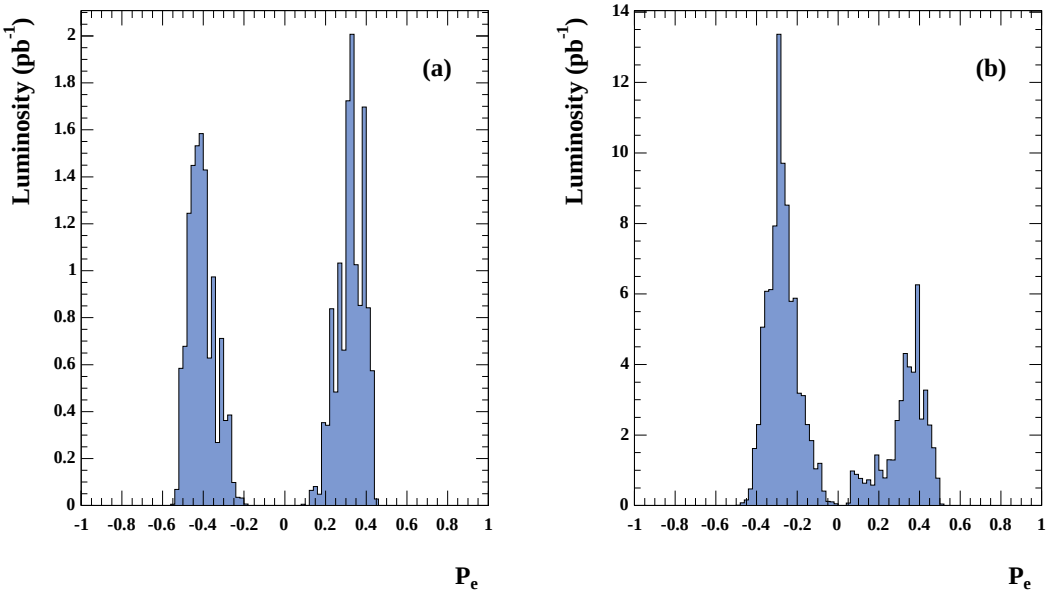

Figure 6.2: The integrated luminosity collected with the ZEUS detector in bins of P_e, for the (a) 2004 e^+p and (b) 2004 - 2005 e^-p (b) running periods.

6.3.1 First level trigger

The FLT is divided into 64 slots, each with a designated function such as accepting a certain kind of physics event. The slot used to select CC events, slot 60, required that events passed at least one of the following three branches:

1. $P_{T,miss} > 5$ GeV **AND** E_T(-2IR) > 5 GeV **AND** at least one vertex track.
2. $P_{T,miss} > 8$ GeV **AND** any track.
3. $P_{T,miss} > 8$ GeV **AND** $E_{FCAL} > 10$ GeV.

$P_{T,miss}$ is the missing transverse momentum, calculated using equation 4.2, and E_T is the transverse energy, calculated using equation 4.1. At the FLT, the sums in these calculations are performed over CAL towers and -nIR means that the n innermost rings of FCAL cells around the beam pipe were not included in the sum.

At the FLT, tracks were identified by running a pattern-recognition algorithm over the hits in three of the CTD superlayers. A vertex track at the FLT means that the identified track pointed back to the nominal interaction vertex at $Z = 0$ cm. Requiring a vertex track helped to ensure that the event was caused by an ep collision.

With the requirement of a vertex track, the first branch of slot 60 accepted events detected predominantly in the central region of the detector. The second branch had a slightly looser tracking requirement and no cut on E_T but a tighter cut on $P_{T,miss}$, to control the background rate. The third branch was designed to accept events detected in the forward region of the detector, so it had no tracking requirement and demanded at least 10 GeV of energy in the FCAL.

In addition to the above criteria, further cuts were applied to minimise the background rate. Vetoes from the C5 counter and Veto Wall rejected events caused by interactions outside of the detector. Beamgas events were removed using the Loose or Tight Track Vetoes, which rejected events with a large number of tracks not pointing to the interaction vertex. Events were classified according to their

number of tracks and number of vertex tracks, as illustrated in Figure 6.3. The Tight Track Veto, which was applied to the CC slot during e^+p data-taking, rejected class 2 and class 8 events and the Loose Track Veto, which was applied during e^-p data-taking, rejected class 2 events.

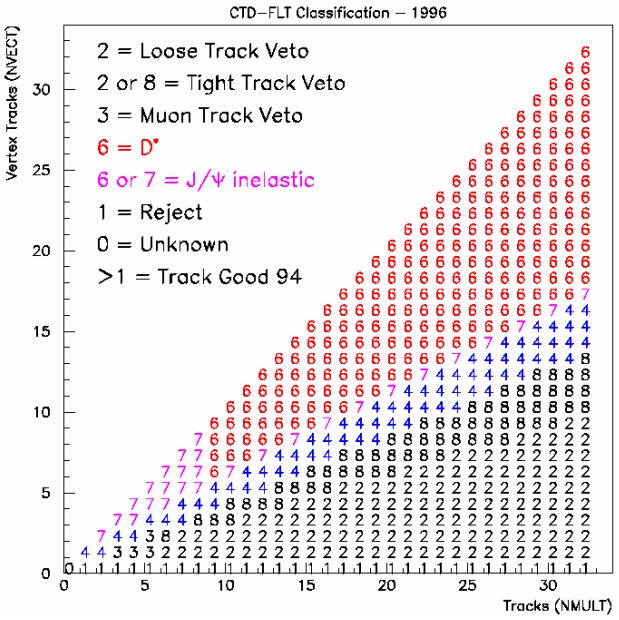

Figure 6.3: The classification of events according to their number of tracks and vertex tracks at the FLT.

Further background rejection was provided by the Fast Clear. Slot 60 had two Fast Clear requirements:

- $P_{T,miss} > 8$ GeV **AND NOT** beamgas.

An event was identified as beamgas if:

- the highest energy RCAL cluster had more than 50 GeV of energy **AND**
- its maximum energy tower was in the first inner ring around the beam pipe.

If an event did not satify the above Fast Clear requirements, it was rejected.

During 2005, the high luminosity delivered by HERA, combined with occasional bad background conditions, led to an FLT deadtime that was sometimes undesirably high. In order to reduce the deadtime, the background rejection at the CC FLT was improved by splitting slot 60 into two slots: slot 60 and slot 63. Slot 60

required events to pass at least one of these branches:

1. $P_{T,miss} > 5$ GeV **AND** E_T(-2IR) > 5 GeV **AND** at least one vertex track.
2. $P_{T,miss} > 11.5$ GeV **AND** any track.
3. $P_{T,miss} > 11.5$ GeV **AND** $E_{FCAL} > 10$ GeV.

Slot 63 required events to pass at least one of these branches:

1. $P_{T,miss} > 5$ GeV **AND** E_T(-2IR) > 5 GeV **AND** at least one vertex track.
2. $P_{T,miss} > 8$ GeV **AND** any track.
3. $P_{T,miss} > 11.5$ GeV **AND** $E_{FCAL} > 10$ GeV.

Both slots had the same Fast Clear and veto requirements as the original slot 60, except that slot 63, with a lower $P_{T,miss}$ requirement in branch 2, additionally required $\delta > 3$ GeV at the Fast Clear.

Studies with previously accepted data events, that had passed the CC offline selection, and CC MC, predicted that the tightened CC FLT selection would cause only a very small decrease in CC offline efficiency, around 0.3%, and that the lost events would be low-Q^2, low-y and mid-x events. A sample of passthrough events[1] was used to provide the estimate that the CC FLT output rate would decrease by around 30%, leading to a significant decrease in FLT deadtime.

Five other FLT slots (39, 40, 41, 43 and 44) were used to accept CC events that could have been rejected by slots 60 and 63. They were defined as follows:

- **Slot 39**: $E_{BEMC} \geq 3$ GeV **AND** an isolated electron in the BCAL **AND** at least one good track.
- **Slot 40**: $E_{EMC} \geq 25$ GeV.
- **Slot 41**: E_T(-2IR) ≥ 30 GeV.
- **Slot 43**: E_T(-2IR) ≥ 12 GeV **AND** at least one good track.

[1]Passthrough events are events taken by a pre-scaled random trigger and provide unbiased samples of data events arriving at each level of the trigger.

- **Slot 44**: $E_{BEMC} \geq 10$ GeV **AND** $E_{REMC} \geq 3$ GeV **AND** an isolated electron in the BCAL **AND** at least one vertex track.

At the FLT, E_{EMC} is the energy measured in the EMC, excluding the three FCAL inner rings and one RCAL inner ring of cells around the beampipe. E_{BEMC} and E_{REMC} are the sums of the energies measured in the EMC in the BCAL and the RCAL, respectively, again excluding the first inner ring of cells around the beampipe in the RCAL. All slots applied the Tight Track Veto, except slot 39, which applied the Loose Track Veto. The Veto Wall and C5 vetoes were also applied to all five slots.

Figure 6.4 shows the inclusive and exclusive number of CC data events accepted by each slot. Most were taken by the CC slots (60 and 63) but there was a small number of exclusive events accepted by the other slots.

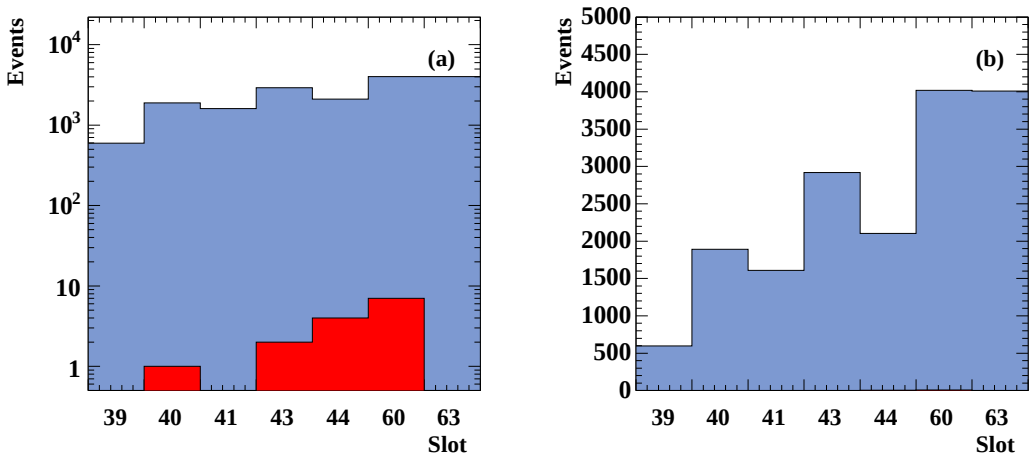

Figure 6.4: The inclusive (blue) and exclusive (red) number of CC data events accepted by each FLT slot plotted on (a) logarithmic and (b) linear scales. These plots only contain events taken after slots 60 and 63 were modified.

6.3.2 Second level trigger

At the SLT, the extra time available compared to the FLT allowed more detailed and precise tracking and calorimeter information to be calculated for each event. CAL cells without zero suppression, rather than towers, were used, which

improved the energy and angular resolution of the CAL, and a more detailed tracking algorithm provided an estimate of the ep interaction vertex position with improved accuracy.

At the SLT, one slot was designed to accept CC events, which were required to pass at least one of the following four branches:

1. At least one track **AND** $P_{T,miss} > 6$ GeV **AND** E_T(-IR) > 6 GeV **AND** CTD data size cut.
2. $P_{T,miss} > 9$ GeV **AND** E_T(-IR) > 8 GeV **AND** $E_{FCAL} > 20$ GeV.
3. $P_{T,miss} > 9$ GeV **AND** $E_{FCAL} > 80$ GeV **AND** $\frac{P^2_{T,miss}}{E_T} > 4.41$ GeV.
4. At least one track **AND** $\delta > 6$ GeV **AND** $\frac{P^2_{T,miss}}{E_T} > 2.25$ GeV.

The CTD data size cut, which was only applied to the $e^{-}p$ data, rejected background events characterised by a large amount of activity in the CTD.

Branches 1 and 4 required at least one track, so tended to accept events detected in the central region of the detector. Branches 2 and 3 accepted more forward events as they had no tracking requirement and demanded some minimum energy measured in the FCAL.

Figure 6.5 shows the inclusive and exclusive number of CC data events accepted by each branch of the CC SLT.

In addition to passing at least one of the above four branches, CC events also had to meet the following criteria:

- CAL timing information was consistent with ep bunch crossing time **OR** at least one track and a Z vertex position was found; and
- $|p_Y| > 3$ GeV **OR** $P_{T,miss} > 15$ GeV **OR** E_T(-IR) > 6 GeV **OR** $P_{T,miss}/p_Z > 0.06$.

Here, $|p_Y|$ was calculated as follows:

$$|p_Y| = |\sum_i p_Y^i| \ , \tag{6.1}$$

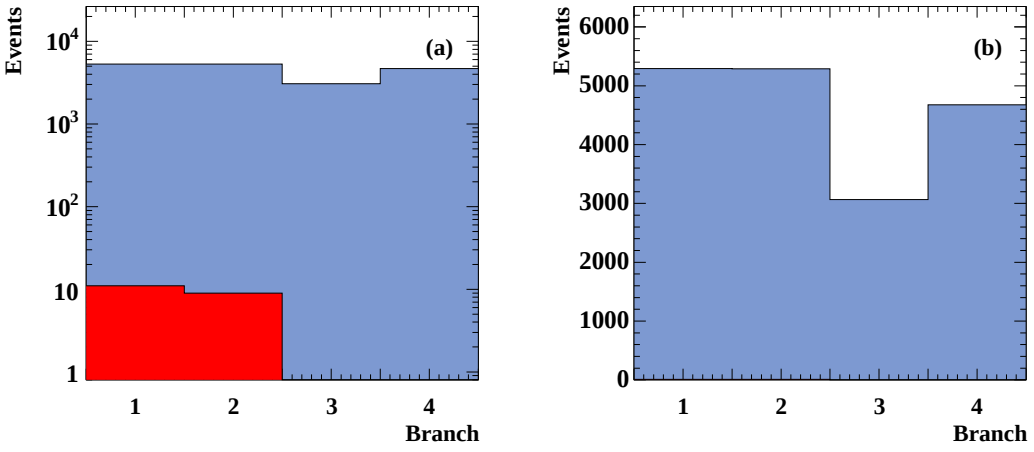

Figure 6.5: The inclusive (blue) and exclusive (red) number of CC data events passing through each branch of the CC SLT slot plotted on (a) logarithmic and (b) linear scales.

where the sum was performed over CAL cells.

The first requirement helped ensure that events originated from ep collisions. The second requirement, the off-beam proton veto, was designed to reject off-beam proton events. These protons had drifted out of the proton bunches in the X direction, causing the measurement of a small amount of $P_{T,miss}$ with a low value of $|p_Y|$, and they tended to deposit most of their energy in the FCAL, which caused low values of $P_{T,miss}/p_Z$. During 2005, the off-beam proton veto was tightened to reduce the CC SLT output rate, becoming:

- $|p_Y| > 5$ GeV **OR** $P_{T,miss} > 15$ GeV **OR**
  E_T(-IR) > 6 GeV **OR** $P_{T,miss}/p_Z > 0.08$.

Before tightening the online selection, the efficiency of the tighter off-beam proton veto was checked using a sample of data already collected, that had passed the offline CC selection cuts, and CC MC. It was found that none of the selected data events would have been rejected by the tightened off-beam proton veto and the CC MC predicted only a very small worsening in the offline CC efficiency, by less than 0.1%. The MC events that would be rejected were found to be low-y, low-Q^2 and mid-x events.

A sample of SLT passthrough events was used to estimate the change in SLT output rate caused by the tightened off-beam proton veto. It was estimated that the rate of events passing the CC SLT slot would reduce by around 40%, although this figure was highly dependent on the actual running conditions. Figure 6.6 shows the CC SLT output rate, plotted as a function of ZEUS run number, for runs before and after the tightening of the off-beam proton veto. After the veto was tightened there were fewer runs with very high rates and the mean rate of all runs fell.

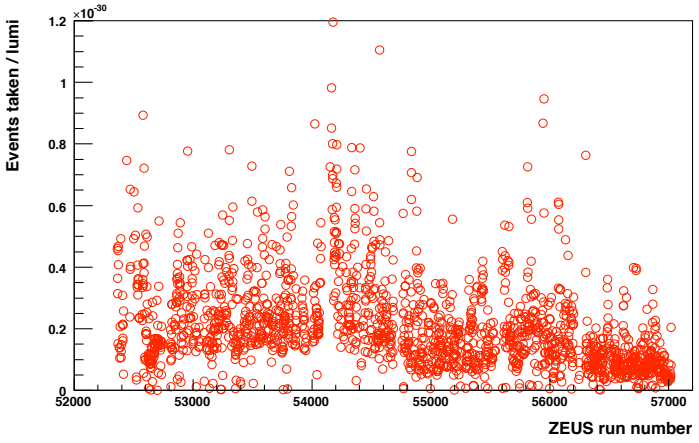

Figure 6.6: The output rate of the CC SLT slot plotted against ZEUS run number during e^-p data-taking. The tighter off-beam proton veto was enforced from run 56244 onwards and, as expected, a decrease in the output rate was observed.

6.3.3 Third level trigger

At the TLT, even more time was available and, as the reconstruction algorithms were almost as precise as those used offline, the selection cuts were even tighter than at the SLT. Two TLT slots, called EXO2 and EXO6, were used to accept CC events.

EXO2 required that events met all of the following criteria:

- $P_{T,miss} > 6$ GeV.
- At least one good track.
- A good vertex.

- Timing information in the upper and lower halves of the CAL was consistent with the *ep* bunch crossing time.

Requiring timing information in the upper and lower halves of the CAL that was consistent with the bunch crossing time was an effective way of rejecting events caused by cosmic muons passing through the detector.

EXO6 required that events met all of the following criteria:

- Not an off-beam proton.
- $P_{T,miss} > 8$ GeV.
- Passed the CC slot at the SLT.
- Timing information in the upper and lower halves of the CAL was consistent with the *ep* bunch crossing time.
- Vertex position was consistent with an *ep* interaction.
- Not too many tracks not originating from the interaction vertex **OR** a good vertex found using at least two tracks.
- A vertex position was found **OR** E_T(-IR) > 10 GeV.
- A good track was found at the FLT **OR** $E_{FCAL} > 10$ GeV **OR** $E_{FHAC}/E < 1.95$.

Events were identified as off-beam protons if they met all of the following criteria:

- E_T(-IR) < 10 GeV.
- $P_{T,miss} < 25$ GeV.
- $P_{T,miss}/E_T < 0.7$.
- $\delta < 10$ GeV.
- $P_{T,miss}/p_Z < 0.08$.
- $|p_Y| < 4$ GeV.

Two of these criteria were tightened slightly during 2005, to reject even more background, becoming:

- $P_{T,miss}/p_Z < 0.09$.
- $|p_Y| < 6$ GeV.

At the same time, EXO2 was also modified by adding two more requirements:

- Passed the CC slot at the SLT.
- Not an off-beam proton.

In EXO2, off-beam protons had the same definition as in EXO6.

Studies with previously selected CC data events showed that none of these data events would have been lost with the tighter CC TLT cuts. CC MC studies predicted a tiny decrease in the CC offline efficiency, of around 0.02%. Furthermore, these changes to the CC TLT reduced the TLT output rate significantly, as illustrated in Figure 6.7.

6.4 Pre-selection

After requiring that an event passed the CC trigger, the following cuts were applied to reduce the amount of data to be analysed:

- $P_{T,miss} > 7$ GeV **AND** $P_{T,miss}$(-IR) > 7 GeV.

6.5 Kinematic cuts

In order to exclude regions where the background rate was very high or where the detector was unable to satisfactorily reconstruct events, the following kinematic requirements were made:

- $Q^2_{JB} > 200$ GeV^2 **AND** $y_{JB} < 0.9$.

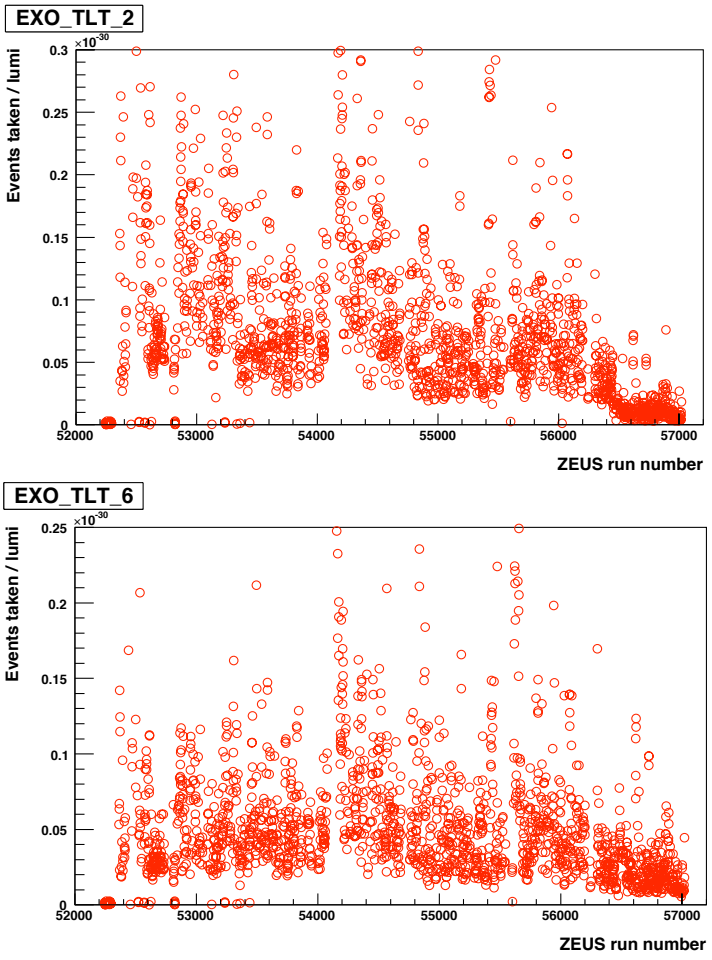

Figure 6.7: The output rate of the CC TLT slots, EXO2 and EXO6, plotted against ZEUS run number during $e^{-}p$ data-taking. From run 56244 the background rejection at the CC SLT was tightened causing a decrease in the CC TLT output rate. From run 56476 the tighter CC TLT selection was applied causing a further decrease in the CC TLT output rate.

6.6 Charged current selection

CC events were selected and background was rejected by requiring a minimum value of $P_{T,miss}$. A tighter cut was required for events with $\gamma_0 \leq 0.4$ radians, since they were outside the CTD acceptance region and no tracking information was available for background rejection.

Events with $\gamma_0 \leq 0.4$ radians were required to have:

- $P_{T,miss} > 14$ GeV **AND** $P_{T,miss}$(-IR) > 12 GeV.

Events with $\gamma_0 > 0.4$ radians were required to have:

- $P_{T,miss} > 12$ GeV **AND** $P_{T,miss}$(-IR) > 10 GeV
  AND $P_{T,miss}$(-2IR) > 8 GeV.

Figures 6.8 to 6.10 show distributions of $P_{T,miss}$, $P_{T,miss}$(-IR) and $P_{T,miss}$(-2IR), where all selection cuts have been applied, except for the cut on the variable plotted. In the accepted regions, generally the data is well-described by the MC and any effect on the extracted cross sections, caused by small differences between the data and the MC distributions, is studied and evaluated in section 7.4.8.

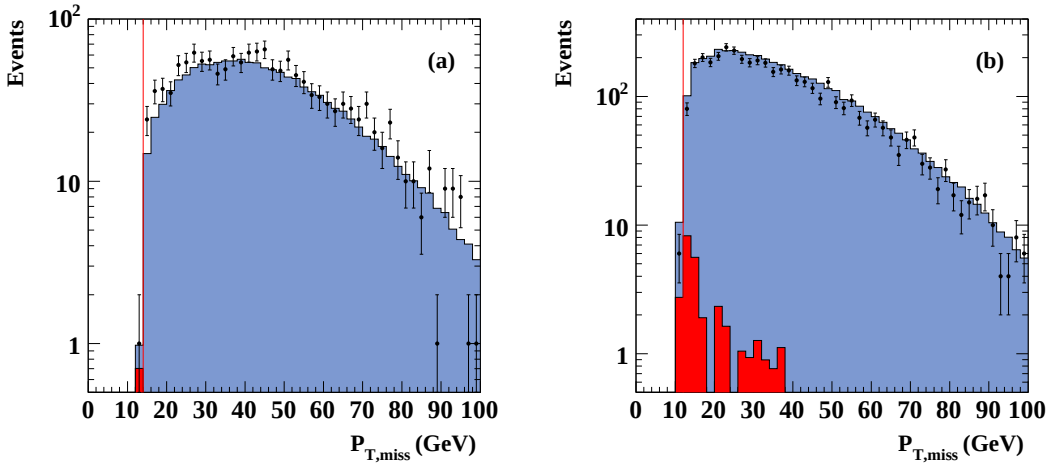

Figure 6.8: The $P_{T,miss}$ distribution for (a) $\gamma_0 \leq 0.4$ radians and (b) $\gamma_0 > 0.4$ radians, with all selection cuts applied except for the cuts on $P_{T,miss}$. The blue histograms are the CC MC, the red histograms are the SM background MC and the points are the data. The red lines show the minimum accepted values of $P_{T,miss}$.

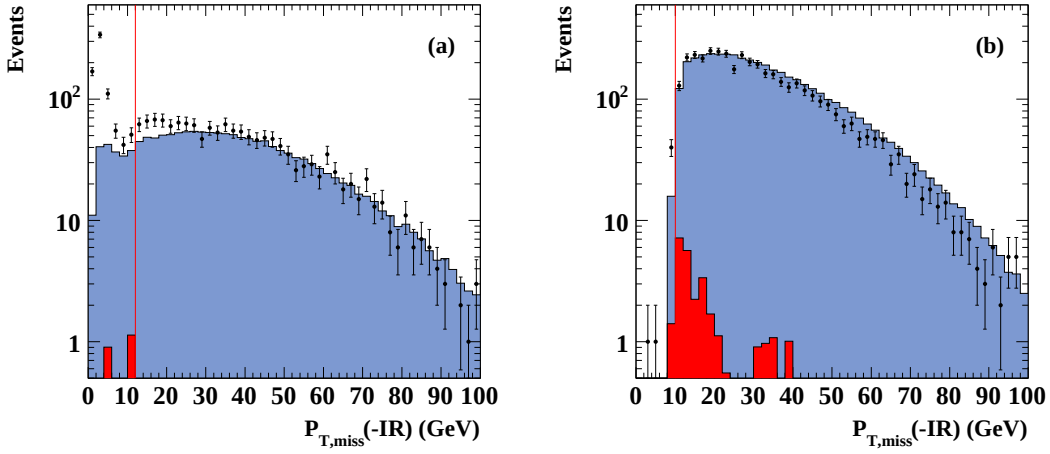

Figure 6.9: The $P_{T,miss}$(-IR) distribution for (a) $\gamma_0 \leq 0.4$ radians and (b) $\gamma_0 > 0.4$ radians, with all selection cuts applied except for the cuts on $P_{T,miss}$(-IR). The blue histograms are the CC MC, the red histograms are the SM background MC and the points are the data. The red lines show the minimum accepted values of $P_{T,miss}$(-IR).

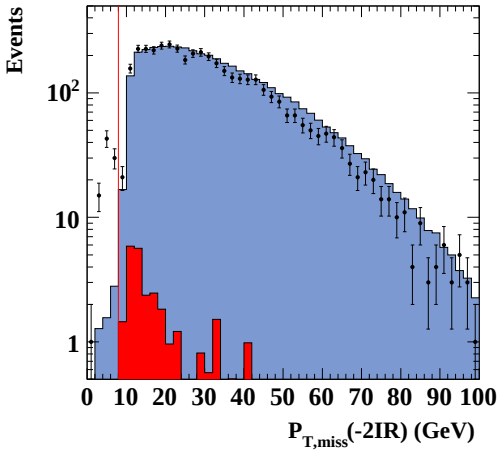

Figure 6.10: The $P_{T,miss}$(-2IR) distribution for $\gamma_0 > 0.4$ radians, with all selection cuts applied except for the cut on $P_{T,miss}$(-2IR). The blue histogram is the CC MC, the red histogram is the SM background MC and the points are the data. The red line shows the minimum accepted value of $P_{T,miss}$(-2IR).

6.7 Background rejection

This section covers both SM and non-ep background rejection. Different cuts were applied depending on whether an event had $\gamma_0 > 0.4$ radians (high-γ_0), where tracking information could be used, or $\gamma_0 \leq 0.4$ radians (low-γ_0), where no tracking information was available and other information had to be used.

6.7.1 High-γ_0 background rejection

The following cuts were applied to high-γ_0 events.

Vertex position

To reject events not initiated by an ep collision, the Z vertex position reconstructed from tracks was required to lie in the following range:

- $|Z_{vtx}| < 50$ cm.

Figure 6.11 shows the Z vertex distributions for high-γ_0 e^+p and e^-p events, after all selection cuts have been applied, expect for the Z vertex cut. The systematic uncertainty on the extracted cross sections caused by differences between the data and MC Z vertex distributions is studied and evaluated in section 7.4.8.

Beamgas rejection

To reject events caused by beamgas interactions, events were required to satisfy all of the following conditions:

- Number of good tracks ≥ 1.
- Number of good tracks $> 0.3 \times$ (Number of tracks - 20).
- $|\Delta\phi| < \begin{cases} 0.5 \text{ radians} & \text{for events with } P_{T,miss} < 45 \text{ GeV} \\ 1.0 \text{ radians} & \text{for events with } P_{T,miss} \geq 45 \text{ GeV}. \end{cases}$

Here, good tracks were tracks fitted to the primary vertex, with a P_T of at least 0.2 GeV and a polar angle inside the CTD acceptance region (between 15° and

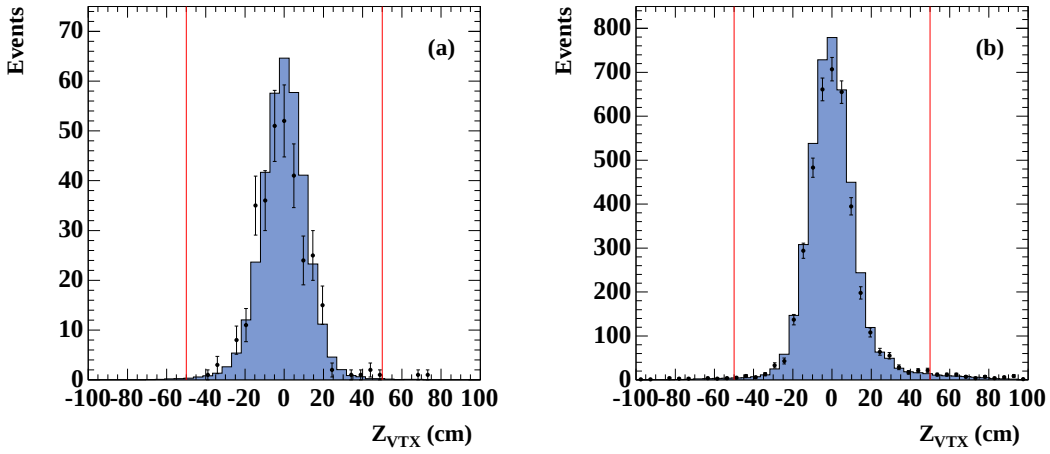

Figure 6.11: The Z vertex distribution reconstructed from tracks for high-γ_0 events with all selection cuts applied except for the Z_{VTX} cut, for (a) e^+p and (b) e^-p collisions. The histograms are the MC and the points are the data. The red lines indicate the accepted region.

164°). $\Delta\phi$ is the difference between the azimuthal angle of $P_{T,miss}$ measured using the CAL and the azimuthal angle of $P_{T,miss}$ calculated from the good tracks.

The tracking cuts were designed to reject beamgas events, which tended to have many tracks not originating from the interaction vertex. They were tuned by creating so-called beamgas-enriched samples of data and MC. These samples had the Q^2_{JB} cut reduced to 50 GeV^2, the high-γ_0 $P_{T,miss}$ and $P_{T,miss}$(-IR) cuts both reduced to 7 GeV, no cut on $P_{T,miss}$(-2IR) and neither the tracking nor the $|\Delta\phi|$ cuts applied. Figure 6.12 shows the tracking distributions for these samples.

Large values of $|\Delta\phi|$ were typical of beamgas events and there was more background at low values of $P_{T,miss}$, so the $|\Delta\phi|$ cut was tighter in this region. Figure 6.13 shows the distribution of $|\Delta\phi|$, with all cuts applied except for the cut on $|\Delta\phi|$.

In the accepted regions of the tracking and $|\Delta\phi|$ distributions in Figures 6.12 and 6.13, the data and MC agreement is reasonable, although there are some small differences. The systematic uncertainties on the extracted cross sections caused by these differences are studied and evaluated in section 7.4.8.

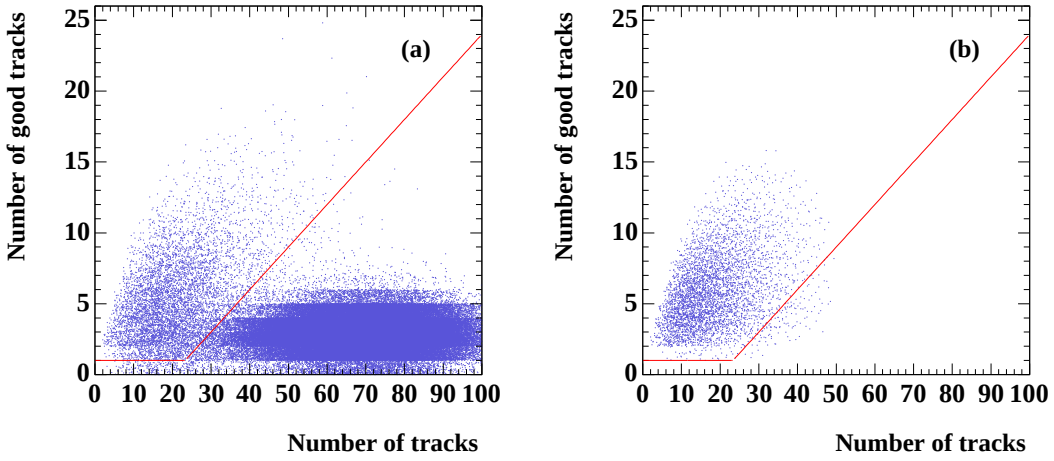

Figure 6.12: The number of good tracks plotted against the number of tracks for high-γ_0 beamgas-enriched (a) data and (b) CC MC samples. The red lines indicate the minimum number of good tracks accepted, as a function of the number of tracks.

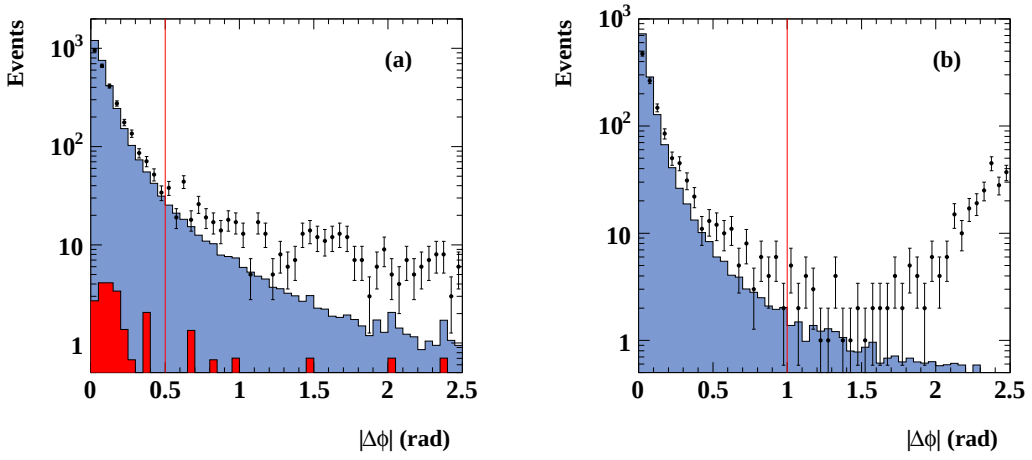

Figure 6.13: The $|\Delta\phi|$ distribution for high γ_0 events with all selection cuts applied except for the $|\Delta\phi|$ cut, with (a) $P_{T,miss} < 45$ GeV and (b) $P_{T,miss} \geq 45$ GeV. The blue histograms are CC MC, the red histograms are PHP MC and the points are the data. The red lines indicate the maximum accepted value of $|\Delta\phi|$.

Photoproduction rejection

PHP events were distinguished from CC events using the ratio of the anti-parallel and parallel components of the hadronic transverse momentum, V_{AP} and V_P, which were defined as follows:

$$V_{AP} = -\sum_i \overrightarrow{P}_{T,i} \cdot \overrightarrow{n}_{P_{T,miss}} \quad \text{for} \quad \overrightarrow{P}_{T,i} \cdot \overrightarrow{n}_{P_{T,miss}} < 0 \quad \text{and} \tag{6.2}$$

$$V_P = \sum_i \overrightarrow{P}_{T,i} \cdot \overrightarrow{n}_{P_{T,miss}} \quad \text{for} \quad \overrightarrow{P}_{T,i} \cdot \overrightarrow{n}_{P_{T,miss}} > 0. \tag{6.3}$$

Here, the sums were performed over CAL energy deposits and $\overrightarrow{n}_{P_{T,miss}} = \overrightarrow{P}_{T,miss}/P_{T,miss}$.

CC events tended to produce a fairly collimated distribution of hadronic energy deposits and therefore they had low values of V_{AP}/V_P, whereas PHP events tended to be less collimated and therefore they had higher values of V_{AP}/V_P.

The sums in equations 6.3 and 6.2 could be performed over energy deposits defined in three different ways:

- CAL cells.
- Cone islands.
- ZEUS energy flow objects (ZUFOs)[2].

CC and PHP MC samples were created with all cuts applied, except for the cut on V_{AP}/V_P. These samples were used to plot the fractional CC rejection against the fractional PHP rejection, for each of the methods of calculating V_{AP}/V_P, as shown in Figure 6.14. Calculating V_{AP}/V_P from CAL cells, which had the finest granularity of the three methods, was seen to give the greatest fractional PHP rejection for the smallest signal loss and hence this method was chosen.

Using the same MC samples, the V_{AP}/V_P cut was then tuned so that for events with $P_{T,miss} < 20$ GeV, the expected number of PHP events was 2% of the number of CC events and for events with $20 \leq P_{T,miss} < 30$ GeV, the expected number of

[2]ZUFOs combine tracking and CAL information to identify energy deposits associated with single particles arriving at the CAL.

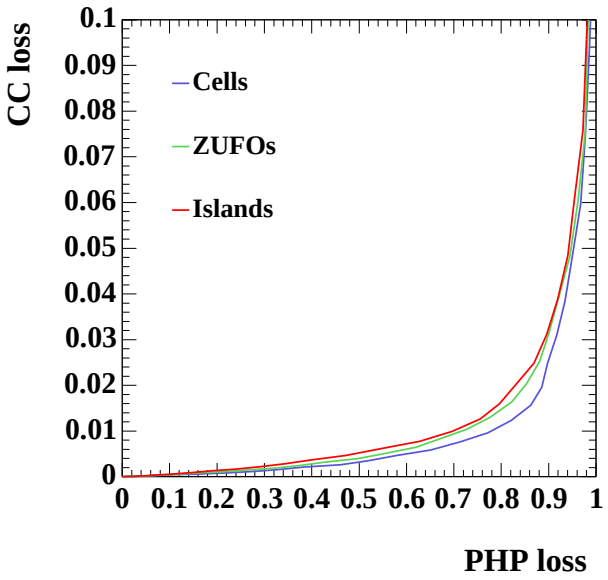

Figure 6.14: The fractional CC rejection plotted against the fractional PHP rejection, for V_{AP}/V_P calculated from CAL cells (blue), ZUFOs (green) and cone islands (red).

PHP events was 0.5% of the number of CC events. Figure 6.15 shows the expected number of PHP events as a fraction of the expected number of CC events, plotted against the maximum accepted value of V_{AP}/V_P, in the two $P_{T,miss}$ ranges.

The tuned cuts were then defined as follows:

$$V_{AP}/V_P < \begin{cases} 0.23 & \text{for events with } P_{T,miss} < 20 \text{ GeV} \quad \text{and} \\ 0.40 & \text{for events with } 20 \leq P_{T,miss} < 30 \text{ GeV}. \end{cases}$$

In the final e^-p sample, this gave an expected PHP rate that was 0.3% of the CC rate.

Figure 6.16 shows the V_{AP}/V_P distributions of data and MC samples with all cuts applied except the V_{AP}/V_P cut, in the two $P_{T,miss}$ ranges. Generally the agreement between the data and the MC in the accepted ranges is good. The systematic uncertainty on the extracted cross sections caused by an uncertainty in the normalisation of the PHP MC is studied and evaluated in section 7.4.5.

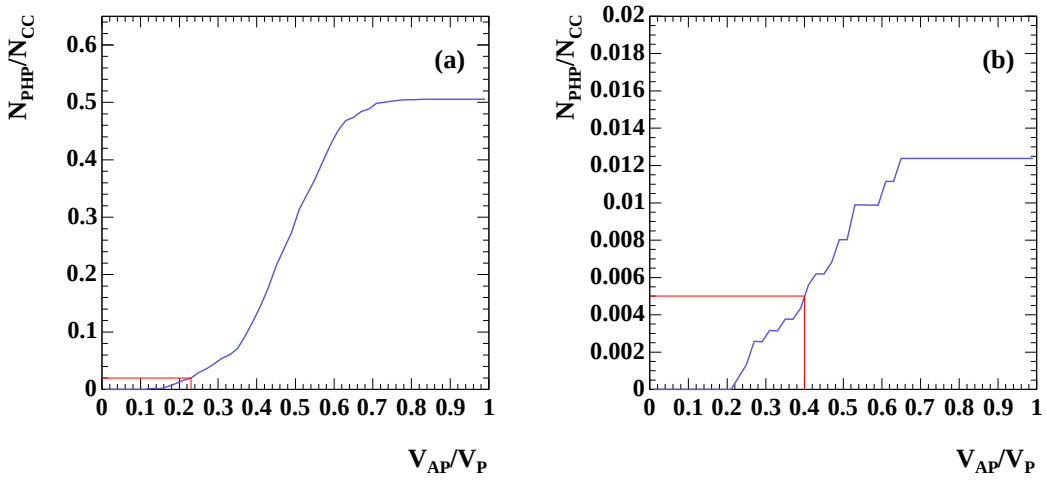

Figure 6.15: The expected number of PHP events as a fraction of the expected number of CC events, plotted against the maximum accepted value of V_{AP}/V_P, for (a) $P_{T,miss} < 20$ GeV and (b) $20 \leq P_{T,miss} < 30$ GeV. The red lines indicate the tuned values for the V_{AP}/V_P cuts.

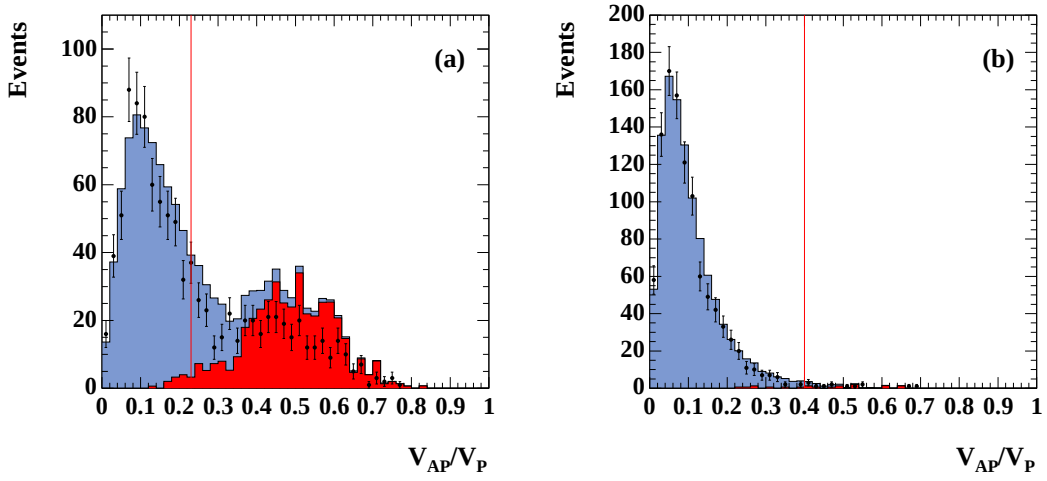

Figure 6.16: The V_{AP}/V_P distributions for (a) $P_{T,miss} < 20$ GeV and (b) $20 \leq P_{T,miss} < 30$ GeV. The blue histograms are CC MC, the red histograms are PHP MC and the points are the data, with all selection cuts applied except the cuts on V_{AP}/V_P. The red lines show the maximum accepted value of V_{AP}/V_P.

Neutral current rejection

Candidate NC events were identified using a neural network called SINISTRA95 [119], which searches for electrons in the final state. Events with at least one candidate electron were rejected if they met all of the following conditions:

- $P_{T,miss} < 30$ GeV.
- $\delta > 30$ GeV.
- $E_e > 4$ GeV.
- $E_{\rm cone} - E_e < 5$ GeV.
- $P_e^{\rm track}/E_e > 0.25$ if $15^\circ < \theta_e < 164^\circ$.
- $E_T^e > 2$ GeV if $\theta_e > 164^\circ$.

Here, E_e is the energy of the highest probability candidate electron, $E_{\rm cone}$ is the energy measured in a cone of radius 0.8 in the $\eta - \phi$ plane[3] around the electron and $P_e^{\rm track}$, E_T^e and θ_e are the momentum, transverse energy and polar angle of the electron track measured in the CTD, respectively.

δ was required to be greater than 30 GeV since it peaks at twice the energy of the incoming electron, 55 GeV, for NC events and at close to zero for CC events. Requiring a low value of $E_{\rm cone} - E_e$ helped to ensure that events with electromagnetic energy deposits in jets were not rejected and a minimum value of $P_e^{\rm track}/E_e$ was required since, for electrons, this quantity peaks at around one. Figure 6.17 shows distributions of $P_{T,miss}$, δ, E_e and $P_e^{\rm track}/E_e$ after all selection cuts except NC rejection have been applied.

6.7.2 Low-γ_0 background rejection

The following cuts were applied to low-γ_0 events.

[3] η is pseudorapidity, defined as $\eta = -\ln\tan(\theta/2)$.

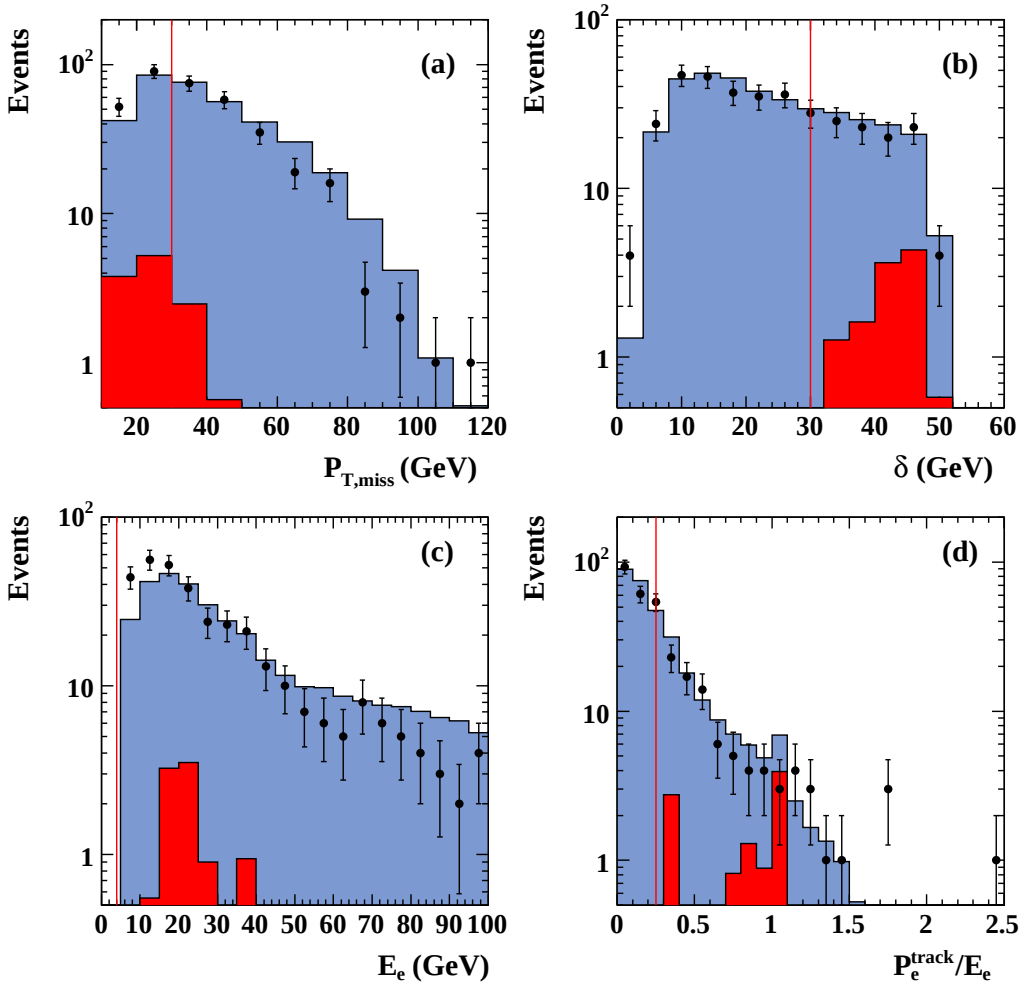

Figure 6.17: The (a) $P_{T,miss}$, (b) δ, (c) E_e and (d) P_e^{track}/E_e distributions after all selection cuts except NC rejection. The blue histograms are CC MC, the red histograms are NC MC and the points are data. The red lines show the limits of the accepted ranges.

Vertex position

To reject events not originating from an ep collision, the Z vertex position reconstructed from FCAL timing information was required to lie in the following range:

- $|Z_{vtx}| < 50$ cm.

Figure 6.18 shows the Z vertex distributions for low-γ_0 e^+p events, after all selection cuts have been applied expect for the Z vertex cut. This cut was not applied to the e^-p data and MC since, at the time of writing, the FCAL timing vertex routine was not available for these data.

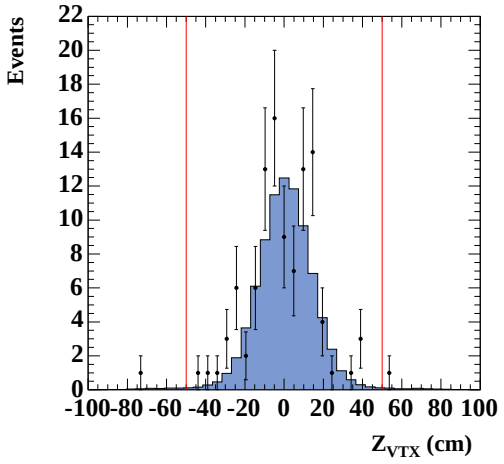

Figure 6.18: The Z vertex distribution reconstructed from FCAL timing information, for low-γ_0 events with all selection cuts applied except for the Z_{VTX} cut, for e^+p collisions. The histograms are MC and the points are the data. The red lines indicate the accepted region.

Halo muon rejection

Halo muon events were removed from the data by rejecting events with a narrow energy deposit, or cluster, in the FCAL and an associated energy deposit in the RCAL. The FCAL cluster was identified by starting with the FCAL cell with the highest transverse energy (defined in equation 4.1) and adding in neighbouring cells if their energy was greater than 100 MeV, until no more cells could be added.

The associated RCAL energy was then defined as:

$$E_{\text{RCAL, associated}} = \sum_i E_i, \tag{6.4}$$

where the sum was performed over all RCAL cells with

$$\sqrt{(x_i - x_0)^2 + (y_i - y_0)^2} < 30 \text{ cm}. \tag{6.5}$$

Here, x_i and y_i are the x and y coordinates of the RCAL cell and x_0 and y_0 are the x and y coordinates of the highest E_T FCAL cell.

Events were rejected if they met all of the following conditions:

- $N_x < 4$ cells.
- $N_y < 4$ cells.
- $E_{\text{RCAL, associated}} > 50$ MeV.

Here, N_x and N_y are the FCAL cluster dimensions in x and y, measured in CAL cells. These variables are plotted in Figure 6.19 for data and CC MC, with all cuts applied except for the halo muon rejection cuts and the eye scan (described in section 6.7.3).

Halo muon events were also rejected by requiring a minimum number of EMC and HAC cells in the highest energy condensate in the FCAL. Condensates were formed by merging adjacent cells if their energies were greater than 20 MeV for EMC cells and 50 MeV for HAC cells. Events were then required to satisfy both of the following criteria:

- $N_{FEMC} > 30$ OR $N_{FHAC1} > 20$.
- $0.2 < N_{FHAC}/N_{FCAL} < 0.65$.

Here, N_{FEMC} is the number of FEMC cells, N_{FHAC1} is the number of cells in the first FHAC layer, N_{FHAC} is the total number of FHAC cells and N_{FCAL} is the total number of FCAL cells, in the highest energy FCAL condensate.

Figure 6.20 shows the distributions of these variables for CC data and MC, with all selection cuts applied except for the halo muon rejection cuts and the eye scan.

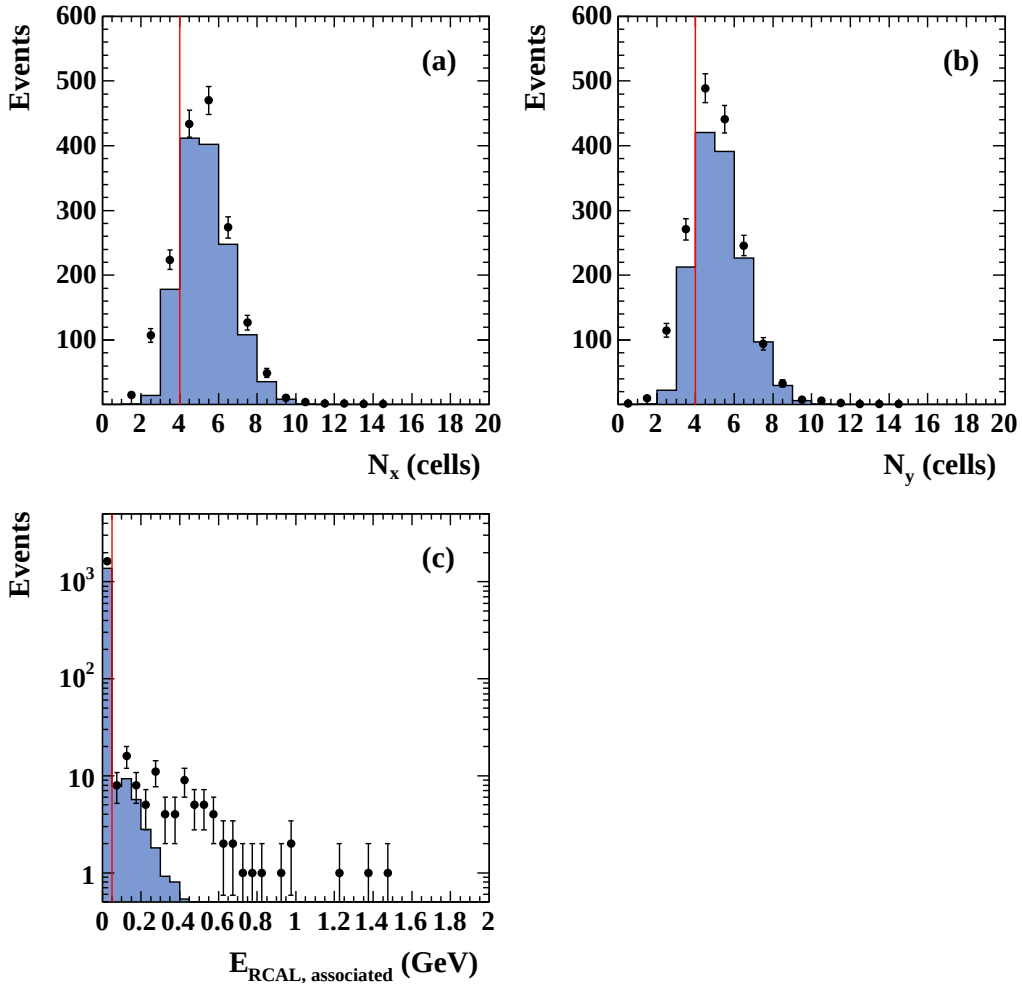

Figure 6.19: Distributions of (a) the FCAL cluster width in x, (b) the FCAL cluster width in y and (c) the associated energy in the RCAL, for CC MC (histograms) and data (points) with all selection cuts applied except for the halo muon rejection cuts and the eye scan. The red lines show the limits of the accepted values.

The background is seen to peak at low values of N_{FEMC} and N_{FHAC1}. In the accepted ranges, the MC description of the data is reasonable but there are some differences between the data and MC, particularly in the N_{FHAC1} distribution, where the data peaks at a higher value than the MC. However, as the CC inefficiency caused by applying this cut is <1%, the associated systematic uncertainty on the cross-section measurements was found to be negligible, when compared to the systematic uncertainties associated with the other selections cuts studied in section 7.4.8.

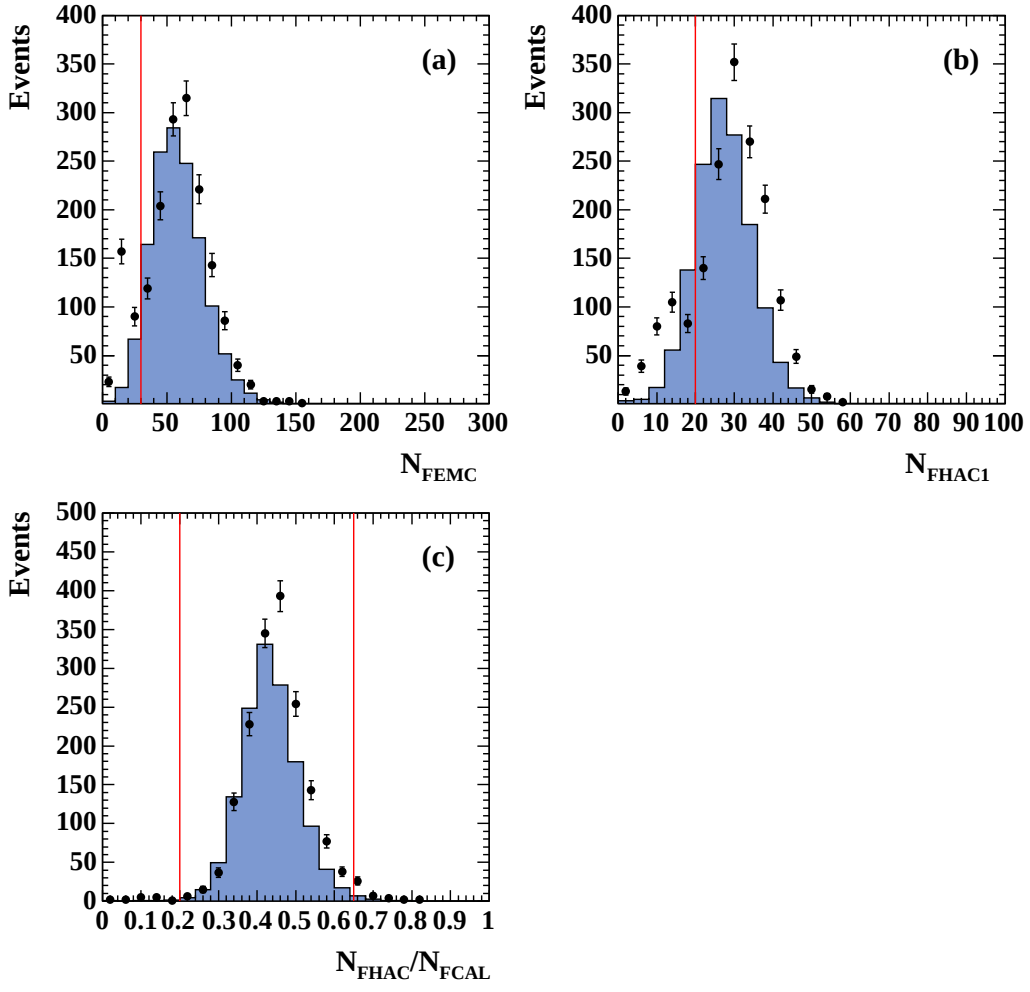

Figure 6.20: Distributions of (a) the number of EMC cells, (b) the number of HAC1 cells and (c) the ratio of the number of HAC cells to the total number of cells in the highest energy condensate in the FCAL, for CC MC (histograms) and data (points) with all selection cuts applied except for the halo muon rejection cuts and the eye scan. The red lines show the limits of the accepted values.

Off-beam proton rejection

Events were identified as off-beam protons and rejected if they met all of the following criteria:

- $P_{T,miss}$(-IR) < 45 GeV.
- $\delta < 15$ GeV.
- $P_{T,miss}/P_Z < 0.2$.
- $|P_Y| < 4$ GeV.

Figure 6.21 shows plots of these variables for CC data and MC, with all selection cuts applied except for the off-beam proton rejection cuts.

6.7.3 Non-*ep* rejection

These cuts were applied for all values of γ_0 to reject remaining non-*ep* events.

Electromagnetic and hadronic energy comparison

Various types of non-*ep* background, in particular halo or cosmic muon events, can be identified by comparing the amount of energy measured in the EMC and HAC sections of the CAL. A halo muon passing through the BCAL, for example, will tend to deposit most of its energy in one layer of the BCAL and halo muons arriving in the FCAL will tend to deposit a higher fraction of their energy in FHAC2 than a typical *ep* event.

In order to study these cuts, non-*ep* enriched samples of data and MC were created, which had all cuts applied except for halo muon rejection, electromagnetic and hadronic energy comparison cuts, off-beam proton rejection and the CAL timing cuts. Figure 6.22 shows plots of the fraction of energy deposited in different sections of the CAL for the non-*ep* enriched samples of data and MC, illustrating the ranges where the non-*ep* background is highest.

Events were rejected that met any of the following criteria:

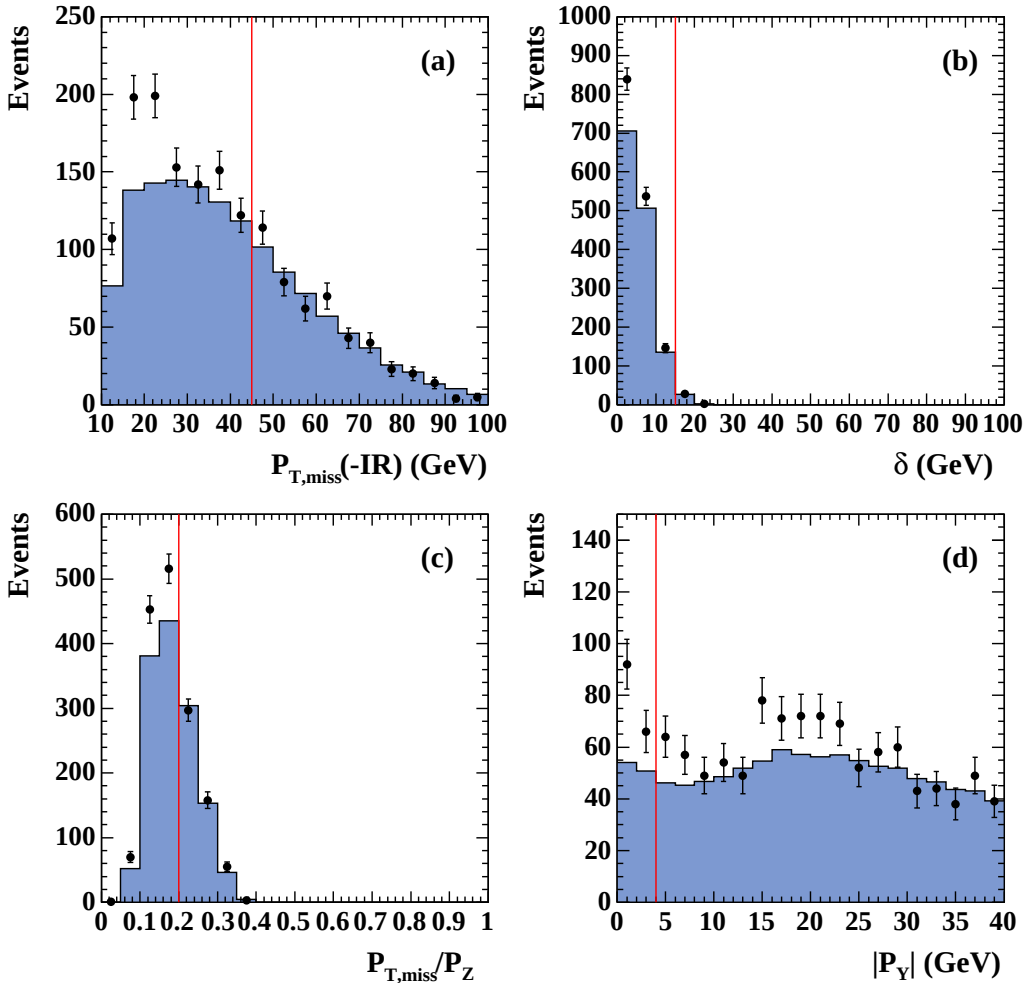

Figure 6.21: The (a) $P_{T,miss}$(-IR), (b) δ, (c) $P_{T,miss}/P_Z$ and (d) $|P_Y|$ distributions for CC MC (histograms) and data (points), with all cuts applied except for the off-beam proton rejection cuts. The red lines show the limits of the accepted values.

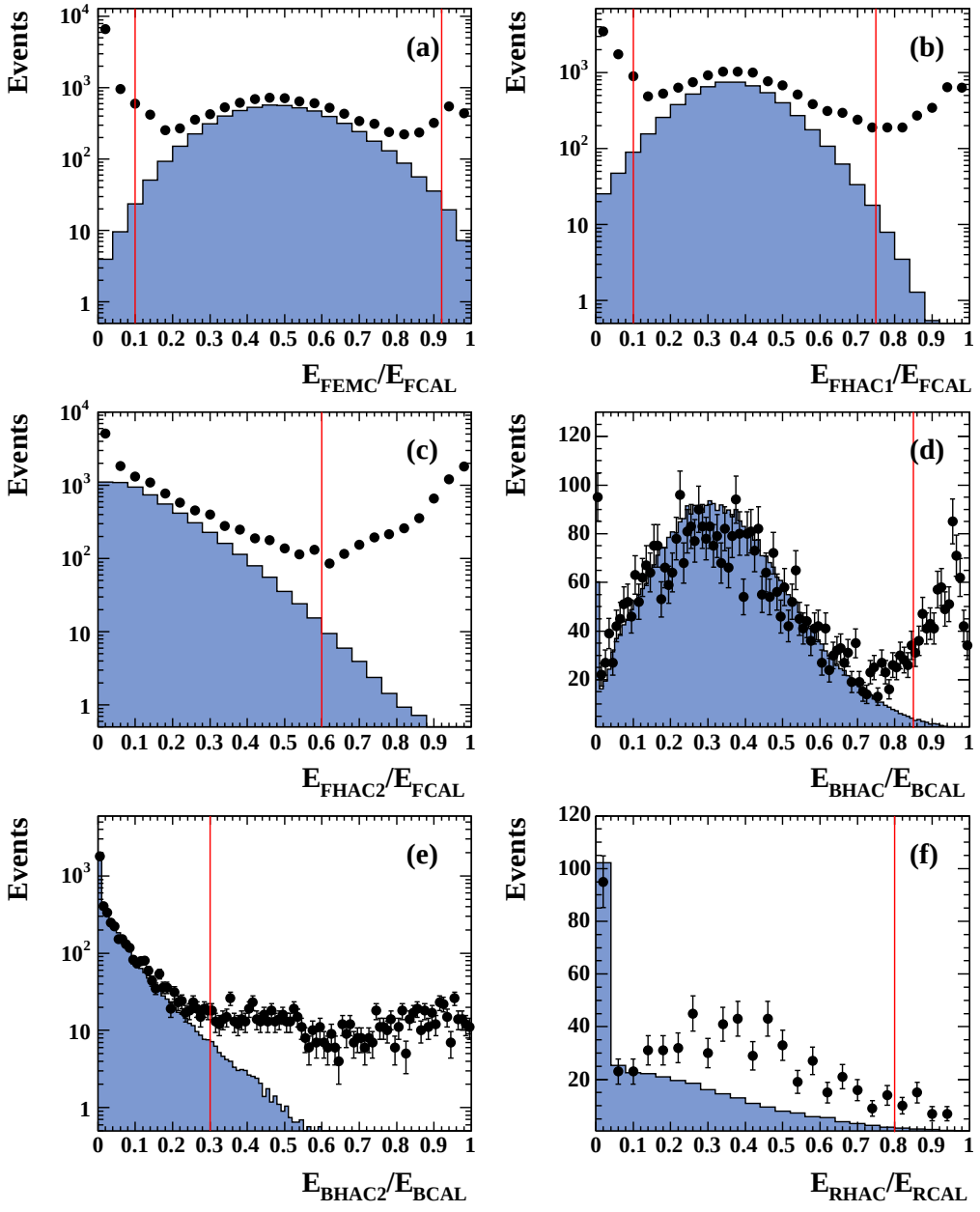

Figure 6.22: The (a) E_{FEMC}/E_{FCAL}, (b) E_{FHAC1}/E_{FCAL}, (c) E_{FHAC2}/E_{FCAL}, (d) E_{BHAC}/E_{BCAL}, (e) E_{BHAC2}/E_{BCAL} and (f) E_{RHAC}/E_{RCAL} distributions, for non-*ep* enriched samples of CC MC (histograms) and data (points). The red lines show the edges of the ranges of accepted values.

- If $E_{FCAL} > 2$ GeV:
  - $E_{FEMC}/E_{FCAL} > 0.92$ or
  - $E_{FEMC}/E_{FCAL} < 0.1$ or
  - $E_{FHAC1}/E_{FCAL} > 0.75$ or
  - $E_{FHAC1}/E_{FCAL} < 0.1$ or
  - $E_{FHAC2}/E_{FCAL} > 0.6$.
- If $E_{BCAL} > 2$ GeV:
  - $E_{BHAC}/E_{BCAL} > 0.85$ or
  - $E_{BHAC2}/E_{BCAL} > 0.3$.
- If $E_{RCAL} > 2$ GeV:
  - $E_{RHAC}/E_{RCAL} > 0.8$.

Figure 6.23 shows plots of the fraction of energy deposited in different sections of the CAL for CC data and MC, with all cuts applied except for the non-*ep* rejection cuts listed above. In the accepted ranges, generally the data and MC agreement is good.

Spark rejection

In order to remove any events with $P_{T,miss}$ created by a so-called spark or discharge in a single CAL PMT, events were rejected if they met any of the following conditions:

- Highest E_T cell is an EMC cell **AND** $E_{T,cell}/E_T > 0.8$.
- Highest E_T cell is a HAC cell **AND** $E_{T,cell}/E_T > 0.7$.
- $P_{T,miss}(-\text{imbalance})/P_{T,miss} < 0.5$.
- $P_{T,miss}(-\text{imbalance})/P_{T,miss} > 2.0$.

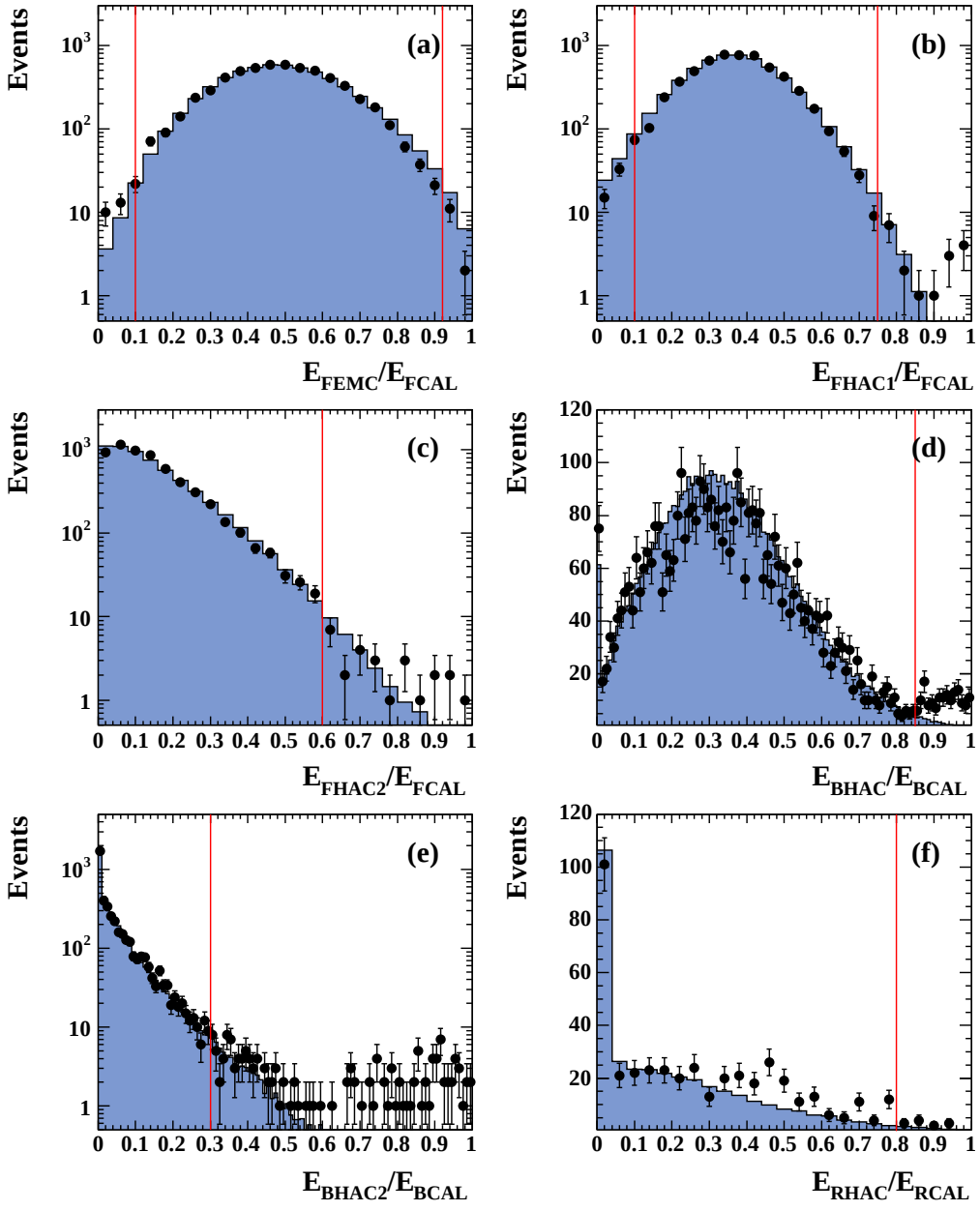

Figure 6.23: The (a) E_{FEMC}/E_{FCAL}, (b) E_{FHAC1}/E_{FCAL}, (c) E_{FHAC2}/E_{FCAL}, (d) E_{BHAC}/E_{BCAL}, (e) E_{BHAC2}/E_{BCAL} and (f) E_{RHAC}/E_{RCAL} distributions, for CC MC (histograms) and data (points) with all cuts applied except for the non-ep rejection cuts. The red lines show the edges of the ranges of accepted values.

Here, $E_{T,cell}$ is the transverse energy of the highest E_T cell and $P_{T,miss}(-\text{imbalance})$ is $P_{T,miss}$ calculated without the highest E_T cell.

CAL timing

CAL timing information was used to reject events for which the timing was not consistent with the *ep* bunch crossing time. In addition, if the times measured in the forward and rear, or upper and lower sections of the CAL differed by a significant amount, then this was indicative of a non-*ep* event, such as a halo or cosmic muon, passing through the detector.

Data events were required to meet all of the following criteria:

- $E_{FCAL} \leq 3$ GeV **OR** $N_{FPMT} < 3$ **OR** $|T_{FCAL}| < 5$ ns.
- $E_{FCAL} \leq 0.6$ GeV **OR** $N_{FPMT} < 3$ **OR** $|T_{FCAL}| < 6$ ns.
- $E_{BCAL} \leq 3$ GeV **OR** $N_{BPMT} < 3$ **OR** $|T_{BCAL}| < 5$ ns.
- $E_{RCAL} \leq 1.5$ GeV **OR** $N_{RPMT} < 3$ **OR** $|T_{RCAL}| < 5$ ns.
- $E_{CAL} \leq 0.6$ GeV **OR** $N_{PMT} < 3$ **OR** $|T_{RCAL}| < 5$ ns.
- $E_{RCAL} \leq 1.5$ GeV **OR** $E_{FCAL} \leq 1.5$ GeV **OR**
  $N_{RPMT} < 3$ **OR** $N_{FPMT} < 3$ **OR**
  -7 ns $< T_{FCAL} - T_{RCAL} <$ 6 ns.
- $E_{UCAL} \leq 2$ GeV **OR** $E_{DCAL} \leq 2$ GeV **OR**
  $N_{UPMT} < 3$ **OR** $N_{DPMT} < 3$ **OR**
  -6 ns $< T_{UCAL} - T_{DCAL} <$ 6 ns.

Here, E is the energy measured in a given section of the CAL, N_{PMT} are the number of PMTs, in a given section of the CAL, from which the timing measurements were calculated and T is the time measured for energy deposits in a given CAL section. U and D refer to the upper and lower halves of the CAL, respectively.

Figures 6.24 and 6.25 show the timing cuts applied to data events in different sections of the CAL.

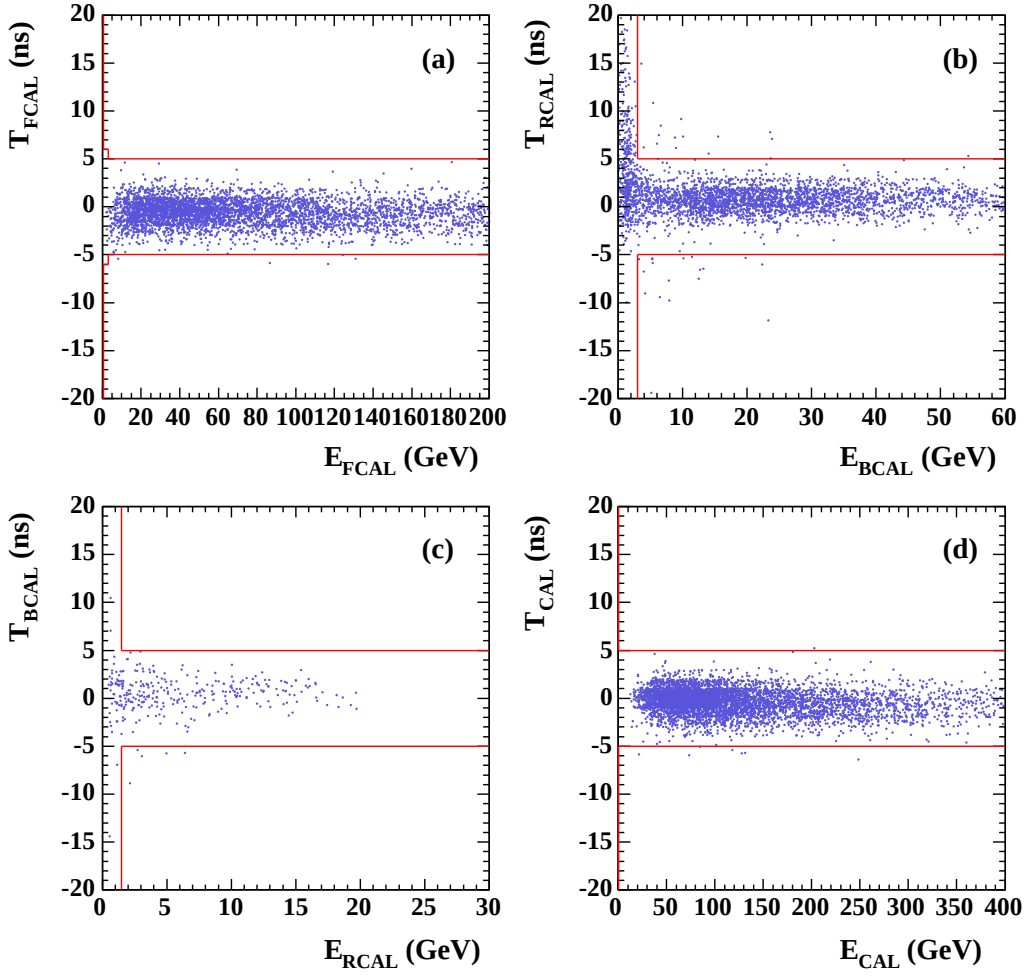

Figure 6.24: Distributions of (a) T_{FCAL} against $E_{FCAL,\,T}$, (b) T_{BCAL} against $E_{BCAL,\,T}$, (c) T_{RCAL} against $E_{RCAL,\,T}$ and (d) T_{CAL} against $E_{CAL,\,T}$ for data with all selection cuts applied except for the CAL timing cuts. The red lines indicate the accepted ranges.

The timing cuts were not applied to the MC as the CAL timing is not well simulated. However, the inefficiency of these cuts was checked with a NC data sample and was found to be insignificant.

Eye scan

The event displays of data events that had passed all the selection cuts were scanned by eye and events which could be clearly identified as cosmic or halo

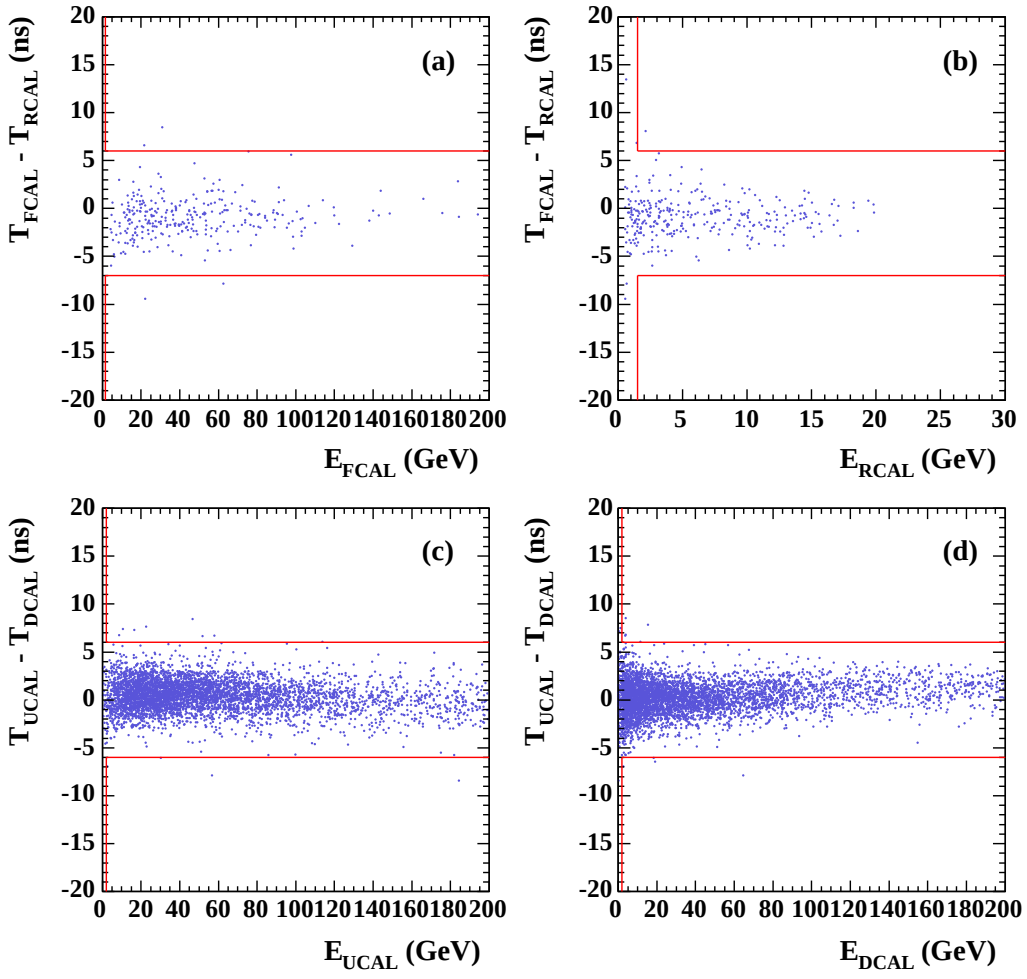

Figure 6.25: Distributions of (a) $T_{FCAL} - T_{RCAL}$ against $E_{FCAL,\,T}$, (b) $T_{FCAL} - T_{RCAL}$ against $E_{RCAL,\,T}$, (c) $T_{UCAL} - T_{DCAL}$ against $E_{UCAL,\,T}$ and (d) $T_{UCAL} - T_{DCAL}$ against $E_{DCAL,\,T}$ for data with all selection cuts applied except for the timing cuts. The red lines indicate the accepted ranges.

muons passing through the detector were rejected. Figure 6.26 shows examples of one cosmic and two halo muon events.

6.8 Selection summary

Table 6.2 shows the numbers of e^+p and e^-p data and CC MC events left after each selection cut.

Selection	**e^+p**		**e^-p**	
	Data	**MC (%)**	**Data**	**MC (%)**
Trigger and pre-selection	1,032,270	735.5	8,374,630	8,902
Q^2 and y	235,757	653.4 (100.0)	1,519,560	8,113 (100.0)
$P_{T,miss}$	137,117	596.9 (91.4)	853,187	7,523 (92.7)
Z_{VTX}	20,557	564.1 (86.3)	237,306	7,136 (88.0)
V_{AP}/V_P	13,306	525.2 (80.4)	220,161	6,835 (84.3)
Beamgas rejection	3,952	466.2 (71.4)	41,439	6,167 (76.0)
NC rejection	3,951	464.5 (71.1)	41,338	6,144 (75.7)
HAC and EMC comparison	512	446.0 (68.3)	6,384	5,859 (72.2)
Halo muon rejection	457	441.4 (67.5)	5,897	5,794 (71.4)
Off-beam proton rejection	448	436.1 (66.7)	5,769	5,727 (70.6)
Spark rejection	429	436.1 (66.7)	5,656	5,727 (70.6)
CAL timing	425	436.1 (66.7)	5,593	5,727 (70.6)
Eye scan	410	436.1 (66.7)	5,516	5,727 (70.6)

Table 6.2: The number of e^+p and e^-p data and CC MC events left after each selection cut. The percentage of MC events compared to the number of MC events after the trigger and kinematic cuts is given in brackets.

Table 6.3 shows the numbers of e^+p and e^-p data and MC events after all selection cuts have been applied, for positive and negative values of P_e. The expected SM background rate ranges from 0.5% in the e^-p sample with negative P_e to 1.4% in the e^+p sample with negative P_e.

The distributions of the selected e^+p and e^-p data events in the $Q^2 - x$ plane are

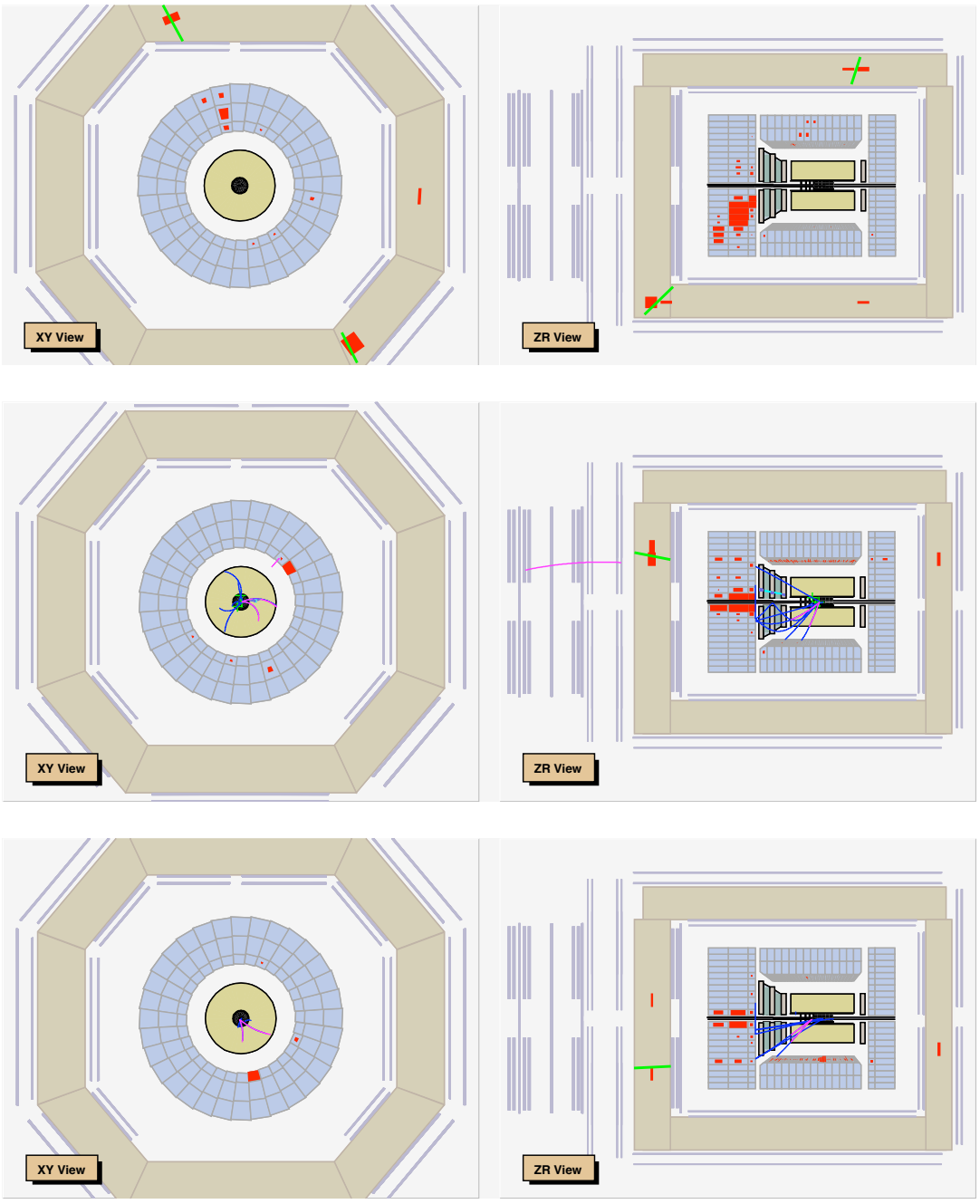

Figure 6.26: One cosmic and two halo muon events in the ZEUS detector, shown in the X-Y and Z-r planes. Such events were rejected by eye scan.

	$\mathbf{P_e}$	**Data**	**CC**	**NC**	**PHP**	**Di-μ/τ**	**W**	**BG rate (%)**
e^+p	-0.41	117	128.0	0.3	0.9	0.4	0.2	1.4
	$+0.32$	293	308.1	0.3	1.0	0.5	0.2	0.6
e^-p	-0.27	4320	4505	3.2	12.1	3.7	1.2	0.5
	$+0.33$	1196	1223	1.6	6.3	1.9	0.6	0.9

Table 6.3: The number of e^+p and e^-p data and CC, NC, PHP, di-muon, di-tau and single W-production MC events after all selection cuts have been applied, for positive and negative longitudinal lepton beam polarisation. The final column gives the expected SM background rate as a percentage of the expected number of CC events.

shown in Figures 6.27 and 6.28.

6.9 Data and Monte Carlo comparison

Data and MC distributions after all selection cuts are compared in Figures 6.29 and 6.30 for e^+p and e^-p collisions. Overall the MC describes the data well and can therefore be used to extract the cross sections.

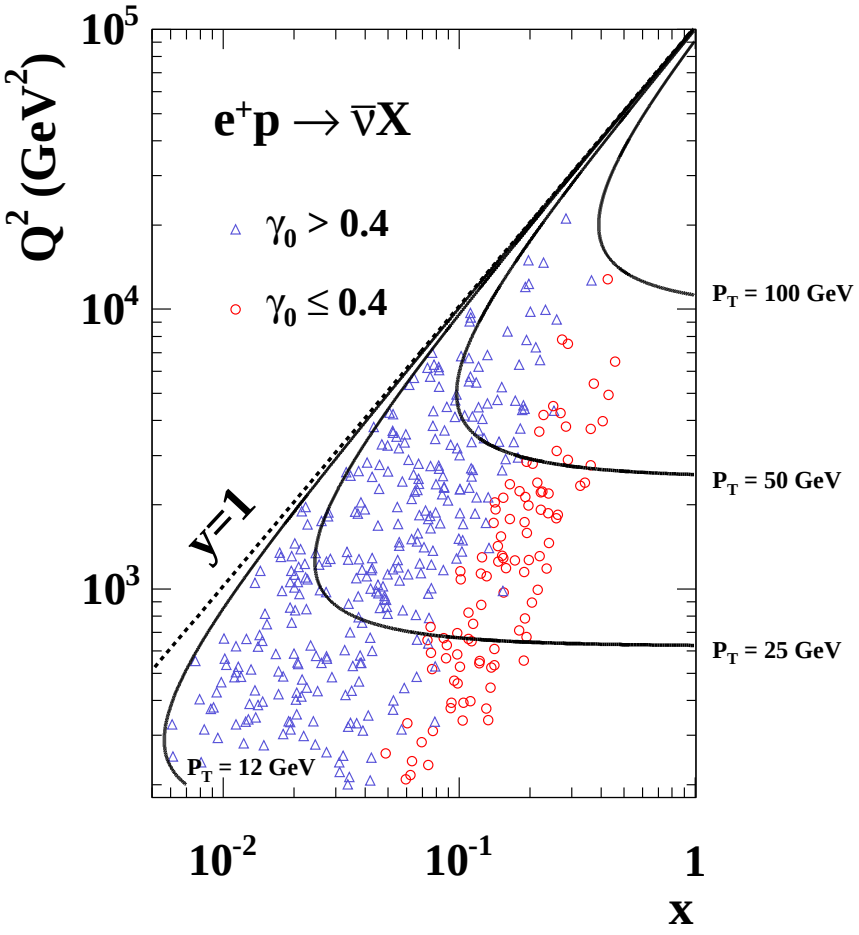

Figure 6.27: The e^+p CC data events passing all selection cuts plotted in the $Q^2 - x$ plane. The blue triangles are the high γ_0 events and the red circles are the low γ_0 events. The solid lines are contours of fixed P_T and the dashed line is $y = 1$.

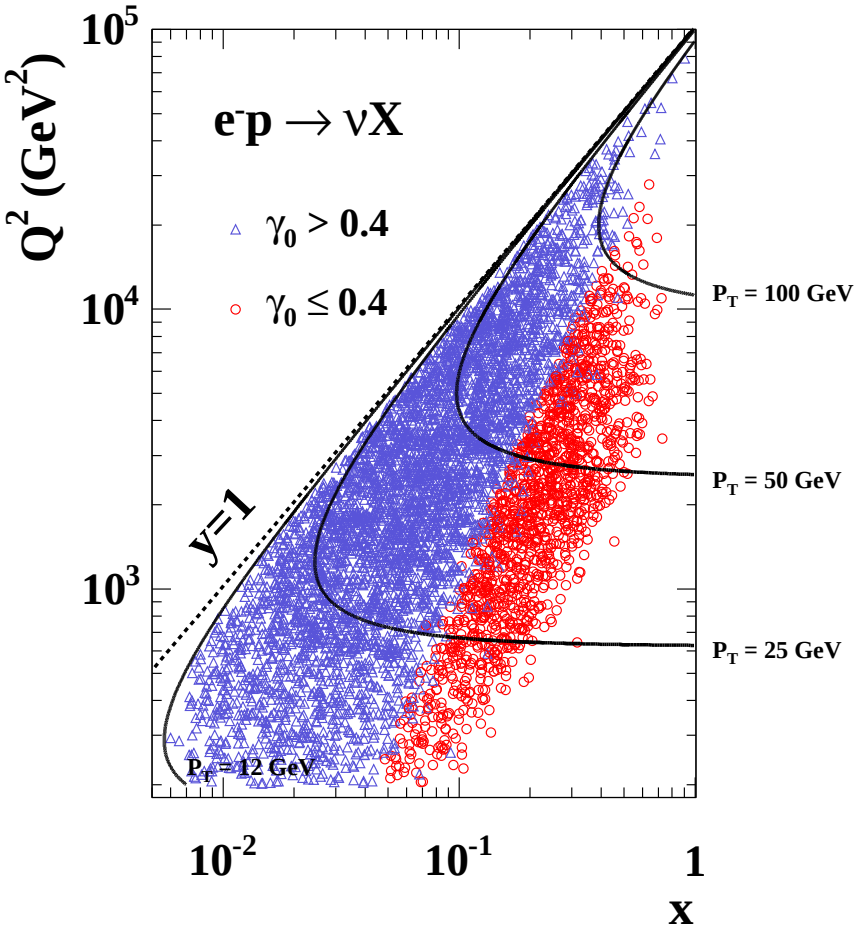

Figure 6.28: The e^-p CC data events passing all selection cuts plotted in the $Q^2 - x$ plane. The blue triangles are the high γ_0 events and the red circles are the low γ_0 events. The solid lines are contours of fixed P_T and the dashed line is $y = 1$.

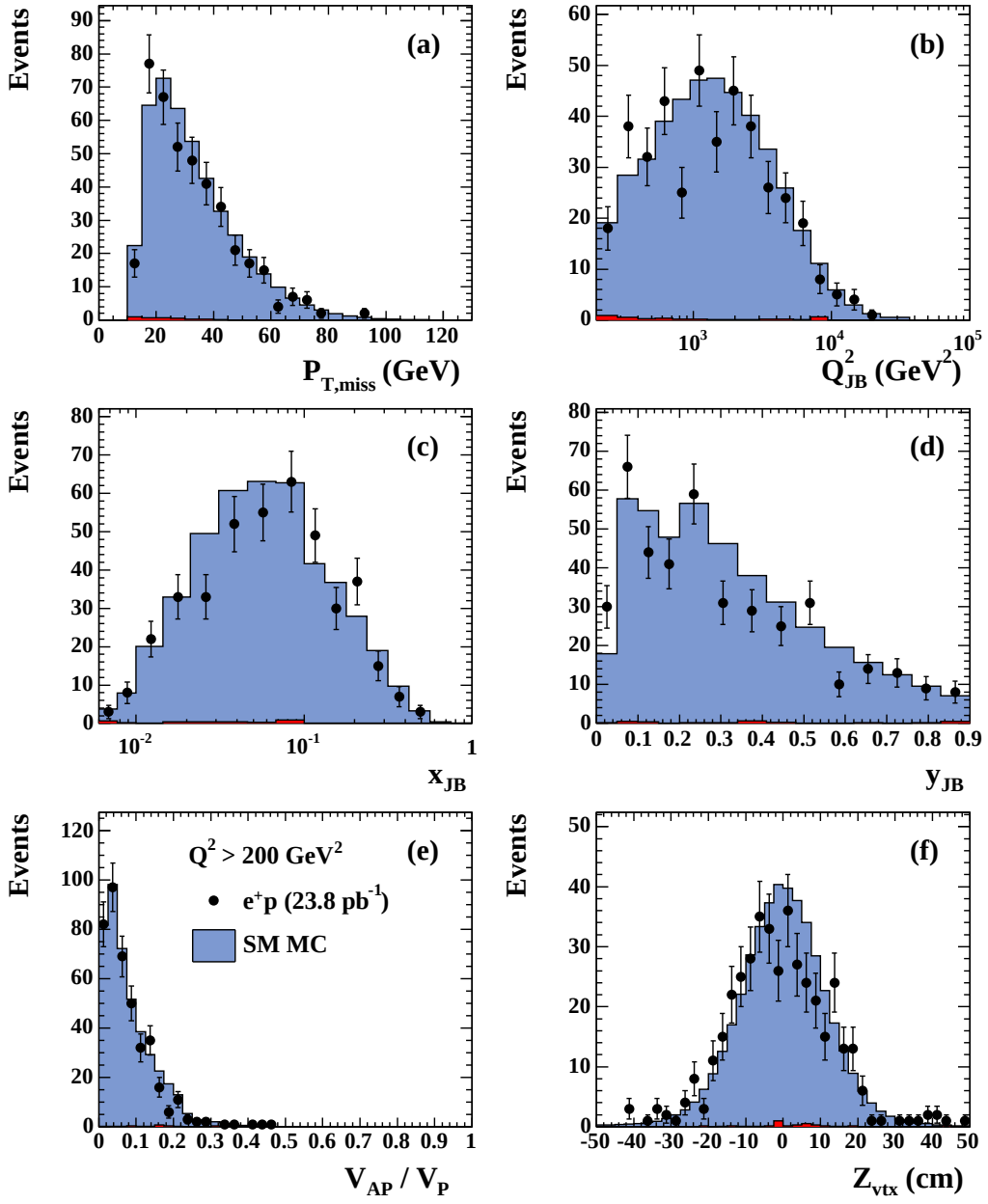

Figure 6.29: The distributions of (a) $P_{T,miss}$, (b) Q^2_{JB}, (c) x_{JB}, (d) y_{JB}, (e) V_{AP}/V_P and (f) Z_{VTX}, for e^+p collisions after all selection cuts have been applied. The blue histograms are CC MC, the red histograms are background MC and the points are the data.

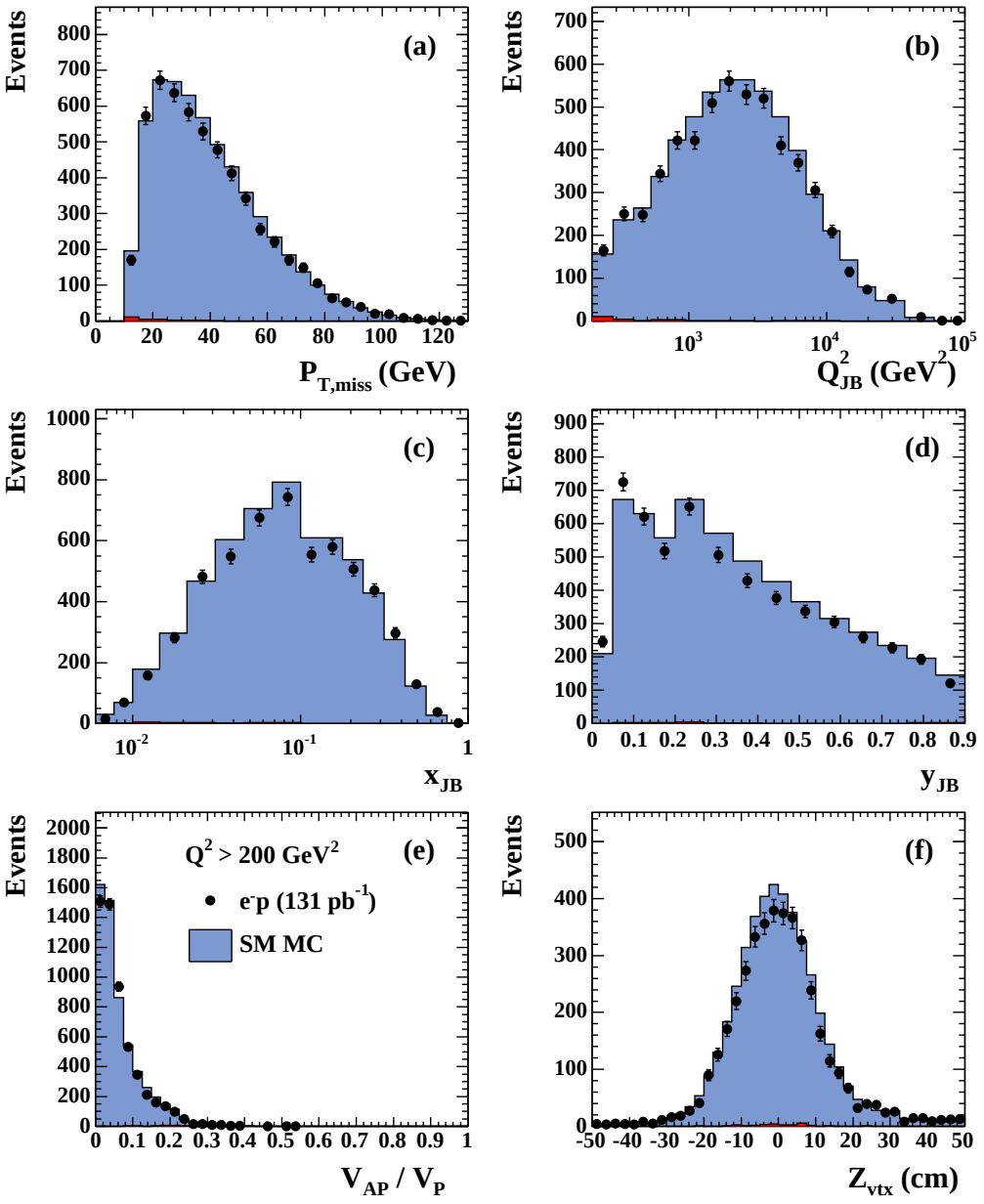

Figure 6.30: The distributions of (a) $P_{T,miss}$, (b) Q^2_{JB}, (c) x_{JB}, (d) y_{JB}, (e) V_{AP}/V_P and (f) Z_{VTX}, for e^-p collisions after all selection cuts have been applied. The blue histograms are CC MC, the red histograms are background MC and the points are the data.

Chapter 7

Results and discussion

This chapter presents measurements of single-differential, total and reduced cross sections for $e^{\pm}p$ CC DIS and explains how they were obtained. First, the resolutions and biases of the kinematic variables in single-differential and reduced cross-section bins are discussed. This is followed by studies of the acceptance, purity and efficiency. Using these studies, the binning for the single-differential and reduced cross sections is defined. The cross-section extraction method is described and eventual systematic uncertainties on the measurements are evaluated.

The single-differential cross-sections $d\sigma/dQ^2$, $d\sigma/dx$ and $d\sigma/dy$ and the total cross sections are presented for e^+p and e^-p collisions with positive and negative values of P_e. The measurements are compared to the SM predictions and measurements made by the H1 Collaboration. A linear fit is performed to the total cross sections as a function of P_e and from the fit an upper limit on the cross section for right-handed CC interactions in $e^{\pm}p$ is derived. This is then converted into a lower limit on the mass of a W_R boson. The reduced cross sections are extracted for e^+p and e^-p collisions at $P_e = 0$ and the measurements are compared to the SM predictions for the reduced cross sections and the separate contributions from the quark and anti-quark PDFs.

7.1 Cross section binning

The single-differential cross-sections $d\sigma/dQ^2$, $d\sigma/dx$ and $d\sigma/dy$ were measured in bins of Q^2, x and y, respectively, and the reduced cross sections were measured in double bins of Q^2 and x. When defining the boundaries of the bins, the resolution and bias of the kinematic variables in each bin as well as the acceptance, purity and efficiency were all considered.

7.1.1 Resolution and bias

The resolution and bias of the reconstructed kinematic variables are important for cross section extraction since they can cause events to migrate between bins. The resolution and bias of the corrected kinematic variables in single-differential cross-section bins of Q^2, x and y and reduced cross-section bins of Q^2 and x were presented in Figures 5.1 and 5.2. Generally it was found that there was very little bias in all single-differential and reduced cross-section bins and that the resolution was between 10% and 20%.

7.1.2 Acceptance, purity and efficiency

Acceptance, purity and efficiency were calculated from CC MC and are defined in each cross section bin as follows:

$$\text{Acceptance} = \frac{N_{\text{measured}}}{N_{\text{generated}}}\,, \tag{7.1}$$

$$\text{Purity} = \frac{N_{\text{measured and generated}}}{N_{\text{measured}}} \quad \text{and} \tag{7.2}$$

$$\text{Efficiency} = \frac{N_{\text{measured and generated}}}{N_{\text{generated}}}\,, \tag{7.3}$$

where N_{measured} is the number of events that passed all selection cuts and were reconstructed in the kinematic bin of interest and $N_{\text{generated}}$ is the number of events generated with the true value of the kinematic variable in the given bin.

The acceptance depends on the selection cuts and the geometry of the ZEUS detector. The purity quantifies the effect of migrations between kinematic bins.

High values of purity mean that there are few events migrating into a given bin. The efficiency is the product of the acceptance and the purity and describes the fraction of events that are selected in their true kinematic bin. It is desirable to have as high as an efficiency as possible, as this will minimise any systematic uncertainty arising from differences between the MC and the data.

Table 7.1 lists the acceptance, purity and efficiency for the total cross-section measurements for e^+p and e^-p collisions with $Q^2 > 200$ GeV^2.

	e^+p	e^-p
Acceptance (%)	53.6	60.3
Purity (%)	99.1	99.5
Efficiency (%)	53.2	60.0

Table 7.1: The acceptance, purity and efficiency calculated using CC MC for e^+p and e^-p total cross sections.

Figures 7.1 and 7.2 show the acceptance, purity and efficiency in single-differential cross-section bins of Q^2, y and x and in reduced cross-section bins of x and Q^2, for e^+p and e^-p collisions.

In the single-differential cross-section bins, the acceptance ranges from around 20-30% at low-Q^2, high-y and high-x, to around 70% in the mid-region of each kinematic variable. The efficiency follows similar trends ranging from around 20% to around 60%. The purity is fairly constant at around 60-70% for all values of Q^2 but decreases from around 90% to around 60% as y increases and increases from around 60% to around 90% with increasing x.

The same trends are seen in the reduced cross-section bins in Q^2 and x, where the acceptance ranges from as little as a few percent in bins at the edge of the accepted kinematic region up to 70-80% at high values of Q^2. The purity ranges from around 30% to around 70%, with slightly lower values in bins on the edge of the accepted kinematic region. The efficiency varies between around 20% at low values of Q^2 to around 50%, also with slightly lower values in bins on the edge of the accepted kinematic region.

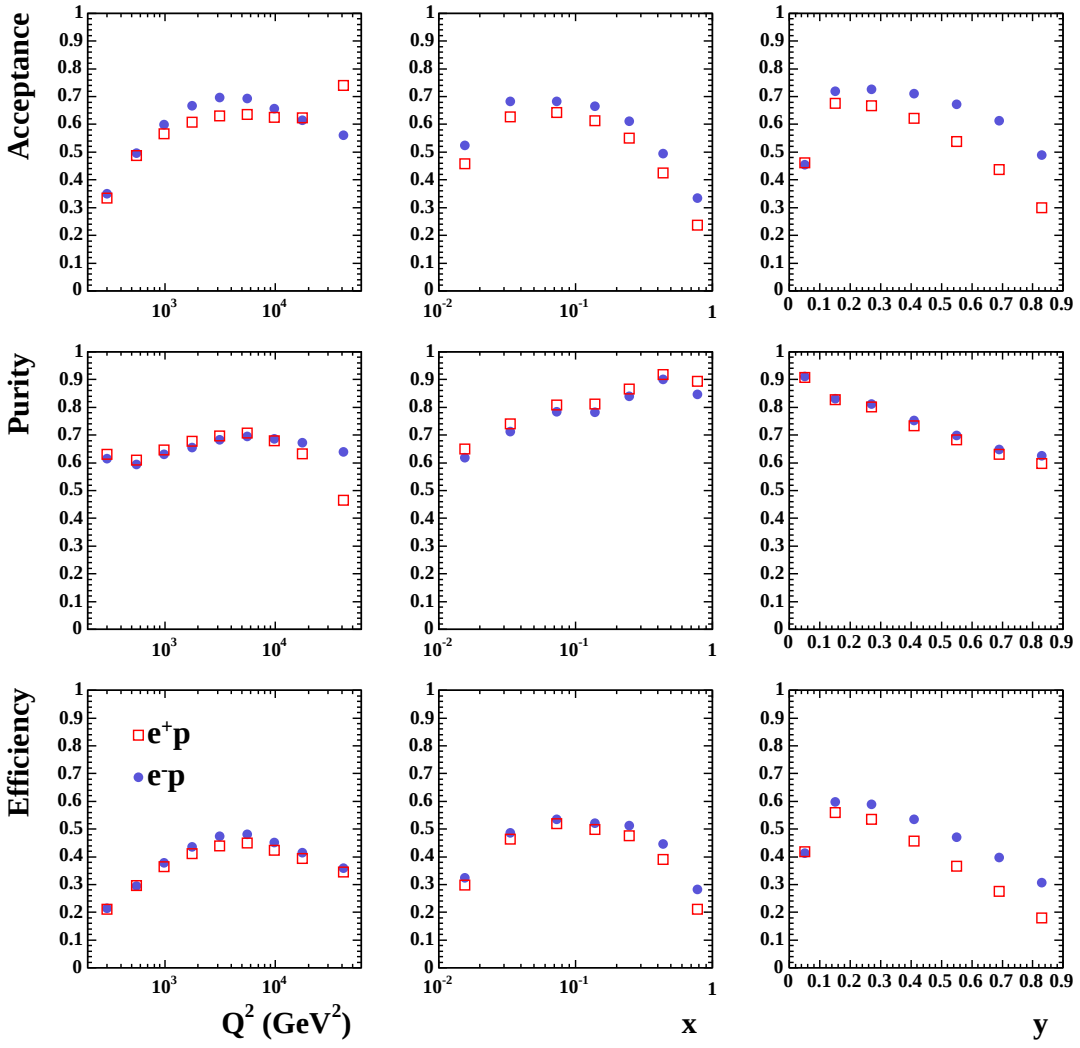

Figure 7.1: Acceptance, purity and efficiency in bins of Q^2, x and y for e^+p (red squares) and e^-p (blue circles) collisions.

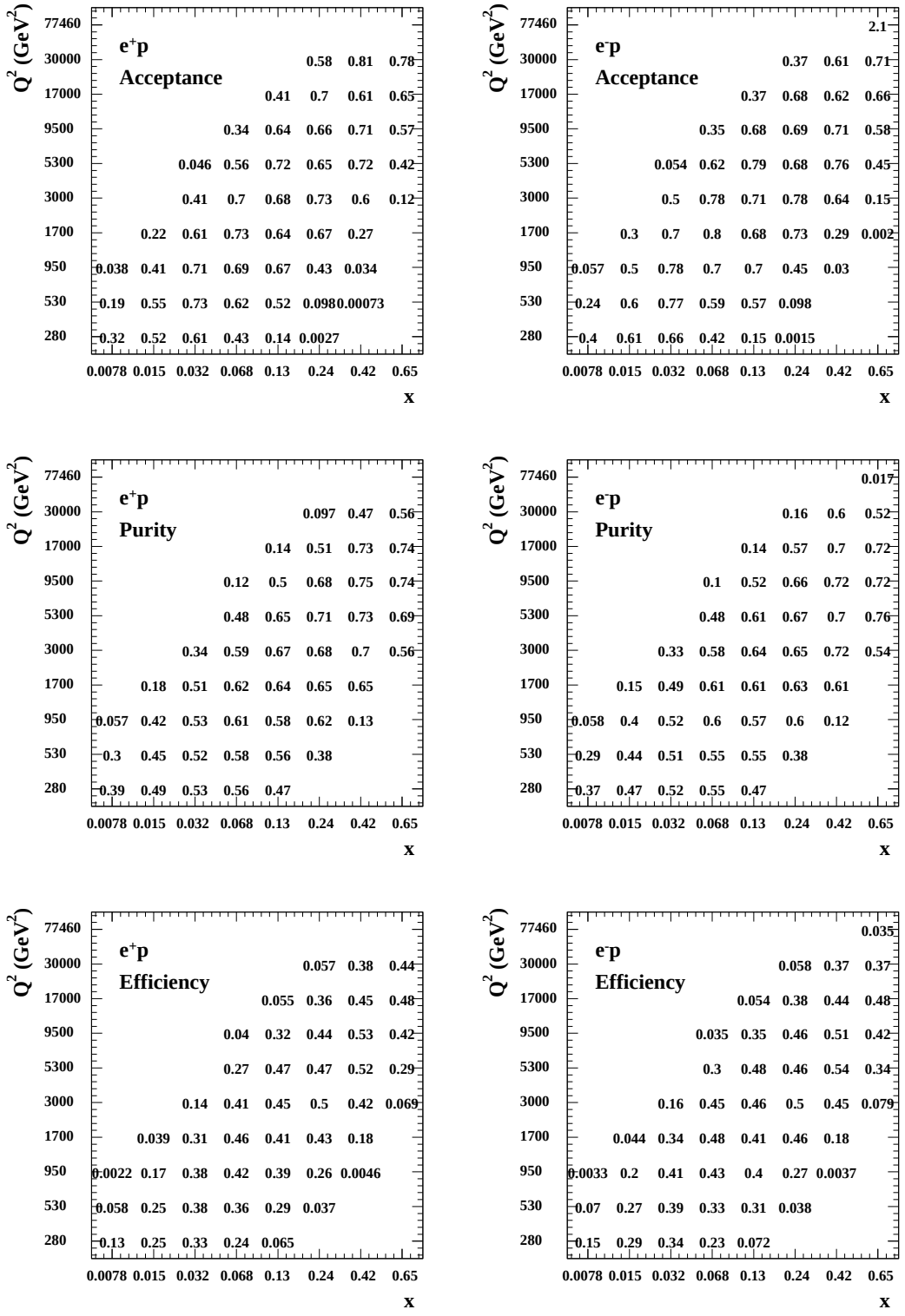

Figure 7.2: Acceptance, purity and efficiency in bins of Q^2 and x for e^+p and e^-p collisions.

7.1.3 Bin definitions

Tables 7.2 to 7.5 list the bin centres and boundaries for the single-differential cross-section measurements as functions of Q^2, x and y and the reduced cross-section measurements as a function of both Q^2 and x. The single-differential and reduced cross sections were extracted at the linear bin centre of the y bins and at the logarithmic bin centre of the Q^2 and x bins, except in the highest x bin where the cross section $d\sigma/dx$ falls precipitously and hence the extraction was made at a slightly lower x value.

Bin centre ($\mathbf{GeV^2}$)	**Lower edge ($\mathbf{GeV^2}$)**	**Upper edge ($\mathbf{GeV^2}$)**
280	200	400
530	400	711
950	711	1265
1,700	1,265	2,249
3,000	2,249	4,000
5,300	4,000	7,113
9,500	7,113	12,469
17,000	12,469	22,494
30,000	22,494	60,000

Table 7.2: The bin definitions for the single-differential cross-section $d\sigma/dQ^2$ as a function of Q^2.

Bin centre	**Lower edge**	**Upper edge**
0.015	0.010	0.021
0.032	0.021	0.046
0.068	0.046	0.100
0.130	0.100	0.178
0.240	0.178	0.316
0.420	0.316	0.562
0.650	0.562	1.000

Table 7.3: The bin definitions for the single-differential cross-section $d\sigma/dx$ as a function of x.

Nine bins in Q^2 were defined for the single-differential cross-sections $d\sigma/dQ^2$, covering Q^2 values from 200 GeV^2 to 60,000 GeV^2. The seven central Q^2 bins had equal spacing in $\log Q^2$. The lowest and highest Q^2 bins were made slightly

Bin centre	Lower edge	Upper edge
0.05	0.00	0.10
0.15	0.10	0.20
0.27	0.20	0.34
0.41	0.34	0.48
0.55	0.48	0.62
0.69	0.62	0.76
0.83	0.76	0.9

Table 7.4: The bin definitions for the single-differential cross-section $d\sigma/dy$ as a function of y.

wider to reduce the fractional background contamination in the lowest Q^2 bin and to improve the statistical precision in the highest Q^2 bin. However, in the highest Q^2 bin no e^+p CC events were collected, so only e^-p cross sections were measured.

For the single-differential cross-section $d\sigma/dx$, seven bins in x were defined, ranging from 0.01 to 1.0. Since the resolution of x_{JB} improves with increasing x, the three lowest bins, which covered x values from 0.01 to 0.1, had a wider spacing in $\log x$ than the four highest bins. In the highest x bin no e^+p CC events were collected, so only e^-p cross sections were measured.

Seven bins in y were used for the single-differential cross-section $d\sigma/dy$. This cross section changes fairly dramatically at low values of y so the two lowest y bins were defined with narrower widths than the other bins.

The reduced cross-section bins in Q^2 and x were defined with the same boundaries as the single-differential cross sections. The e^-p data had a sufficient number events to extract the reduced cross section in all bins. Measurements from the e^+p data were only made in bins with at least five data events.

7.2 Cross section extraction

The electroweak Born-level total cross sections for $e^\pm p$ CC DIS, with average longitudinal lepton beam polarisation P_e, were extracted from the data and MC

Q^2 bin centre ($\mathbf{GeV^2}$)	Q^2 lower edge ($\mathbf{GeV^2}$)	Q^2 upper edge ($\mathbf{GeV^2}$)	x bin centre	x lower edge	x upper edge
280	200	400	0.015	0.010	0.021
280	200	400	0.032	0.021	0.046
280	200	400	0.068	0.046	0.100
280	200	400	0.13	0.100	0.178
530	400	711	0.015	0.010	0.021
530	400	711	0.032	0.021	0.046
530	400	711	0.068	0.046	0.100
530	400	711	0.13	0.100	0.178
950	711	1265	0.015	0.010	0.021
950	711	1265	0.032	0.021	0.046
950	711	1265	0.068	0.046	0.100
950	711	1265	0.13	0.100	0.178
950	711	1265	0.24	0.178	0.316
1,700	1,265	2,249	0.032	0.021	0.046
1,700	1,265	2,249	0.068	0.046	0.100
1,700	1,265	2,249	0.13	0.100	0.178
1,700	1,265	2,249	0.24	0.178	0.316
1,700	1,265	2,249	0.42	0.316	0.562
3,000	2,249	4,000	0.032	0.021	0.046
3,000	2,249	4,000	0.068	0.046	0.100
3,000	2,249	4,000	0.13	0.100	0.178
3,000	2,249	4,000	0.24	0.178	0.316
3,000	2,249	4,000	0.42	0.316	0.562
5,300	4,000	7,113	0.068	0.046	0.100
5,300	4,000	7,113	0.13	0.100	0.178
5,300	4,000	7,113	0.24	0.178	0.316
5,300	4,000	7,113	0.42	0.316	0.562
5,300	4,000	7,113	0.65	0.562	1.000
9,500	7,113	12,469	0.13	0.100	0.178
9,500	7,113	12,469	0.24	0.178	0.316
9,500	7,113	12,469	0.42	0.316	0.562
9,500	7,113	12,469	0.65	0.562	1.000
17,000	12,469	22,494	0.24	0.178	0.316
17,000	12,469	22,494	0.42	0.316	0.562
17,000	12,469	22,494	0.65	0.562	1.000
30,000	22,494	60,000	0.42	0.316	0.562
30,000	22,494	60,000	0.65	0.562	1.000

Table 7.5: The bin definitions for the reduced cross section as a function of Q^2 and x.

simulation using the following formula:

$$\sigma^{\mathrm{CC}}_{\mathrm{meas}}(e^{\pm}p) = \frac{N_{\mathrm{data}} - N_{\mathrm{BG}}}{N_{\mathrm{CC}}} \sigma^{\mathrm{CC\ SM}}_{0,\ \mathrm{Born}}(1 \pm P_e), \tag{7.4}$$

where $\sigma^{\mathrm{CC}}_{\mathrm{meas}}$ is the measured total cross section for $Q^2 > 200$ GeV^2, corrected to the Born level, N_{data} is the number of data events passing the selection cuts, N_{BG} is the number of SM background events passing the selection cuts, estimated from the MC simulation, N_{CC} is the number of CC events passing the selection cuts, estimated from the CC MC simulation, and $\sigma^{\mathrm{CC\ SM}}_{0,\ \mathrm{Born}}$ is the SM prediction for the Born-level cross section for $P_e = 0$ and $Q^2 > 200$ GeV^2.

Both the MC and the SM prediction, $\sigma^{\mathrm{CC\ SM}}_{0,\ \mathrm{Born}}$, used the CTEQ5D PDFs and were calculated at leading order in QCD, ensuring a consistent extraction method. The detector acceptance, initial state radiation and events migrating between bins were all accounted for in the MC.

Single-differential and reduced cross sections were extracted at the bin centres defined in Tables 7.2 to 7.5 using equation 7.4 evaluated separately for each kinematic bin.

7.3 Statistical uncertainties

The statistical uncertainty on the cross-section measurements accounts for the uncertainties on both the number of data and the number of MC events, although the latter was generally insignificant.

The uncertainty on the number of data events was determined as follows:

$$\delta N_{\mathrm{data}} = \begin{cases} \sqrt{N_{\mathrm{data}}} & \text{if } N_{\mathrm{data}} > 12 \text{ and} \\ 67\% \text{ C.L. limit} & \text{if } N_{\mathrm{data}} \leq 12, \end{cases} \tag{7.5}$$

where the 67% confidence level limit was calculated using Poisson statistics.

The uncertainty on the number of MC events was determined as follows:

$$\delta N_{\mathrm{MC}} = \sqrt{\sum_i w_i^2}, \tag{7.6}$$

where the sum was performed over all generated MC events and w_i is the weight that was attributed to each event.

The statistical uncertainties on the data and on the number of MC events were then combined to give the statistical uncertainty on the cross-section measurement, $\delta\sigma^{\pm}_{\text{stat}}$, for $e^{\pm}p$ collisions as follows:

$$\delta\sigma^{\pm}_{\text{stat}} = \sqrt{\left(\frac{\delta N_{\text{data}}}{N_{\text{CC}}}\right)^2 + \left(\frac{\delta N_{\text{BG}}}{N_{\text{CC}}}\right)^2 + \left(\frac{\delta N_{\text{CC}}(N_{\text{data}} - N_{\text{BG}})}{N^2_{\text{CC}}}\right)^2} \cdot \sigma^{\text{CC SM}}_{0,\ \text{Born}}(1 \pm P_e). \tag{7.7}$$

7.4 Systematic uncertainties

Various theoretical and experimental uncertainties can affect the extracted cross-section measurements. These effects were studied to estimate the systematic uncertainty on the cross-section measurements.

In the following plots of the systematic uncertainties, where there were not enough data events in a given bin for the cross section to be measured, the uncertainty on the cross-section measurement in that bin is set to zero.

7.4.1 Parton shower model

In order to estimate the effect of different parton shower models on the extracted cross sections, CC events were generated using two different models, as described in section 4.1. ARIADNE, which employs the colour dipole model, provided the nominal cross section measurements and MEPS, which uses the matrix element parton shower model, allowed the systematic uncertainty on the cross sections to be estimated.

The cross sections were extracted using each MC sample and the fractional uncertainty on the cross section was defined as follows:

$$\delta\sigma = \pm\left(\frac{\sigma_0 - \sigma_{\text{sys}}}{2 \times \sigma_0}\right), \tag{7.8}$$

where σ_0 is the nominal cross section and σ_{sys} is the cross section extracted using the MEPS MC.

Figures 7.3 and 7.4 show the fractional uncertainty on the cross sections from the parton shower model in single-differential and reduced cross-section bins for e^+p and e^-p collisions. The uncertainty was found to be largest at low-Q^2 and low-x, where it was around 2-4% in the single-differential cross-section bins and 5-6% in the reduced cross-section bins.

7.4.2 F_L

The MC events were simulated at leading order in QCD, so F_L=0. Although this was accounted for in the extraction method, the neglection of next-to-leading-order QCD contributions in the MC could introduce a bias into the extracted measurements. In order to assess the impact on the cross-section measurements, the CC MC events were re-weighted by the SM Born-level cross section at NLO in QCD, including the F_L contribution, and the cross sections were re-extracted. The uncertainty on the cross section was determined using equation 7.8, where σ_{sys} was the cross section extracted using the re-weighted MC.

Figures 7.5 and 7.6 show the fractional uncertainty on the cross sections from the uncertainty in accounting for next-to-leading-order QCD contributions in the MC. The cross-section uncertainties are shown in single-differential and reduced cross-section bins for e^+p and e^-p collisions. The uncertainty was largest at low-x and high-y, where it reached around 2% to 4%.

7.4.3 Electroweak radiative corrections

The electroweak radiative corrections to the Born-level cross section, described in section 2.5.1, were included in the MC simulation using the HERACLES program [89]. It has been shown that the HERACLES calculations are generally in good agreement with other calculations [120] and consequently the systematic uncertainty associated with these corrections was assumed to be negligible.

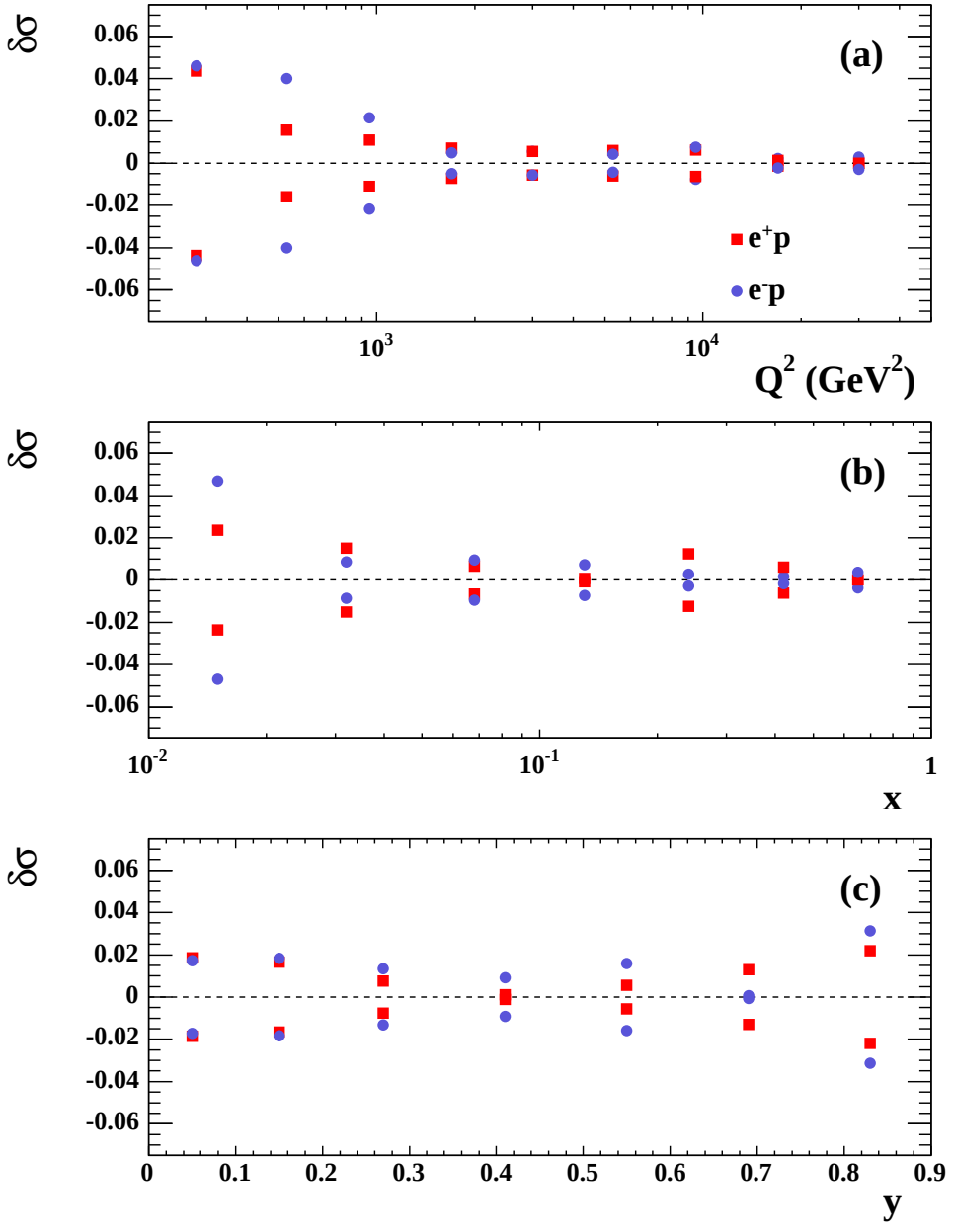

Figure 7.3: The fractional systematic uncertainty on the differential cross-section measurements (a) $d\sigma/dQ^2$, (b) $d\sigma/dx$ and (c) $d\sigma/dy$ from the parton shower model. The red squares (blue circles) indicate the uncertainty on the e^+p (e^-p) cross sections.

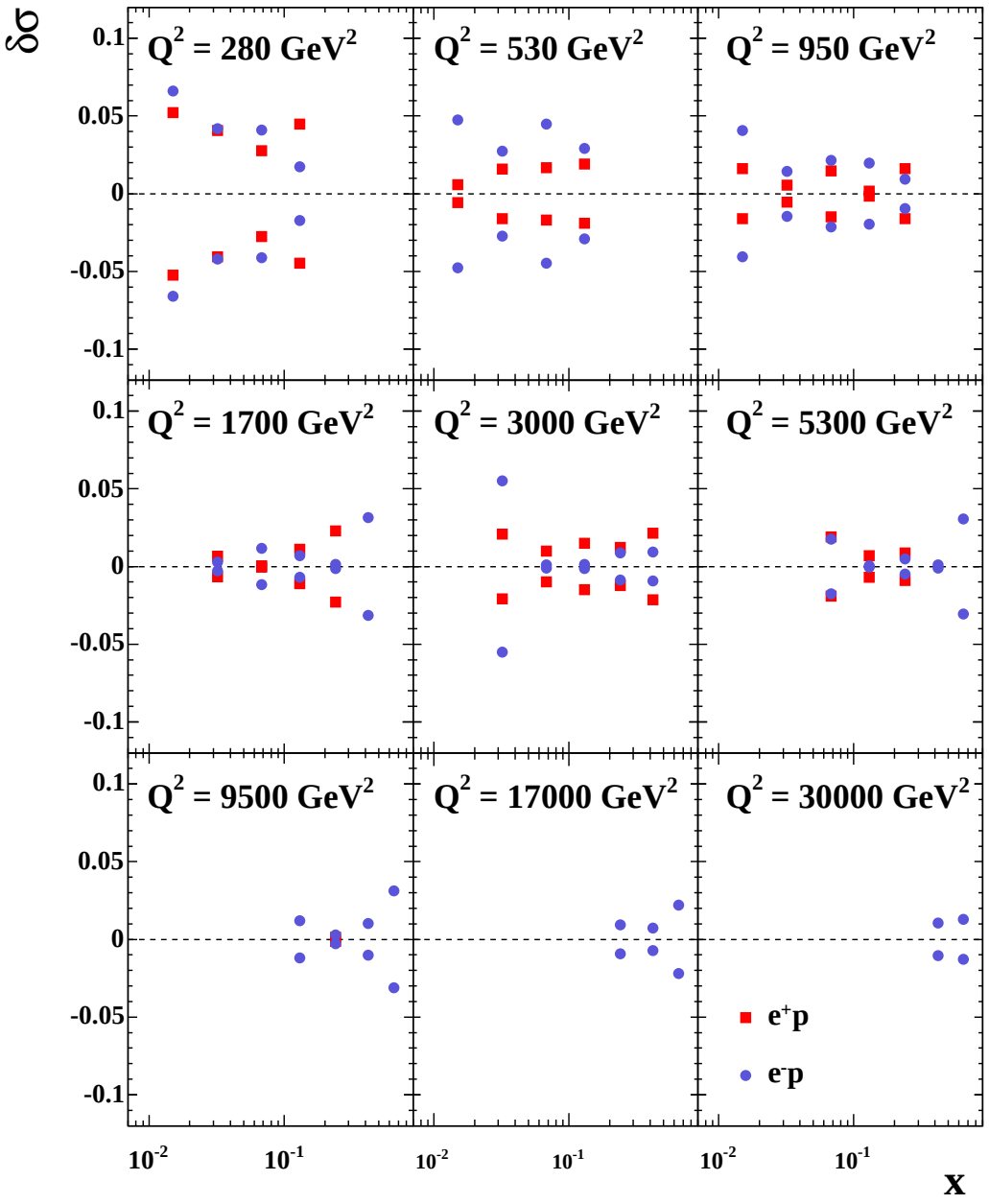

Figure 7.4: The fractional systematic uncertainty on the reduced cross-section measurement in bins of x and Q^2 from the parton shower model. The red squares and blue circles indicate the uncertainty on the e^+p and e^-p cross sections, respectively.

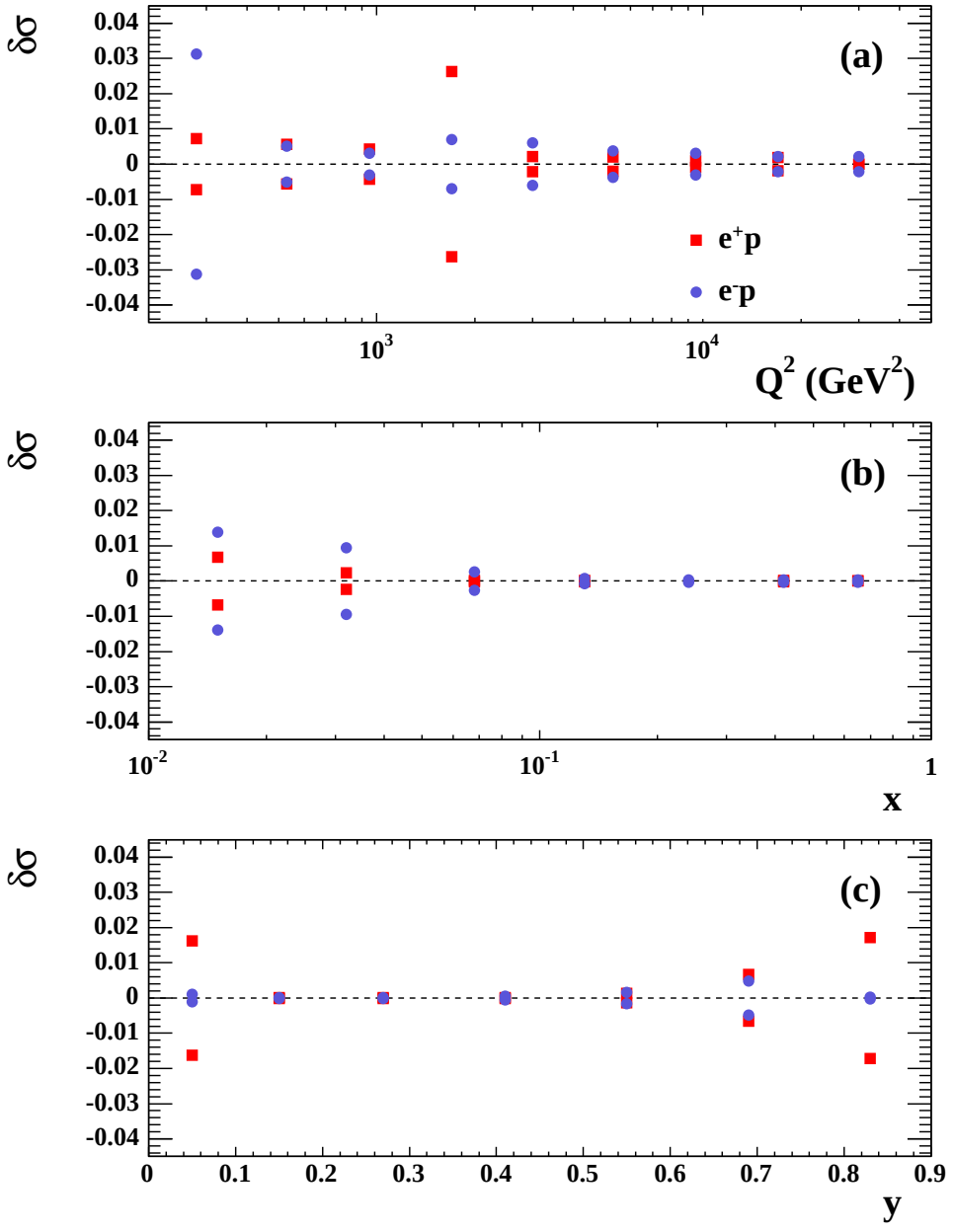

Figure 7.5: The fractional systematic uncertainty on the differential cross-section measurements (a) $d\sigma/dQ^2$, (b) $d\sigma/dx$ and (c) $d\sigma/dy$ from the exclusion of F_L from the MC. The red squares (blue circles) indicate the uncertainty on the e^+p (e^-p) cross sections.

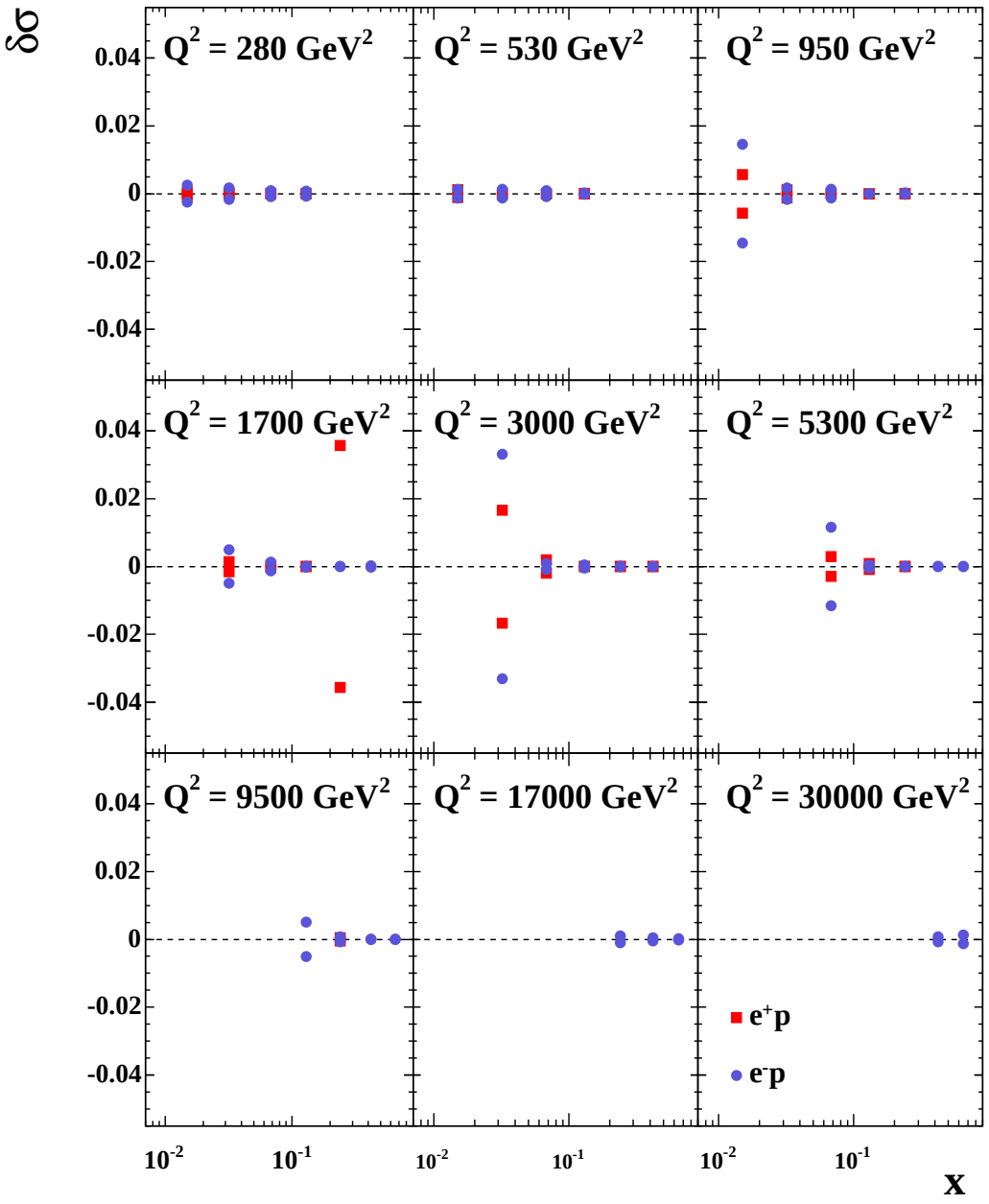

Figure 7.6: The fractional systematic uncertainty on the reduced cross-section measurement in bins of x and Q^2 from the exclusion of F_L from the MC. The red squares and blue circles indicate the uncertainty on the e^+p and e^-p cross sections, respectively.

7.4.4 Parton density functions

The CTEQ5D PDFs [95] were used to simulate the CC MC events, as described in section 4.1. In order to estimate the effect of the PDF uncertainty on the measured cross sections, the MC events were re-weighted by $\pm\delta(x, Q^2)$, where $\delta(x, Q^2)$ was the fractional uncertainty on the reduced cross section from the ZEUS-JETS PDFs [23]. After re-weighting, the cross sections were extracted again and the difference between these and the nominal cross sections was taken to be the systematic uncertainty. The systematic uncertainty was found to be negligible across the entire kinematic range.

7.4.5 Photoproduction normalisation

An uncertainty in the normalisation of the PHP MC can cause an uncertainty in the measured cross sections. The uncertainty in the PHP normalisation was estimated by plotting the V_{AP}/V_P distribution for data and MC events with $\gamma_0 < 0.4$ radians and $P_{T,miss} < 20$ GeV, with all selection cuts applied except for the cut on V_{AP}/V_P, as shown in Figure 7.7 (a). A likelihood fit was performed to these distributions, varying the normalisation of the PHP MC until it produced the best description of the data. The fit resulted in a normalisation factor of 0.47 ± 0.05, which is in agreement with previous similar studies that obtained a value of 0.57 ± 0.09 [121]. The V_{AP}/V_P distribution with the PHP MC normalised by the factor of 0.47 is shown in Figure 7.7 (b).

As a somewhat conservative estimate of the systematic uncertainty from the PHP normalisation, the PHP normalisation was varied by a factor of ± 0.60, which was chosen as it is slightly larger than the normalisation factor of 0.47 ± 0.05. The resulting changes in the extracted cross sections were taken as the systematic uncertainty. These uncertainties are illustrated in Figures 7.8 and 7.9 for e^+p and e^-p collisions. In most cross-section bins the uncertainty was negligible, but it reached around 1-2% in the lowest Q^2 and x bins and up to 5% at $Q^2 = 950$ GeV^2 and in the highest y bin.

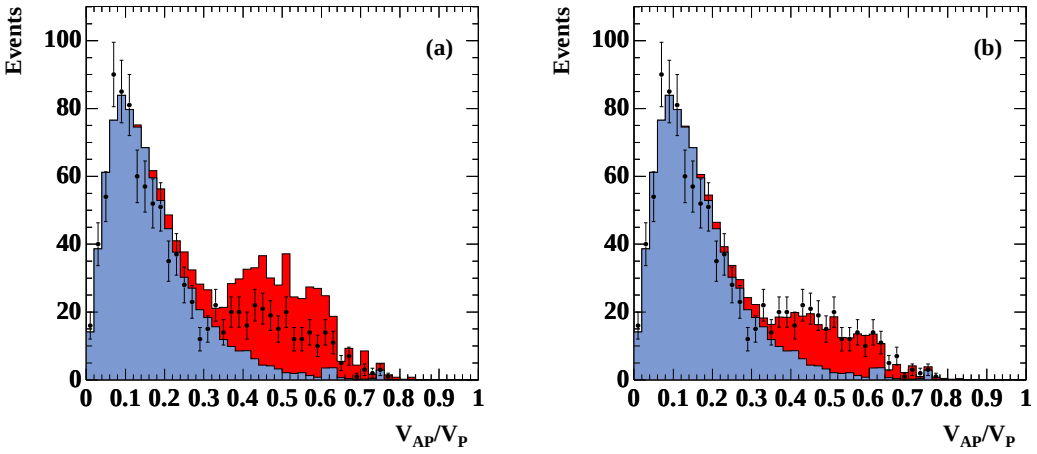

Figure 7.7: Normalising the PHP MC to the V_{AP}/V_P distribution for events with $\gamma_0 > 0.4$ radians and $P_{T,miss} < 20$ GeV and all selection cuts applied except the cut on V_{AP}/V_P. The distributions are plotted (a) before and (b) after re-weighting the PHP MC. The points are the data, the blue histograms are all SM MC except the PHP MC and the red histograms are the PHP MC.

7.4.6 Calorimeter energy scale

The CAL energy scale was calibrated using NC data and compared with MC to estimate its uncertainty [39, 40]. The energy scale was estimated using the Double Angle method to calculate the expected amount of P_T in the CAL, independently of the energy scale, and then comparing this to the measured P_T. The difference between the CAL energy scale from data and from MC was around 2% for the RCAL and 1% for the BCAL and FCAL. The energy scale in the MC was varied by these values and the cross sections were re-extracted. The difference between these cross sections and the nominal values was taken as the uncertainty.

Figures 7.10 and 7.11 show the fractional uncertainty on the single-differential and reduced cross sections from the CAL energy scale for e^+p and e^-p collisions. The uncertainty was found to be largest at high-Q^2 and high-x, where it reached up to 10-15% in single-differential cross-section bins and as much as 40% in the highest Q^2 and x bin of the reduced cross section.

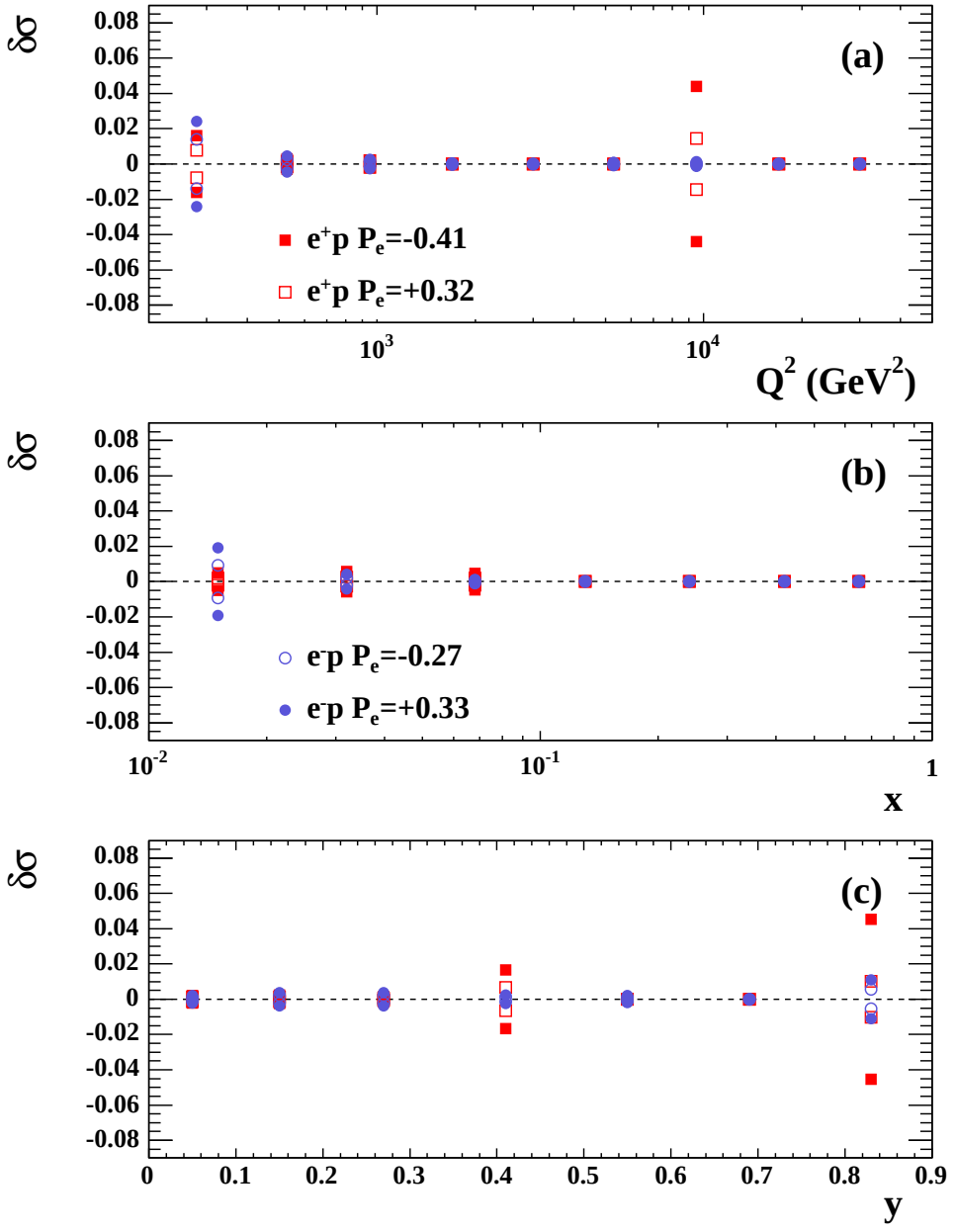

Figure 7.8: The fractional systematic uncertainty on the differential cross-section measurements (a) $d\sigma/dQ^2$, (b) $d\sigma/dx$ and (c) $d\sigma/dy$ from the PHP normalisation uncertainty. The open and filled red squares (blue circles) indicate the uncertainty on the e^+p (e^-p) cross sections for different values of lepton beam longitudinal polarisation.

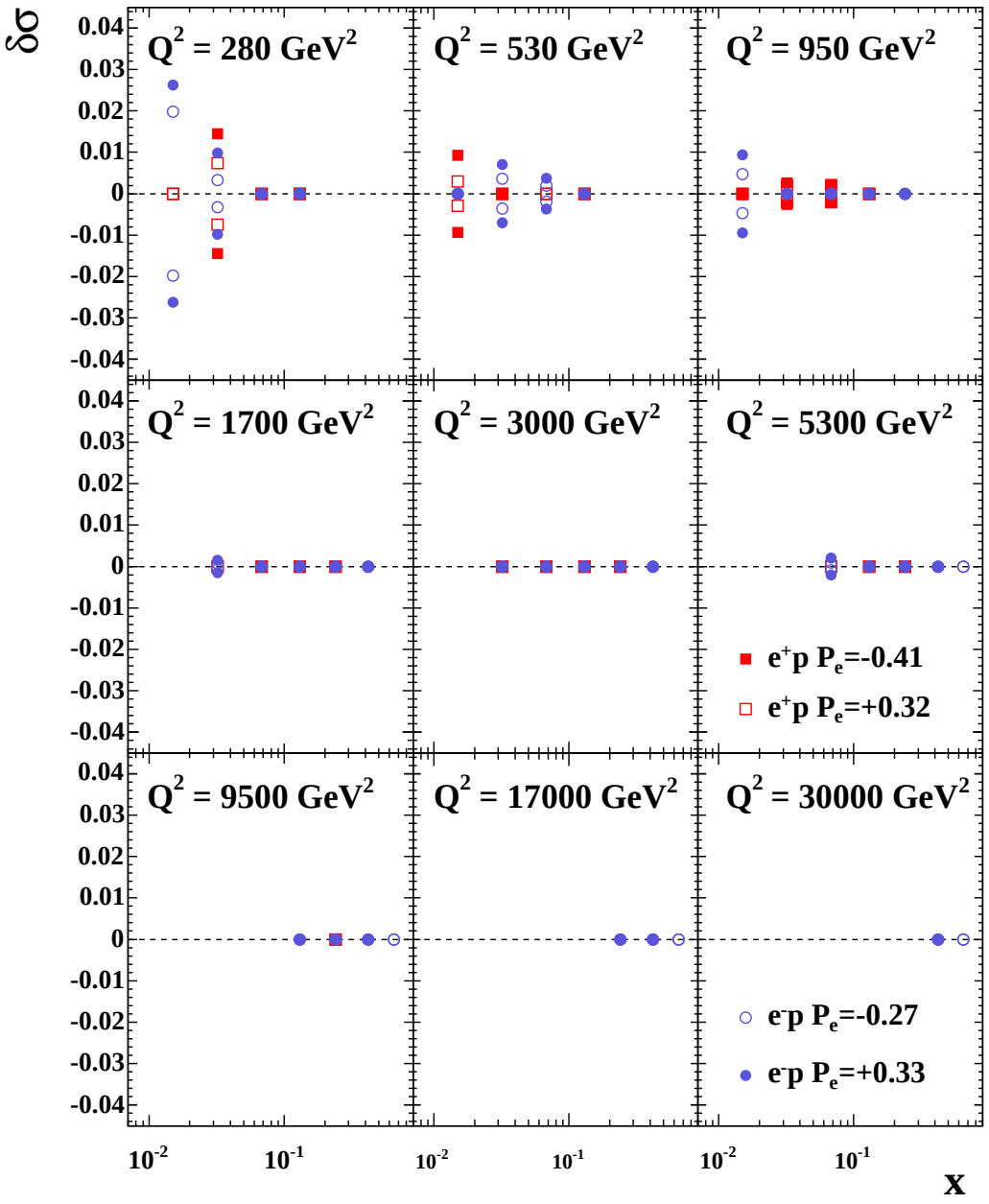

Figure 7.9: The fractional systematic uncertainty on the reduced cross-section measurement in bins of x and Q^2 from the PHP normalisation uncertainty. The open and filled red squares (blue circles) indicate the uncertainty on the e^+p (e^-p) cross sections for different values of lepton beam longitudinal polarisation.

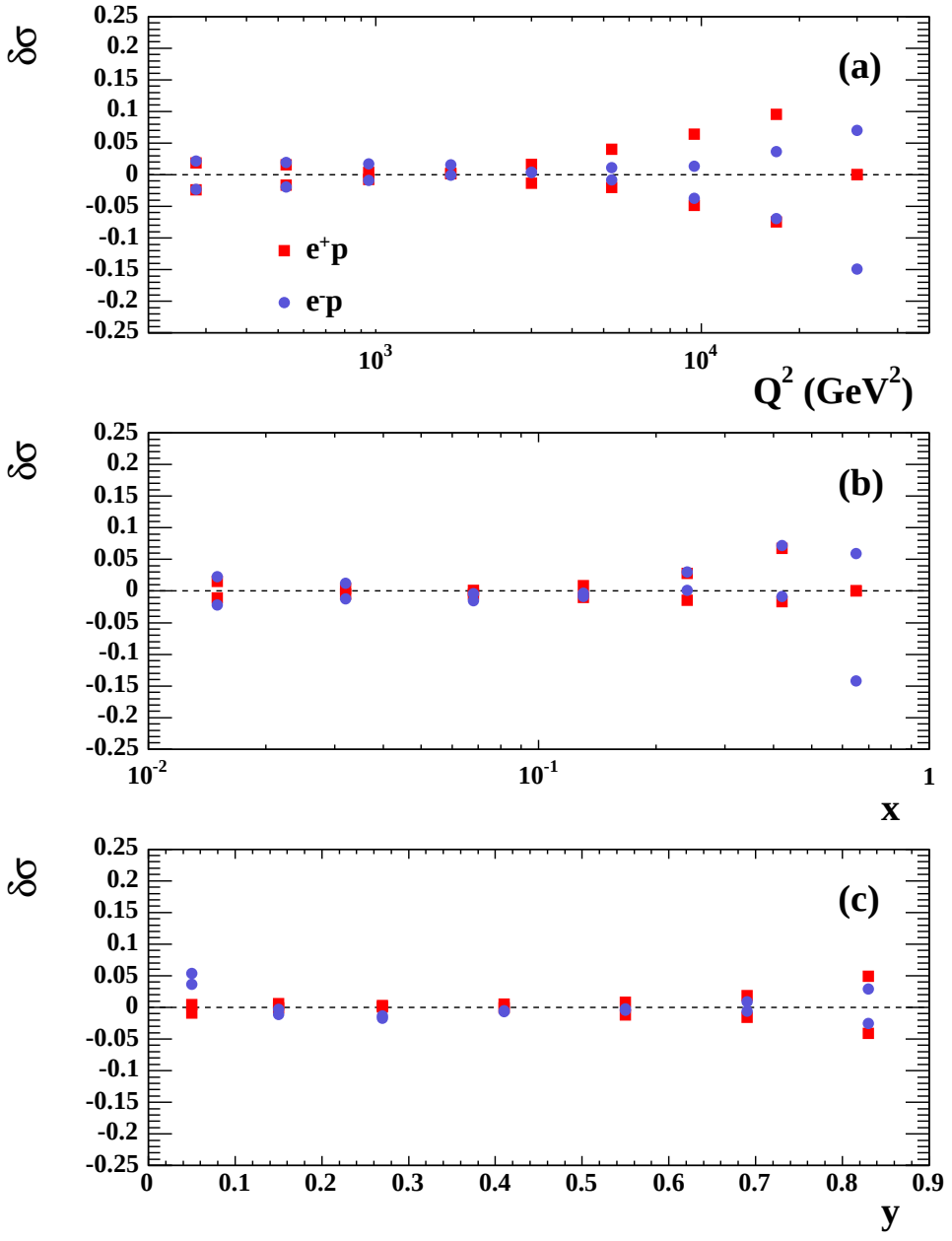

Figure 7.10: The fractional systematic uncertainty on the differential cross-section measurements (a) $d\sigma/dQ^2$, (b) $d\sigma/dx$ and (c) $d\sigma/dy$ from the uncertainty on the CAL energy scale. The red squares (blue circles) indicate the uncertainty on the e^+p (e^-p) cross sections.

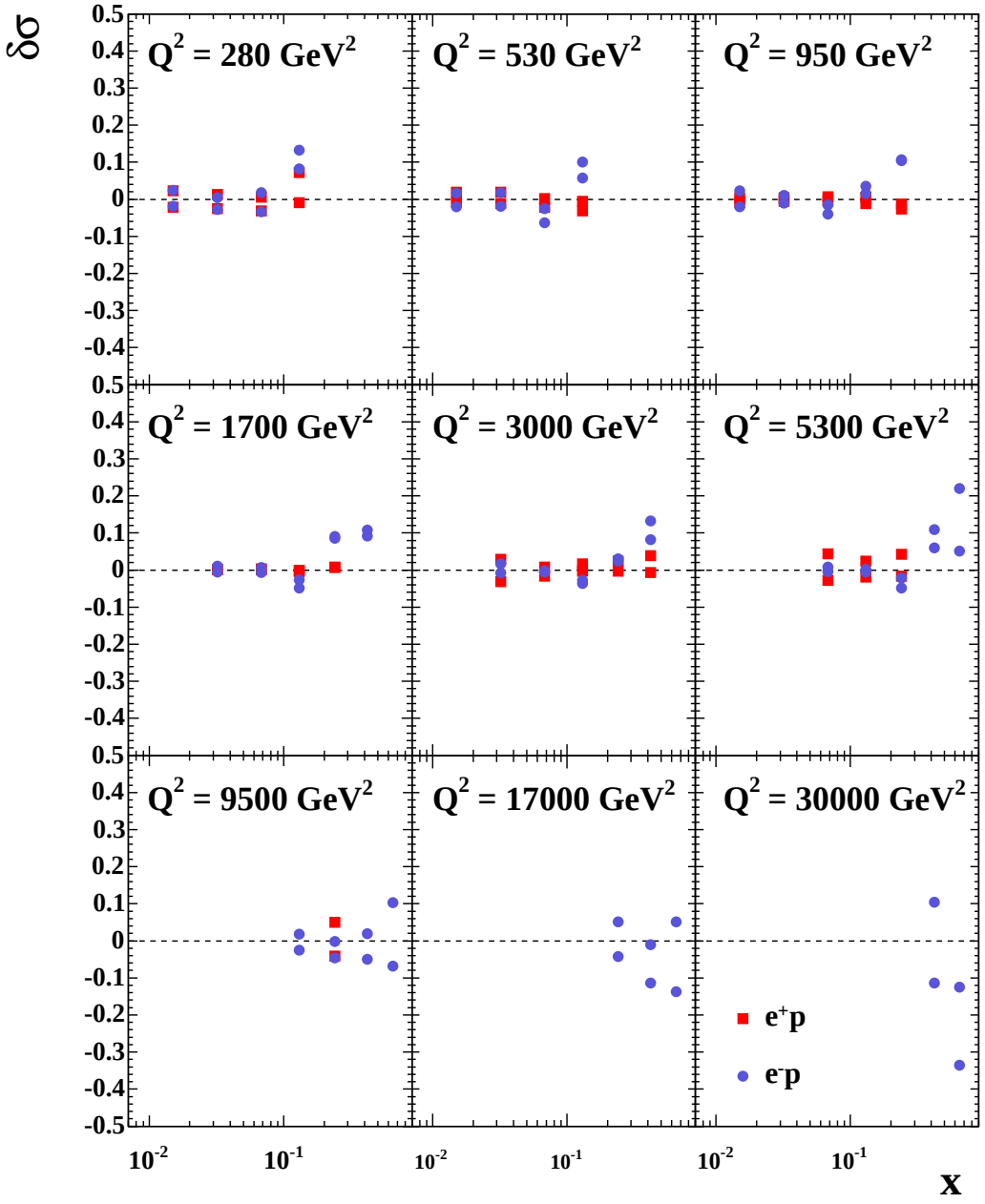

Figure 7.11: The fractional systematic uncertainty on the reduced cross-section measurement in bins of x and Q^2 from the uncertainty on the CAL energy scale. The red squares and blue circles indicate the uncertainty on the e^+p and e^-p cross sections, respectively.

7.4.7 Trigger efficiency

The CC FLT has a lower $P_{T,miss}$ cut than the offline cut to compensate for the worse resolution at the FLT. It is important to check that the FLT CC efficiency is well-simulated in the MC, since a discrepancy could result in a bias in the measured cross sections. The CC FLT efficiency was estimated as a function of the offline $P_{T,miss}$ for CC data and MC events, using events taken by an independent slot with no cut on $P_{T,miss}$. The efficiency was defined as follows:

$$\text{Efficiency} = \frac{N_{\text{CC slot AND independent slot}}}{N_{\text{independent slot}}} \ , \tag{7.9}$$

where $N_{\text{independent slot}}$ is the number of events accepted by the independent slot and $N_{\text{CC slot AND independent slot}}$ is the number of events taken by both the CC slot and the independent slot.

Figure 7.12 shows the efficiency plotted as a function of $P_{T,miss}$ for CC data and MC. The efficiencies were parametrised by fitting the following function:

$$\text{Efficiency}(P_{T,miss}) = 0.5 + 0.5 \times \tanh\left(\frac{P_{T,miss} - p}{q}\right), \tag{7.10}$$

where p and q were allowed to vary.

The CC FLT efficiency in the MC is generally slightly higher than in the data. To estimate the uncertainty on the cross sections arising from this difference, the MC events that were only accepted by the CC slot were re-weighted to the efficiency of the data and the cross sections were re-extracted. The fractional uncertainty on the cross sections was then estimated using equation 7.8. Generally the uncertainty was negligible, reaching at most around 1% at low-Q^2.

7.4.8 Selection efficiencies

If the distributions that are cut on in the CC selection are not well-simulated in the MC, this can cause a bias in the extracted cross-section measurements. The efficiencies of the selection cuts were checked using NC data and MC, with the final state electron (or positron) removed, thus mimicking CC events. These were

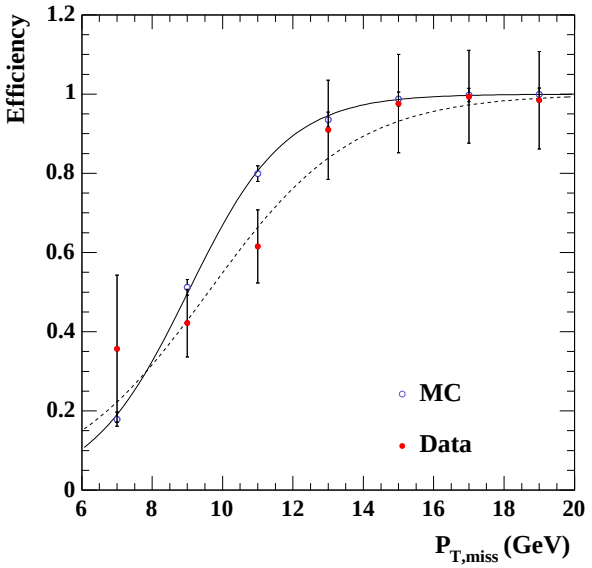

Figure 7.12: CC FLT efficiency as a function of $P_{T,miss}$ for CC data (filled red points) and MC (open blue points). The full and dashed lines show the results of a fit to the MC and data points, respectively.

called pseudo-CC samples. Pseudo-CC data was used instead of real CC data since the NC cross section is much higher, providing a clean, large data sample for comparison with the MC.

The efficiency of a given cut, $\mathcal{C}$, was defined as:

$$\text{Efficiency}(\mathcal{C}) = \frac{N_{\text{passing all cuts}}}{N_{\text{passing all cuts except } \mathcal{C}}} \ , \tag{7.11}$$

where $N_{\text{passing all cuts}}$ is the number of events passing all selection cuts and $N_{\text{passing all cuts except } \mathcal{C}}$ is the number of events passing all selection cuts except for the cut $\mathcal{C}$.

The efficiencies for the $P_{T,miss}$, $P_{T,miss}$(-IR), $P_{T,miss}$(-2IR), Z_{VTX}, tracking and $|\Delta\phi|$ cuts were evaluated in bins of either γ_0 or $P_{T,miss}$, depending on which variable the efficiency was most sensitive to. These efficiencies are shown in Figures 7.13 and 7.14 and the agreement between data and MC is generally good. However, there are some differences, for example in the tracking, $P_{T,miss}$ and $P_{T,miss}$(-IR) efficiencies.

In order to estimate the effect on the cross-section measurements caused by dif-

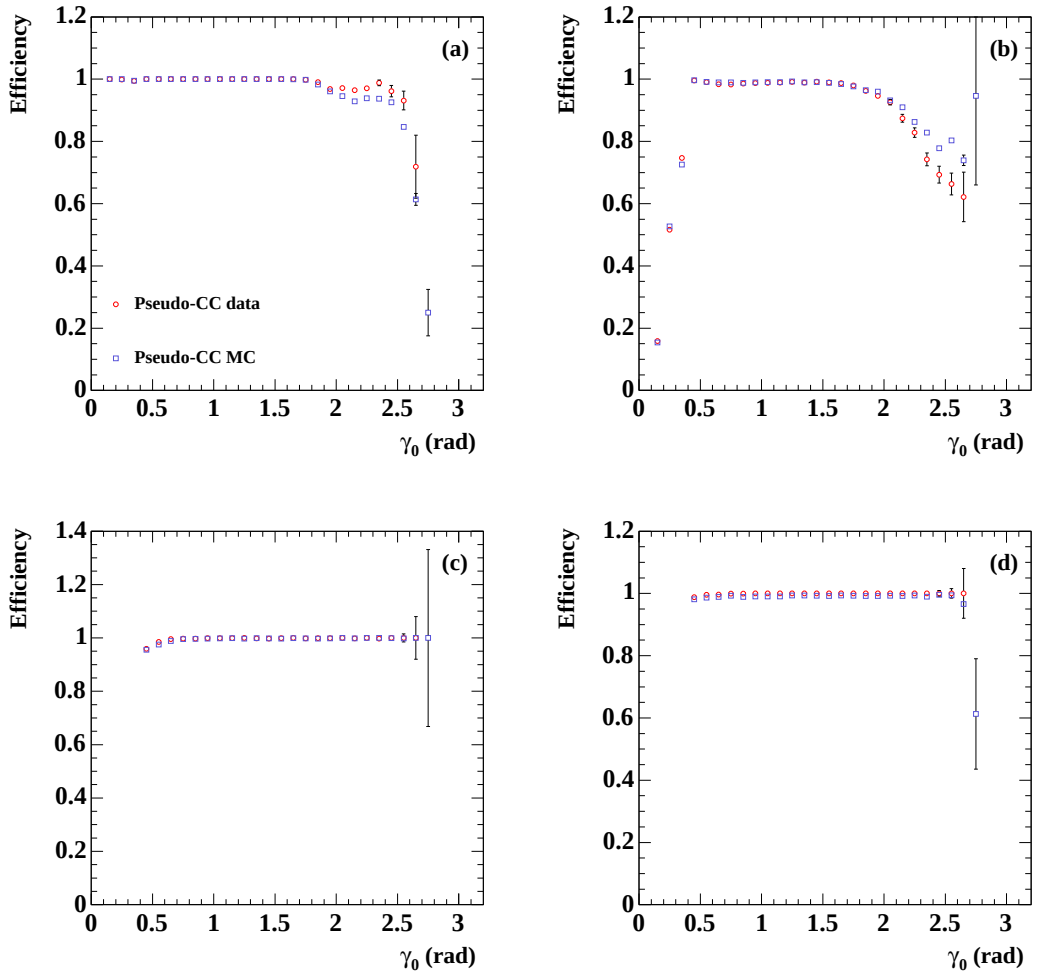

Figure 7.13: The efficiency of the (a) $P_{T,miss}$, (b) $P_{T,miss}$(-IR), (c) $P_{T,miss}$(-2IR) and (d) Z_{VTX} cuts as a function of γ_0 evaluated with pseudo-CC data (red circles) and MC (blue squares).

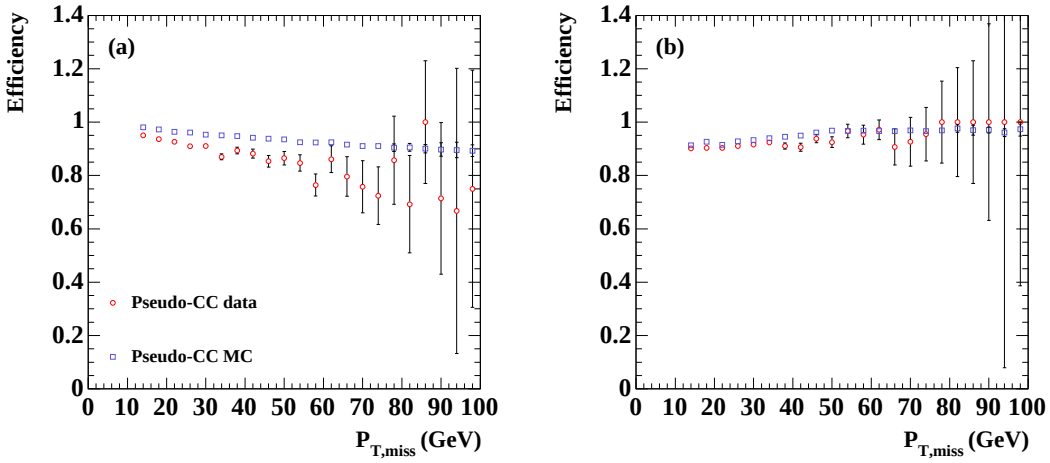

Figure 7.14: The efficiency of the (a) tracking and (b) $|\Delta\phi|$ cuts as a function of $P_{T,miss}$ evaluated using pseudo-CC data (red circles) and MC (blue squares).

ferent efficiencies in data and MC, the CC MC was re-weighted as a function of γ_0 or $P_{T,miss}$ by a correction factor, which was defined as:

$$\text{Correction} = \frac{\text{Data efficiency}}{\text{MC efficiency}} \ . \tag{7.12}$$

Figures 7.15 and 7.16 show the correction factors for each of the cuts.

After re-weighting the MC, the cross sections were re-extracted and the systematic uncertainty on the cross-section measurements was estimated using equation 7.8. Figures 7.17 to 7.28 show the systematic uncertainties from the selection cut efficiencies on the single-differential and reduced cross-section measurements for e^+p and e^-p collisions. For most cuts the uncertainty was insignificant, reaching at most 1% or 2%. The largest uncertainty came from the tracking cut, which reached around 10% at high-Q^2.

7.4.9 Track Veto efficiency

As described in section 6.3.1, the CC FLT used the Tight and Loose Track Vetoes during e^+p and e^-p data-taking, respectively. Studies had shown that the inefficiencies of the tracking vetoes were not well simulated, so the CC MC events were re-weighted as a function of γ to account for this. The systematic uncertainty

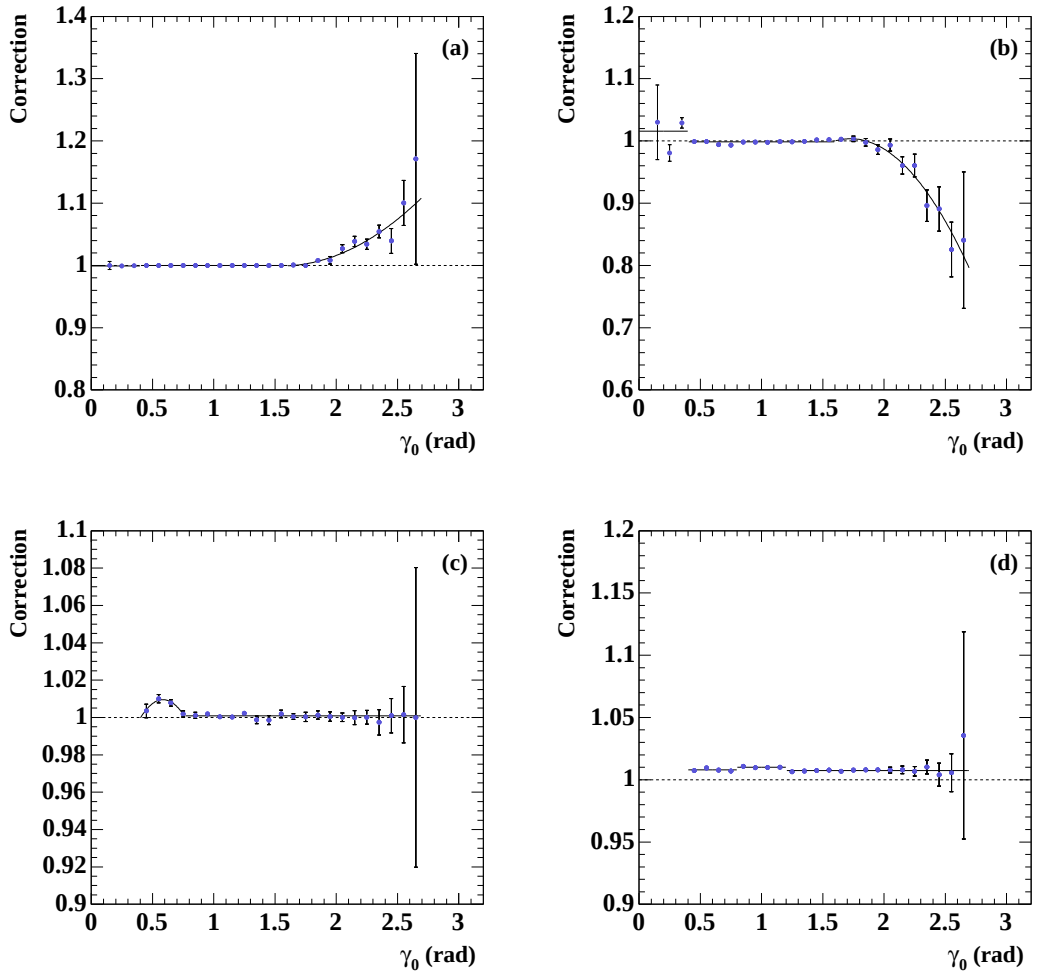

Figure 7.15: The correction factors applied to the CC MC as a function of γ_0 to estimate the systematic uncertainty from the (a) $P_{T,miss}$, (b) $P_{T,miss}$(-IR), (c) $P_{T,miss}$(-2IR) and (d) Z_{VTX} cuts.

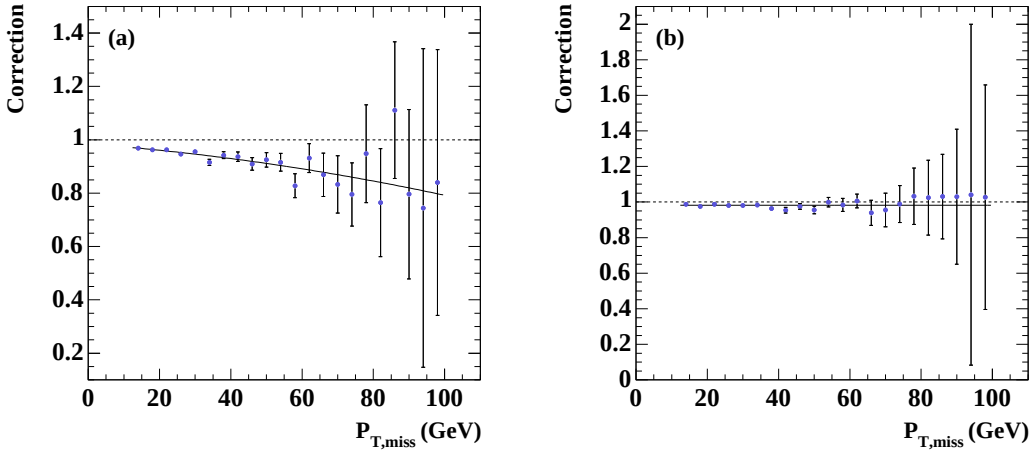

Figure 7.16: The correction factors applied to the CC MC as a function of $P_{T,miss}$ to estimate the systematic uncertainty from the (a) tracking and (b) $|\Delta\phi|$ cuts.

on the cross-section measurements from the re-weighting was estimated to be 1% for the Tight Track Veto and negligible for the Loose Track Veto [122].

7.4.10 Vertex re-weighting

The Z vertex distribution in the MC was weighted to follow the distribution measured from NC data events selected without any cut on the Z_{VTX} position. The uncertainty in this re-weighting was estimated to have negligible effect on the extracted cross-section measurements [122].

7.4.11 Total systematic uncertainty

All of the systematic uncertainties described in this section were added in quadrature to give the total systematic uncertainty on the cross-section measurements, not including the uncertainty on the luminosity or polarisation measurements. Figures 7.29 and 7.30 show the total fractional uncertainty on the single-differential and reduced cross sections for e^+p and e^-p collisions.

The fractional systematic uncertainty on the single-differential cross-section measurements was generally around a few percent and reached up to 15-20% at high

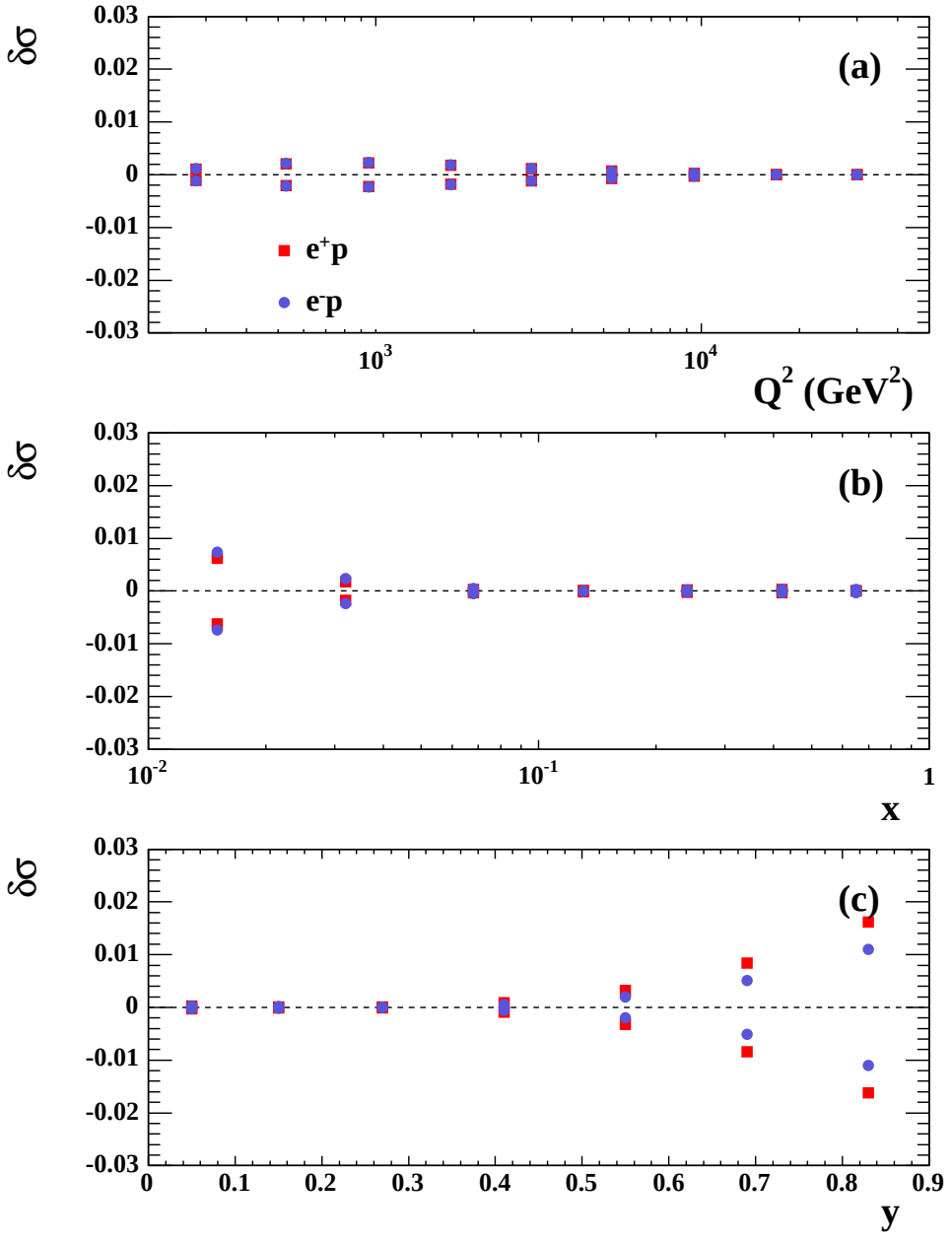

Figure 7.17: The fractional systematic uncertainty on the differential cross-section measurements (a) $d\sigma/dQ^2$, (b) $d\sigma/dx$ and (c) $d\sigma/dy$ from the uncertainty on the $P_{T,miss}$ selection cut efficiency. The red squares (blue circles) indicate the uncertainty on the e^+p (e^-p) cross sections.

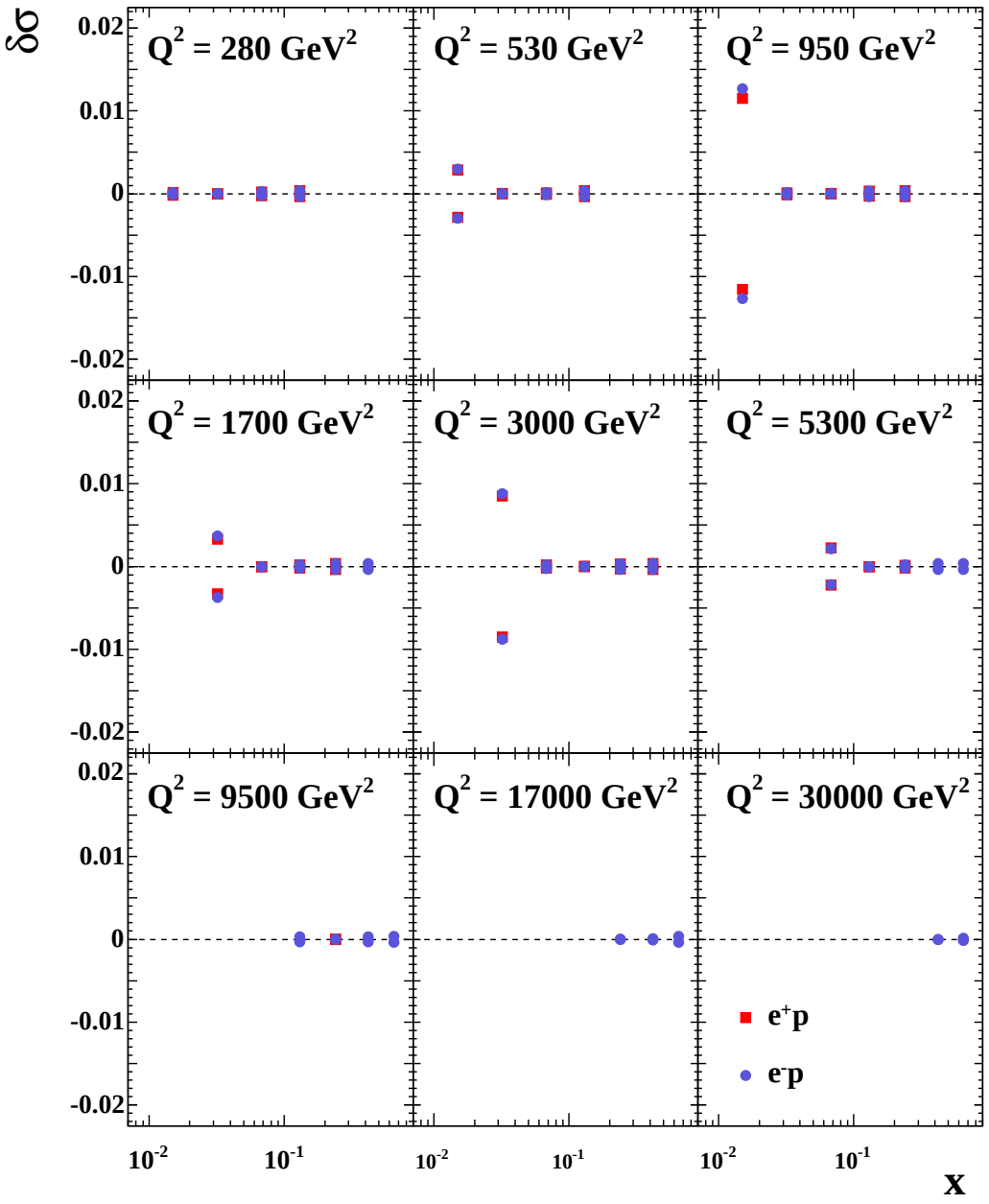

Figure 7.18: The fractional systematic uncertainty on the reduced cross-section measurement in bins of x and Q^2 from the uncertainty on the $P_{T,miss}$ selection cut efficiency. The red squares and blue circles indicate the uncertainty on the e^+p and e^-p cross sections, respectively.

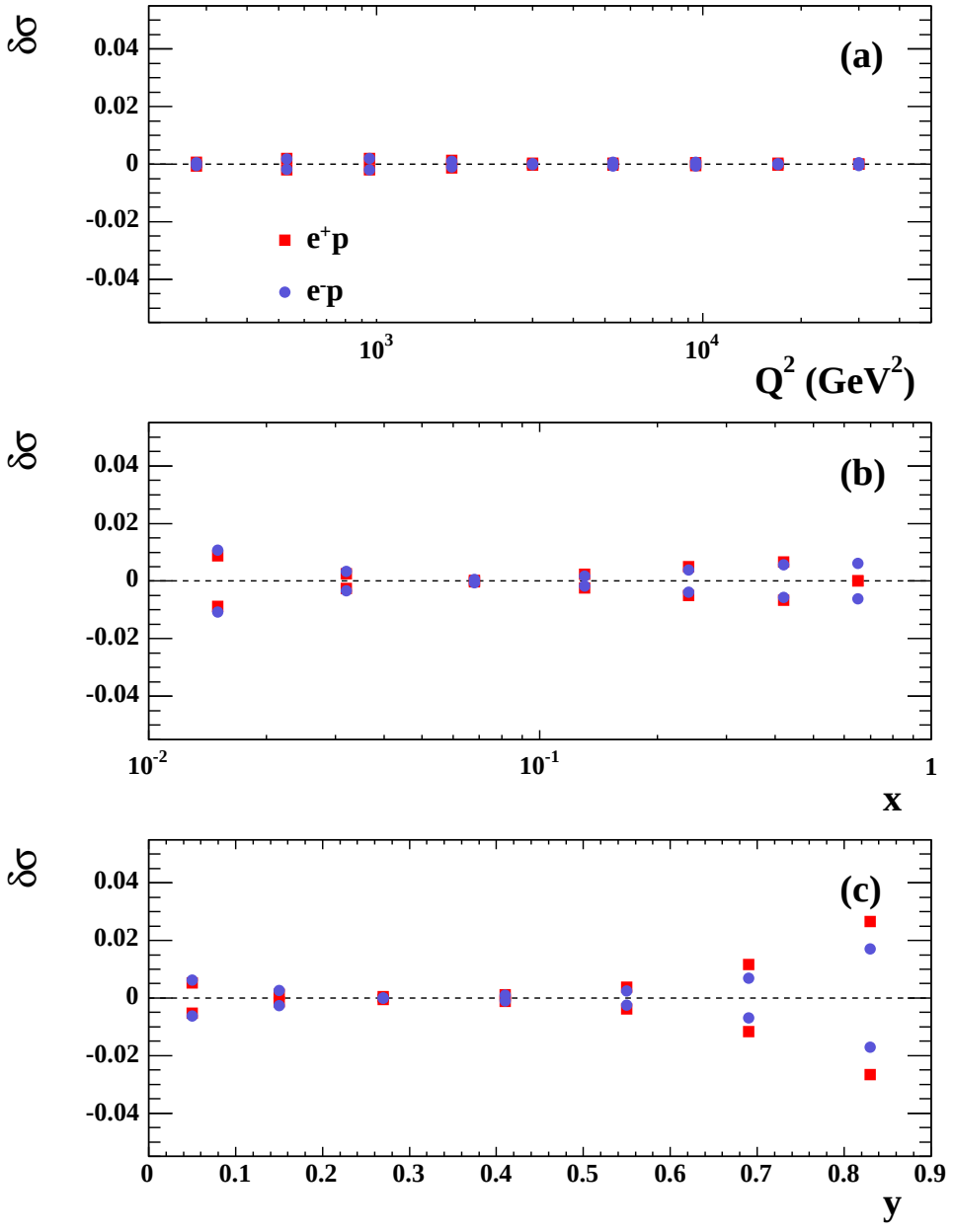

Figure 7.19: The fractional systematic uncertainty on the differential cross-section measurements (a) $d\sigma/dQ^2$, (b) $d\sigma/dx$ and (c) $d\sigma/dy$ from the uncertainty on the $P_{T,miss}$(-IR) selection cut efficiency. The red squares (blue circles) indicate the uncertainty on the e^+p (e^-p) cross sections.

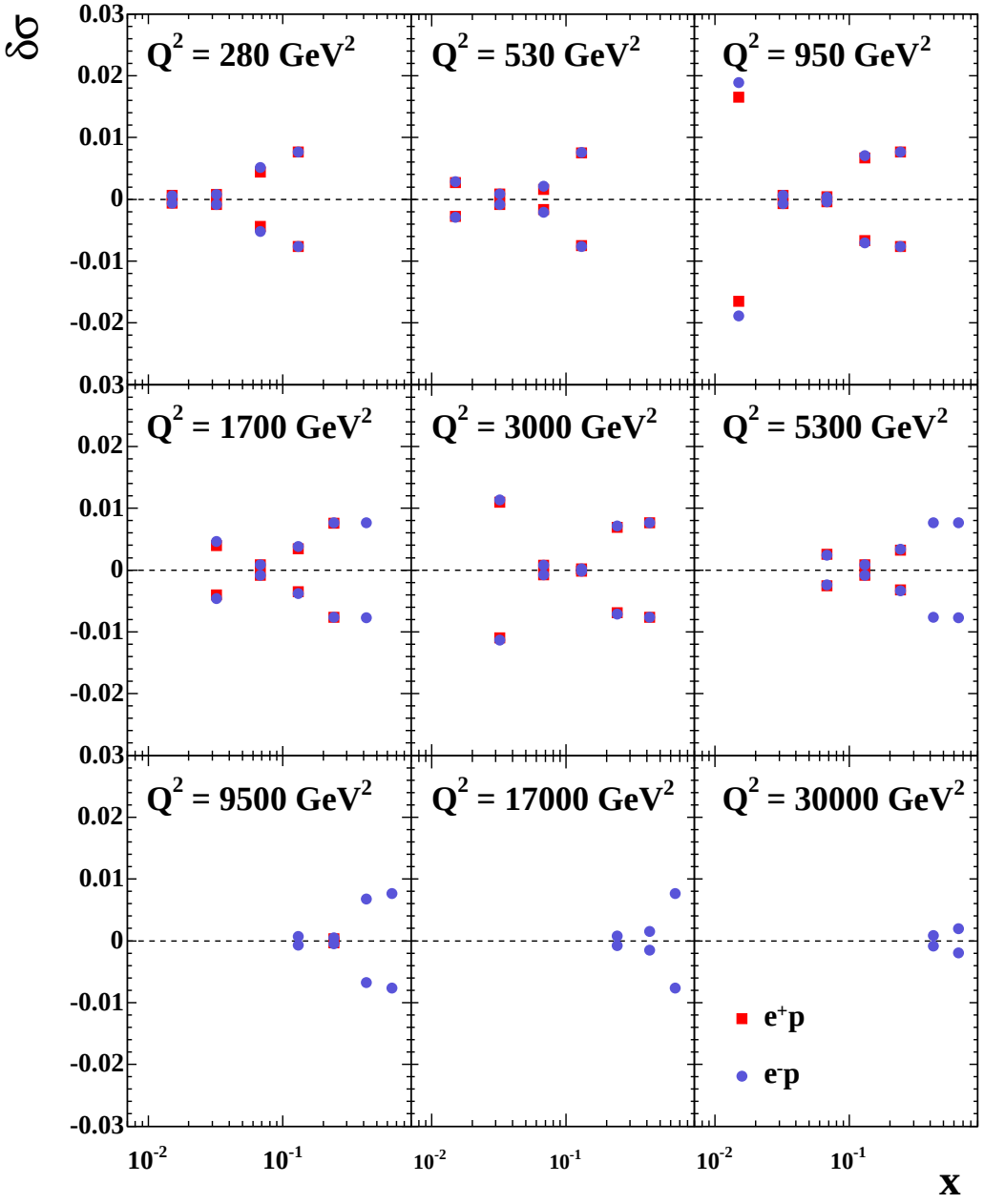

Figure 7.20: The fractional systematic uncertainty on the reduced cross-section measurement in bins of x and Q^2 from the uncertainty on the $P_{T,miss}$(-IR) selection cut efficiency. The red squares and blue circles indicate the uncertainty on the e^+p and e^-p cross sections, respectively.

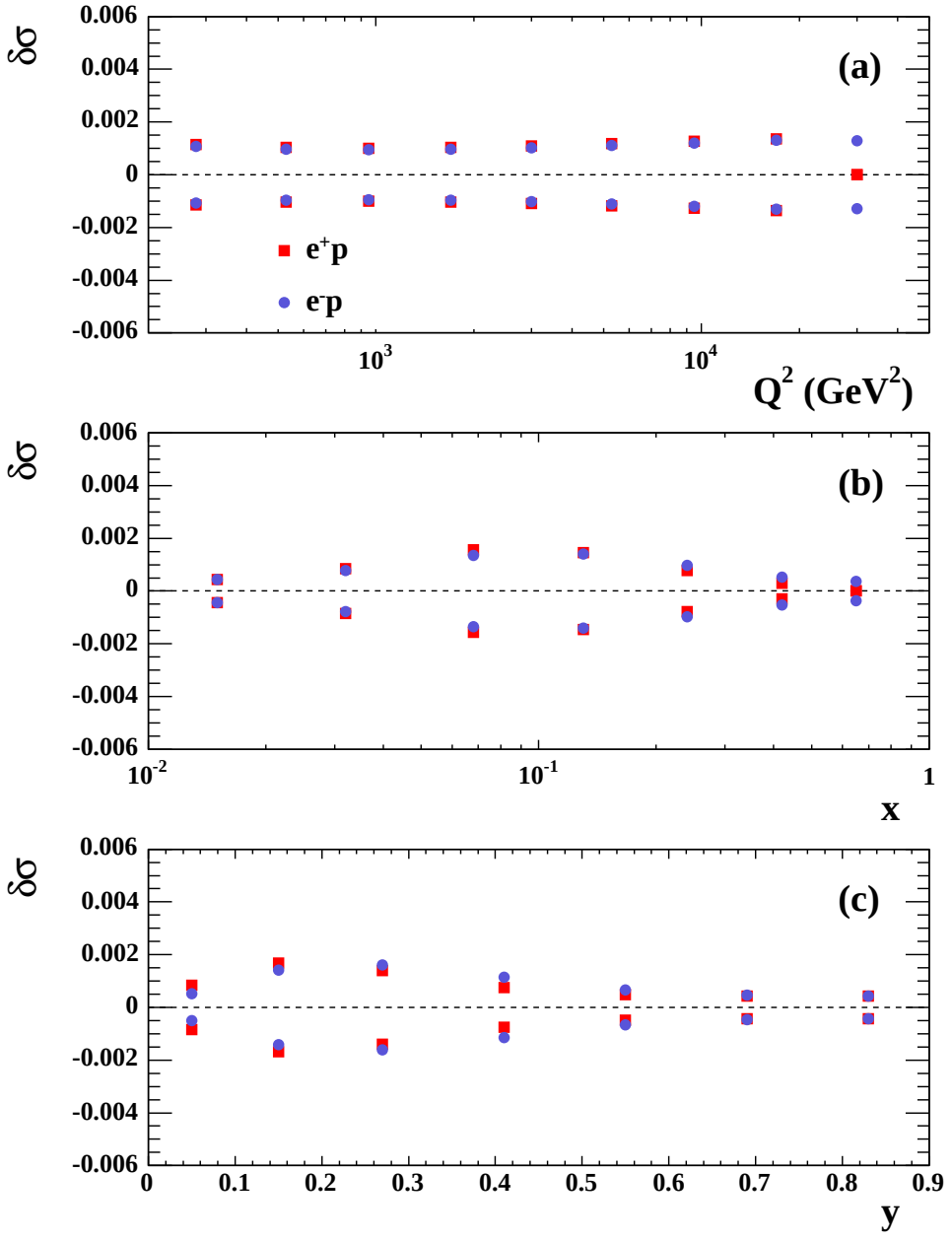

Figure 7.21: The fractional systematic uncertainty on the differential cross-section measurements (a) $d\sigma/dQ^2$, (b) $d\sigma/dx$ and (c) $d\sigma/dy$ from the uncertainty on the $P_{T,miss}$(-2IR) selection cut efficiency. The red squares (blue circles) indicate the uncertainty on the e^+p (e^-p) cross sections.

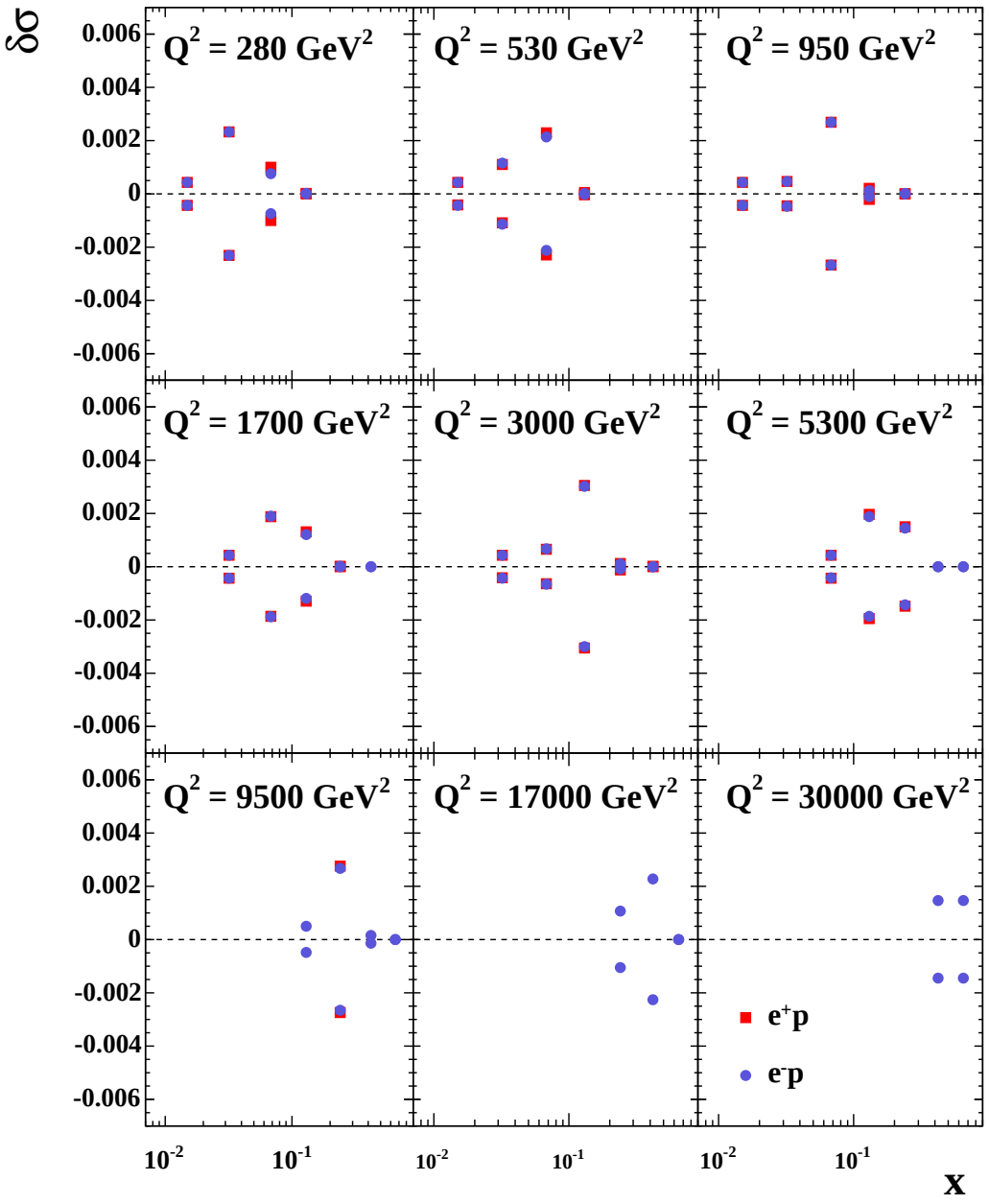

Figure 7.22: The fractional systematic uncertainty on the reduced cross-section measurement in bins of x and Q^2 from the uncertainty on the $P_{T,miss}$(-2IR) selection cut efficiency. The red squares and blue circles indicate the uncertainty on the e^+p and e^-p cross sections, respectively.

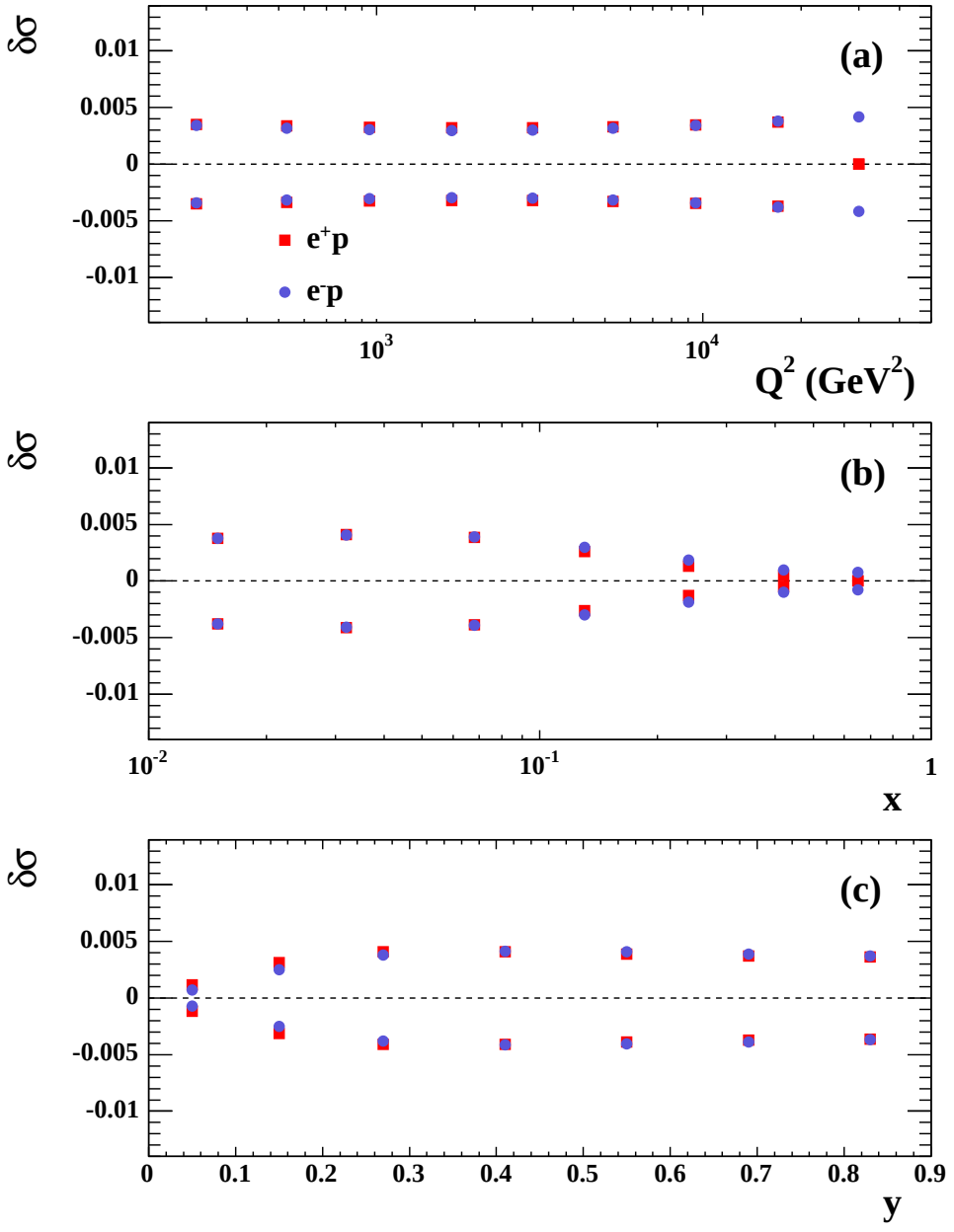

Figure 7.23: The fractional systematic uncertainty on the differential cross-section measurements (a) $d\sigma/dQ^2$, (b) $d\sigma/dx$ and (c) $d\sigma/dy$ from the uncertainty on the Z_{VTX} selection cut efficiency. The red squares (blue circles) indicate the uncertainty on the e^+p (e^-p) cross sections.

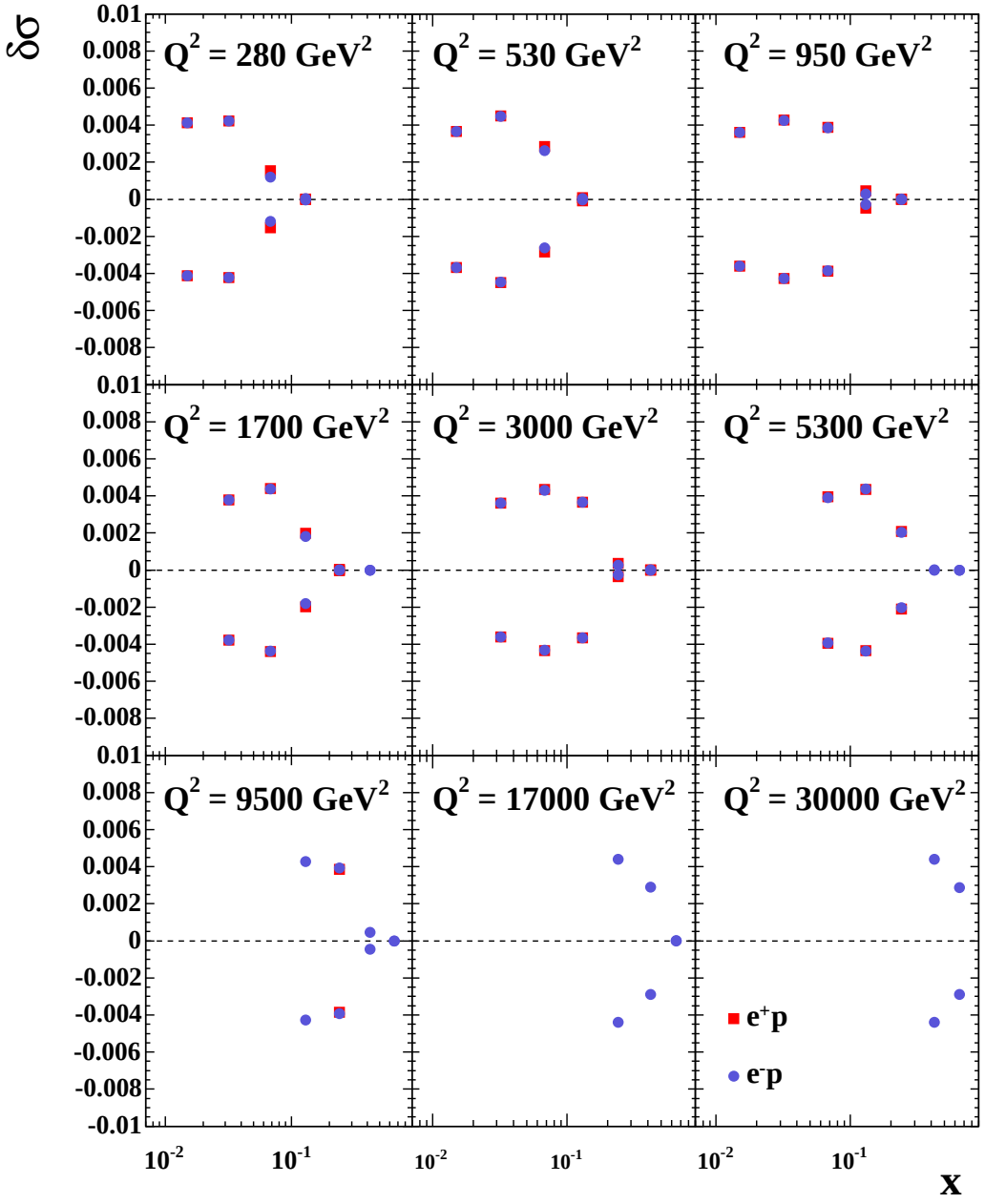

Figure 7.24: The fractional systematic uncertainty on the reduced cross-section measurement in bins of x and Q^2 from the uncertainty on the Z_{VTX} selection cut efficiency. The red squares and blue circles indicate the uncertainty on the e^+p and e^-p cross sections, respectively.

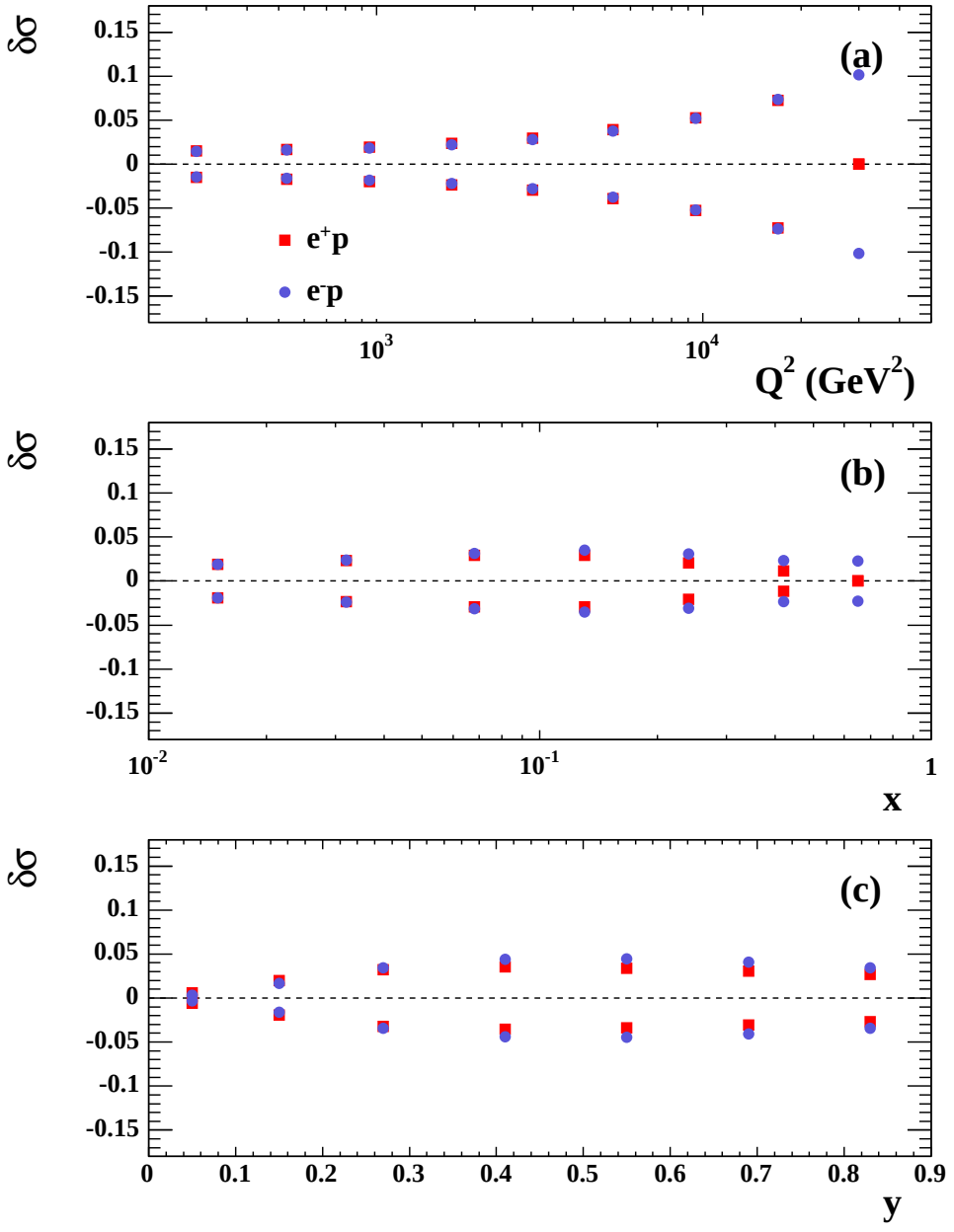

Figure 7.25: The fractional systematic uncertainty on the differential cross-section measurements (a) $d\sigma/dQ^2$, (b) $d\sigma/dx$ and (c) $d\sigma/dy$ from the uncertainty on the tracking selection cut efficiency. The red squares (blue circles) indicate the uncertainty on the e^+p (e^-p) cross sections.

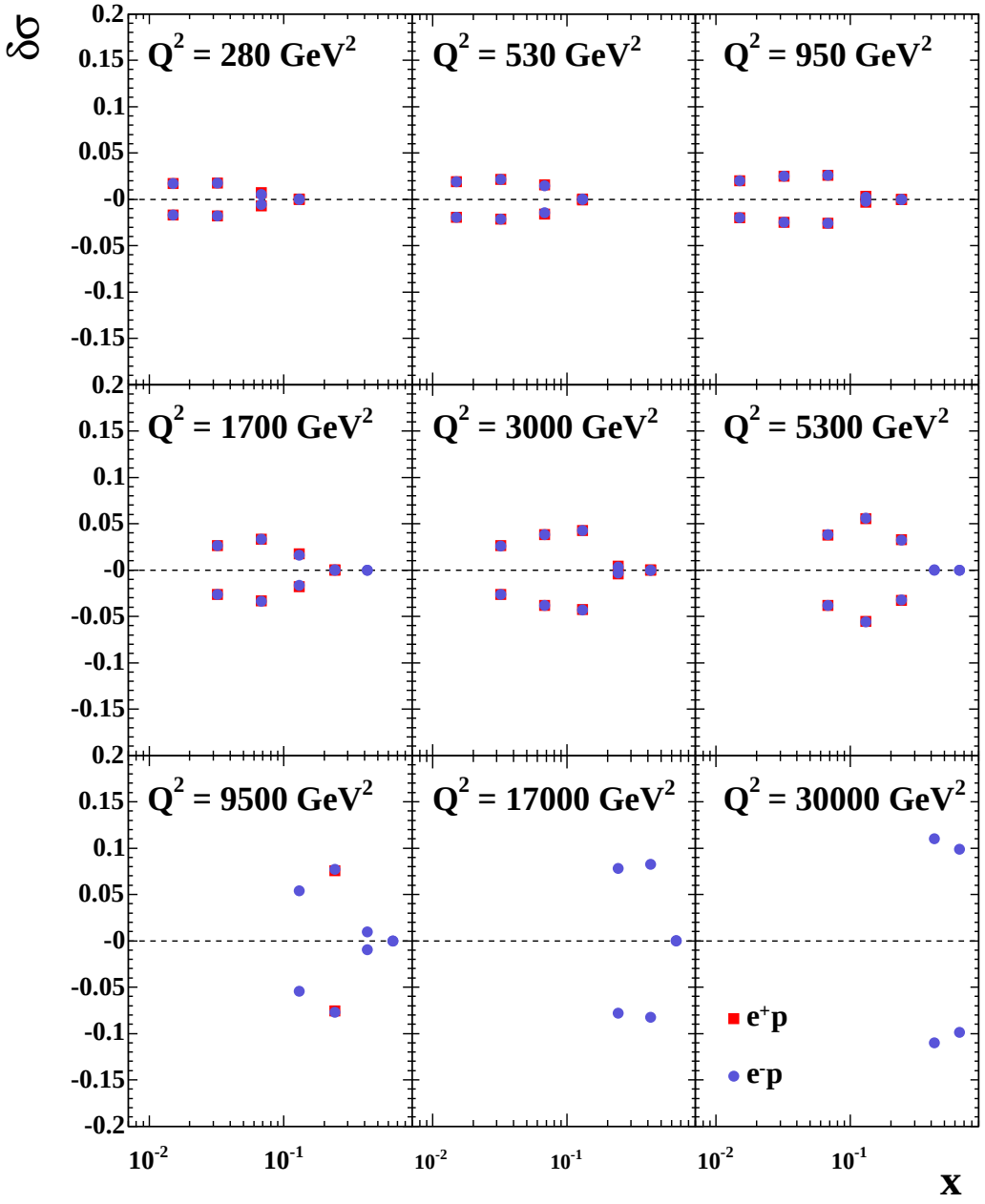

Figure 7.26: The fractional systematic uncertainty on the reduced cross-section measurement in bins of x and Q^2 from the uncertainty on the tracking selection cut efficiency. The red squares and blue circles indicate the uncertainty on the e^+p and e^-p cross sections, respectively.

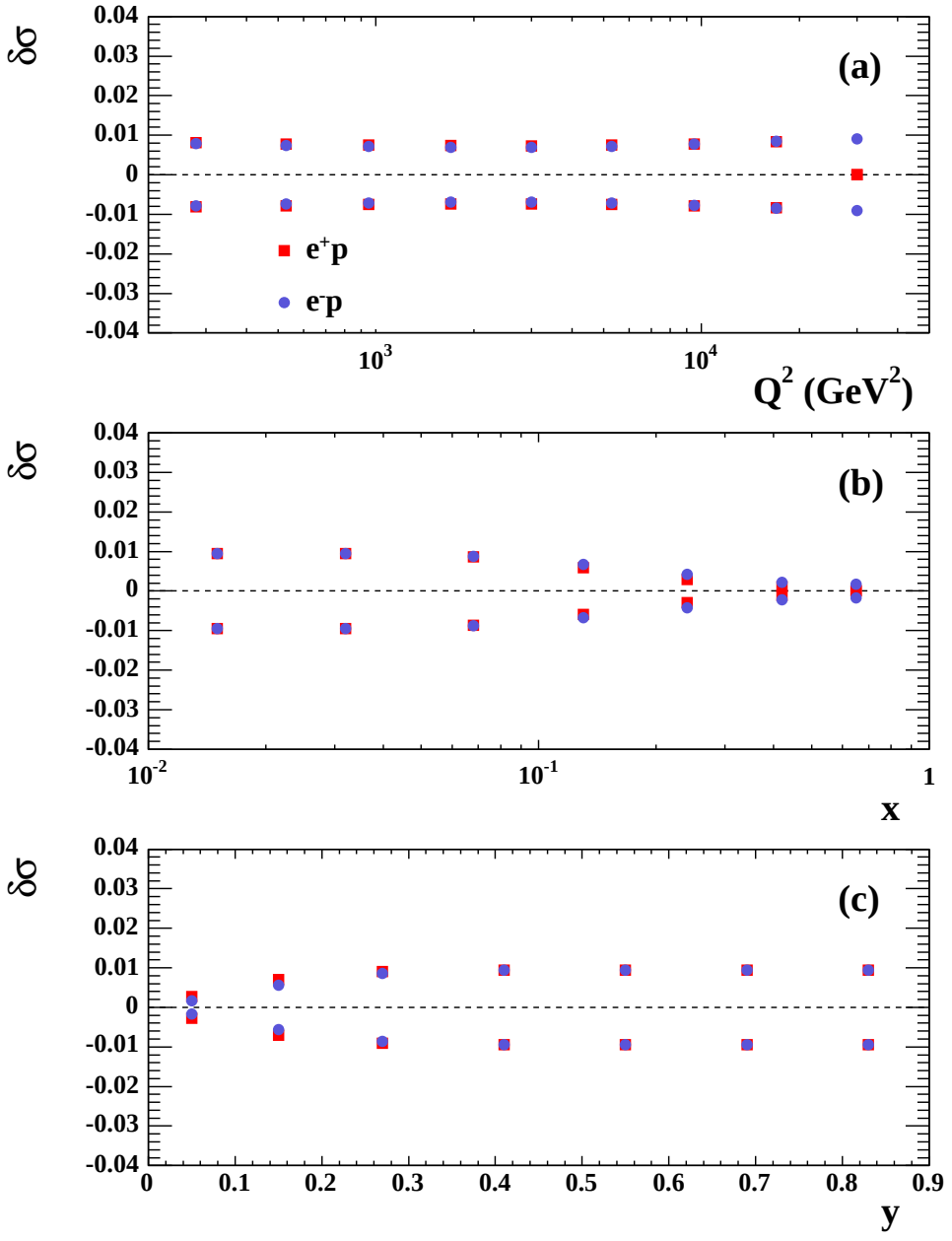

Figure 7.27: The fractional systematic uncertainty on the differential cross-section measurements (a) $d\sigma/dQ^2$, (b) $d\sigma/dx$ and (c) $d\sigma/dy$ from the uncertainty on the $|\Delta\phi|$ selection cut efficiency. The red squares (blue circles) indicate the uncertainty on the e^+p (e^-p) cross sections.

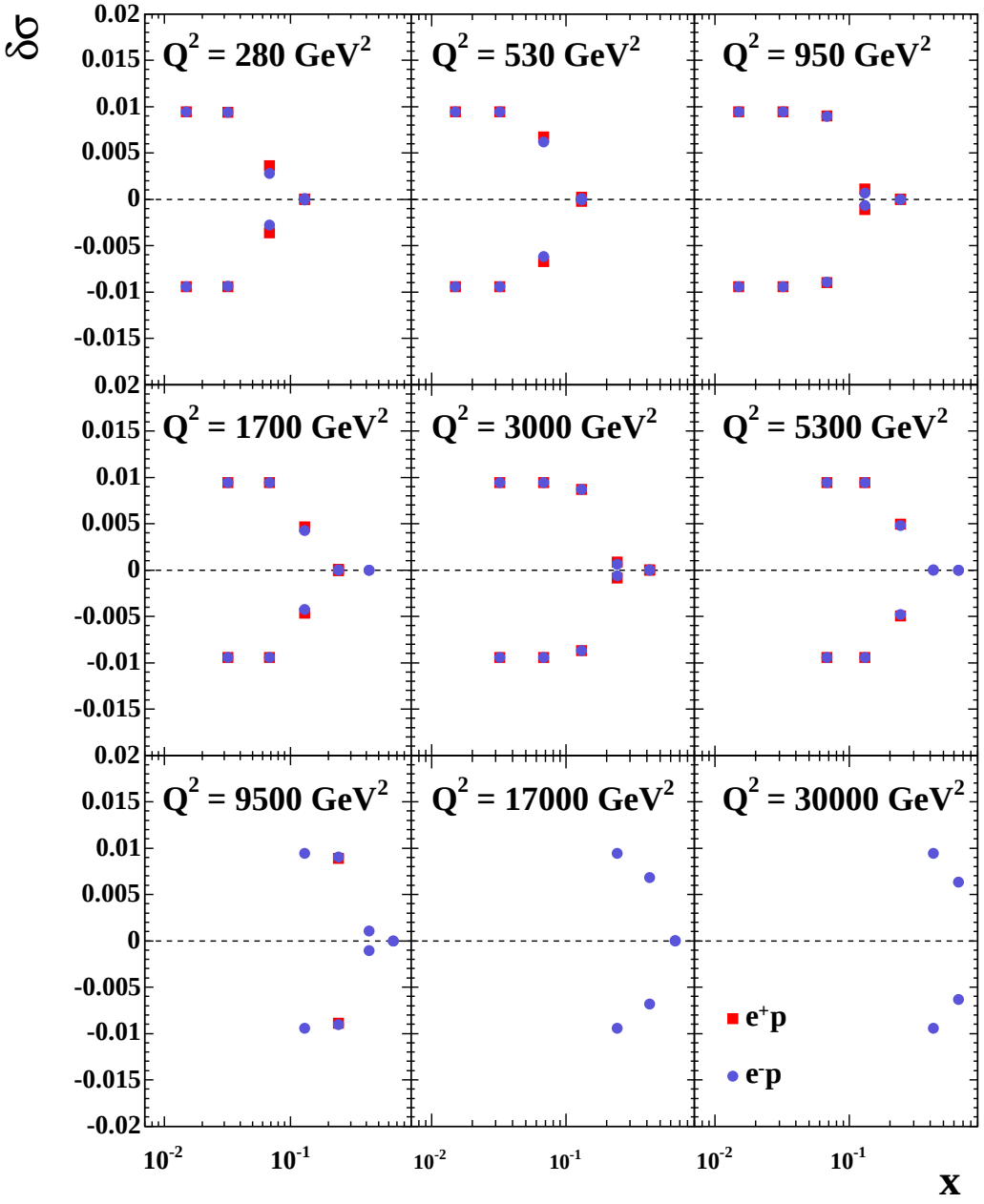

Figure 7.28: The fractional systematic uncertainty on the reduced cross-section measurement in bins of x and Q^2 from the uncertainty on the $|\Delta\phi|$ selection cut efficiency. The red squares and blue circles indicate the uncertainty on the e^+p and e^-p cross sections, respectively.

values of Q^2 and x. The fractional systematic uncertainty on the reduced cross-section measurements reached up to 20-40% at high-Q^2 and high-x.

7.5 Single-differential cross sections

The measurements of the single-differential cross-sections $d\sigma/dQ^2$, $d\sigma/dx$ and $d\sigma/dy$ for e^+p and e^-p collisions with positive and negative values of P_e are presented in Figure 7.31 and compared to the SM predictions evaluated using the ZEUS-JETS and CTEQ6D PDFs. The error bars do not include the uncertainty from the luminosity or polarisation measurements, which would simply cause a scaling up or down of all the points. The values of the single-differential cross-section measurements are listed in Tables A.1 to A.6.

Figure 7.32 shows the fractional difference between the single-differential cross-section measurements and the SM predictions, evaluated with the ZEUS-JETS PDFs. Generally a good agreement is seen with the SM prediction, although the measured cross-section $d\sigma/dy$ is not so well-described by the theory in the mid-y region, with both the e^+p and e^-p measurements tending to lie slightly below the SM expectation. The expected dependence on P_e is observed across the whole kinematic range.

7.6 Total cross sections

The total cross-section measurements for CC DIS with $Q^2 > 200$ GeV^2 with statistical and systematic uncertainties are listed in Table 7.6. The uncertainty on P_e is given, but the uncertainty on the luminosity measurement is not included in the systematic uncertainty.

These measurements are presented in Figure 7.33 and compared to the SM predictions evaluated with ZEUS-JETS and CTEQ6D PDFs. The uncertainty on the polarisation measurement is shown by the horizontal error bar, which is too small to be visible. The measurements agree with both predictions within ex-

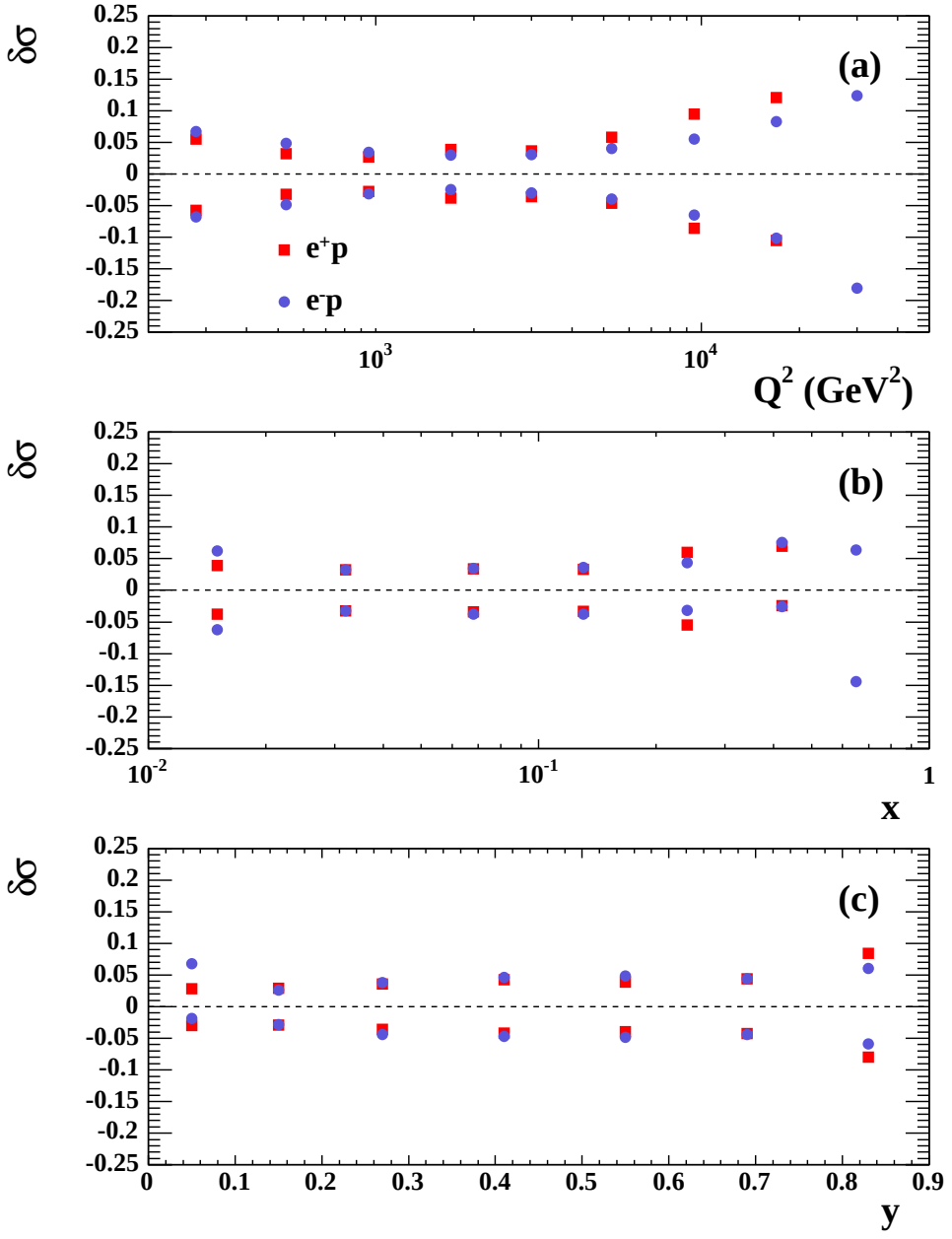

Figure 7.29: The total fractional systematic uncertainty on the differential cross-section measurements (a) $d\sigma/dQ^2$, (b) $d\sigma/dx$ and (c) $d\sigma/dy$. The red squares (blue circles) indicate the uncertainty on the e^+p (e^-p) cross sections.

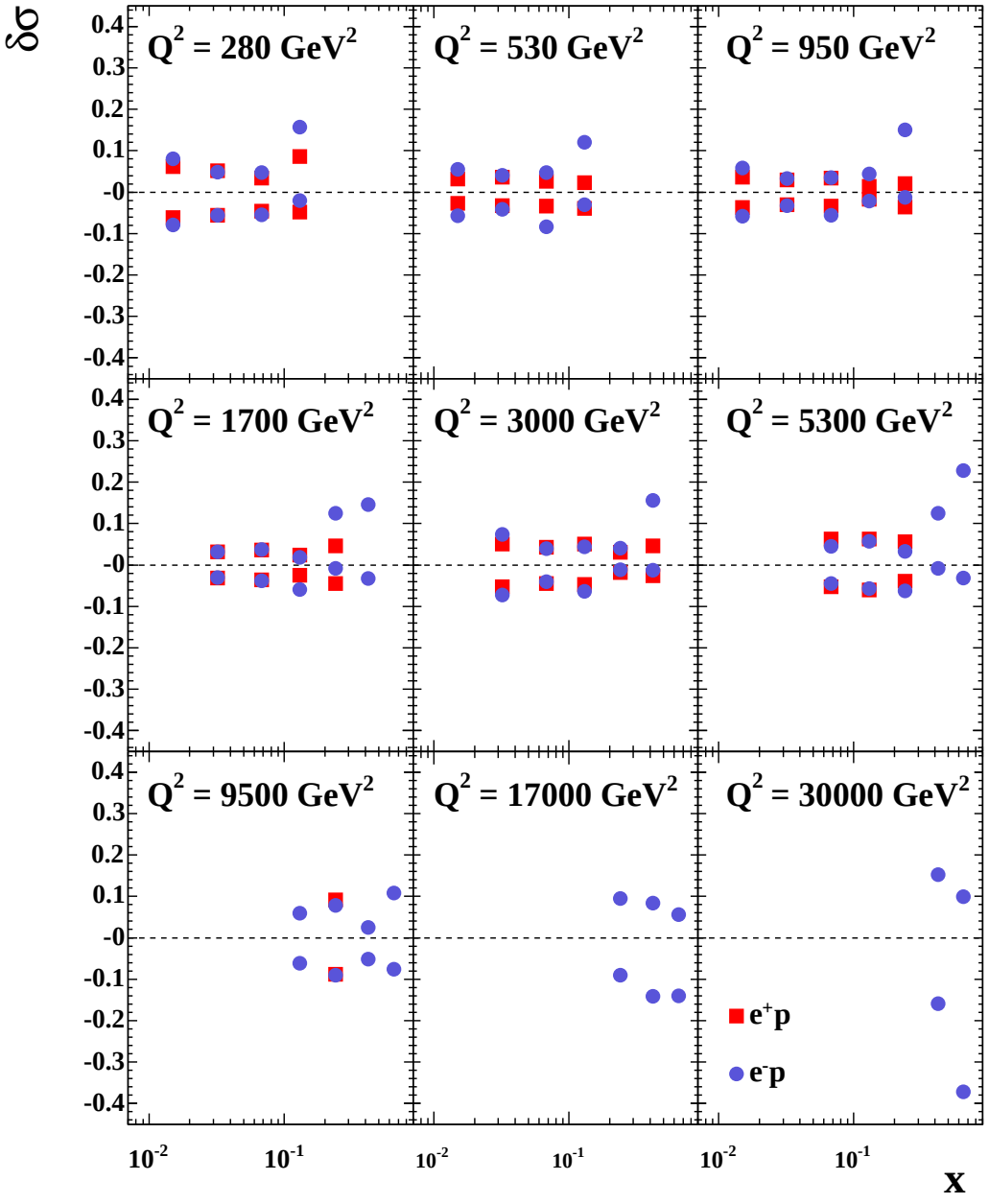

Figure 7.30: The total fractional systematic uncertainty on the reduced cross-section measurements in bins of x and Q^2. The red squares (blue circles) indicate the uncertainty on the e^+p (e^-p) cross sections.

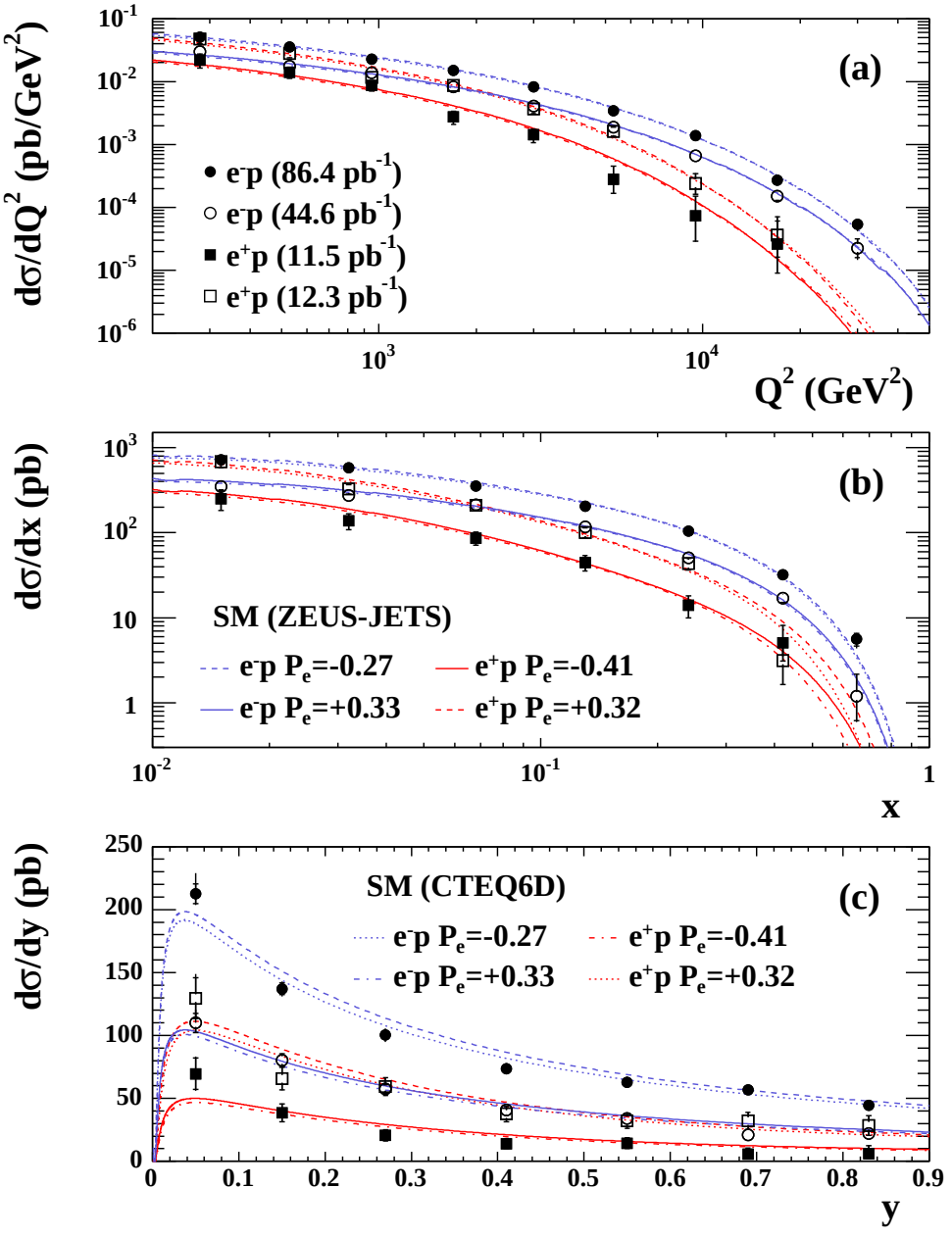

Figure 7.31: Measurements of the single-differential cross sections for CC DIS (a) $d\sigma/dQ^2$, (b) $d\sigma/dx$ and (c) $d\sigma/dy$. The squares indicate measurements of e^+p cross sections and the circles show e^-p cross sections. Open and filled points represent negative and positive values of P_e, respectively. The inner error bars show the statistical uncertainty and the outer error bars show the statistical and systematic uncertainties added in quadrature. The measurements are compared to the SM predictions evaluated with the ZEUS-JETS and CTEQ6D PDFs, which are illustrated by curves for e^+p and e^-p collisions. The full, dashed, dotted and dashed-dotted lines represent different values of longitudinal lepton beam polarisations and different PDFs, as indicated in the figure.

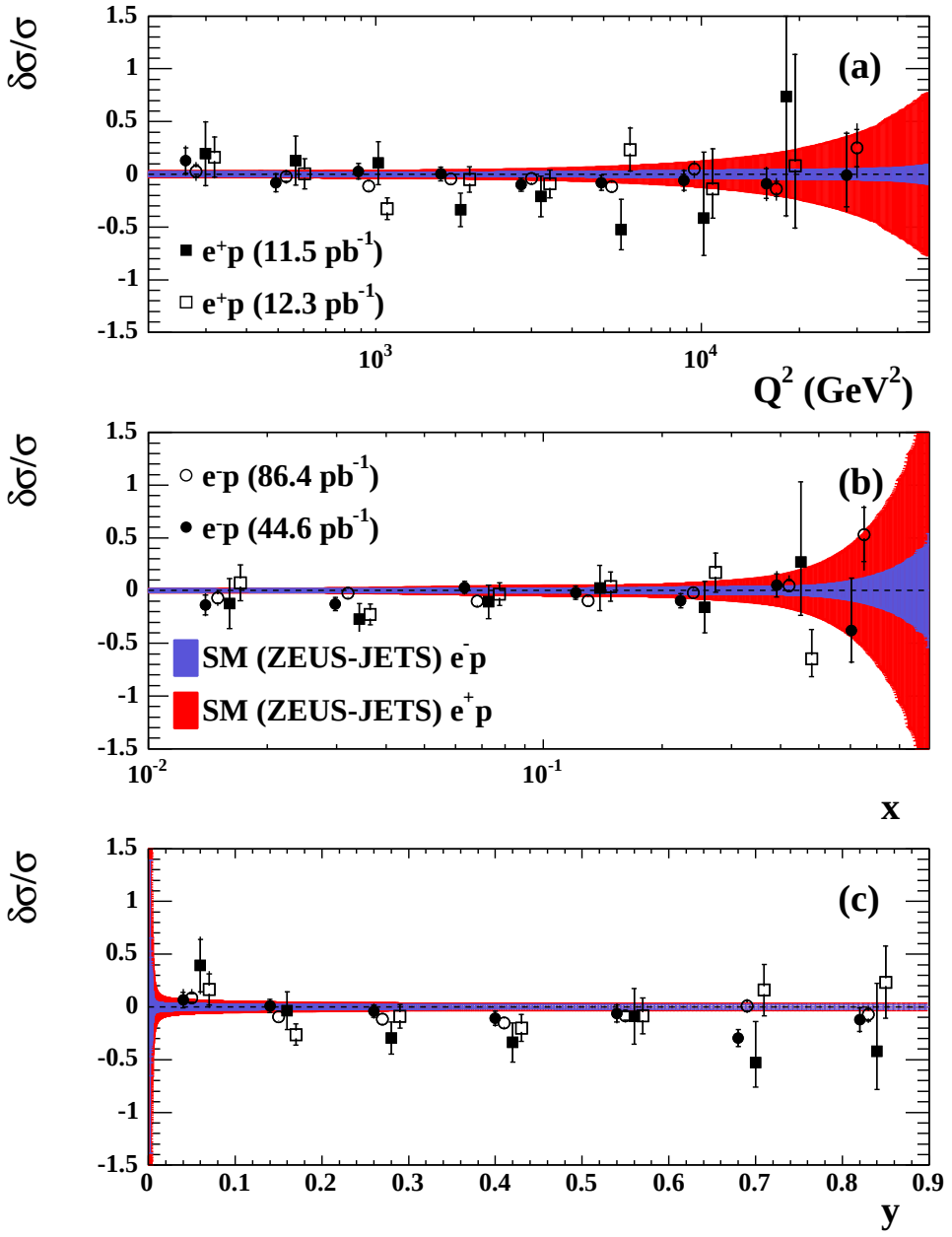

Figure 7.32: The fractional difference between the measurements of the single-differential cross sections for CC DIS, (a) $d\sigma/dQ^2$, (b) $d\sigma/dx$ and (c) $d\sigma/dy$, and the theoretical prediction evaluated with the ZEUS-JETS PDFs. The shaded bands represent the uncertainty on the SM prediction from the ZEUS-JETS PDFs. The squares are the measurements of the e^+p cross sections and the circles are the e^-p cross sections. Open and filled points represent negative and positive values of P_e, respectively. The inner error bars show the statistical uncertainty and the outer error bars show the statistical and systematic uncertainties added in quadrature.

	P_e	σ (pb)	δ_{stat} (pb)	δ_{sys} (pb)
e^+p	-0.41±0.01	19.2	±1.8	±0.6
	+0.32±0.01	44.8	±2.6	±1.4
e^-p	-0.27±0.01	83.2	±1.3	±2.6
	+0.33±0.02	44.5	±1.3	±1.4

Table 7.6: The total cross section measurements for CC DIS with $Q^2 > 200$ GeV^2 with statistical and systematic uncertainties for e^+p and e^-p collisions with positive and negative values of P_e.

perimental and theoretical uncertainties, although a slightly better agreement is observed with the CTEQ6D predictions.

The H1 Collaboration have also measured cross sections for CC DIS in e^+p and e^-p collisions with longitudinally polarised lepton beams [43, 123]. The total cross sections were measured in the kinematic range $Q^2 > 400$ GeV^2 and $y < 0.9$. In order to compare the results in this thesis with the H1 results, the following conversion factors, $\mathcal{C}$, were calculated using CTEQ5D PDFs [95] and applied to the total cross-section measurements:

$$\mathcal{C} = \frac{\sigma^{\text{CC}}(Q^2 > 400 \text{ GeV}^2, y < 0.9)}{\sigma^{\text{CC}}(Q^2 > 200 \text{ GeV}^2)} = \begin{cases} 0.791 & \text{for } e^+p \text{ collisions and} \\ 0.841 & \text{for } e^-p \text{ collisions.} \end{cases}$$

Figure 7.34 shows the converted cross sections compared with the H1 measurements and SM predictions. A good agreement is seen with the H1 measurements for the e^+p and e^-p CC total cross sections with both positive and negative values of P_e.

7.7 Right-handed charged current

A linear fit was performed to the CC DIS total cross-section measurements as a function of P_e and extrapolated to $P_e = \pm 1$ to extract values of the cross sections for right-handed CC interactions in e^-p and e^+p collisions. From these values, upper limits on the cross sections were set, which were then converted into lower limits on the mass of a W_R boson.

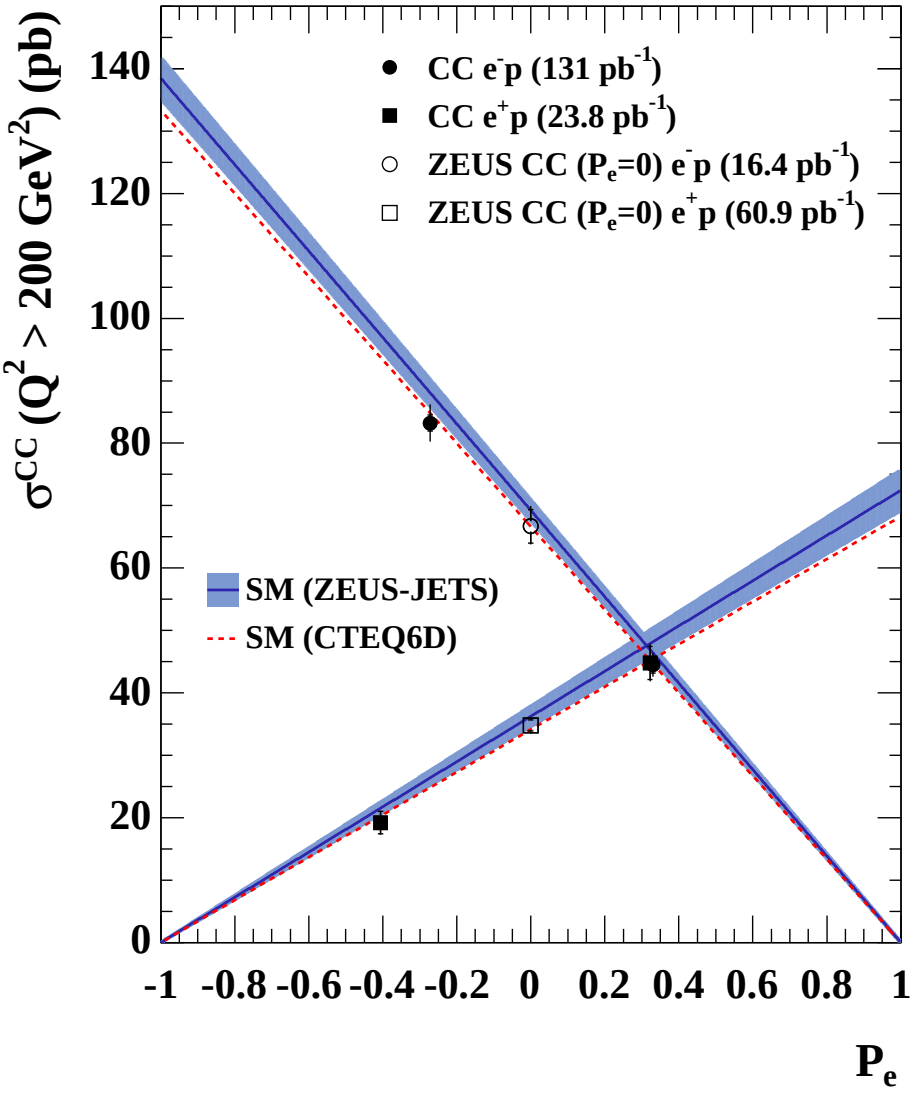

Figure 7.33: Total CC DIS cross sections for $Q^2 > 200$ GeV^2 for e^-p (full circular points) and e^+p (full square points) collisions with positively and negatively longitudinally polarised lepton beams. The inner bars show the statistical uncertainty and the outer bars show the statistical and systematic uncertainties added in quadrature. The open points show previous ZEUS measurements with HERA-I data at $P_e = 0$ for e^-p (circles) and e^+p (squares) collisions. The red dashed line is the SM prediction evaluated with the CTEQ6D PDFs. The solid blue line is the SM prediction evaluated with ZEUS-JETS PDFs and the pale blue band shows the uncertainty from the PDF on this prediction.

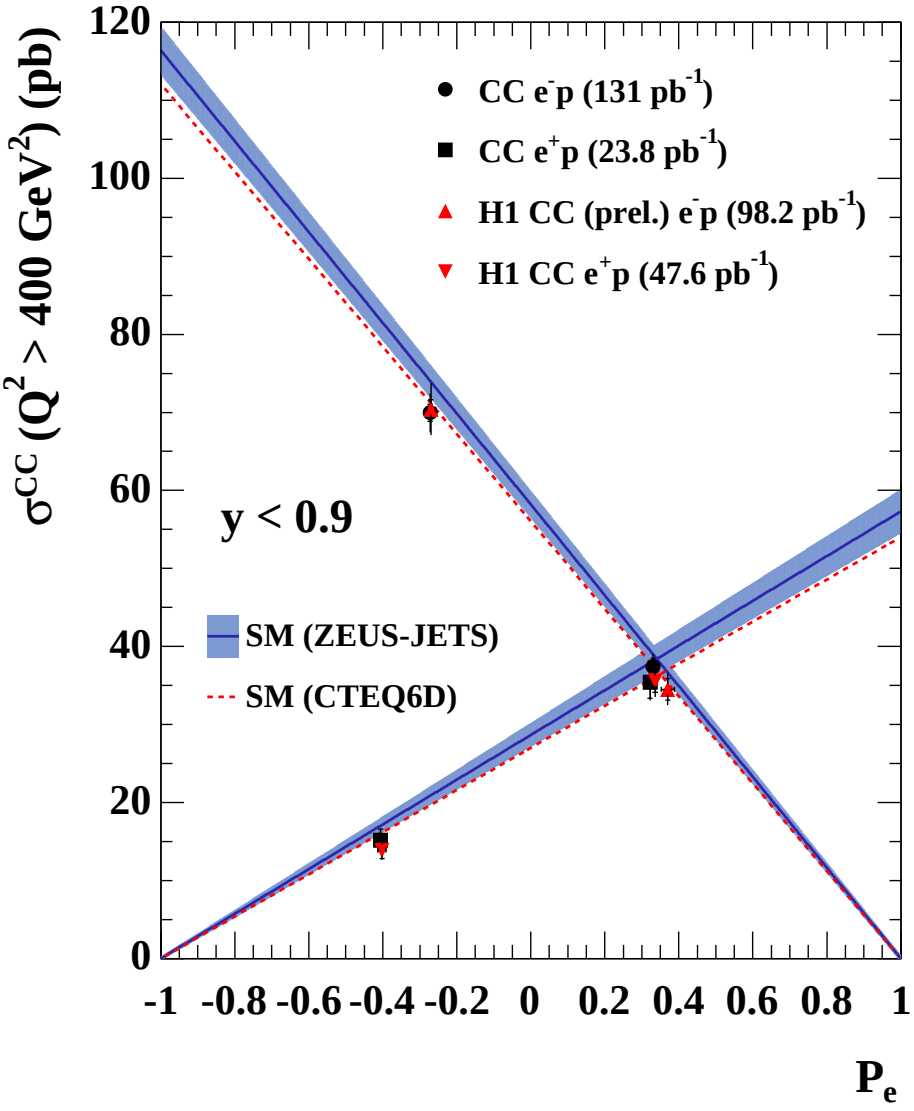

Figure 7.34: Total CC DIS cross sections for $Q^2 > 400$ GeV^2 and $y < 0.9$ for e^-p (full circular points) and e^+p (full square points) collisions with positively and negatively longitudinally polarised lepton beams. The inner bars show the statistical uncertainty and the outer bars show the statistical and systematic uncertainties added in quadrature. The red triangles show measurements made by the H1 Collaboration for e^-p and e^+p collisions. The red dashed line is the SM prediction evaluated with the CTEQ6D PDFs. The solid blue line is the SM prediction evaluated with the ZEUS-JETS PDFs and the pale blue band shows the uncertainty from the PDF on this prediction.

7.7.1 Right-handed CC cross sections

Upper limits on the cross sections for right-handed CC interactions in e^+p and e^-p collisions were extracted separately. First, the three measurements (at $P_e < 0$, $P_e = 0$ and $P_e > 0$), with their statistical uncertainties, were fitted as a function of P_e using the following function:

$$\sigma^{\mathrm{CC}}(e^{\pm}p) = m(P_e \pm 1) + c, \tag{7.13}$$

where m and c were allowed to vary.

This parametrisation was chosen since the cross section for right-handed CC interactions in $e^{\pm}p$ collisions, which is the value of the fitted cross section extrapolated to $P_e = \mp 1$, was then simply given as follows:

$$\sigma^{\mathrm{CC}}_{\mathrm{RH}}(e^{\pm}p) = c. \tag{7.14}$$

From this fit, the central values of m and c were estimated with their statistical uncertainties, δm and δc, and the covariance, cov_{cm}, between the two parameters.

The measured points were then shifted by the various systematic uncertainties and the fit was re-performed after each shift. Points were shifted together if the systematic uncertainty was judged to be correlated or anti-correlated between the points. Table 7.7 lists the uncertainties by which the measurements were shifted and any correlation between the points.

The differences between the original fit and the fits to the shifted points were added in quadrature to estimate the total systematic uncertainty on the fit, $\delta_{\mathrm{sys}}(P_e)$.

The total uncertainty on the fit, $\delta\sigma(e^{\pm}p)(P_e)$, was then estimated using the following expression:

$$\delta\sigma(e^{\pm}p)(P_e) = \sqrt{\delta m^2(P_e \pm 1)^2 + \delta c^2 + 2(P_e \pm 1)\mathrm{cov}_{cm} + \delta_{\mathrm{sys}}(P_e)^2}, \tag{7.15}$$

which, at $P_e = \mp 1$, simplified to the following expression:

$$\delta\sigma(e^{\pm}p)(P_e = \mp 1) = \delta\sigma^{\mathrm{CC}}_{\mathrm{RH}}(e^{\pm}p) = \sqrt{\delta c^2 + \delta_{\mathrm{sys}}(P_e = \mp 1)^2}. \tag{7.16}$$

Uncertainty	**Applied to**	**Correlation**
Luminosity	$P_e = 0$	-
Total systematic	$P_e = 0$	-
P_e	$P_e \neq 0$	Anti-correlated
Luminosity	$P_e \neq 0$	Correlated
Hadronisation model	$P_e \neq 0$	Correlated
F_L	$P_e \neq 0$	Correlated
PDF	$P_e \neq 0$	Correlated
PHP normalisation	$P_e \neq 0$	Correlated
Energy scale	$P_e \neq 0$	Correlated
Trigger efficiency	$P_e \neq 0$	Correlated
$P_{T,miss}$ efficiency	$P_e \neq 0$	Correlated
$P_{T,miss}$(-IR) efficiency	$P_e \neq 0$	Correlated
$P_{T,miss}$(-2IR) efficiency	$P_e \neq 0$	Correlated
Vertex efficiency	$P_e \neq 0$	Correlated
Tracking efficiency	$P_e \neq 0$	Correlated
$\|\Delta\phi\|$ efficiency	$P_e \neq 0$	Correlated
Track veto	$P_e \neq 0$	Correlated

Table 7.7: The systematic shifts applied to the CC total cross sections and the correlation between the points.

Figure 7.35 shows the fits to the measured e^+p and e^-p points with bands illustrating the total uncertainty on the fits.

Extrapolating the fits to $P_e = \mp 1$ gave the following values of the cross sections for right-handed CC interactions in e^+p and e^-p DIS with $Q^2 > 200$ GeV^2:

$$\sigma^{\mathrm{CC}}_{\mathrm{RH}}(e^+p) = -1.8 \pm 4.1 \text{ (stat.)} \, ^{+1.1}_{-1.4} \text{ (sys.) pb.}$$

$$\sigma^{\mathrm{CC}}_{\mathrm{RH}}(e^-p) = 1.6 \pm 3.9 \text{ (stat.)} \, ^{+3.1}_{-3.4} \text{ (sys.) pb.}$$

The systematic uncertainties quoted include the uncertainty from the luminosity and polarisation measurements. The dominant contribution to the systematic uncertainty came from the uncertainty on P_e. This contributed $^{+0.9}_{-1.0}$ pb and $^{+3.1}_{-3.4}$ pb to the e^+p and e^-p systematic uncertainties, respectively. In comparison, the contribution from the other systematic uncertainties was almost negligible, especially in the e^-p case. Both cross sections are consistent, within uncertainties, with the SM prediction of zero.

Upper limits were set on the right-handed cross sections by assuming Gaussian

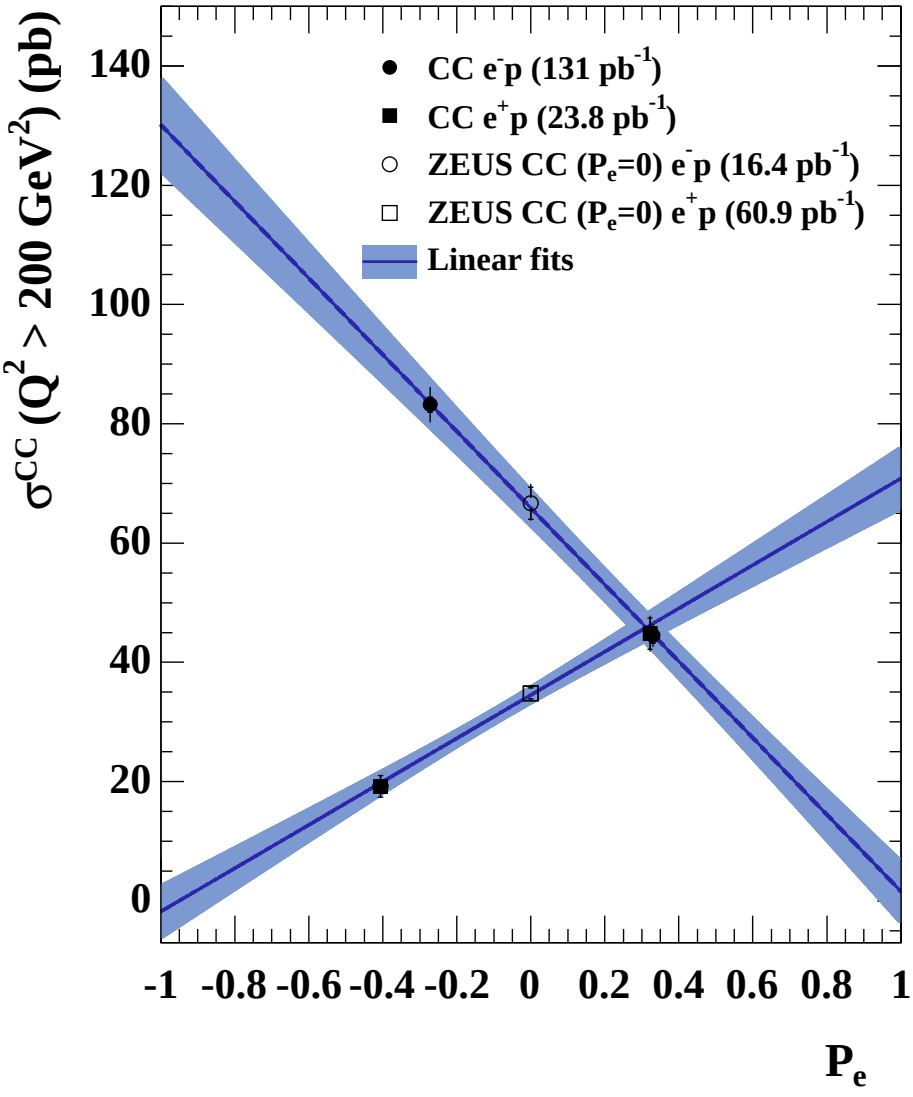

Figure 7.35: The linear fits to the e^+p and e^-p total cross-section measurements. The dark blue lines show the results of the fits and the light blue bands show the combined statistical and systematic uncertainties on the fits. The points are the measurements and the inner bars show the statistical uncertainty and the outer bars show the combined statistical and systematic uncertainty.

errors with a width, $\delta_{\rm tot}$, given by the statistical and mean systematic uncertainties combined in quadrature. The mean systematic uncertainty was defined as $(\delta^+_{\rm sys} + \delta^-_{\rm sys})/2$. The 95% confidence level upper limits were then calculated using the following expression:

$$\sigma^{\rm CC}_{\rm RH} < c + 1.645 \cdot \delta_{\rm tot} \ \text{ at 95\% C.L.}, \tag{7.17}$$

which gave the following upper limits on the cross sections for right-handed CC interactions in e^+p and e^-p DIS with $Q^2 > 200$ GeV^2:

$$\sigma^{\rm CC}_{\rm RH}(e^+p) < 5.2 \text{ pb at 95\% C.L.}$$

$$\sigma^{\rm CC}_{\rm RH}(e^-p) < 10.0 \text{ pb at 95\% C.L.}$$

7.7.2 The mass of the W_R boson

The cross-section calculation program HECTOR [124] was used to calculate the cross section for right-handed CC interactions in e^+p and e^-p DIS, as a function of the mass of the W_R boson, M_{W_R}. In making this calculation, the following two assumptions were made:

- The coupling strength is the same as in SM CC interactions.
- The propagator dependence on M_{W_R} is the same as the dependence on M_W in SM CC interactions.

Using this calculation, the upper limits on the cross sections for right-handed CC interactions from the separate e^+p and e^-p fits were converted into lower limits on M_{W_R}, as illustrated in Figure 7.36.

The limit set on M_{W_R} from e^+p CC DIS was:

$$M_{W_R} > 170 \text{ GeV at 95\% C.L.}$$

and from e^-p CC DIS was:

$$M_{W_R} > 180 \text{ GeV at 95\% C.L.}$$

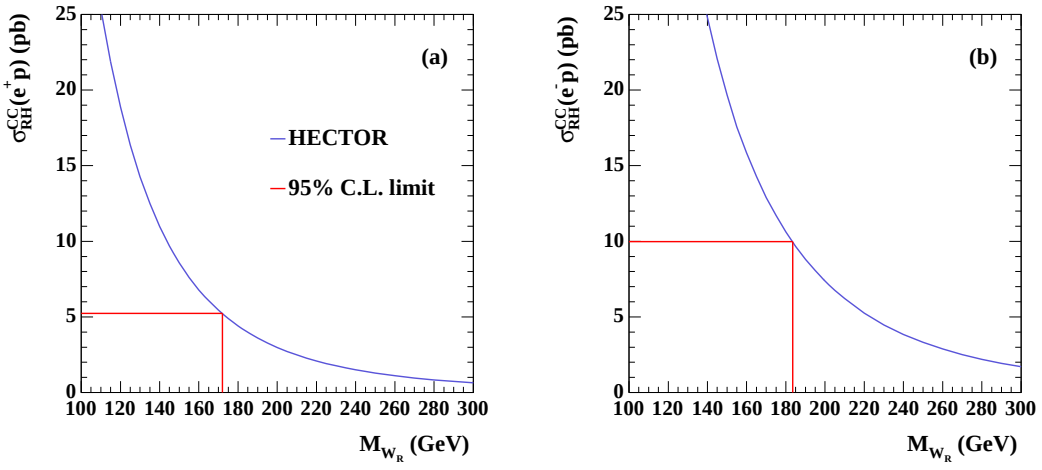

Figure 7.36: The 95% confidence level upper limits on the total cross section for right-handed CC interactions in (a) e^+p and (b) e^-p DIS with $Q^2 > 200$ GeV^2 and the corresponding lower limits on M_{W_R}, calculated using the program HECTOR.

As discussed in Chapter 2, various other experiments have set limits on the mass of a W_R boson. However, as these limits depend on factors such as the mass of the right-handed neutrinos, the mixing matrix for right-handed quarks, the right-handed coupling constant and whether the right-handed neutrino is Dirac or Majorana, they are not directly comparable with the limits obtained above.

The UA2 experiment at CERN [45] performed a direct search for the W_R boson and placed a lower limit on its mass, M_{W_R} at 261 GeV, which is valid for any mass of the right-handed neutrino. If the mass of the right-handed neutrino is assumed to be much less than M_{W_R}, then the lower limit on M_{W_R} increased to 652 GeV. The lower limit on M_{W_R} set by the DØ experiment [46] is at 720 GeV, in the case that the mass of the right-handed neutrino is much less than M_{W_R}. In the case that the mass of the right-handed neutrino is less than $\frac{1}{2}M_{W_R}$, then the lower limit on M_{W_R} falls to 650 GeV. The CDF experiment [47] has set a lower limit on M_{W_R} at 652 GeV, assuming that the right-handed neutrino is stable and has a mass much less than M_{W_R}.

7.8 Reduced cross sections

The reduced cross sections for CC DIS were calculated from the whole e^+p and e^-p data samples, with P_e corrected to $P_e = 0$ by the factor $1/(1 \pm P_e)$. Measurements of the reduced cross sections are shown in Figures 7.37 and 7.38 and compared with the SM predictions evaluated with the CTEQ6D and ZEUS-JETS PDFs. The uncertainties from the luminosity and polarisation measurements are not included in the error bars. The PDF contributions, separated out into the quark and anti-quark contributions, are also shown in the figures. The values of the cross-section measurements are given in Tables A.7 and A.8.

In the case of the e^+p cross sections, the results are seen to agree well with the SM prediction evaluated with both the CTEQ6D and ZEUS-JETS PDFs. The e^-p measured cross sections in the mid-x and mid-Q^2 region tend to lie slightly beneath the the SM predictions using the ZEUS-JETS PDFs, although slightly better agreement is seen with the CTEQ6D PDFs. In the high-x region the e^-p measurements agree well with the predictions from both PDFs.

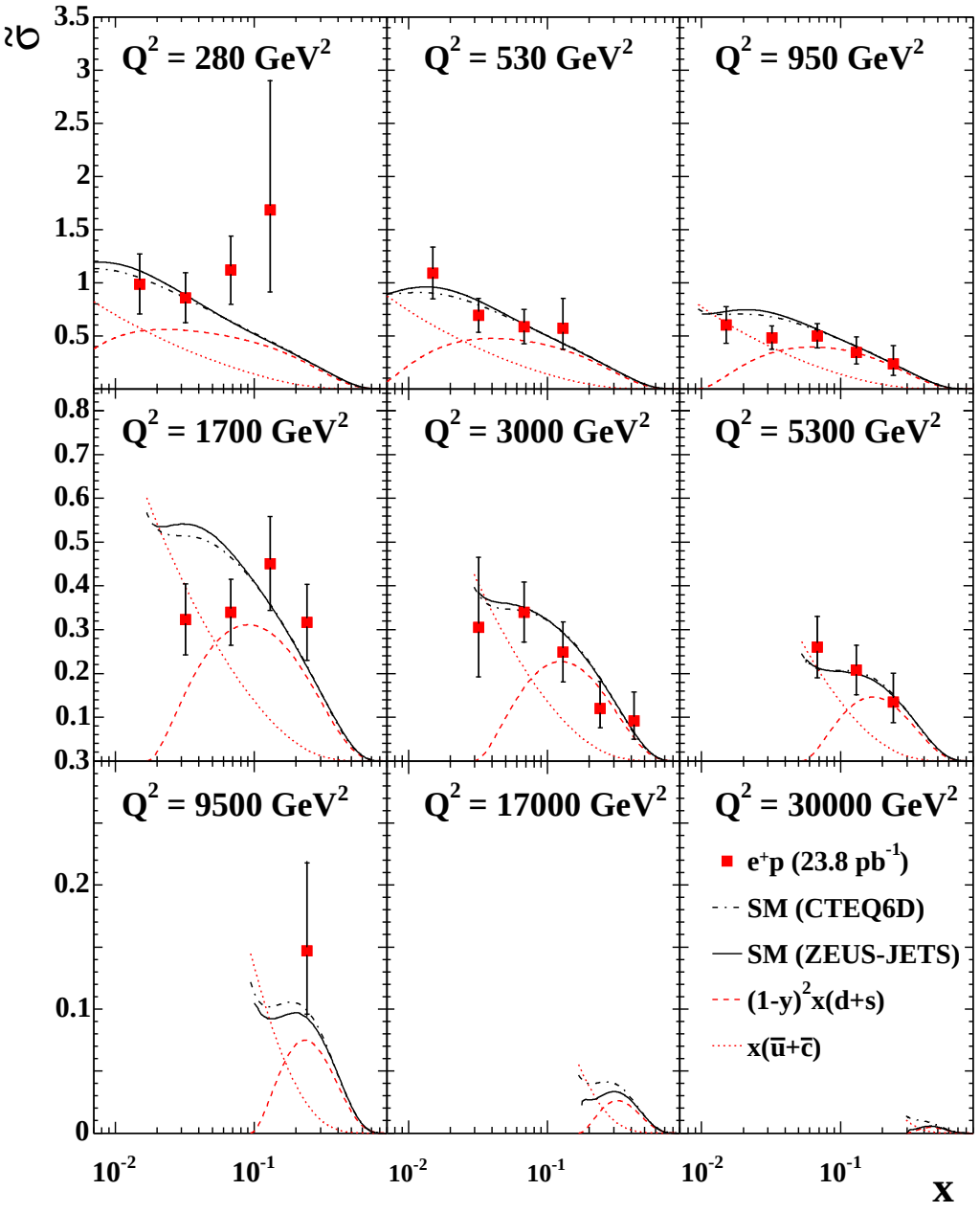

Figure 7.37: Measurements of the reduced cross sections as a function of x in fixed bins of Q^2 for e^+p collisions, with the longitudinal lepton beam polarisation weighted to $P_e = 0$. The inner error bars show the statistical uncertainty and the outer error bars show the combined statistical and systematic uncertainty. The measurements are compared to the SM prediction evaluated using the CTEQ6D and ZEUS-JETS PDFs, shown by the dot-dash and full black lines, respectively. The dashed and dotted red lines represent the PDF contributions $(1-y)^2x(d+s)$ and $x(\bar{u}+\bar{c})$, respectively, calculated using the ZEUS-JETS PDFs.

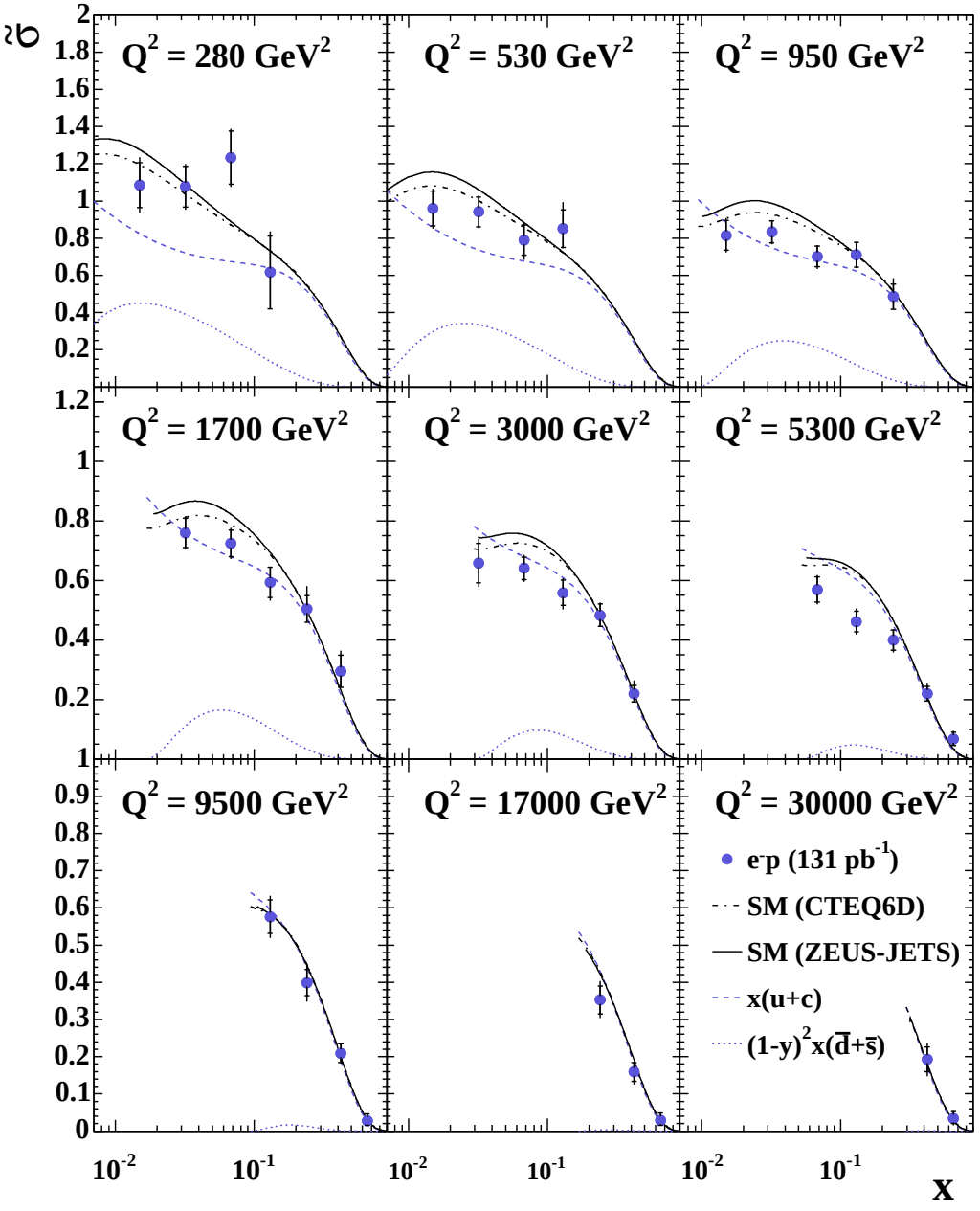

Figure 7.38: Measurements of the reduced cross sections as a function of x in fixed bins of Q^2 for e^-p collisions with the longitudinal lepton beam polarisation weighted to $P_e = 0$. The inner error bars show the statistical uncertainty and the outer error bars show the combined statistical and systematic uncertainty. The measurements are compared to the SM prediction evaluated using the CTEQ6D and ZEUS-JETS PDFs, shown by the dot-dash and full black lines, respectively. The dashed and dotted blue lines represent the PDF contributions $x(u + c)$ and $(1 - y)^2 x(\bar{d} + \bar{s})$, respectively, calculated using the ZEUS-JETS PDFs.

Chapter 8

Summary and conclusions

Cross-section measurements for CC DIS with longitudinally polarised lepton beams are presented. The measurements were made from data collected in the years 2004 to 2005, using the ZEUS detector at HERA. An integrated luminosity of 23.8 pb^{-1} from e^+p collisions was analysed and 131 pb^{-1} from e^-p collisions. These data were split into samples with positive and negative values of P_e.

The single-differential cross-sections $d\sigma/dQ^2$, $d\sigma/dx$ and $d\sigma/dy$ were measured for CC DIS in $e^{\pm}p$ collisions at positive and negative values of P_e. The measurements agreed well with the SM prediction and the expected dependence on P_e was observed across the whole kinematic range of the analysis.

Total cross sections for CC DIS in $e^{\pm}p$ collisions with $Q^2 > 200$ GeV^2 were measured at positive and negative values of P_e. These measurements agreed well with the SM prediction and with similar measurements made by the H1 Collaboration.

Straight lines were fitted to the total cross-section measurements as a function of P_e, to extract values of the cross section for right-handed CC interactions in $e^{\pm}p$ DIS. The statistical and systematic uncertainties were evaluated and the extrapolated right-handed CC cross sections in e^+p and e^-p DIS both agreed with the SM prediction of zero, confirming the absence of right-handed CC from the SM. The main contribution to the systematic uncertainty on the right-handed cross sections came from the uncertainty on P_e.

The extrapolated right-handed cross sections were converted into upper limits on the cross sections for right-handed CC DIS in $e^{\pm}p$ collisions. These upper limits on the cross sections were converted into lower limits on the mass of a right-handed W boson. The $e^{+}p$ fit produced a lower limit of 170 GeV and the $e^{-}p$ fit gave a lower limit of 180 GeV, both at a 95% confidence level. Although these limits are somewhat lower than those found by various other experiments, they are not dependent on factors such as the mass of the right-handed neutrinos, the mixing matrix for right-handed quarks, the right-handed coupling constant and whether the right-handed neutrino is Dirac or Majorana.

Reduced double-differential cross sections for CC DIS were extracted at $P_e = 0$ from $Q^2 = 280$ GeV^2 to $Q^2 = 30,000$ GeV^2 for $e^{-}p$ collisions and to $Q^2 = 9,500$ GeV^2 for $e^{+}p$ collisions. Overall the measurements agreed reasonably well with the SM prediction, although the $e^{-}p$ measurements tended to lie below the prediction in the mid-x and mid-Q^2 region. These measurements will provide information for PDF fits to help constrain the proton valence quark distributions.

Looking ahead to future ZEUS CC measurements, the increased $e^{+}p$ and $e^{-}p$ luminosities will improve the precision of the cross-section measurements. The $e^{+}p$ cross sections will be especially valuable for fitting the less well constrained d quark PDF. In addition, use of new forward tracking measurements from the ZEUS detector could help improve the efficiency of low-γ_0 background rejection. An improvement in the systematic uncertainty on P_e is anticipated from both the TPOL and a new cavity LPOL [125], which will significantly improve the uncertainty on the extrapolated cross section for right-handed CC interactions and therefore also the limit on M_{W_R}.

Appendix A

Cross section measurements

A.1 Single differential cross sections

P_e	Q^2 (GeV^2)	N_{data}	N_{CC}	N_{BG}	$d\sigma/dQ^2$ (pb/GeV^2)	δ_{stat} (pb/GeV^2)	δ_{sys} (pb/GeV^2)
-0.41	280	17	13.5	0.7	0.0220	± 0.0056	$^{+0.0012}_{-0.0013}$
-0.41	530	24	20.5	0.3	0.0142	± 0.0029	± 0.0005
-0.41	950	30	26.4	0.2	0.0086	± 0.0016	± 0.0002
-0.41	1700	18	27.0	0.1	0.00274	± 0.00065	$^{+0.00011}_{-0.00010}$
-0.41	3000	17	21.6	0.1	0.00143	± 0.00035	± 0.00005
-0.41	5300	6	12.7	0.1	0.00028	$^{+0.00017}_{-0.00011}$	$^{+0.00002}_{-0.00001}$
-0.41	9500	3	4.8	0.3	0.000073	$^{+0.000079}_{-0.000044}$	$^{+0.000007}_{0.000006}$
-0.41	17000	2	1.2	0.0	0.000026	$^{+0.000035}_{-0.000017}$	± 0.000003
+0.32	280	39	32.6	0.7	0.0476	± 0.0078	$^{+0.0026}_{-0.0027}$
+0.32	530	51	49.4	0.4	0.0280	± 0.0040	± 0.0009
+0.32	950	44	63.7	0.2	0.0117	± 0.0018	± 0.0003
+0.32	1700	62	65.0	0.1	0.0087	± 0.0011	± 0.0002
+0.32	3000	47	51.9	0.1	0.00366	± 0.00054	$^{+0.00014}_{-0.00013}$
+0.32	5300	37	30.6	0.1	0.00163	± 0.00027	$^{+0.00009}_{-0.00007}$
+0.32	9500	10	11.6	0.3	0.00024	$^{+0.00011}_{-0.00008}$	± 0.00002
+0.32	17000	3	3.0	0.0	0.000036	$^{+0.000035}_{-0.000020}$	± 0.000004

Table A.1: Measurements of the CC DIS cross section $d\sigma/dQ^2$ in bins of Q^2 for e^+p collisions with $P_e = -0.41$ and $P_e = +0.32$. The statistical and systematic uncertainties on the measurements are given and the number of data, CC MC and background MC events in each bin are also listed.

P_e	x	N_{data}	N_{CC}	N_{BG}	$d\sigma/dx$ (pb)	δ_{stat} (pb)	δ_{sys} (pb)
-0.41	0.015	14	15.4	0.2	251	± 68	$^{+10}_{-9}$
-0.41	0.032	24	32.1	0.4	137	± 29	± 4
-0.41	0.068	33	36.6	0.6	87	± 15	± 3
-0.41	0.13	23	23.0	0.1	44.8	± 9.4	± 1.5
-0.41	0.24	12	13.8	0.0	14.0	± 4.0	± 0.8
-0.41	0.42	6	3.8	0.0	5.1	$^{+3.1}_{-2.0}$	$^{+0.4}_{-0.1}$
+0.32	0.015	41	37.2	0.2	690	± 110	± 30
+0.32	0.032	61	77.3	0.5	326	± 42	± 10
+0.32	0.068	85	88.0	0.7	209	± 23	± 7
+0.32	0.13	56	55.2	0.1	101	± 14	± 3
+0.32	0.24	40	33.1	0.1	43.2	± 6.8	$^{+1.7}_{-1.3}$
+0.32	0.42	4	9.2	0.0	3.2	$^{+2.5}_{-1.5}$	$^{+0.2}_{-0.1}$

Table A.2: Measurements of the CC DIS cross section $d\sigma/dx$ in bins of x for e^+p collisions with $P_e = -0.41$ and $P_e = +0.32$. The statistical and systematic uncertainties on the measurements are given and the number of data, CC MC and background MC events in each bin are also listed.

P_e	y	N_{data}	N_{CC}	N_{BG}	$d\sigma/dy$ (pb)	δ_{stat} (pb)	δ_{sys} (pb)
-0.41	0.05	32	22.1	0.3	70	± 12	± 6
-0.41	0.15	30	30.0	0.2	38.6	± 7.1	± 1.5
-0.41	0.27	22	30.0	0.2	20.6	± 4.4	± 0.7
-0.41	0.41	14	20.0	0.5	14.0	± 3.9	± 0.5
-0.41	0.55	12	13.0	0.0	14.4	± 4.2	± 0.5
-0.41	0.69	4	8.2	0.1	5.9	$^{+4.8}_{-2.9}$	± 0.3
-0.41	0.83	3	4.7	0.4	6.0	$^{+6.6}_{-3.7}$	$^{+0.4}_{-0.1}$
+0.32	0.05	64	53.0	0.3	130	± 16	± 10
+0.32	0.15	55	72.2	0.3	65.7	± 8.9	$^{+2.6}_{-2.5}$
+0.32	0.27	68	72.4	0.2	59.3	± 7.2	± 1.9
+0.32	0.41	40	48.2	0.5	37.6	± 6.0	± 1.3
+0.32	0.55	29	31.3	0.1	32.2	± 6.0	± 1.1
+0.32	0.69	23	19.8	0.1	32.0	± 6.7	$^{+1.2}_{-1.0}$
+0.32	0.83	14	11.3	0.4	28.3	± 7.8	$^{+2.0}_{-0.7}$

Table A.3: Measurements of the CC DIS cross section $d\sigma/dy$ in bins of y for e^+p collisions with $P_e = -0.41$ and $P_e = +0.32$. The statistical and systematic uncertainties on the measurements are given and the number of data, CC MC and background MC events in each bin are also listed.

P_e	Q^2 (GeV^2)	N_{data}	N_{CC}	N_{BG}	$d\sigma/dQ^2$ (pb/GeV^2)	δ_{stat} (pb/GeV^2)	δ_{sys} (pb/GeV^2)
-0.27	280	318	298.1	9.3	0.0513	$\pm$0.0030	$\pm$0.0033
-0.27	530	471	470.7	2.8	0.0358	$\pm$0.0017	$\pm$0.0017
-0.27	950	642	704.5	2.9	0.02253	$\pm$0.00090	$^{+0.00077}_{-0.00070}$
-0.27	1700	832	862.6	1.3	0.01500	$\pm$0.00053	$^{+0.00044}_{-0.00037}$
-0.27	3000	836	865.0	0.8	0.00825	$\pm$0.00029	$\pm$0.00025
-0.27	5300	608	687.6	1.5	0.00343	$\pm$0.00014	$\pm$0.00014
-0.27	9500	414	396.9	1.3	0.001395	$\pm$0.000069	$^{+0.000077}_{-0.000091}$
-0.27	17000	146	174.7	0.3	0.000273	$\pm$0.000023	$^{+0.000023}_{-0.000028}$
-0.27	30000	51	44.2	0.1	0.0000544	$\pm$0.0000077	$^{+0.0000067}_{-0.0000098}$
+0.33	280	97	80.9	4.8	0.0297	$\pm$0.0021	$\pm$0.0020
+0.33	530	121	127.7	1.4	0.0177	$\pm$0.0016	$\pm$0.0009
+0.33	950	202	191.2	1.5	0.01371	$\pm$0.00097	$^{+0.00047}_{-0.00043}$
+0.33	1700	237	234.1	0.7	0.00828	$\pm$0.00054	$^{+0.00024}_{-0.00021}$
+0.33	3000	213	234.8	0.4	0.00407	$\pm$0.00028	$\pm$0.00012
+0.33	5300	172	186.6	0.8	0.00188	$\pm$0.00014	$^{+0.00008}_{-0.00007}$
+0.33	9500	101	107.7	0.7	0.000658	$\pm$0.000066	$^{+0.000036}_{-0.000043}$
+0.33	17000	42	47.4	0.1	0.000152	$\pm$0.000024	$^{+0.000013}_{-0.000015}$
+0.33	30000	11	12.0	0.1	0.0000227	$^{+0.0000092}_{-0.0.0000068}$	$^{+0.0000028}_{-0.0000041}$

Table A.4: Measurements of the CC DIS cross section $d\sigma/dQ^2$ in bins of Q^2 for e^-p collisions with $P_e = -0.27$ and $P_e = +0.33$. The statistical and systematic uncertainties on the measurements are given and the number of data, CC MC and background MC events in each bin are also listed.

P_e	x	N_{data}	N_{CC}	N_{BG}	$d\sigma/dx$ (pb)	δ_{stat} (pb)	δ_{sys} (pb)
-0.27	0.015	350	367.1	6.2	715	± 39	± 43
-0.27	0.032	828	837.3	4.4	580	± 20	± 18
-0.27	0.068	1081	1172.5	4.4	352	± 11	$^{+12}_{-13}$
-0.27	0.13	875	956.4	1.3	205.3	± 7.0	$^{+7.5}_{-7.7}$
-0.27	0.24	754	759.6	0.7	104.1	± 3.8	$^{+4.5}_{-3.3}$
-0.27	0.42	335	313.2	0.0	32.2	± 1.8	$^{+2.4}_{-0.8}$
-0.27	0.65	36	22.8	0.1	5.62	± 0.95	$^{+0.36}_{-0.81}$
+0.33	0.015	90	99.6	3.2	350	± 38	± 22
+0.33	0.032	202	227.2	2.2	273	± 19	± 9
+0.33	0.068	337	318.2	2.3	212	± 12	$^{+7}_{-8}$
+0.33	0.13	258	259.6	0.7	117.3	± 7.3	$^{+4.3}_{-4.4}$
+0.33	0.24	189	206.2	0.3	50.5	± 3.7	$^{+2.2}_{-1.6}$
+0.33	0.42	91	85.0	0.0	16.9	± 1.8	$^{+1.3}_{-0.4}$
+0.33	0.65	4	6.2	0.0	1.20	$^{+0.96}_{-0.58}$	$^{+0.08}_{-0.17}$

Table A.5: Measurements of the CC DIS cross section $d\sigma/dx$ in bins of x for e^-p collisions with $P_e = -0.27$ and $P_e = +0.33$. The statistical and systematic uncertainties on the measurements are given and the number of data, CC MC and background MC events in each bin are also listed.

P_e	y	N_{data}	N_{CC}	N_{BG}	$d\sigma/dy$ (pb)	δ_{stat} (pb)	δ_{sys} (pb)
-0.27	0.05	766	690.6	3.1	212.5	± 7.8	$^{+14.3}_{-4.0}$
-0.27	0.15	874	928.3	4.4	137.1	± 4.7	$^{+3.5}_{-3.9}$
-0.27	0.27	893	972.4	4.2	100.5	± 3.4	$^{+3.8}_{-4.4}$
-0.27	0.41	627	715.5	2.3	73.6	± 3.0	$^{+3.4}_{-3.5}$
-0.27	0.55	502	534.2	1.5	62.9	± 2.8	$^{+3.0}_{-3.1}$
-0.27	0.69	409	399.6	0.8	56.9	± 2.8	± 2.5
-0.27	0.83	249	264.2	3.9	44.4	± 2.9	± 2.6
+0.33	0.05	205	187.4	1.6	109.9	± 7.8	$^{+7.4}_{-2.1}$
+0.33	0.15	265	251.9	2.3	80.3	± 5.0	$^{+2.1}_{-2.3}$
+0.33	0.27	264	263.9	2.2	57.4	± 3.6	$^{+2.2}_{-2.5}$
+0.33	0.41	179	194.2	1.2	40.6	± 3.1	± 1.9
+0.33	0.55	140	145.0	0.8	33.9	± 2.9	$^{+1.6}_{-1.7}$
+0.33	0.69	78	108.4	0.4	21.0	± 2.4	± 0.9
+0.33	0.83	65	71.7	2.0	22.1	± 2.8	± 1.3

Table A.6: Measurements of the CC DIS cross section $d\sigma/dy$ in bins of y for e^-p collisions with $P_e = -0.27$ and $P_e = +0.33$. The statistical and systematic uncertainties on the measurements are given and the number of data, CC MC and background MC events in each bin are also listed.

A.2 Reduced cross sections

x	Q^2 (GeV^2)	N_{data}	N_{CC}	N_{BG}	$\tilde{\sigma}$	δ_{stat}	δ_{sys}
0.015	280	14	14.6	0.1	0.99	± 0.28	± 0.06
0.032	280	16	15.4	0.5	0.86	± 0.23	$^{+0.04}_{-0.05}$
0.068	280	14	8.0	0.1	1.12	± 0.32	$^{+0.04}_{-0.05}$
0.13	280	5	1.4	0.0	1.7	$^{+1.2}_{-0.8}$	± 0.1
0.015	530	23	18.6	0.3	1.09	± 0.24	$^{+0.04}_{-0.03}$
0.032	530	21	24.0	0.1	0.69	± 0.16	$^{+0.03}_{-0.02}$
0.068	530	15	15.6	0.1	0.59	± 0.16	± 0.02
0.13	530	9	6.8	0.0	0.57	$^{+0.28}_{-0.20}$	$^{+0.01}_{-0.02}$
0.015	950	14	16.2	0.0	0.60	± 0.17	± 0.02
0.032	950	22	31.0	0.2	0.48	± 0.11	± 0.01
0.068	950	22	24.6	0.2	0.50	± 0.11	± 0.02
0.13	950	11	13.0	0.0	0.34	$^{+0.15}_{-0.11}$	$^{+0.00}_{-0.01}$
0.24	950	5	4.9	0.0	0.24	$^{+0.17}_{-0.11}$	$^{+0.00}_{-0.01}$
0.032	1700	18	28.9	0.0	0.323	± 0.081	± 0.010
0.068	1700	23	32.3	0.1	0.340	± 0.075	± 0.012
0.13	1700	20	16.2	0.0	0.45	$0\pm .11$	± 0.01
0.24	1700	15	10.1	0.0	0.317	± 0.087	± 0.014
0.032	3000	8	10.1	0.1	0.30	$^{+0.16}_{-0.11}$	± 0.02
0.068	3000	28	29.3	0.1	0.340	± 0.068	± 0.015
0.13	3000	15	18.2	0.0	0.249	± 0.068	± 0.012
0.24	3000	8	12.5	0.0	0.119	$^{+0.063}_{-0.044}$	$^{+0.004}_{-0.002}$
0.42	3000	5	3.4	0.0	0.092	$^{+0.066}_{-0.042}$	$^{+0.004}_{-0.002}$
0.068	5300	16	13.8	0.2	0.260	± 0.070	$^{+0.016}_{-0.014}$
0.13	5300	15	15.3	0.0	0.208	± 0.057	± 0.013
0.24	5300	9	10.0	0.0	0.135	$^{+0.065}_{-0.047}$	$^{+0.008}_{-0.005}$
0.24	9500	9	6.0	0.0	0.147	$^{+0.071}_{-0.051}$	± 0.013

Table A.7: Measurements of the CC DIS reduced cross section in bins of Q^2 and x for e^+p collisions at $P_e = 0$. The statistical and systematic uncertainties on the measurements are given and the number of data, CC MC and background MC events in each bin are also listed.

x	Q^2 (GeV^2)	N_{data}	N_{CC}	N_{BG}	$\tilde{\sigma}$	δ_{stat}	δ_{sys}
0.015	280	120	120.0	6.9	1.09	±0.12	±0.09
0.032	280	133	121.1	2.4	1.08	±0.11	$^{+0.05}_{-0.06}$
0.068	280	99	66.9	0.6	1.23	±0.14	$^{+0.06}_{-0.07}$
0.13	280	13	14.7	0.0	0.62	±0.20	$^{+0.10}_{-0.01}$
0.015	530	141	153.6	0.4	0.960	±0.093	$^{+0.053}_{-0.054}$
0.032	530	191	193.8	2.4	0.941	±0.079	±0.039
0.068	530	124	128.8	1.1	0.789	±0.082	$^{+0.038}_{-0.066}$
0.13	530	93	74.8	0.2	0.85	±0.10	$^{+0.10}_{-0.03}$
0.015	950	144	156.4	2.1	0.815	±0.079	$^{+0.048}_{-0.047}$
0.032	950	264	284.6	0.3	0.833	±0.059	±0.027
0.068	950	208	237/0	0.8	0.702	±0.056	$^{+0.025}_{-0.039}$
0.13	950	153	144.4	0.2	0.711	±0.066	$^{+0.031}_{-0.015}$
0.24	950	69	68.7	0.2	0.486	±0.067	$^{+0.073}_{-0.006}$
0.032	1700	310	323.1	1.1	0.760	±0.050	$^{+0.024}_{-0.023}$
0.068	1700	338	354.7	0.4	0.724	±0.045	±0.027
0.13	1700	178	195.2	0.2	0.594	±0.051	$^{+0.011}_{-0.035}$
0.24	1700	169	157.9	0.2	0.504	±0.045	$^{+0.063}_{-0.004}$
0.42	1700	39	29.0	0.0	0.295	±0.054	$^{+0.043}_{-0.010}$
0.032	3000	132	141.4	0.4	0.659	±0.066	$^{+0.048}_{-0.047}$
0.068	3000	380	413.8	0.7	0.641	±0.038	$^{+0.025}_{-0.026}$
0.13	3000	229	256.5	0.1	0.558	±0.042	$^{+0.025}_{-0.035}$
0.24	3000	218	206.1	0.1	0.483	±0.038	$^{+0.020}_{-0.006}$
0.42	3000	84	80.0	0.0	0.220	±0.028	$^{+0.034}_{-0.003}$
0.068	5300	242	266.7	2.0	0.569	±0.042	$^{+0.026}_{-0.026}$
0.13	5300	235	300.2	0.2	0.462	±0.035	±0.026
0.24	5300	182	200.7	0.0	0.400	±0.034	$^{+0.013}_{-0.025}$
0.42	5300	109	99.7	0.0	0.219	±0.024	$^{+0.027}_{-0.002}$
0.65	5300	12	6.2	0.0	0.068	±0.023	$^{+0.015}_{-0.002}$
0.13	9500	220	209.7	0.8	0.576	±0.045	$^{+0.034}_{-0.036}$
0.24	9500	170	180.4	0.1	0.399	±0.035	$^{+0.031}_{-0.036}$
0.42	9500	92	84.5	0.0	0.209	±0.025	$^{+0.005}_{-0.011}$
0.65	9500	6	7.1	0.0	0.028	$^{+0.019}_{-0.013}$	$^{+0.003}_{-0.002}$
0.24	17000	116	132.8	0.3	0.353	±0.038	$0^{+.033}_{-0.032}$
0.42	17000	54	62.5	0.0	0.159	±0.025	$^{+0.013}_{-0.023}$
0.65	17000	6	6.3	0.0	0.029	$^{+0.020}_{-0.013}$	$^{+0.002}_{-0.004}$
0.42	30000	44	40.2	0.0	0.193	±0.033	$^{+0.029}_{-0.031}$
0.65	30000	8	6.7	0.1	0.034	$^{+0.019}_{-0.014}$	$^{+0.003}_{-0.013}$

Table A.8: Measurements of the CC DIS reduced cross section in bins of Q^2 and x for e^-p collisions at $P_e = 0$. The statistical and systematic uncertainties on the measurements are given and the number of data, CC MC and background MC events in each bin are also listed.

Bibliography

[1] HERA. A proposal for a Large Electron-Proton Colliding Beam Facility at DESY. DESY HERA-81-10, 1981.

[2] R. P. Feynman. Very High-Energy Collisions of Hadrons. *Phys. Rev. Lett.*, 23:1415–1417, 1969.

[3] F. Halzen and A. Martin. *Quarks and Leptons: An Introductory Course in Modern Particle Physics*. John Wiley and Sons, 1984.

[4] A. C. Bencenuti *et. al.* A high statistics measurement of the proton structure functions $F_2(x, Q^2)$ and R from deep inelastic muon scattering at high Q^2. *Phys. Lett.*, B 223:485, 1989.

[5] M. Arneodo *et. al.* Measurement of the proton and deuteron structure functions, F_{2p} and F_{2d}, and of the ratio σ_L/σ_T. *Nucl. Phys.*, B 483:3, 1997.

[6] M. R. Adams *et. al.* Proton and deuteron structure functions in muon scattering at 470 GeV. *Phys. Rev.*, D 54:3006, 1996.

[7] W. G. Seligman *et. al.* Improved Determination of α_s From Neutrino-Nucleon Scattering. *Phys. Rev. Lett.*, 79:1213, 1997.

[8] The ZEUS Collaboration. The ZEUS Detector Status Report. `http://www-zeus.desy.de/bluebook/bluebook.html`, 1993.

[9] The H1 Collaboration. The H1 detector at HERA. *Nucl. Inst. Meth.*, A 386:310–347, 1997.

[10] J. D. Bjorken and E. A. Paschos. Inelastic electron-proton and γ-proton scattering and the structure of the nucleon. *Phys. Rev.*, 185, 1975.

[11] G. Miller *et. al.* $e^- p$ scattering at large momentum transfers and the inelastic structure functions of the proton. *Phys. Rev.*, D 5:528, 1972.

[12] H. W. Kendall. Deep inelastic scattering: Experiments on the proton and the observation of scaling. *Rev. Mod. Phys.*, 63:597–614, 1991.

[13] C. G. Callan and D. J. Gross. High energy electroproduction and the constitution of the electric current. *Phys. Rev. Lett.*, 22:156–159, 1969.

[14] J. Friedman. Deep inelastic scattering: Comparisons with the quark model. *Rev. Mod. Phys.*, 63:615–627, 1991.

[15] D. H. Perkins. Proceedings of the XVI International Conference on High Energy Physics. Chicago and NAL. Vol. 4, 189, 1972.

[16] S. Chekanov *et. al.* Measurement of the neutral current cross section and F_2 structure function for deep inelastic e^+p scattering at HERA. *Eur. Phys. J*, C 21:443–471, 2001.

[17] C. Adloff *et. al.* Measurement and QCD Analysis of Neutral and Charged Current Cross Sections at HERA. *Eur. Phys. J*, C 30:1–32, 2003.

[18] ZEUS-ONLY QCD fit. Preliminary results presented at the 39^{th} Rencontres de Moriond on QCD and High Energy Hadronic Interactions., 2004.

[19] V. N. Gribov and L. N. Lipatov. Deep Inelastic *ep* scattering in Perturbation Theory. *Sov. J. Nucl. Phys*, 15:438, 1972.

[20] L. N. Lipatov. *Sov. J. Nucl. Phys*, 20:96, 1975.

[21] Y. L. Dokshitzer. Calculation of the structure functions for deep inelastic scattering and e^+e^- annihilation by perturbation theory in quantum chromodynamics. *Sov. Phys. JETP*, 46:641–653, 1977.

[22] G. Altarelli and G. Parisi. Asymptotic freedom in parton language. *Nucl. Phys.*, B 126:298–318, 1977.

[23] S. Chekanov *et. al.* An NLO CDQ analysis of inclusive cross-section and jet-production data from the ZEUS experiment. *Eur. Phys. J*, C 42:1–16, 2005.

[24] S. Chekanov *et. al.* ZEUS next-to-leading-order QCD analysis of data on deep inelastic scattering. *Phys. Rev.*, D 67:012007, 2003.

[25] A. D. Martin *et. al.* Parton distributions and the LHC: W and Z production. *Eur. Phys. J*, C 14:133–145, 2000.

[26] S. Kretzer *et. al.* CTEQ6 Parton Distributions with Heavy Quark Mass Effects. *Phys. Rev.*, D 69, 2004.

[27] H1 and ZEUS Collaborations. Electroweak Neutral Currents at HERA. Proceedings submitted to 33^{rd} International Conference on High Energy Physics, ICHEP06, Moscow., July 2006.

[28] A. M. Cooper-Sarkar *et. al.* High-Q^2 deep inelastic scattering at HERA. *J. Phys.*, G 25:1387–1409, 1999.

[29] S. Chekanov *et. al.* Measurement of high-Q^2 e^-p neutral currect cross sections at HERA and the extraction of xF_3. *Eur. Phys. J*, C 28:175–201, 2003.

[30] S. Chekanov *et. al.* High-Q^2 neutral currect cross section in e^+p deep inelastic scattering at $\sqrt{s} = 318$ GeV. *Phys. Rev.*, D 70, 2004.

[31] C. Adloff *et. al.* Measurement of neutral and charged current cross-sections in positron-proton collisions at large momentum transfer. *Eur. Phys. J*, C 13:609, 2000.

[32] C. Adloff *et. al.* Measurement of neutral and charged current cross-sections in electron-proton collisions at high Q^2. *Eur. Phys. J*, C 19:269, 2001.

[33] S. Chekanov *et. al.* Measurement of high-Q^2 neutral current deep inelastic scattering cross sections with a longitudinally polarised electron beam at HERA. Proceedings submitted to 33^{rd} International Conference on High Energy Physics, ICHEP06, Moscow., July 2006.

[34] R. Devenish and A. M. Cooper-Sarkar. *Deep Inelastic Scattering.* Oxford University Press, 2003.

[35] S. Chekanov *et. al.* QCD and Electroweak analysis of the ZEUS NC and CC inclusive and jet cross sections. Presented at the 33^{rd} International Conference on High Energy Physics, ICHEP06, Moscow., July 2006.

[36] D. Acosta *et. al. Phys. Rev.*, D 70:032002, 2005.

[37] Aleph Coll., Delphi Coll., L3 coll., OPAL Coll., and SLD Coll. *Phys. Rep.*, 427:257, 2006.

[38] A. Aktas *et. al.* A determination of electroweak parameters at HERA. *Phys. Lett.*, B 632:35, 2006.

[39] S. Chekanov *et. al.* Measurement of high-Q^2 charged currect cross sections in e^+p deep inelastic scattering at HERA. *Eur. Phys. J*, C 32:1–16, 2003.

[40] S. Chekanov *et. al.* Measurement of high-Q^2 charged currect cross sections in e^-p deep inelastic scattering at HERA. *Phys. Lett.*, B 539:197–217, 2003.

[41] S. Chekanov *et. al.* Erratum. *Phys. Lett.*, B 552:308, 2003.

[42] S. Chekanov *et. al.* Measurement of High-Q^2 Deep Inelastic Scattering Cross Sections with a Longitudinally Polarised Positron Beam at HERA. *Phys. Lett.*, B, 2006.

[43] A. Aktas *et. al.* First Measurement of Charged Current Cross Sections at HERA with Longitudinally Polarised Positrons. *Phys. Lett.*, B 634:173, 2006.

[44] M. Kuze and Y. Sirois. Search for Particles and Forces Beyond the Standard Model at HERA ep and Tevatron $p\bar{p}$ Colliders. DESY Note, DESY-02-156. hep-ex/0211048, 2002.

[45] J. Alitti *et. al.* A search for new intermediate vector bosons and excited quarks decaying to two-jets at the CERN $p\bar{p}$ collider. *Nucl. Phys.*, B 400:3–22, 1993.

[46] S. Abachi *et. al.* Search for Right-Handed W bosons and Heavy W' in $p\bar{p}$ Collisions at $\sqrt{s} = 1.8$ TeV. *Phys. Rev. Lett.*, 76:3271–3276, 1996.

[47] F. Abe *et. al.* Search for Charged Bosons Heavier than the W Boson in $p\bar{p}$ Collisions at $\sqrt{s} = 1800$ GeV. *Phys. Rev. Lett.*, 74:2900–2094, 1995.

[48] R.G. Milner on behalf of the HERMES Collabortation. The HERMES Experiment. *Nucl. Phys.*, A 622:16–30, 1997.

[49] E. Hartouni *et. al.* An Experiment to Study CP Violation in the B System Using an Internal Target at the HERA Proton Ring. Design Report, DESY-PRC 95/01, 1995.

[50] F. Willeke. Summary of the HERA Proton-Positron Luminosity Run 2004. HERA Note, HERA-04-01, 2004.

[51] U. Schneekloth. The HERA Luminosity Upgrade. HERA Note, HERA-98-05, 1998.

[52] G. Ingelman, A. De Roeck, and R. Klanner, editors. *Future Physics at HERA*. DESY, 1995-1996. `http://www.desy.de/~heraws96/`.

[53] K. Long and K.P. Schüler. Polarisation measurements on $e^{\pm}$ beams. *Nucl. Inst. Meth.*, A 494:75–80, 2002.

[54] A. A. Sokolov and I. M. Ternov. On Polarization and Spin Effects in the Theory of Synchrotron Radiation. *Sov. Phys. Dokl.*, 8:1203, 1964.

[55] D.P. Barber *et. al.* The first achievement of longitudinal spin polarization in a high energy electron storage ring. *Phys. Lett.*, B 343:436–443, 1995.

[56] D.P. Barber *et. al.* High spin polarization at the HERA electron storage ring. *Nucl. Inst. Meth.*, A 338:166–184, 1994.

[57] T. Behnke *et. al.* A New Analysis for the Transverse Polarimeter at HERA II. POL2000 Group, DESY, July 2004.

[58] D.P. Barber *et. al.* The HERA polarimeter and the first observation of electron spin polarization at HERA. *Nucl. Inst. Meth.*, A 329:79–111, 1993.

[59] See, for example, Encyclopedia of Laser Physics and Technology. `http://www.rp-photonics.com/pockels_cells.html`.

[60] J. Böhme. Precision measurement with the transverse polarimeter at HERA II. *Eur. Phys. J.*, C 33:1067–1069, 2004.

[61] F. Corriveau, V. Garibyan, O. Ota, and S. Schmitt. Calibration of the HERA Transverse Polarimeter for the 2003/2004 Data. POL2000 Group, DESY, 2004.

[62] U. Stösslein, M. Kataoka, K. Nagano, C. Fry, A. Tapper, and L. Bellagamba. Requirements for the lepton beam polarisation at HERA II. ZEUS Note, ZEUS-05-003, 2005.

[63] O. Ota. Measurement of lepton beam polarisation and HERA. ZEUS Note, ZEUS-05-012, 2005.

[64] T. Behnke *et. al.* The Transverse Polarimeter (TPOL) Test Beam at CERN in July-August 2001. POL2000 Group, DESY, 2002.

[65] M. Beckmann *et. al.* The Longitudinal Polarimeter at HERA. *Nucl. Inst. Meth.*, A 479:334–348, 2002.

[66] A. Airapetian, R. Fabbri, and B. Zihlmann. Data Quality of LPOL Measurements. POL2000 Group, DESY, 2004.

[67] M. Derrick *et. al.* Design and construction of the ZEUS barrel calorimeter. *Nucl. Inst. Meth.*, A 309:77–100, 1991.

[68] A. Andersen *et. al.* Construction and beam test of the ZEUS forward and rear calorimeter. *Nucl. Inst. Meth.*, A 309:101–142, 1991.

[69] A. Bernstein *et. al.* Beam tests of the ZEUS barrel calorimeter. *Nucl. Inst. Meth.*, A 336:23–52, 1993.

[70] R. Yoshida. Introduction to Calorimetry and the ZEUS Calorimeter. ZEUS Lecture Series, DESY, November 2000.

[71] R. Pawlak. Vertex reconstruction from FCAL timing. ZEUS Note, ZEUS-98-040, 1998.

[72] B. Foster *et. al.* The design and construction of the ZEUS central tracking detector. *Nucl. Inst. Meth.*, A 338:254–283, 1994.

[73] R. Hall-Wilton, N. McCubbin, P. Nylander, M. Sutton, and M. Wing. The CTD Tracking Resolution. ZEUS Note, ZEUS-99-024, 1999.

[74] R. Carlin. The ZEUS microvertex detector. *Nucl. Inst. Meth.*, A 511:32–37, 2003.

[75] T. Haas. The ZEUS microvertex detector. *Nucl. Inst. Meth.*, A 549:37–43, 2005.

[76] H. Bethe and W. Heitler. *Proc. Roy. Soc.*, A 146:83, 1934.

[77] J. Chwastowski, J. Figiel, A. Kotarba, K. Olkiewicz, and L. Suszycki. Aerogel Cherenkov detectors for the luminosity measurement at HERA. *Nucl. Inst. Meth.*, A 504:222–227, 2003.

[78] J. Andruszków *et. al.* Luminosity Measurement in the ZEUS Experiment. ZEUS Note, ZEUS-01-004, 2001.

[79] M. Helbich *et. al.* The Spectrometer System for Measuring ZEUS Luminosity at HERA. Technical Report, ZEUS Spectrometer Group. Submitted to Nucl. Instr. Meth., 2005.

[80] Y. Ning *et. al.* Luminosity Spectrometer Measurement. ZEUS Note, ZEUS-05-006, 2005.

[81] M. Helbich *et. al.* The Spectrometer System for Measuring ZEUS Luminosity at HERA. ZEUS Note, ZEUS-06-002, 2006.

[82] R. Carlin, W.H. Smith, K. Tokushuku, and L.W. Wiggers. The trigger of ZEUS, a flexible system for a high bunch crossing rate collider. *Nucl. Inst. Meth.*, A 379:542–544, 1996.

[83] W.H Smith *et. al.* The ZEUS calorimeter first level trigger. *Nucl. Inst. Meth.*, A 355:278–294, 1995.

[84] B. G. Bylsma *et. al.* A fast cluster finding processor for the ZEUS calorimeter. *Nucl. Inst. Meth.*, A 337:512–520, 1994.

[85] G.P. Heath *et. al.* The ZEUS first level tracking trigger. *Nucl. Inst. Meth.*, A 315:431–435, 1992.

[86] A. Quadt, R.C.E. Devenish, S. Topp-Jørgensen, M. Sutton, H.A.J.R. Uijterwaal, A.F. Byrne, and D.M. Gingrich. The design and performance of the ZEUS central tracking detector second-level trigger. *Nucl. Inst. Meth.*, A 438:472–501, 1999.

[87] H. Spiesberger. HERACLES and DJANGOH: Event Generation for *ep* Interactions at HERA Including Radiative Processes. See `http://www.desy.de/ hspiesb/djangoh.html`, 1998.

[88] G. Ingelman, A. Edin, and J. Rathsman. LEPTO 6.5 - A Monte Carlo generator for deep inelastic lepton-nucleon scattering. *Comp. Phys. Comm.*, 101:108–134, 1997.

[89] H. Spiesberger. HERACLES. An Event Generator for ep Interactions at HERA Including Radiative Processes. See `http://www.desy.de/ hspiesb/heracles.html`, 1996.

[90] L. Lönnblad. Ariadne version 4 - A program for simulation of QCD cascardes implementing the colour dipole model. *Comp. Phys. Comm.*, 71:15–31, 1992.

[91] G. Ingelman, A. Edin, and J. Rathsman. A Monte Carlo generator for deep inelastic lepton-nucleon scattering. *Comp. Phys. Comm.*, 101:108, 1997.

[92] T. Sjöstrand. LEPTO 6.5 - A Monte Carlo generator for deep inelastic lepton-nucleon scattering. *Comp. Phys. Comm.*, 39:347–407, 1986.

[93] T. Sjöstrand and M Bengtsson. The Lund Monte Carlo for jet fragmentation and e^+e^- physics - JETSET Version 6.3 - an update. *Comp. Phys. Comm.*, 43:367–379, 1987.

[94] T. Sjöstrand. High-energy-physics event generation with PYTHIA 5.7 and JETSET 7.4. *Comp. Phys. Comm.*, 82:74–89, 1994.

[95] H.L. Lai *et. al.* Global QCD Analysis of Parton Structure of the Nucleon: CTEQ5 Parton Distributions. *Eur. Phys. J.*, C 12:375–392, 2000.

[96] S. Aid *et. al.* A measurement and QCD analysis of the proton structure function $F_2(x, Q^2)$ at HERA. *Nucl. Phys.*, B 470:3, 1996.

[97] C. Adloff *et. al.* A measurement of the proton structure function $F_2(x, Q^2)$ at low x and low Q^2 at HERA. *Nucl. Phys.*, B 497:3, 1997.

[98] J. Breitweg *et. al.* ZEUS results on the measurement and phenomenology of F_2 at low x and low Q^2. *Eur. Phys. J.*, C 7:609, 1999.

[99] G. Moreno *et. al.* Dimuon production in proton-copper collisions at $\sqrt{s} =$ 38.8 GeV. *Phys. Rev.*, D 43:2815, 1991.

[100] E. A. Hawker *et. al.* Measurement of the Light Antiquark Flavor Asymmetry in the Nucleon Sea. *Phys. Rev. Lett.*, 80:3715, 1998.

[101] F. Abe *et. al.* FERMILAB-PUB-98-207, 1998.

[102] B. Abbott *et. al. Phys. Rev. Lett.*

[103] F. Bedeschi. Talk at Hadron Collider Physics Conference, Bombay, January 1999.

[104] G. Marchesini, B.R. Webber, G. Abbiendi, I.G. Knowles, M.H. Seymour, and L. Stanco. HERWIG 5.1 - a Monte Carlo event generator for simulating hadron emission reactions with interfering gluons. *Comp. Phys. Comm.*, 67:465–508, 1992.

[105] T. Abe. GRAPE-Dilepton (Version 1.1) A generator for dilepton production in *ep* collisions. *Comp. Phys. Comm.*, 136:126–147, 2001.

[106] U. Baur, J.A.M. Vermaseren, and D. Zeppenfeld. Electroweak vector boson production in high-energy ep collisions. *Nucl. Phys.*, B 375:3–44, 1992.

[107] F. Jaquet and A. Blondel. Proceedings of the study of an *ep* facility for Europe. DESY-79-48, 1979.

[108] W. Buchmüller and G. Ingelman, editors. *Physics at HERA*. DESY, 1991.

[109] H. Lim. Noise for 2002/2003 data. Presentation at New Data Tools Meeting, DESY, February 2004.

[110] M. Martinez. Calorimeter Noisy Cells Study for 1998-2000 ZEUS Data. ZEUS Note, ZEUS-00-016, 2000.

[111] A. Savin. Study of Calorimeter Noise in the 1996 data. ZEUS Note, ZEUS-98-007, 1998.

[112] N. Tuning. ZUFOs: Hadronic final state reconstruction with calorimeter, tracking and backsplash correction. ZEUS Note, ZEUS-01-021, 2001.

[113] J. Grosse-Knetter. Energy Correction for Islands. ZEUS Note, ZEUS-97-039, 1997.

[114] J. Grosse-Knetter. Corrections for the hadronic final state. ZEUS Note, ZEUS-98-031, 1998.

[115] G. F. Hartner. VCTRAK Briefing: Program and Math. ZEUS Note, ZEUS-98-058, 1998.

[116] R. Frühwirth. Application of Kalman filtering to track and vertex fitting. *Nucl. Inst. Meth.*, A 262:444, 1987.

[117] E. Maddox. A Kalman filter track fit for the ZEUS microvertex detector. ZEUS Note, ZEUS-03-008, 2003.

[118] E. Maddox. *Study of heavy quark production at HERA using the ZEUS microvertex detector*. PhD thesis, NIKHEF, University of Amsterdam, December 2004. ISBN 90-9018-763-4.

[119] H. Abramowicz, Allen Caldwell, and Ralph Sinkus. Neural Network based Electron Identification in the ZEUS Calorimeter. DESY Note, DESY-95-054. hep-ex/9505004, 1995.

[120] L. Lönnblad. Ariadne version 4 - A program for simulation of QCD cascades implementing the colour dipole model. *Comp. Phys. Comm.*, 71:15–31, 1992.

[121] M. Kataoka. *Measurement of the Polarisation Dependence of Charged Current Cross Sections in $e+p$ Deep Inelastic Scattering at $\sqrt{s} = 318$ GeV.* PhD thesis, Nara Women's University, January 2005.

[122] K. Nagano. High-Q^2 NC e^+ updates. Talk given at the ZEUS High Q^2 meeting at DESY. ZEUS internal note in preparation., September 2005.

[123] A. Aktas *et. al.* Charged current interactions in *ep* scattering at HERA with longitudinally polarised electrons. Proceedings submitted to 33^{rd} International Conference on High Energy Physics, ICHEP06, Moscow., July 2006.

[124] A. Arbuzov *et. al.* HECTOR 1.00 : A program for the calculation of QED, QCD and electroweak corrections to *ep* and $l^{\pm}N$ deep inelastic neutral and charged current scattering. *Comp. Phys. Comm.*, 94:128, 1996.

[125] E. Barrelet *et. al.* Proposal to Upgrade the Longitudinal Polarimeter. Submitted to the October 2000 DESY PRC. 00-02., 2000.

Acknowledgements

I would like to thank my supervisors, Ken Long and Paul Dauncey, for their invaluable support, advice and guidance throughout my PhD. I owe a huge thank you to Alex Tapper, for his constant supply of advice, encouragement and guidance in Hamburg and back at Imperial. Thank you also to Daniel Bowerman, for his excellent help and advice during my work on CALICE.

I am grateful for much detailed advice from Kunihiro Nagano and Enrico Tassi. I would like to thank the POL2000 and ZEUS trigger groups for their guidance and lively discussions.

Living in Hamburg was great experience, thanks mostly to the many students and post-docs I met. In particular, I would like to thank the other UK students, Mark, Philip, Paul, Billy and John, for many happy memories and a black eye.

I would like to thank the students in my year at Imperial, and the colleagues that I have had coffee, lunch, dinner and the odd drink with over the last few years, for being such a friendly and supportive group to work with.

Thank you to all my family and friends who have supported me during my PhD and especially to those who braved the Ryanair experience and visited me in Hamburg - it was really great having you stay.

Thank you to Jason for countless weekends spent in Hamburg. Thanks for all the cups of tea you made while I was writing up and mostly for just being there, whenever I needed you.

I acknowledge the financial support of the Particle Physics and Astronomy Research Council.